THE MEASUREMENT OF THE RARE DECAY K-PLUS TO PI-PLUS, NEUTRINO, AND ANTI-NEUTRINO

by

JOSS IVES

B.Sc., The University of Saskatchewan, 2000
M.Sc., The University of Saskatchewan, 2003

A THESIS SUBMITTED IN PARTIAL FULFILLMENT OF
THE REQUIREMENTS FOR THE DEGREE OF

DOCTOR OF PHILOSOPHY

in

THE FACULTY OF GRADUATE STUDIES

(Physics)

THE UNIVERSITY OF BRITISH COLUMBIA

(Vancouver)

December 2008

Abstract

Brookhaven National Laboratory experiment E949 was designed to search for the rare K meson decay $K^+ \to \pi^+ \nu \bar{\nu}$, a decay sensitive to physics beyond the Standard Model. While previous data analyses dealt with the high π^+ momentum region accessible for this reaction, this thesis concentrates on the lower range between 140 and 199 MeV/c. Analysis of this low π^+ momentum region was performed to search for additional evidence of the process $K^+ \to \pi^+ \nu \bar{\nu}$. A blind analysis technique was used to avoid bias when developing the selection criteria used to suppress the competing background processes. The blind analysis technique was based on identifying background sources *a priori* and only examining the signal region once all selection criteria and background estimates had been finalized. The background estimates were performed using a technique known as a "bifurcation method", which relied on using two uncorrelated selection criteria to suppress each background source. The analysis of an exposure of 1.71×10^{12} K^+ decays resulted in an observation of three events with an estimated background of $0.927 \pm 0.168(stat.) \,^{+0.320}_{-0.237}(sys.)$ events and a single event sensitivity of $(4.28 \pm 0.43) \times 10^{-10}$. Using a likelihood method, the three candidate events observed here were combined with the previous E787 and E949 results, yielding a branching ratio of $\mathcal{B}(K^+ \to \pi^+ \nu \bar{\nu}) = \left(1.73^{+1.15}_{-1.05}\right) \times 10^{-10}$ at the 68% confidence level. This branching ratio is consistent with the prediction of the Standard Model, $(0.85 \pm 0.07) \times 10^{-10}$.

Contents

List of Tables

List of Figures

Glossary

A	Acceptance;
AD	Active Degrader;
ADC	Analog-to-Digital Converter;
AGS	Alternating Gradient Synchrotron;
B4	B4 Hodoscope;
BEAMCUTS	The set of beam cuts consisting of B4DEDX, B4CCD, B4TRS, BWTRS, CKTRS, CKTAIL, CPITRS, CPITAIL, UPVTRS, RVTRS, B4ETCON, TGGEO, TGQUALT, TIMCON and TGTCON. See Appendix D for descriptions of the individual cuts;
BeO	BeO Beryllium-oxide;
bg	Background-level expressed as a number of events expected in the signal region;
BNL	Brookhaven National Laboratory;
BV	Barrel Veto;
BVL	Barrel Veto Liner;
BWPC	Beam Wire proportional chambers;
BWPC1	Upstream beam wire proportional chamber;
BWPC2	Downstream beam wire proportional chamber;
CO	Collar;
CCD	500 MHz transient digitizers based on a gallium arsenide charged-coupled device;
CEX	Charged Exchange;
C_K	Kaon Čerenkov Counter;

C_π	Pion Čerenkov Counter;
CKM	Cabibbo-Kobayashi-Maskawa;
CP	Charge-Parity;
CsI	Cesium Iodide;
ct	Charged track;
CUT1	The set of bifurcation cuts that are inverted to create the normalization branch;
CUT2	The set of bifurcation cuts that are inverted to create the rejection branch upon which to measure the rejection of CUT1;
DAQ	DAQ Data Acquisition;
DIF	Decay-in-Flight;
DPV	Downstream Photon Veto;
EC	End Cap;
EC1	Upstream End Cap;
EC2	Downstream End Cap;
etot	Kinetic energy of the charged track;
FCNC	Flavor-Changing Neutral Current;
FERA	Fast Encoding and Readout ADC;
IC	I-counter;
$K_{\mu 2}$	$K^+ \to \mu^+ \nu_\mu$;
$K_{\mu 2\gamma}$	$K^+ \to \mu^+ \nu \gamma$;
$K_{\mu 3}$	$K^+ \to \mu^+ \pi^0 \nu$;
K_{e4}	$K^+ \to \pi^+ \pi^- e^+ \nu$;
$K_{\pi 2}$	$K^+ \to \pi^+ \pi^0$;
$K_{\pi 2\gamma}$	$K^+ \to \pi^+ \pi^0 \gamma$;
$\mathrm{KB_{live}}$	The number of K^+s that entered the target while the detector was live (available to register a trigger);

KINCUTS	The set of kinematic cuts consisting of LAYER14, COS3D, LAYV4, ZFRF, ZUTOUT, UTCQUAL, PRRF, RSDEDX and RNGMOM. See Appendix D for descriptions of the individual cuts;
LED	Light-Emitting diode;
LESBIII	Low-Energy Separated Beamline III;
μCO	Microcollar;
PAW	Physics Analysis Workstation;
PMT	Photo-Multiplier Tube;
PNN1	The signal region above the $K_{\pi 2}$ momentum peak;
PNN2	The signal region below the $K_{\pi 2}$ momentum peak;
ptot	Momentum of the charged track;
PV	Photon Veto;
R	Rejection;
RSSC	RSSC Range-Stack Straw Chamber;
RSSCAT	The name of the group of cuts consisting of the range stack track quality cuts RSDEDX and PRRF. See Appendix D for descriptions of the individual cuts;
rtot	Range in plastic scintillator of the charged track from the kaon decay point to the stopping counter in the Range-Stack;
RV	RV Ring Veto;
SCF	Online Range-Stack stopping-counter-finder
SES	Single Event Sensitivity;
SM	Standard Model;
T•2	Coincidence between first two layers of the Range-Stack in the same sector;
TD	Transient Digitizers;
TDC	TDC Time-to-Digital Converter;
TDCUTS	Either the loose set of TD cuts *TDLOOSE* or the tight set of TD cuts *TDTIGHT* depending on the context;

TDLOOSE	The set of TD cuts consisting of IPIFLG, ELVETO, TDFOOL and the loose version of TDVARNN. See Appendix D for descriptions of the individual cuts;
TDTIGHT	The set of TD cuts consisting of IPIFLG, ELVETO, TDFOOL, EV5 and the tight version of TDVARNN. See Appendix D for descriptions of the individual cuts;
TG	Target;
TGCUTS	The set of target quality cuts consisting of B4EKZ, TGZFOOL, EPITG, EPIMAXK, TARGF, DTGTTP, RTDIF, DRP, TGK-TIM, EIC, TIC, TGEDGE, TGDEDX, TGENR, TGER, PI-GAP, TGB4, KIC, PHIVTX, OPSVETO, TGLIKE, TIMKF, NPITG, ALLKFIT, TPICS, EPIONK, CHI567, CHI5MAX, VERRNG, ANGLI, CCD31FIB, CCDBADFIT, CCDBADTIM, CCDPUL. See Appendix D for descriptions of the individual cuts;
θ	Polar angle of charged track determined by UTC;
RS	Range-Stack;
t_k	Average time of the kaon fiber hits in the target;
t_{pi}	Average time of the pion fiber hits in the target;
t_{rs}	Time of the charged track in the Range Stack;
UMC	E949 Monte Carlo simulation;
UPV	Upstream Photon Veto;
UTC	Ultra-Thin Drift Chamber;
VC	V-counter;
WLS	Wavelength-Shifting;
X_0	Radiation Lengths.

Chapter 1

Introduction

The Standard Model (SM) describes the interaction of elementary particles through the electroweak and strong forces, but does not include a quantum description of gravity. The SM leaves many questions unanswered, such as: what caused the dominance of matter over anti-matter in our Universe (known as the baryon asymmetry), how do neutrinos acquire their mass, and why are there three copies of each lepton and quark?

In the search for new physics beyond the Standard Model, two approaches can be taken. The first approach is to search directly for heavy particles by producing them at increasingly powerful accelerators or by observation of very-high-energy cosmic rays. The second approach is to measure to very high precision, quantities predicted by the SM in an attempt to find discrepancies between the measured and predicted quantities. One example of this second approach is the measurement of the branching ratio of the rare decay $K^+ \to \pi^+ \nu \bar{\nu}$.

This chapter discusses the branching ratio of $K^+ \to \pi^+ \nu \bar{\nu}$ as predicted by the SM and by other new physics models. This chapter also contains a brief history of measurements of the $K^+ \to \pi^+ \nu \bar{\nu}$ branching ratio.

1.1 Theory and Motivation

The Sakharov conditions [90] are regarded as the necessary conditions to explain the baryon asymmetry in our universe. Any theory for baryon asymmetry must satisfy the three Sakharov conditions: (1) baryon number violating reactions must exist, (2) C and CP-violation must exist, and (3) there must be a deviation from equilibrium.

The CP-transformation combines the two transformations of charge conjugation (C) and parity (P). Under the C-transformation, each particle is converted to its own anti-particle via a change in sign of all the internal quantum numbers (charge, strangeness, baryon number, etc...), and under the P-transformation, space is inverted ($\vec{r} \rightarrow -\vec{r}$). Under the combined CP-transformation, a left-handed electron e_L^- comes out a right-handed positron e_R^+. Presently, the sources of CP-violation in the SM only account for a small portion of the CP-violation needed to produce the observed baryon asymmetry. Particle physics experiments are constantly searching for new sources of CP-violation, and rare decays such as $K^+ \rightarrow \pi^+ \nu \bar{\nu}$ are sensitive to new CP-violating physics.

The first observation of a CP-violating decay occurred at Brookhaven National Laboratory (BNL) in 1964, in an experiment involving the neutral K meson sector [36]. Thus far, violation of CP-symmetry has been observed only in the B and K meson sectors [1, 17], from rare decay amplitudes and from the mixing of the neutral mesons with their anti-particles.

1.2 *CP*-Violation and Weak Interactions

In the SM, the six flavors of quarks are classified into three generations or families: up (u) and down (d), charm (c) and strange (s), and top (t) and bottom (b). For each of these families, the first listed quark has an electric charge of $+2/3$ and the second has an electric charge of $-1/3$. Only through weak interactions can these quarks transform from

one to another. The charged-current processes, mediated by the charged intermediate W^+ or W^- bosons, allow a quark to transform into another quark having a different charge (such as $d \rightarrow u + W^-$). The neutral-current process, mediated by the neutral Z^0 boson, cannot directly transform a quark into another quark of different flavor but same charge, i.e. $s \rightarrow d$. This type of transformation, known as a flavor-changing neutral current (FCNC) process, is forbidden at tree level and suppressed at the one-loop level due to the Glashow-Iliopoulos-Maiani (GIM) mechanism [47].

To understand the origin of the GIM mechanism, we can revisit a time when physicists believed only three quarks existed: u, d and s. Cabibbo [29] introduced an angle (θ_C) to show how the strength of the weak transformations $d \rightarrow u$ and $s \rightarrow u$ as mediated by the W^- differed only by factors of $\cos\theta_C$ and $\sin\theta_C$, respectively. This theory failed to explain why the experimental limits on the rate of FCNC processes such as $K_L^0 \rightarrow \mu^+\mu^-$ and $K^+ \rightarrow \pi^+\nu\bar{\nu}$ were so much lower than the calculated rates. In 1970, the GIM mechanism was proposed to solve this problem by introducing a fourth quark, now called the charm quark. In this theory, there exist the weak eigenstates d' and s' which participate in the weak interactions instead of the regular d and s mass eigenstates. The relationships between the weak and mass eigenstates is written as

$$
\begin{pmatrix} d' \\ s' \end{pmatrix} = \begin{pmatrix} \cos\theta_C & \sin\theta_C \\ -\sin\theta_C & \cos\theta_C \end{pmatrix} \begin{pmatrix} d \\ s \end{pmatrix}.
\tag{1.1}
$$

At tree level, the FCNC processes are forbidden as shown by the following expression
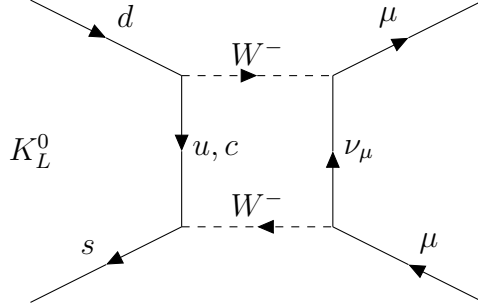
Figure 1.1: The decay $K_L^0 \to \mu^+\mu^-$.

for the neutral current, J^0, expressed without the γ-matrices:

$$
\begin{aligned}
J^0 &= \bar{u}u + \bar{c}c + \bar{d}'d' + \bar{s}'s', \\
&= \bar{u}u + \bar{c}c + (\bar{d}d + \bar{s}s)\cos^2\theta_C + (\bar{d}d + \bar{s}s)\sin^2\theta_C \\
&\quad + (\bar{d}s + \bar{s}d - \bar{d}s - \bar{s}d)\sin\theta_C\cos\theta_C, \\
&= \bar{u}u + \bar{c}c + \bar{d}d + \bar{s}s.
\end{aligned}
\tag{1.2}
$$

Here the FCNC terms, such as $\bar{d}s$ and $\bar{s}d$ cancel each other due to the positive and negative $\sin\theta_C$ terms in the rotations of the weak eigenstates.

The suppression of FCNC processes at the one-loop level can be understood by looking at the $K_L^0 \to \mu^+\mu^-$ decay (Figure 1.1). In the four-quark model, the virtual quark can be either a u or a c. The contributions due to the two different virtual quarks cancel out, since the decay amplitude for the u quark is proportional to $\sin\theta_C\cos\theta_C$ and that for the c quark is proportional to $-\sin\theta_C\cos\theta_C$. If the masses of the u and c quarks were identical the decay would be strictly forbidden, but due to the difference in their masses it proceeds at a very suppressed rate.

The weak eigenstate model can be extended to include all six quarks where the relationship between the weak eigenstates d', s', b' and mass eigenstates d, s, b is given by

the Cabibbo-Kobayashi-Maskawa (CKM) matrix [66],

$$
\begin{pmatrix} d' \\ s' \\ b' \end{pmatrix} = \begin{pmatrix} V_{ud} & V_{us} & V_{ub} \\ V_{cd} & V_{cs} & V_{cb} \\ V_{td} & V_{ts} & V_{tb} \end{pmatrix} \begin{pmatrix} d \\ s \\ b \end{pmatrix}. \tag{1.3}
$$

The SM does not predict the CKM matrix elements, so their magnitudes and phases must be determined experimentally.

The constraints of unitarity connect different matrix elements such that the CKM matrix can be expressed using as few as 4 different parameters. One standard method of parameterizing the matrix involves the real angles θ_{12}, θ_{23}, θ_{13} and the CP-violating angle δ:

$$
V = \begin{pmatrix} c_{12}c_{13} & s_{12}c_{13} & s_{13}e^{-i\delta} \\ -s_{12}c_{23} - c_{12}s_{23}s_{13}e^{-i\delta} & c_{12}c_{23} - s_{12}s_{23}s_{13}e^{-i\delta} & s_{23}c_{13} \\ s_{12}c_{23} - c_{12}s_{23}s_{13}e^{-i\delta} & -c_{12}c_{23} - s_{12}s_{23}s_{13}e^{-i\delta} & c_{23}c_{13} \end{pmatrix}, \tag{1.4}
$$

where $c_{ij} = \cos\theta_{ij}$ and $s_{ij} = \sin\theta_{ij}$, with the i and j representing 1,2,3, the quark generation labels. The angle θ_{12} is the same Cabibbo angle θ_C seen earlier in the four-quark scheme. An approximation proposed by Wolfenstein [98] sets a parameter λ equal to s_{12}, the sine of the Cabibbo angle. The other parameters are real numbers that are of order unity: A, ρ and η. The parameter η describes CP-violation in the SM and a non-zero value of this parameter breaks CP-invariance for weak interactions. The following representation of the matrix expresses the elements in terms of powers of $\lambda = \sin\theta_c \approx 0.22$:

$$
V = \begin{pmatrix} 1 - \frac{\lambda^2}{2} & \lambda & A\lambda^3(\rho - i\eta) \\ -\lambda & 1 - \frac{\lambda^2}{2} & A\lambda^2 \\ A\lambda^3(1 - \rho - i\eta) & -A\lambda^2 & 1 \end{pmatrix} + \mathcal{O}(\lambda^4). \tag{1.5}
$$

Unitarity ($V^\dagger V = 1$) of the CKM matrix implies six unitarity conditions, all of which can be expressed as unitarity triangles which are geometric representations of the unitarity conditions in the complex plane, where the areas of each of the unitarity triangles are equal to half of the Jarlskog invariant [59],

$$J_{CP} = s_{12}^2 s_{23} s_{13} c_{12} c_{23} c_{13} \sin \delta, \tag{1.6}$$

with the definitions of s_{ij} and c_{ij} being the same as defined earlier for Equation (1.4). The unitarity condition of interest for the decay $K^+ \to \pi^+ \nu \bar{\nu}$ is

$$V_{ud} V_{ub}{}^* + V_{cd} V_{cb}{}^* + V_{td} V_{tb}{}^* = 0. \tag{1.7}$$

If the Wolfenstein parameterization from Equation (1.5) is used with the approximations $V_{ud} \simeq V_{tb}^* \simeq 1$ and $V_{cd} \simeq -\lambda$, Equation (1.7) can be rewritten as

$$V_{ub}^* - \lambda V_{cb}^* + V_{td} = 0. \tag{1.8}$$

The triangle shown in Figure 1.2 results from this equation if all sides of the unitarity triangle are normalized such that the baseline has a length equal to 1. In this normalized unitarity triangle, the apex is given by two Wolfenstein parameters, $\bar{\rho} = \rho(1 - \frac{\lambda^2}{2})$ and $\bar{\eta} = \eta(1 - \frac{\lambda^2}{2})$ [27].

Thus far, K and B mesons are the only mesons that have shown evidence of CP violation in their decay processes. As can be seen in Figure 1.3, comparisons of $\bar{\rho}$ and $\bar{\eta}$ from independent measurements in the K and B sectors can be used to either verify the Standard Model description of CP-violation as explained by the CKM phase, or to signal new physics.
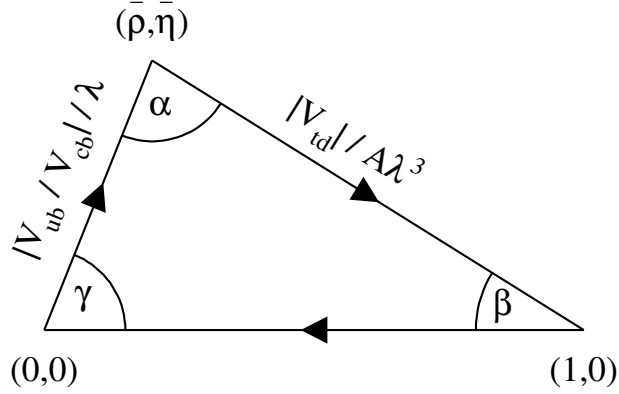
Figure 1.2: A unitarity triangle in the $\rho - \eta$ plane. The length of the bottom side is normalized to unity and the lengths of the other two sides can be expressed by the CKM matrix elements $|V_{td}|/A\lambda^3$ and $|V_{ub}/V_{cb}|/\lambda$. Reprinted figure with permission from S. Adler *et al.* (E949 Collaboration), Phys. Rev. D **77** 052003 (2008), http://link.aps.org/abstract/PRD/v77/e052003. Copyright 2008 by the American Physical Society.
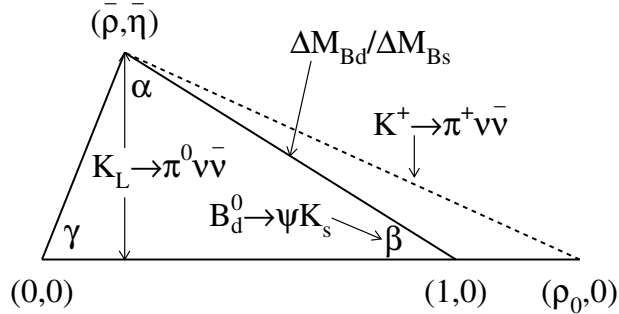
Figure 1.3: The unitarity triangle as determined by B and K decays. The angle β measured from the *CP*-violating asymmetry ($\mathcal{A}_{CP}$) in the decay $B_d^0 \to J/\psi K_s^0$ can be compared with that from the ratio $\mathcal{B}(K_L^0 \to \pi^0 \nu\bar{\nu})/\mathcal{B}(K^+ \to \pi^+ \nu\bar{\nu})$. The magnitude of V_{td} extracted from the ratio of mass differences ($\Delta M_{B_s}/\Delta M_{B_d}$) from $B_s - B_d$ mixing can be compared with that extracted from $\mathcal{B}(K^+ \to \pi^+ \nu\bar{\nu})$. Reprinted figure with permission from S. Adler *et al.* (E949 Collaboration), Phys. Rev. D **77** 052003 (2008), http://link.aps.org/abstract/PRD/v77/e052003. Copyright 2008 by the American Physical Society.
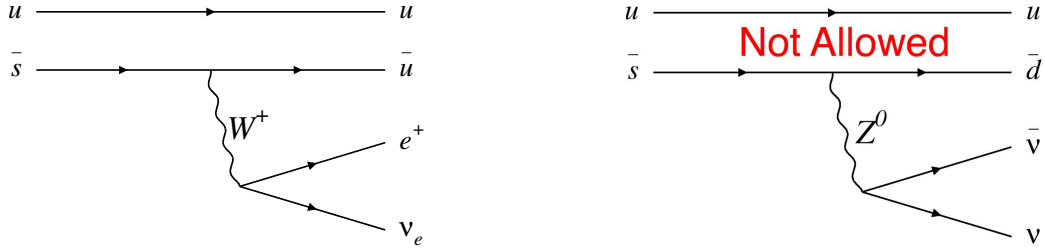
Figure 1.4: The first-order weak charged-current $K^+ \to \pi^0 e^+ \nu_e$ decay (left), which is allowed in the Standard Model. The first-order neutral-current $K^+ \to \pi^+ \nu \bar{\nu}$ diagram (right) shows a process which is not allowed in the Standard Model. Figures reproduced from [72].

1.3 $K^+ \to \pi^+ \nu \bar{\nu}$ in the Standard Model

As discussed in Section 1.2, the decay $K^+ \to \pi^+ \nu \bar{\nu}$ is a FCNC process, prohibited in the SM at tree level (see Figure 1.4), but allowed at the one-loop level. The leading order diagrams describing this decay are shown in Figure 1.5.

The weak amplitude for the process $\bar{s} \to (\bar{u}, \bar{c}, \bar{t}) \to \bar{d}$, as seen in the diagrams of Figure 1.5, is represented as

$$\mathcal{M} \sim \sum_{i=u,c,t} V_{is}^* V_{id} \frac{\gamma^\mu q_\mu + m_i}{q^2 - m_i^2}, \tag{1.9}$$

where the index $i = u, c, t$ denotes the quark flavor, V_{ij} represents the CKM matrix element, γ^μ the Dirac matrices, q_μ the momentum transfer, and m_i the quark masses. Unitarity of the CKM matrix would cause $\mathcal{M}$ to vanish if the quarks all had equal masses, however, the variation of quark masses due to the breaking of flavor symmetry allows this decay to proceed at a very small rate. Due to its very large mass relative to the up and charm quarks, the top quark provides the dominant contribution to the $K^+ \to \pi^+ \nu \bar{\nu}$ branching ratio through the coupling of top to down quarks, the CKM matrix element V_{td}.

The following calculation of the branching ratio $K^+ \to \pi^+ \nu \bar{\nu}$ follows the method from
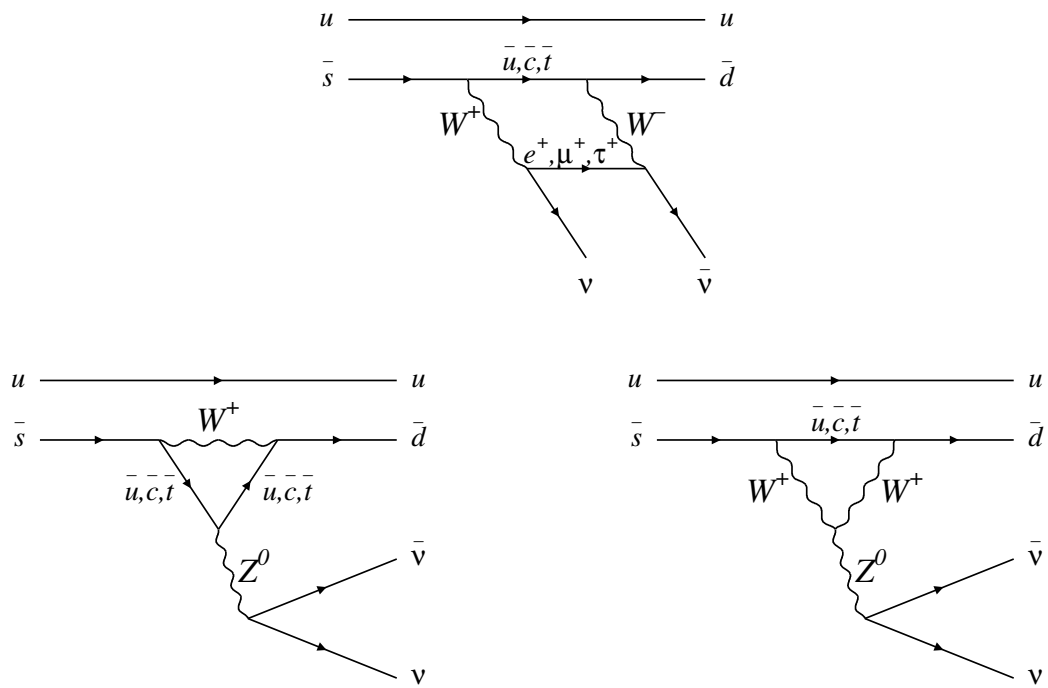
Figure 1.5: The second-order weak processes that contribute to the $K^+ \rightarrow \pi^+ \nu \bar{\nu}$ branching ratio are a "Box" diagram (upper) and two "Z-penguin" diagrams (lower). Reprinted figure with permission from S. Adler *et al.* (E949 Collaboration), Phys. Rev. D **77** 052003 (2008), http://link.aps.org/abstract/PRD/v77/e052003. Copyright 2008 by the American Physical Society.

[28] and [25]. The low-energy effective Hamiltonian in the SM can be written as

$$\mathcal{H}_{eff}^{SM} = \frac{G_F}{\sqrt{2}} \frac{\alpha}{2\pi \sin^2 \Theta_W} \sum_{l=e,\mu,\tau} \left(V_{cs}^* V_{cd} X^l(x_c) + V_{ts}^* V_{td} X(x_t) \right) (\bar{s}d)_{V-A} (\bar{\nu}_l \nu_l)_{V-A}, \quad (1.10)$$

where the index $l = e, \mu, \tau$ denotes lepton flavor, Θ_W is the electroweak mixing angle, α is the fine structure constant, and G_F is the Fermi coupling. The functions $X^l(x_c)$ and $X(x_t)$, where $x_j \equiv m_j^2/M_W^2$, summarize the contributions from the charm and top quarks respectively and include QCD corrections at next-to-next-to-leading order (NNL0).

The uncertainty in the function $X(x_t)$ is dominated by the experimental uncertainty on the top quark mass in the minimal subtraction scheme, a renormalization scheme frequently used in quantum chromodynamics. The top quark mass in the minimal subtraction scheme is $m_t(m_t) = (163.01 \pm 1.43)$ GeV [48], giving a value for $X(x_t)$ of

$$X(x_t) = 1.443 \pm 0.017. \quad (1.11)$$

The perturbative charm contribution is described in terms of the parameter

$$P_c(X) \equiv \frac{1}{\lambda^4} \left(\frac{2}{3} X^e(x_c) + \frac{1}{3} X^\tau(x_c) \right) = 0.372 \pm 0.015, \quad (1.12)$$

where $\lambda = 0.2255$ was used [25].

Using the above definitions and relationships, the $K^+ \to \pi^+ \nu \bar{\nu}$ branching ratio can be written as

$$\mathcal{B}(K^+ \to \pi^+ \nu \bar{\nu}) = \kappa_+ \cdot \left[\left(\frac{\mathrm{Im}\lambda_t}{\lambda^5} X(x_t) \right)^2 + \left(\frac{\mathrm{Re}\lambda_c}{\lambda} (P_c(X) + \delta P_{c,u}) + \frac{\mathrm{Re}\lambda_t}{\lambda^5} X(x_t) \right)^2 \right], \quad (1.13)$$

where $\lambda_i \equiv V_{is}^* V_{id}$ are the CKM matrix elements, and $\delta P_{c,u} = 0.04 \pm 0.02$ represents the

long-distance contributions as calculated in [53]. The term

$$\kappa_+ = (5.173 \pm 0.025) \times 10^{-11} \left[\frac{\lambda}{0.225} \right]^8, \tag{1.14}$$

calculated in [78], summarizes the remaining factors that follow from Equation (1.10), in particular the relevant hadronic mixing elements that can be extracted from leading-order semi-leptonic decays of K^+, K_L and K_S mesons.

Equation (1.13) describes in the $\bar{\rho} - \bar{\eta}$ plane an ellipse with small eccentricity, namely

$$(\sigma \bar{\eta})^2 + (\bar{\rho} - \bar{\rho}_0)^2 = \frac{\sigma \mathcal{B}(K^+ \to \pi^+ \nu \bar{\nu})}{\bar{\kappa}_+ |V_{cb}|^4 X^2(x_t)}, \tag{1.15}$$

where

$$\bar{\rho}_0 \equiv 1 + \frac{\lambda^4 P_c(X)}{|V_{cb}|^2 X(x_t)}, \tag{1.16}$$

$$\sigma \equiv \left(1 - \frac{\lambda^2}{2} \right)^{-2}, \tag{1.17}$$

and

$$\bar{\kappa}_+ \equiv \frac{\kappa_+}{\lambda^8} = (7.87 \pm 0.04) \times 10^{-6}. \tag{1.18}$$

Using (1.13), the SM branching ratio of $K^+ \to \pi^+ \nu \bar{\nu}$ is predicted to be

$$\mathcal{B}(K^+ \to \pi^+ \nu \bar{\nu}) = (0.85 \pm 0.07) \times 10^{-10}. \tag{1.19}$$

A precise measurement of $\mathcal{B}(K^+ \to \pi^+ \nu \bar{\nu})$ is regarded to be one of the cleanest ways to extract $|V_{td}|$. This is due to the following factors:

1. The long-distance contributions to the branching ratio are small [51] and under control. The most recent calculation [53] gives an enhancement to the branching ratio of $(6 \pm 3)\%$;

2. The uncertainty from the hadronic matrix element has been reduced to less than

1% by recent theoretical and experimental developments [78]; and

3. Recent improvements in the calculation of the charm quark contribution [25] have reduced the theoretical uncertainties to $\sim 5\%$.

1.4   Physics Beyond the Standard Model

Since the theoretical uncertainty in the SM prediction of $\mathcal{B}(K^+ \to \pi^+ \nu \bar{\nu})$ is small, a precise measurement can serve as a stringent test of the SM and provide an effective probe for new physics beyond the SM. Predictions of $\mathcal{B}(K^+ \to \pi^+ \nu \bar{\nu})$ have been made for many models beyond the SM and a precise measurement can constrain or reject these models. Since the current experimental limit for the complementary $K_L^0 \to \pi^0 \nu \bar{\nu}$ decay is $\mathcal{B}(K_L^0 \to \pi^0 \nu \bar{\nu}) < 6.7 \times 10^{-8}$ at 90% confidence level [9] and the SM prediction is $\mathcal{B}(K_L^0 \to \pi^0 \nu \bar{\nu}) = (2.49 \pm 0.39) \times 10^{-11}$ [78], many new physics models have the freedom to predict much larger enhancements to $\mathcal{B}(K_L^0 \to \pi^0 \nu \bar{\nu})$ than to $\mathcal{B}(K^+ \to \pi^+ \nu \bar{\nu})$. Some new physics models are discussed briefly below.

In the Littlest Higgs with T-Parity (LHT) model [34], new massive particles are introduced. These new particles include massive partners to the SM particles, but unlike Supersymmetric models [84], the massive partners have the same spin-statistics as their SM partners. Under the new T-parity symmetry, most of these new massive partners are odd and the SM particles even, allowing for the lightest particle with odd T-parity to be stable. The massive quark partners, known as "mirror quarks", have flavor-violating interactions which can impact FCNC processes such as $K^+ \to \pi^+ \nu \bar{\nu}$. Figure 1.6 shows that the predicted relationship between $\mathcal{B}(K^+ \to \pi^+ \nu \bar{\nu})$ and $\mathcal{B}(K_L^0 \to \pi^0 \nu \bar{\nu})$ lies along two branches. The first branch is parallel to the upper bound on the model-independent Grossman-Nir limit, $\mathcal{B}(K_L^0 \to \pi^0 \nu \bar{\nu})/\mathcal{B}(K^+ \to \pi^+ \nu \bar{\nu}) < 4.4$ [50]. In this branch, $\mathcal{B}(K_L^0 \to \pi^0 \nu \bar{\nu})$ can be as high as 5×10^{-10} while $\mathcal{B}(K^+ \to \pi^+ \nu \bar{\nu})$ stays within the bounds of the measured branching ratio of $\mathcal{B}(K^+ \to \pi^+ \nu \bar{\nu}) = 1.47^{+1.30}_{-0.89} \times 10^{-10}$ [11]. The second branch predicts
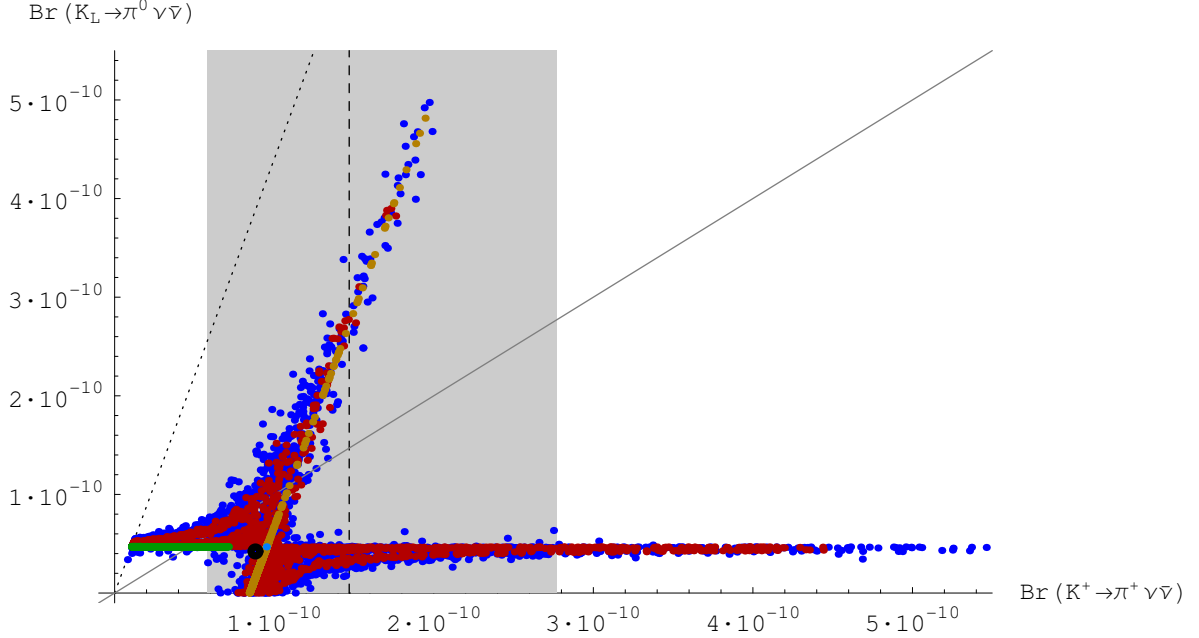
Figure 1.6: Littlest Higgs with T-Parity (LHT) model predictions for the relationship between $\mathcal{B}(K^+ \to \pi^+\nu\bar{\nu})$ and $\mathcal{B}(K_L^0 \to \pi^0\nu\bar{\nu})$. The shaded area represents the 1σ-range for the previous E949 measurement of $\mathcal{B}(K^+ \to \pi^+\nu\bar{\nu}) = 1.47^{+1.30}_{-0.89} \times 10^{-10}$ [11]. The black dotted line shows the model independent Grossman-Nir limit, $\mathcal{B}(K_L^0 \to \pi^0\nu\bar{\nu})/\mathcal{B}(K^+ \to \pi^+\nu\bar{\nu}) < 4.4$ [50]. The blue data points represent the most general LHT model predictions, and the red, green and gold data points represent further constrained scenarios as discussed in [23]. Figure reproduced from [23].

that $\mathcal{B}(K_L^0 \to \pi^0\nu\bar{\nu})$ remains close to its SM prediction, but $\mathcal{B}(K^+ \to \pi^+\nu\bar{\nu})$ can vary from 1×10^{-10} to 5×10^{-10}.

In the minimal 3-3-1 model, the SM $SU(2)_L$ gauge group is extended to $SU(3)_L$ resulting in an additional neutral gauge boson, the Z', which is able to transmit FCNCs at tree-level. The resulting enhancement to $\mathcal{B}(K^+ \to \pi^+\nu\bar{\nu})$ above the SM prediction ranges up to approximately 65% when the Z' mass is small (1 TeV) [88].

It may also be possible that the "nothing" in the observation of $K^+ \to \pi^+ +$ "nothing" is actually the observation of $K^+ \to \pi^+ X^0$, where X^0 is a weakly interacting particle such as a familon, axion or majoron [51]. These particles are Nambu-Goldstone bosons (massless) or pseudo-Nambu-Goldstone bosons (small mass) that arise from spontaneously broken symmetries such as global family symmetries (familon), the Peccei-Quinn symmetry (axion), or baryon-lepton invariance (majoron). The limit set on the branching ratio

of $K^+ \to \pi^+ X^0$ by previous E949 analyses is $\mathcal{B}(K^+ \to \pi^+ X^0) < 0.73 \times 10^{-10}$ at 90% confidence level [11].

1.5   History of $K^+ \to \pi^+ \nu \bar{\nu}$ Experiments

The first published limit on $\mathcal{B}(K^+ \to \pi^+ \nu \bar{\nu})$ came in 1969 from a heavy liquid bubble chamber experiment at the Argonne Zero Gradient Synchrotron. Their initial 90% confidence level upper limit of 10^{-4} [31] was improved four years later to 5.7×10^{-5} [74] after final analysis of the experiment.

A counter/spark-chamber experiment at the Berkeley Bevatron, sensitive only to the most energetic π^+s, improved the limit to 1.4×10^{-6} in 1971. They improved their limit to 5.6×10^{-7} [30] by combining their previous data with data acquired after reconfiguring their detector to be sensitive to π^+s in the 60 to 105 MeV energy range.

In 1981, the limit was improved to 1.4×10^{-7} [13] by an experiment at the KEK Proton Synchrotron using a setup similar to that used by the Berkeley Bevatron experiment.

The E787 experiment, later superseded by the E949 experiment, was initiated at Brookhaven National Laboratory in the early 1980s. From data collected between 1988 and 1991, the E787 experiment achieved an upper limit on the branching ratio at 90% confidence limit of 2.4×10^{-9} [2] and 1.7×10^{-8} [16], for the PNN1 and PNN2 regions, respectively. The PNN1 (PNN2) region is that where the π^+ momentum is greater (less) than that from $K^+ \to \pi^+ \pi^0$ as shown in Figure 3.1.

The detector and beam line were upgraded between 1992 and 1994 [67], and data collection resumed in 1995 and continued through 1998. In these data, two events were observed in the PNN1 region yielding a branching ratio measurement of $\mathcal{B}(K^+ \to \pi^+ \nu \bar{\nu}) = 1.57^{+1.75}_{-0.82} \times 10^{-10}$ [3, 4, 5]. In the PNN2 region, one event, consistent with background, was observed and the limit placed on the branching ratio by measurements in this region was improved to 2.24×10^{-9} [6, 7].

Between 1999 and 2001, the detector and beam line were again upgraded [18], as were the trigger and data acquisition [100]. The E787 experiment was rechristened E949, and despite approval to run for a total of 60 weeks, was funded for only 12 weeks of running, which occurred in 2002. In these data, a third event in the PNN1 region was observed and the combined branching ratio from all three events observed in the PNN1 region was measured to be $\mathcal{B}(K^+ \rightarrow \pi^+ \nu \bar{\nu}) = 1.47^{+1.30}_{-0.89} \times 10^{-10}$ [11]. This thesis describes the search for $K^+ \rightarrow \pi^+ \nu \bar{\nu}$ in the PNN2 region using the 2002 data.

1.6 My Role in the Analysis

After the demise of BNL experiment E926 "KOPIO" in 2005, I joined the E949 collaboration at a time when their analysis of the data in the PNN2 region had just begun.

The results presented in this thesis were reproduced from E949 collaboration internal documents [55] and [56], for both of which I was also one of the authors. These internal documents were cited throughout this thesis to attribute figures and results of studies to others within the collaboration. This section briefly summarizes the work for which I was responsible.

In Chapter 4 "Backgrounds", I was responsible for all the $K_{\pi 2}$-scatter background results (Sections 4.1 and 4.2) and the normalization result for $K_{\pi 2 \gamma}$ (Section 4.3). I also independently verified the results presented for the single-beam (Section 4.6), double-beam (Section 4.7), and muon (Section 4.4) backgrounds, as well as the results of the normalization/data branch studies for the K_{e4} (Section 4.5) and charge exchange (Section 4.8) backgrounds.

In Chapter 5 "Validity Checks", I was responsible for all the validation studies other than the single-cut and double-cut failure studies.

In Chapter 7 "Results", I was responsible for the "signal probability analysis" study. I verified the calculation for the probability of observed candidates being due to background

only and also verified, using independently developed code, many of the likelihood analysis results presented in [56].

Appendices C and E describe work for which I was completely responsible. Appendix C describes the improvements I made to the analysis of target pulse data known as the "target CCD fitter". Appendix E describes my work on the class of cuts known as the target pulse cuts. This work included improvements to the cuts CCDPUL and CCDBADTIM and development of the cut CCDBADTIM. These target pulse cuts were critical in the suppression of the large $K^+ \rightarrow \pi^+\pi^0$ target-scatter background and work on these cuts accounted for a large fraction of my contributions to this analysis.

Chapter 2

Experimental Method

In Brookhaven National Laboratory (BNL) experiment E949, the low-momentum (710 MeV/c) K^+ beam was stopped in an active scintillator target. Identification of the $K^+ \to \pi^+ \nu \bar{\nu}$ decay involved the observation of a π^+ in the absence of other coincident activity. The charged decay particle was identified as a π^+ by the measured momentum, energy and range, and by the observation of the $\pi^+ \to \mu^+ \to e^+$ decay sequence. The detector featured full 4π-steradian photon veto coverage and the entire E949 spectrometer was situated in a 1-Tesla solenoidal magnetic field along the beam direction. The detector is shown in Figure 2.1. E949 superseded BNL experiment E787, with upgrades taking place from 1999-2001. A summary of these upgrades can be found in Appendix A.

This chapter briefly describes the various detector systems and triggers used in the E949 experiment. The coordinate system used when describing the detector is as follows:

- The z-direction was positive along the direction of travel of the beam (downstream);

- The x- and y-directions were the horizontal and vertical directions with respect to the z-direction. The y-direction pointed vertically up.

Details of the data acquisition, storage and processing can be found in Appendix B.
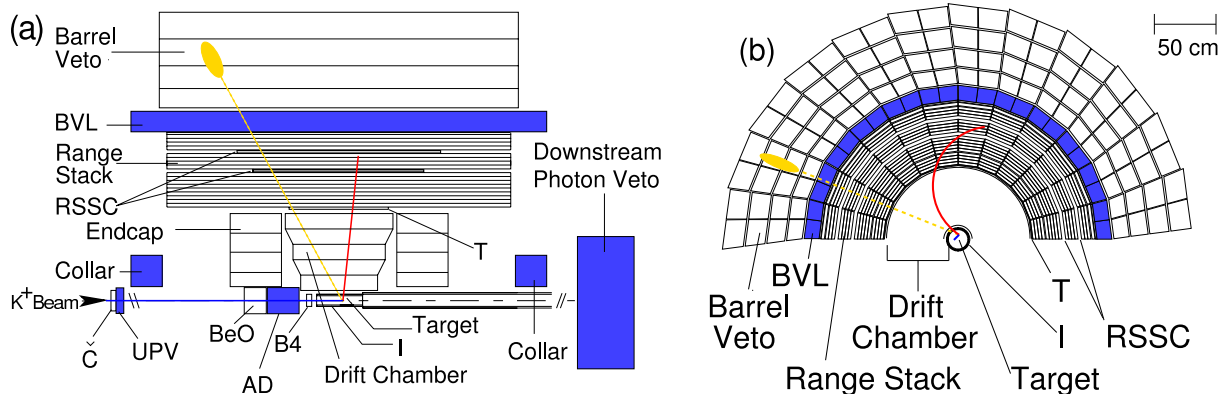
Figure 2.1: Schematic side (a) and end (b) views of the upper half of the E949 detector. Reprinted figure with permission from S. Adler *et al.* (E949 Collaboration), Phys. Rev. D **77** 052003 (2008), http://link.aps.org/abstract/PRD/v77/e052003. Copyright 2008 by the American Physical Society.

2.1   Kaon Beam

The K^+ beam was produced by a high-intensity 21.5 GeV/c proton beam from the Alternating Gradient Synchrotron (AGS) at Brookhaven National Laboratory (BNL). A schematic view of the AGS accelerator complex is shown in Figure 2.2. During a 2.2 s spill, approximately 6.5×10^{13} protons arrived at the K^+ production target, with spills occurring every 5.4 s. The K^+ production target was made of 6 cm thick platinum located on a water cooled base, with the maximum target temperature being measured at about 700°C.

The Low Energy Separated Beam [40] (LESB III), shown in Figure 2.3, collected and transported K^+s emitted at 0°, along with the 500 π^+s and 500 protons at the production target for every K^+. The beam was momentum-selected by the first dipole magnet (D1 in Figure 2.3). Two electromagnetostatic separators swept away protons and π^+s from the beam resulting in a K^+ to π^+ ratio of 3:1 and negligible proton contamination when the beam arrived at the target. The angular acceptance of LESB III was 12 msr and the momentum acceptance was 4.5% FWHM, with the mean beam momentum arriving at

18
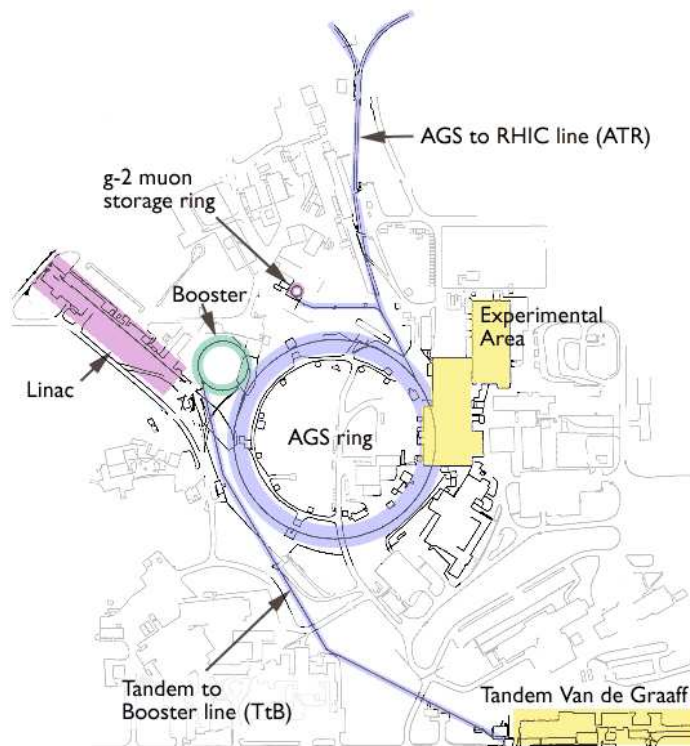
Figure 2.2: Schematic view of the AGS complex, which consisted of a 200 MeV LINAC, a booster and a synchrotron. The secondary beam lines were located in the area marked "experimental area". Figure reproduced from [37].
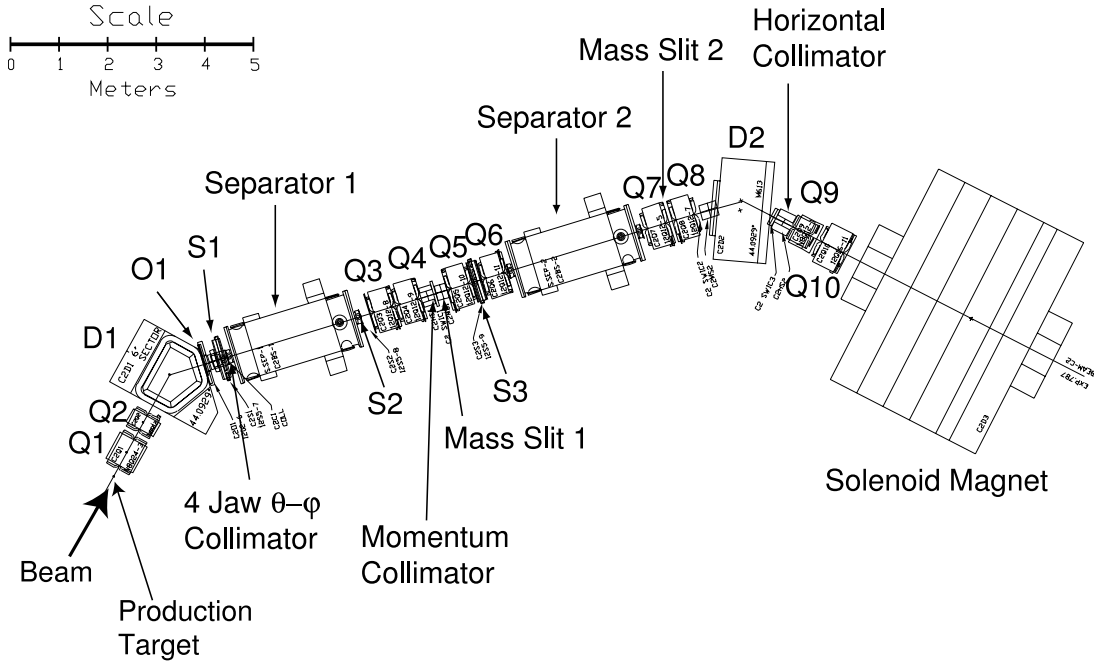
Figure 2.3: Low-energy separated beam line III at BNL. The E949 solenoid magnet is also shown at the end of LESB III. Figure reproduced from [37].

the target being 710 MeV/c.

The typical conditions during data collection were 3.5×10^6 K^+s entered the E949 target per spill and the instantaneous rates in the Čerenkov Counter were 6.3 MHz for K^+s and 1.5 - 2.5 MHz for π^+s.

2.2 Beam Instrumentation

The purposes of the beam instrumentation were K^+ identification, K^+ momentum degradation, and detection of additional particles coincident with the K^+ and its decay particles. In the order encountered by the K^+ beam, these detectors were:

- The B0 counter, a large scintillator counter which counted all charged particles in the beam;

- The Čerenkov counter which identified particles as K^+ or π^+;

- The Upstream Photon Veto (UPV), a 3.1 radiation length plastic scintillator with a large beam hole;

- Two beam wire chambers (BWPC) which monitored the beam profile and identified multiple incoming particles;

- Passive (BeO) and active (copper and scintillator sandwich) degraders that slowed the kaons such that they came to rest in the target;

- The Beam Hodoscope (B4) which detected the position of incoming beam particles just before they entered the target;

- The Ring Veto (RV), an annular plastic scintillator at the same position along the beam direction as the B4 Hodoscope, but at a larger radius.

The Čerenkov counters, BWPCs, degraders and B4 hodoscope are shown in Figure 2.1. The B0 counter did not enter into the analysis, but is mentioned here for completeness.

2.2.1 Čerenkov Counter

The Čerenkov counter identified beam particles as kaons or pions and was located just downstream of the B0 counter. Figure 2.4 shows a side-view of the Čerenkov counter.

The acrylic radiator was 2.5 cm thick and had a refractive index n of 1.49. Based on this refractive index the threshold for Čerenkov radiation in the radiator was

$$\beta_{\check{C}} = \frac{1}{n} = 0.671, \tag{2.1}$$

and the threshold for total internal reflection (TIR) was

$$\beta_{\mathrm{TIR}} = \sqrt{\frac{1}{n^2 - 1}} = 0.905. \tag{2.2}$$
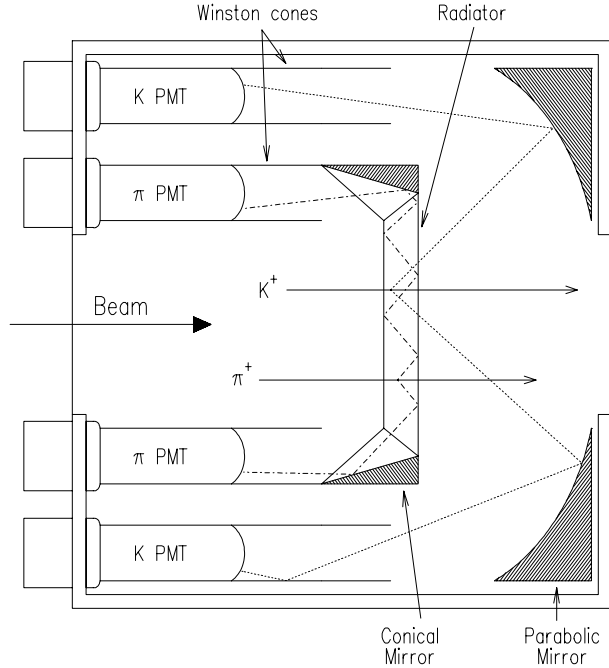
Figure 2.4: Schematic of the side-view of the Čerenkov counter. The incoming K^+ and resulting Čerenkov light are shown in blue. The incoming π^+ and resulting Čerenkov light are shown in red. Figure reproduced from [37].

At a momentum of 710 MeV/c, $\beta_{K^+} = 0.82$ and $\beta_{\pi^+} = 0.98$. The Čerenkov light from the kaons was transmitted at the downstream surface of the radiator and reflected by a parabolic mirror to the outer ring of 14 EMI [43] 9964KB photomultiplier tubes (PMTs), collectively referred to as the K^+ Čerenkov counter (C_K). The Čerenkov light from the pions experienced total internal reflection at the downstream surface of the radiator and was reflected to the inner ring of 14 EMI9964KB PMTs, collectively referred to as the π^+ Čerenkov counter (C_π). The signals from the PMTs were split with 90% being sent to time-to-digital converters (TDCs) via LRS3412 discriminators and the remaining 10% being sent to $\times 10$ amplifiers whose output was sent to 500 MHz transient digitizers based on a gallium arsenide charge-coupled device (CCD) [26]. Gallium arsenide was used because it is a suitable material for construction of high speed devices due to its high electron mobility. The pulse-height information in every 2-ns interval was recorded by the CCDs to reproduce the time development of the pulses and to detect two particles

22

close in time to each other. At the trigger level, a minimum threshold of 5 Čerenkov discriminator channels firing was used for kaons for the KB trigger and for pions for the πB trigger (see Section 2.7 for trigger definitions). The CCD information was used offline for discriminating between multiple incoming beam particles of the same type when the TDCs were unable to distinguish between pile-up signals.

2.2.2 Upstream Photon Veto

Downstream of the Čerenkov counter was the upstream photon veto (UPV). Figure 2.5 shows this 3.1-radiation-length detector made of 12 square layers, 28.4 cm in height and width, of Bicron [89] BC404 plastic scintillator and lead or copper sandwich. The scintillator layers were 2 mm thick. The five upstream-most layers of lead were 2 mm thick and the six remaining lead layers were 1 mm thick. The downstream-most layer was 2.2 mm thick copper instead of lead and formed part of the box holding the layers together. The upstream end of the box was 3.175-mm thick aluminum. There was a 175 mm wide by 40 mm high slot through the detector to allow the beam to pass through. The detector was divided horizontally into two modules of six scintillator segments each. Each scintillator segment was read out by twenty-one 1-mm diameter double-clad wavelength shifting (WLS) fibers coupled to one of the two Hamamatsu R1924 PMTs [52] used to read out the entire detector. The PMT signals were sent to ADCs, TDCs and CCDs. This detector was designed to detect photons traveling in the upstream direction, but it was found that the beam rate was too large and this overwhelmed the detector. Instead, the UPV was used to veto beam particles coincident with the time of the K^+ decay.

2.2.3 Beam Wire Chambers

The two beam wire proportional chambers (BWPCs) monitored the beam profile and identified multiple incoming particles. The first chamber (BWPC1) was located down-
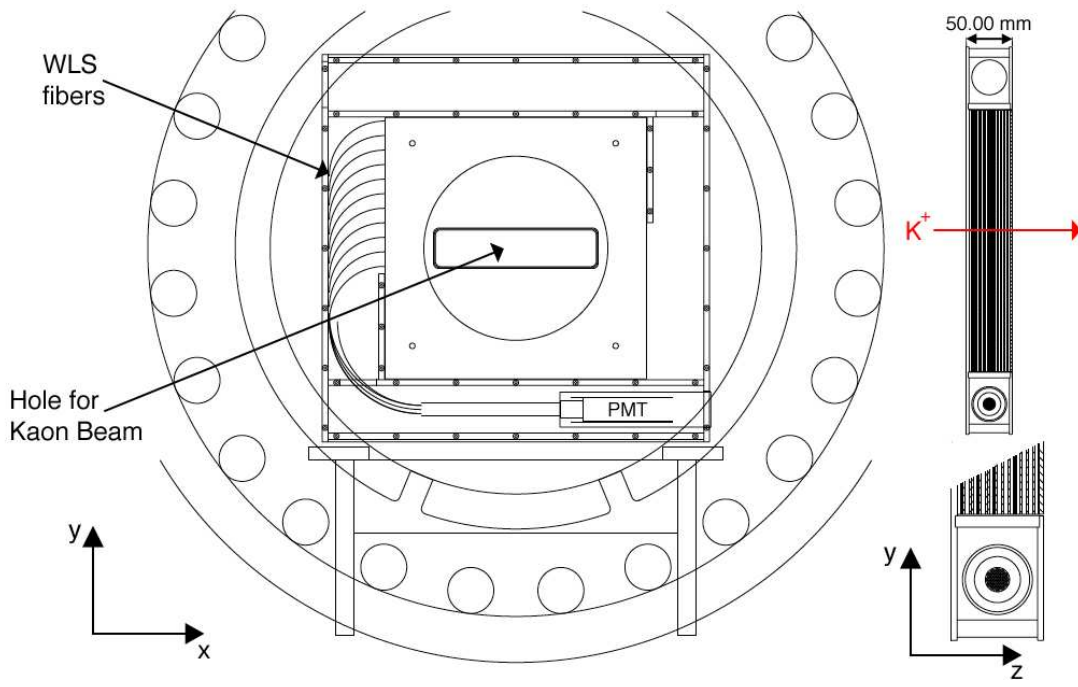
Figure 2.5: Schematic of the Upstream Photon Veto. The figure on the left shows the detector looking from the beam view. The figure in the upper-right shows a cross-section and the figure on the lower-right an enlarged cross-section. The K^+ beam traveled through the horizontal slot in the center of the detector. Figure reproduced from [72].
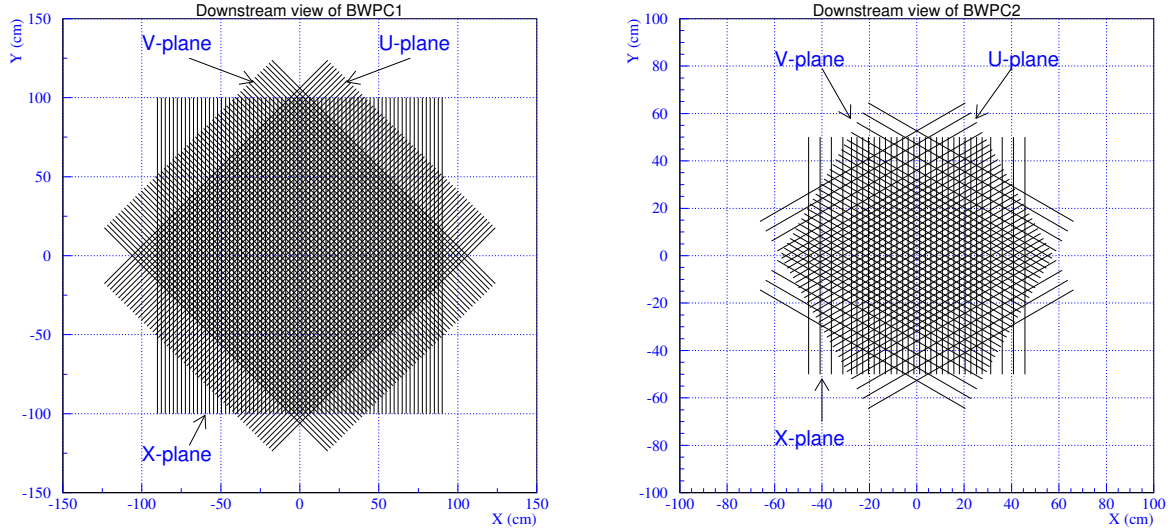
Figure 2.6: Cross-sectional views of the beam wire proportional chambers: the upstream BWPC1 (left) and the downstream BWPC2 (right). Figure reproduced from [37].

stream of the UPV and the second chamber (BWPC2) was located 1.0 m downstream from the first. Both chambers were filled with a recirculated mixture of CF4 (80%) and Isobutane (20%). Cross-sectional views of the BWPCs are shown in Figure 2.6.

BWPC1 contained three planes of 12-μm-diameter gold-plated tungsten anode wires with 1.27 mm wire spacing. The x-plane consisted of 144 anodes running along the vertical. The 120 wires in each of the u- and v-planes were oriented at $\pm 45°$ to the vertical, respectively. These wires were multiplexed by 2 in the readout channels. The total active area of the chamber was 17.8 cm in the horizontal by 5.08 cm in the vertical. The cathode foils were 25-μm thick aluminized mylar coated with carbon and the anode-cathode distance was 3.18 mm.

BWPC2 contained three planes of 12-μm-diameter gold-plated tungsten anode wires with 0.8 mm wire spacing and 120 anodes per plane. The directions of the anodes were vertical in the x-plane, and $\pm 60°$ to the vertical in the u- and v-planes, respectively. Among the 120 anode wires, the central 72 were multiplexed by 3 and the remaining wires were multiplexed by 6 to the readout channels, for a total of 32 readout channels

25

per plane. The cathode foils were 8-μm thick single-sided aluminized mylar coated with carbon and the anode-cathode distance was 1.6 mm.

2.2.4 Degraders

Downstream of BWPC1 were the degraders whose purpose was to slow the kaons such that they came to rest in the target before decaying. The lengths of the degraders were chosen such that mean stopping position in the z-direction for a K^+ in the target was halfway along the of the 24-cm long I-Counter which was used to tag charged decay products before they entered the drift chamber.

The upstream degrader was inactive and consisted of 11.11 cm of beryllium oxide (BeO) followed by 0.48 cm of lucite. BeO was chosen due to its high density (3.0 g/cm^3) and low atomic number. The low atomic number minimizes multiple scattering and thus minimized the spread from the beam axis of the kaons as they came to rest in the target. The reconstruction of the kaon decay in the target was considered less reliable when the decay occurred close to the radial edge of the target.

The downstream degrader was called the Active Degrader (AD) and consisted of 40 layers of 2-mm thick disks of Bicron BC404 scintillator alternated with 2.2-mm thick disks of copper. The diameters of these disks were 13.9 cm and 13.6 cm, respectively. The AD was split into 12 azimuthal segments, with each segment being read out by 14 Bicron BCF99-29-AA-MC wavelength shifting (WLS) fibers sent to a single Hamamatsu R1924 PMT. The output from each PMT was sent to a TDC and a CCD. The PMT signals were multiplexed in groups of four and sent to ADCs. A schematic view of the Active Degrader is shown in Figure 2.7. Measurements from the AD allowed identification of beam particles and detection of activity coincident with K^+ decays.
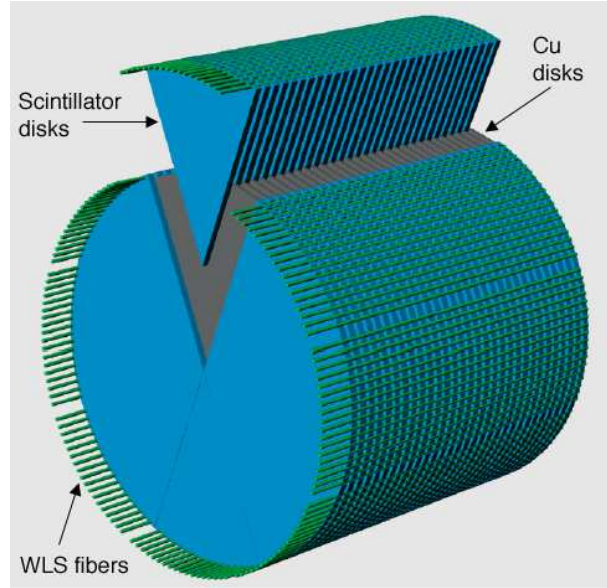
Figure 2.7: Schematic of the Active Degrader. The removed wedge represents one of the sectors. Figure reproduced from [72].

2.2.5   Beam Hodoscope

Downstream of the degraders was the Beam Hodoscope (B4) whose purpose was to detect the entrance position of beam particles into the target and to identify beam particles as K^+ or π^+ by energy loss. As shown in Figure 2.8, the two 11.8-cm diameter planes of the B4 Hodoscope were oriented at angles of $\pm 33.5°$, labeled u and v, respectively, with respect to the horizontal. Each plane consisted of 16 "z-shaped" Bicron BC404 scintillator fingers with a 7.2-mm pitch. The cross-section of each "z-shaped" finger, was 6.35-mm thick in the middle and 3.175-mm at the edges as shown in Figure 2.8. This shape was chosen to reduce the inactive regions and improve the spacial resolution. Three Bicron BCF990290AA-MC WLS fibers were embedded in each finger and connected to a single Hamamatsu H3165-10 PMT read out by TDC, ADC and CCD.
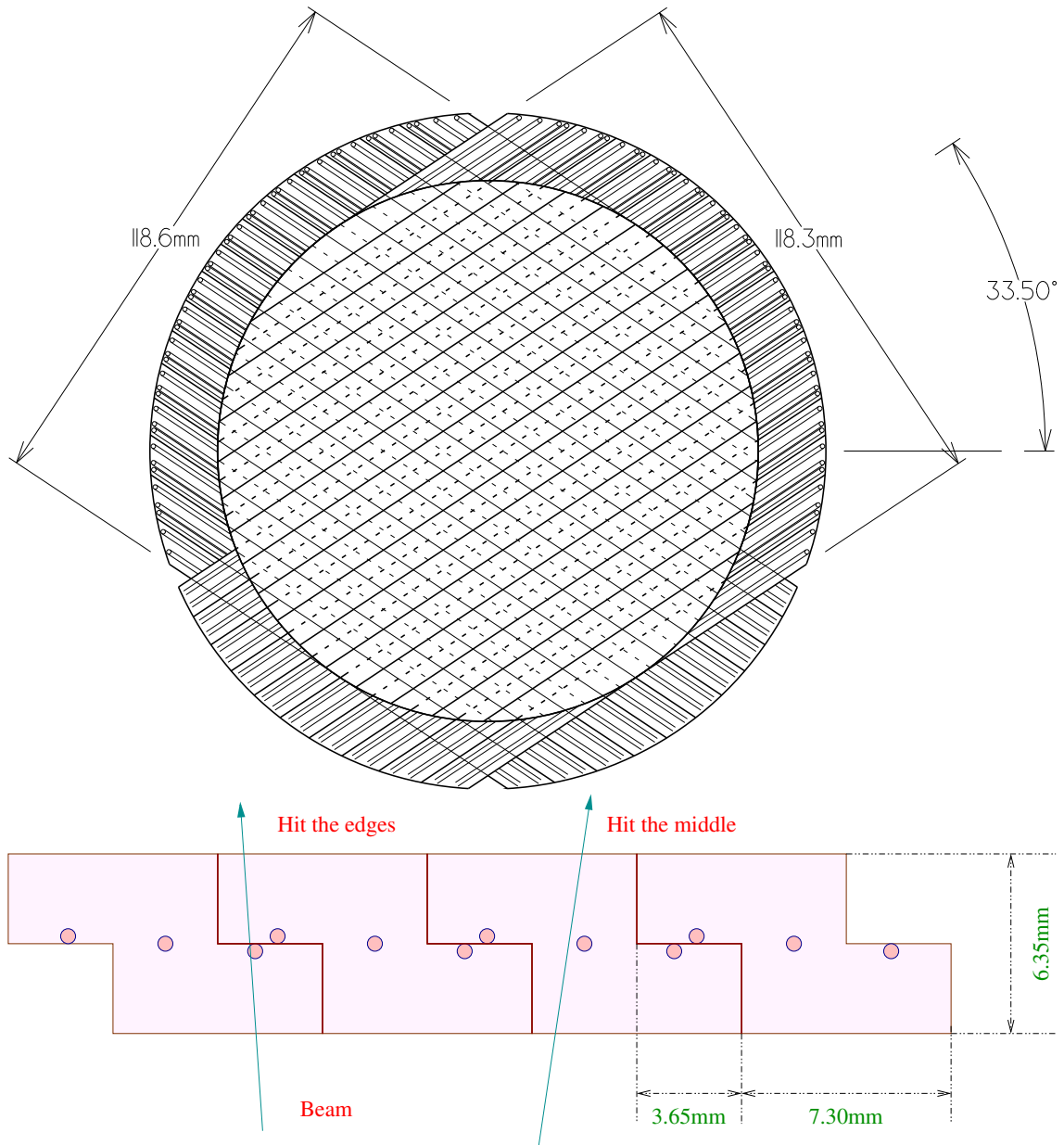
Figure 2.8: The upper figure shows the B4 Hodoscope from the beam view. The segments of the fingers are shown as solid lines for the upstream segments and dashed lines for the downstream segments. The outer ring shows the WLS fibers used to read out the scintillator fingers. The lower figure shows a schematic cross-section of one of the B4 layers with the approximate positions of the three WLS fibers (small circles) in each segment. Figure reproduced from [37].

2.2.6 Ring Veto

The Ring Veto (RV) was located at the same position along the beam direction as the B4 Hodoscope, but at a larger radius. The RV was designed to veto particles passing through the perimeter of the B4 Hodoscope. This annular detector was composed of two 180° arcs of 3.27-mm thick Bicron scintillator with an inner diameter that varied between 11.85 cm and 12.0 cm, and an outer diameter of 14.55 cm. Each of the two elements was read out by a Hamamatsu H3165-10 PMT whose signal was sent to ADC, TDC and CCD.

2.3 Target

The target (shown in Figure 2.9) was a 12-cm diameter cylinder, 3.1 m in length, which was made of 413 5-mm square Bicron BCF10 scintillating fibers. These fibers ran in the direction parallel to the beam and had 0.09-mm thick inactive cladding. Smaller fibers, known as edge fibers, were used to fill the gaps near the outer edge of the target. Each of the 5-mm fibers was connected to a Hamamatsu R1635-02 PMT. The edge fibers were multiplexed into groups of 12 and each group was read out by a single PMT. The PMT signals were sent to ADCs, TDCs and CCDs.

Typical energy deposits in an individual target fiber were on the order of tens of MeV for K^+s traveling along the fiber, and only ~ 1 MeV for π^+s passing perpendicularly through a fiber, where bench tests [46] measured the photoelectron production from these fibers to be 30 photoelectrons per MeV. Pattern recognition was used to assign fibers with deposited energy to the K^+ path (kaon fibers) or the π^+ path (pion fibers) from the K^+ decay (see Section 3.3.4). To cover this large dynamic range, two separate CCD channels were used to read-out the target fibers. Each fiber was read out individually by a "high-gain" CCD channel. The sum of 4-6 randomly positioned fibers was read out by a "low-gain" CCD channel. A double-pulse fit was performed on the CCD information for both the "low-gain" and "high-gain" CCD channels to identify the fiber in which the
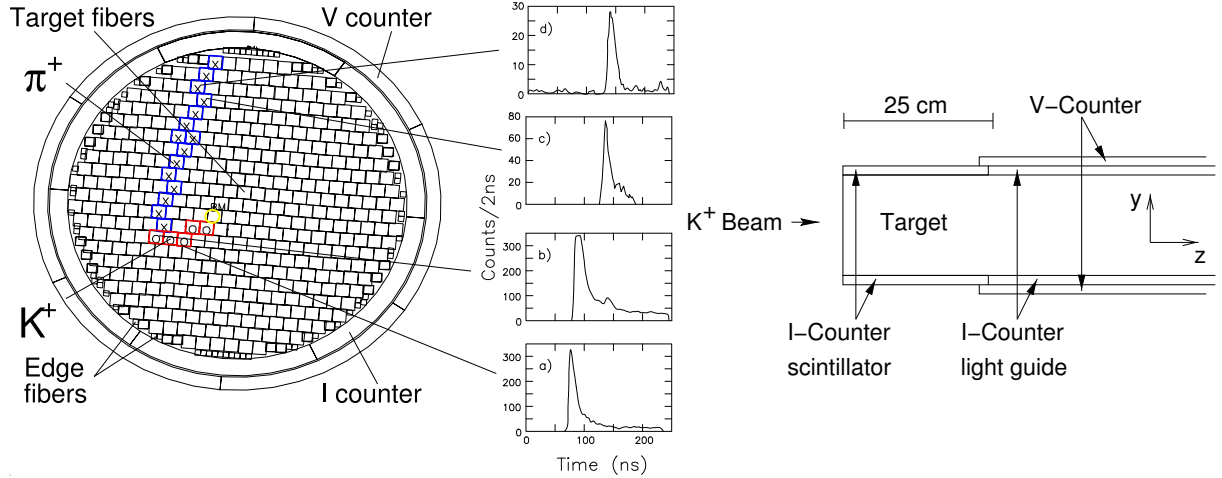
Figure 2.9: End (left) and side (right) views of the target. The CCD pulse-shape information for typical K^+ fibers is shown in the two lower plots "a" and "b", and for typical π^+ fibers in the two upper plots "c" and "d". The target is surrounded the plastic scintillator I-Counter (IC) and V-Counter. Figure reproduced from [37].

decay occurred and to decouple the energies deposited by the K^+ and the π^+ in that fiber. The target CCD fitter is described in more detail in Appendix C.

The fiducial region of the target was defined by two layers of six plastic scintillator counters surrounding the target as shown in Figure 2.9. The inner scintillators (I-counters or ICs) surrounded the target and tagged charged decay products before they entered the drift chamber. The IC was 6.4 mm thick with an inner radius of 6.0 cm and extended 24 cm from the upstream face of the target. The outer scintillators (V-Counters or VCs) overlapped the downstream edge of the IC by 6 mm and detected particles that decayed downstream of the fiducial region of the target. The VC was 5 mm thick and 1.96 m long. To prevent gaps, the VC elements were rotated by 30° with respect to the IC elements. Each IC and VC element was read out by an EMI 9954KB PMT whose signal was sent to ADC, TDC and a 500 MHz transient digitizer (TD) based on a flash ADC [14].
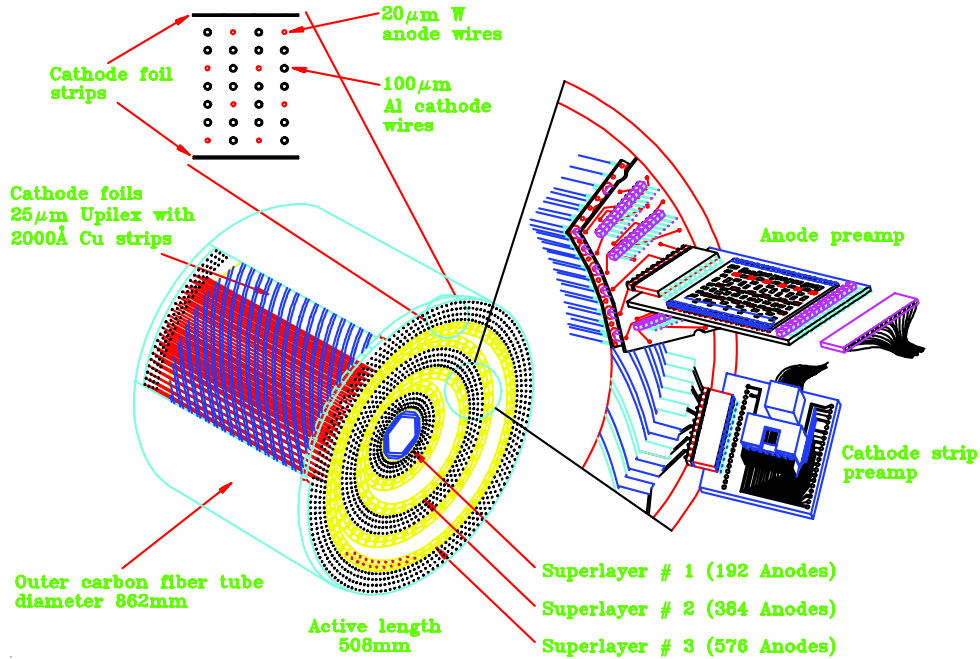
Figure 2.10: Schematic of the Ultra-Thin Chamber. Figure modified from [37].

2.4 Drift Chamber

The drift chamber, called the Ultra Thin Chamber (UTC), was located just outside of the I-counter, with an inner radius of 7.85 cm, an outer radius of 43.31 cm and length of 51 cm. The UTC consisted of three superlayers (see Figure 2.10), each of which had four layers of axially strung 20-μm anode wires made of gold-coated tungsten. Each of the anode wires was surrounded by eight 100-μm grounded gold-coated aluminum cathode wires to form a cell, with adjacent anodes sharing cathode wires. The cells in adjacent layers were staggered by one half of a cell width to resolve the left-right ambiguity. The superlayers were filled with a 49.8%:49.8%:0.4% mixture of argon, ethane and ethanol. The cathode wires were grounded and the anode wires maintained at 2 kV, resulting in a drift velocity of 5 cm/μs and a gain of 8×10^4. Each anode wire was instrumented with an ADC and a TDC. The drift time to the anode wires was used to determine the x-y positions of the charged track.

Each superlayer was sandwiched on either side by a plane of cathode strips, which

31

were aligned helically at a pitch angle of 45°. The cathode strips had a width of 7 mm, a separation of 1 mm and were made of 1200 Å thick copper coated with 300 Å thick nickel, and were mounted on a 25 μm thick Kapton foil. Each cathode strip was instrumented with an ADC and a TDC. The cathode strips were used to determine the track position along the z-direction by means of weighted mean of the induced signal on the anode wires.

The two inactive regions between superlayers were filled with nitrogen gas. Differential pressures of approximately 2 mbar in the five gas volumes supported the cathode foils. The total mass of the UTC was only 2×10^{-3} radiation lengths, excluding the inner and outer support tubes with the attached foils.

The UTC position resolutions (RMS) were approximately 175 μm in the x- and y-directions and 1 mm in the z-direction. The curvature of the charged particle track in the UTC due to the magnetic field was used to determine the momentum. The momentum resolution ($\Delta P/P$) for the two-body $K_{\pi 2}$ decay was 1.1% [22].

2.5   Range-Stack

The Range-Stack (RS) consisted of both scintillator counters and position-sensitive embedded straw chambers, and was located just outside of the UTC with an inner radius of 45.08 cm and an outer radius of 84.67 cm. The RS provided energy and range measurements, information for the observation of the $\pi^+ \rightarrow \mu^+ \rightarrow e^+$ decay sequence and measurement of photon activity.

2.5.1   Range-Stack Scintillator

The RS consisted of 19 layers of Bicron BC408 plastic scintillator, azimuthally segmented into 24 sectors as shown in Figure 2.11. The innermost layer, known as the T-counter, was 0.635 cm thick and 52 cm long. The T-counter defined the fiducial volume for the charged decay products and was thinner than the remaining RS layers to suppress the rate
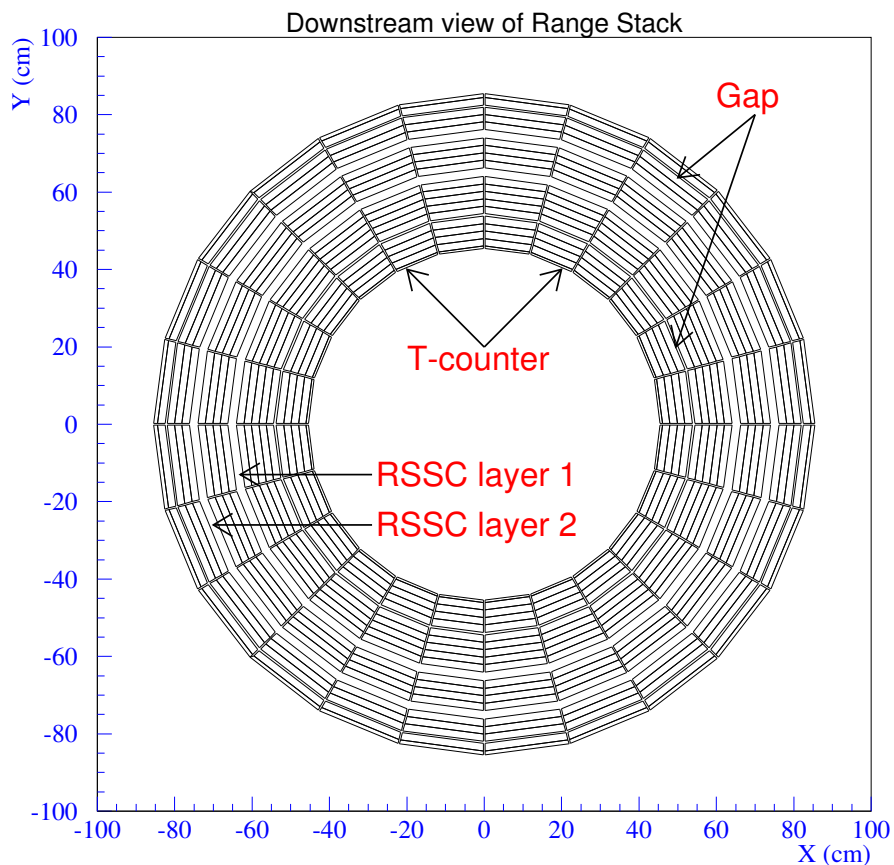
Figure 2.11: End view of the Range-Stack. The two superlayers of Range-Stack Straw Chambers are shown after RS layers 10 and 14. Figure reproduced from [37].

from photon conversions. Each of the T-counter scintillators was read out by seventeen 1-mm-diameter Bicron BCF-92 multiclad WLS fibers coupled to a Hamamatsu R1398 PMT at both the upstream and downstream ends. Layers 2-18 were 1.905 cm thick and 1.82 m long and each scintillator was coupled through light guides to EMI 9954KB PMTs at each end. Layer 19 was installed as part of the E949 upgrade and was used mainly to veto long range charged particles such as muons. This layer was 1.0 cm thick and had the same length and read out method as layers 2-18.

Signals from each PMT were sent to ADCs, TDCs and analog fan-in modules. The TDCs recorded up to 16 hits in a 10.5 μs time window. A time window of this length was

required to reliably capture information from the μ^+ decay, where the μ^+ has a lifetime of 2.2 μs [99]. Each group of four sectors was grouped into a hextant and the signals from the four PMTs in a given layer on a given end of a hextant were summed via the fan-in modules and sent to a TD. The TDs recorded the charge in 2 ns intervals (500 MHz sampling) with a resolution of 8 bits. This provided sufficient pulse-shape information to separate pulses as close as 5 ns apart. The time window used for the TDs was 8 μs until run 47959, 4 μs until run 48227, and 2.5 μs for the remaining runs. To determine the z-position of the interaction in a counter, it was possible to use the end-to-end time differences or the end-to-end ADC information differences.

2.5.2   Range-Stack Straw Chambers

Since the Range-Stack produced only very rough position information, two superlayers of Range-Stack Straw Chambers (RSSCs) were embedded after the 10th and 14th layers of the Range-Stack as shown in Figure 2.11. The position of a hit chamber provided x-y position information and the end-to-end time differences provided the z-position information. Each superlayer consisted of two staggered layers of 3.4 mm radius straw chambers which operated in self-quenching streamer mode at 3450 V. The inner superlayer is shown in Figure 2.11. The gas mixture in these chambers was 67% argon and 33% isobutane with a trace of water. The 50-μm-diameter gold-coated tungsten anode wires of the straw chambers ran parallel to the beam direction. The layers of the inner superlayer had 24 straws per sector with a length of 97.8 cm. The layers of the outer superlayer had 28 straws per sector with a length of 113.0 cm. The z-position resolution was 1.5 cm [73] and more details on the RSSCs can be found in [77].
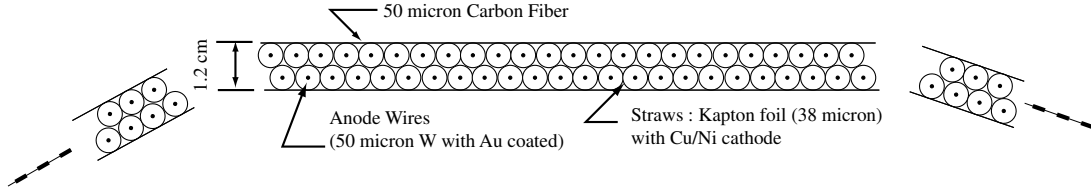
Figure 2.12: End view of the inner superlayer of Range-Stack Straw Chambers. The Straw Chambers ran parallel to the beam direction. Figure reproduced from [72].

2.6   Photon Veto

The E949 detector consisted of the hermetic system of photon detectors shown in Figure 2.1. The photon veto system consisted of almost every detector system in the E949 detector. Detectors whose sole purpose was the detection of photon activity were the Barrel Veto (BV), the Barrel Veto Liner (BVL), the upstream and downstream End Caps (ECs), the upstream and downstream Collars (CO), the downstream Microcollar (μCO) and the Downstream Photon Veto (DPV). Detectors that were part of the photon veto system, but also served other purposes were the AD, target, IC, VC and RS. For a given event, the regions of the target, IC and RS traversed by the charged track were excluded from the photon veto. The thickness of the photon veto in radiation lengths as a function of polar angle is shown in Figure 2.13.

2.6.1   Barrel Veto

The Barrel Veto (BV) was located in the outermost barrel region with an inner radius of 94.5 cm, an outer radius of 145.3 cm, and a length of 1.9 m. The BV covered 2/3 of the 4π sr solid angle photon veto coverage and had a thickness of 14.3 radiation lengths. The BV consisted of 48 azimuthal sectors and four radials layers as shown in Figure 2.14. From innermost to outermost, the radial layers consisted of 16, 18, 20 and 21 alternating layers of 1-mm thick lead and 5-mm thick Bicron BC408 plastic scintillator. The azimuthal boundaries between sectors were tilted so that it was not possible for a photon originating from the target to travel along a gap between sectors. Approximately 30% of the energy

35
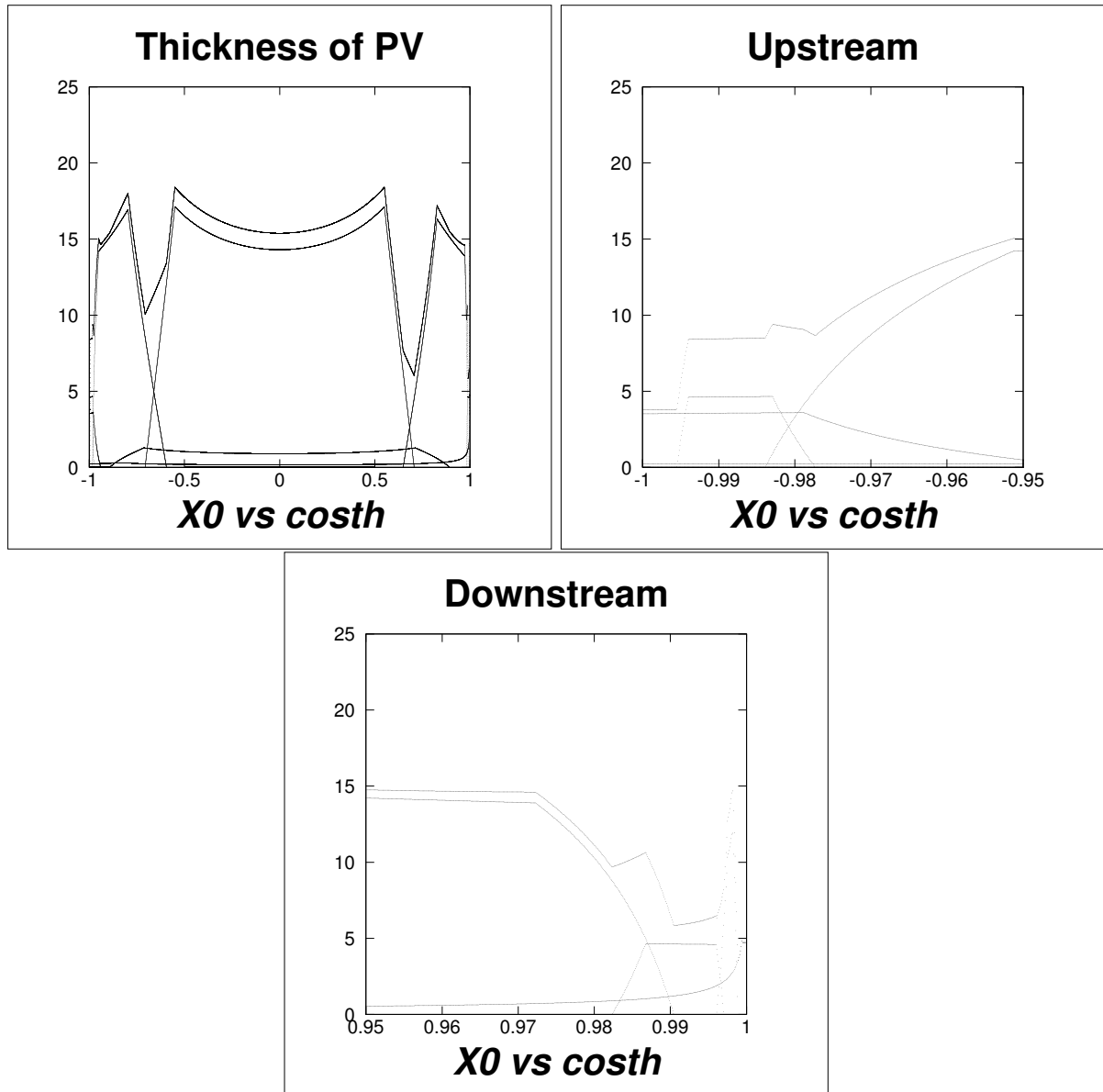
Figure 2.13: Radiation length "X0" versus the cosine of the polar angle "costh" for the photon detector system. The thickness is shown for all angles (top-left), angles closest to the upstream end (top-right), and angles closest to the downstream end (bottom-right). Figure reproduced from [44], courtesy of of Brookhaven National Laboratory.

deposited in the BV was deposited in the scintillator [15]. The upstream and downstream ends of each module were read out by EMI 9821KB PMTs and the signals were sent to ADCs and TDCs.

2.6.2 Barrel Veto Liner

As part of the E949 upgrades (Appendix A), the 2.29 radiation length Barrel Veto Liner (BVL) was installed to replace layers 20 and 21 of the E787 RS for the purpose of improved photon detection. As shown in Figure 2.14, the BVL consisted of 48 2.2-m long azimuthal sectors. Each sector consisted of 12 layers of 1-mm thick lead and 5-mm thick Bicron BC408 plastic scintillator. The BVL was expected to increase the photon veto rejection of $K_{\pi2}$ decays by a factor of two. The upstream and downstream ends of each module were read out by EMI 9821KB PMTs and the signals sent to ADCs and TDCs. Each group of eight adjacent sectors was grouped to form a hextant. Each end of a hextant was read out by a TD. Approximately 30% of the energy deposited in the BVL was deposited in the scintillator.

2.6.3 End Caps

The two End Cap (EC) photon detectors accounted for roughly one-third of the 4π sr photon veto coverage [35]. The upstream EC (EC1) is shown in Figure 2.15 and consisted of 75 undoped Cesium Iodide (CsI) crystals grouped into four rings. The downstream EC (EC2) consisted of 68 crystals, also grouped into 4 rings. The crystals were 25 cm in length, which was equivalent to 13.5 radiation lengths. The PMTs were coupled directly to the crystals via a Sylgard [41] cookie formed over the PMT and a ultraviolet transmitting optical filter that passed only the fast component of the CsI scintillation light and blocked the slow component. The fast component had a decay time of approximately 30 ns at 305 nm and the slow component had a decay time of 680 ns, contributing approximately
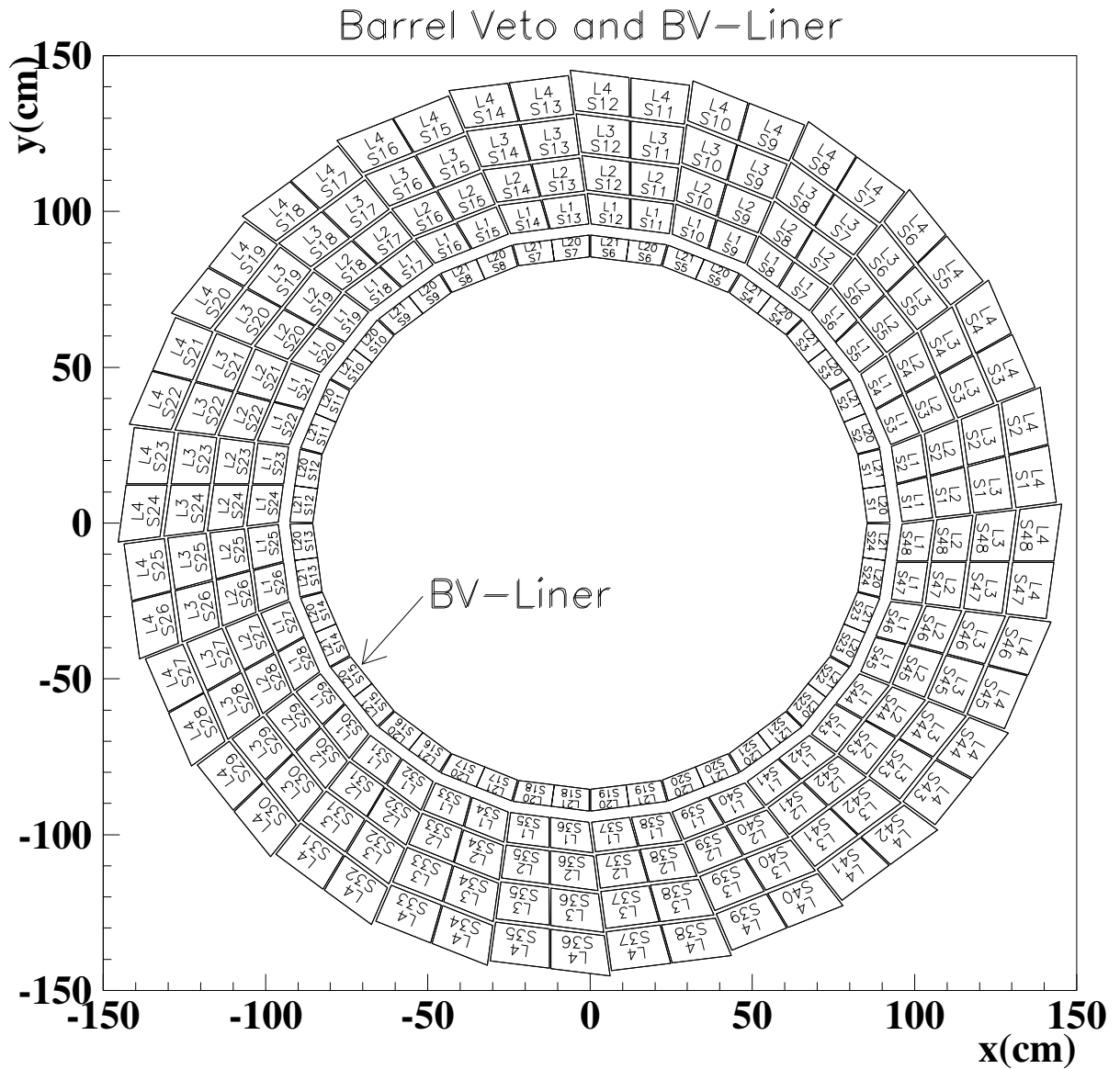
Figure 2.14: End view of the Barrel Veto (four outermost layers) and Barrel Veto Liner (innermost layer). The sets of numbers show the numbering of radial layer and sector. Figure reproduced from [72].
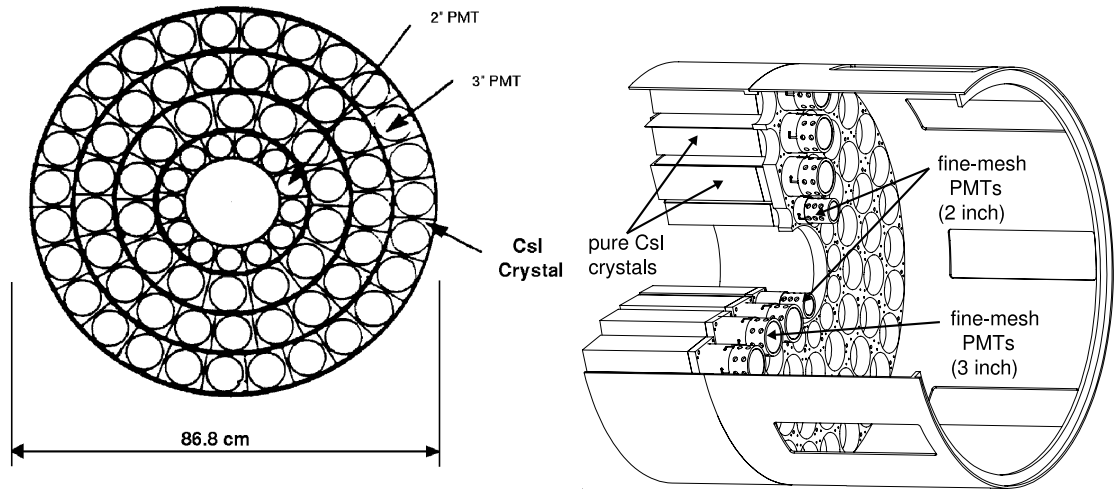
Figure 2.15: End view (left) and schematic of the End Cap assembly (right). Figure reproduced from [37].

20% of the total light output. Fine-mesh PMTs [68] were used due to their ability to maintain high gains in strong magnetic fields. Hamamatsu R5545 2" PMTs were used for the inner ring crystals and Hamamatsu R5545 3" PMTs for the crystals in the three outer rings. The PMT signals were sent to ADCs, CCDs, and constant fraction discriminators (CFDs). The output from the CFDs was used as part of the online photon veto and was also sent to TDCs.

Due to being quite near the beam line, the ECs were exposed to a high count-rate environment and as a result were prone to accidental hits occurring earlier than a given photon hit thereby reducing the efficiency of the photon veto. Offline pulse-finding was performed on the CCD information to separate double pulses close in time and to provide timing information.

2.6.4   Collar

The upstream and downstream Collar (CO) detectors were located beyond the ECs (see Figure 2.1) and covered the small angle region surrounding the beam line. The down-stream CO consisted of twenty-five 2-mm thick lead sheets alternating with 5-mm thick
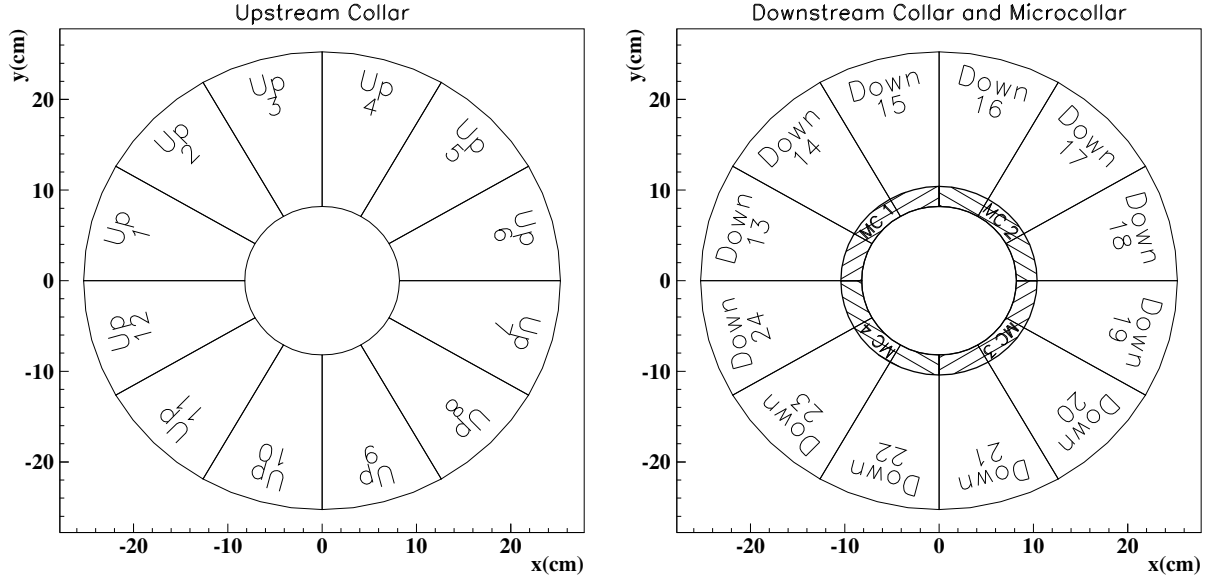
Figure 2.16: Upstream Collar (left), and downstream Collar and Microcollar (right). Element numbers are listed. Figure reproduced from [72].

Bicron BC404 scintillator sheets, providing a thickness along the beamline of about 9 radiation lengths. The upstream CO was of similar construction, but only half the thickness of the downstream one. The COs were each segmented into 12 azimuthal sectors. Each layer of the downstream CO was read out by 16 Bicron BCF99-29AA WLS multiclad fibers glued into grooves in the scintillator layer [82]. All fibers in a given sector were read out together. The fibers were polished and aluminized on one end to provide a reflective surface and the other end was coupled to a 1.17-m long lucite light guide. Each light guide was coupled to an EMI 9954KB PMT in a low magnetic field outside of the magnet. Each layer of the upstream CO was read out out by a lucite light guide coupled to the same type of PMTs outside of the magnet. Signals from the PMTs for each of the COs were sent to ADCs and TDCs.

2.6.5 Microcollar

The Microcollar surrounded the beamline directly downstream of the downstream CO. It had an inner diameter of 15.6 cm, an outer diameter of 20.0cm and a length of 53.0 cm.

40
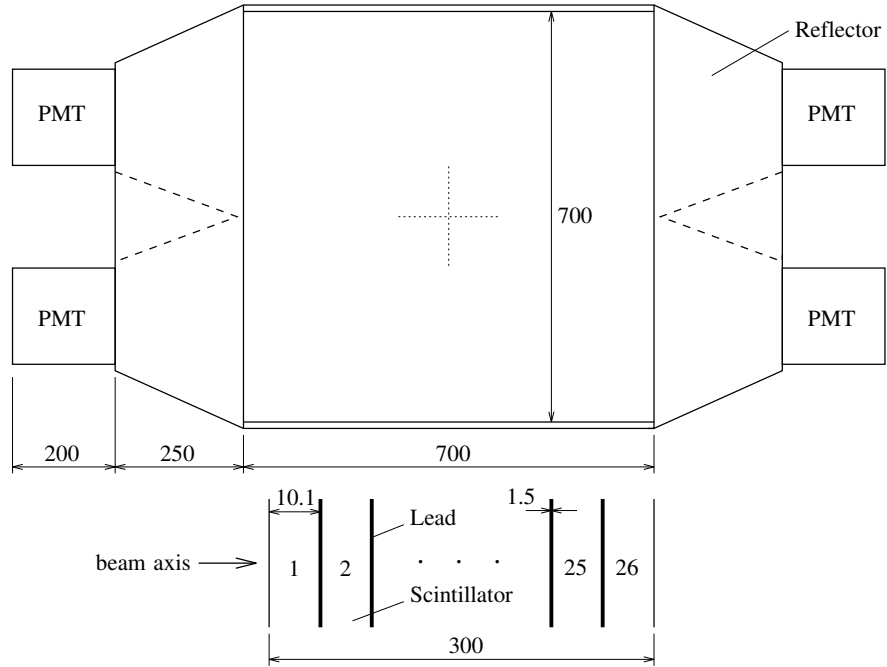
Figure 2.17: Schematic of the Downstream Photon Veto. All dimensions are in mm. Figure reproduced from [72].

It consisted of eight azimuthal sectors containing eight layers of 2 mm scintillating fibers separated by seven layers of 60 μm Pb. The fibers in each group of two adjacent sectors were read out by an EMI9954 PMT whose signal was sent to an ADC and TDC.

2.6.6 Downstream Photon Veto

The Downstream Photon Veto (DPV) was located at the far downstream end of the detector, after the target PMTs. The DPV, shown in Figure 2.17, was a 700 mm by 700 mm square that intersected the beam path. It consisted of 26 sheets of 10-mm thick scintillator alternating with 1.5-mm thick lead, for a total thickness of 7.3 radiation lengths. Each scintillator layer was read out simultaneously by four PMTs whose signals were sent to TDCs and ADCs.

2.7 Trigger

The E949 $\pi\nu\bar{\nu}$ signal triggers selected $K^+ \to \pi^+\nu\bar{\nu}$ events from the large number of K^+ decays and scattered beam particles, with requirements on the range of the π^+ track, the observation of a $\pi^+ \to \mu^+$ decay signature in the RS, the absence of other activity at the time of the observed π^+ track and the presence of a K^+ at an appropriately earlier time.

The trigger was composed of a fast level-0 trigger and a slower level-1 trigger. The level-0 trigger made its decision entirely from logic pulses from various detectors, had a rejection of 10^3 and introduced 38 ns seconds of dead time for every coincident hit in the first two layers of the RS (known as the T●2 trigger) [100]. Rejection is the ratio of the number of events encountered by that trigger to the number of events accepted by that trigger. The dead time is the amount of time that the detector is unable to trigger on subsequent events due to being busy processing information from a previously triggered event. The level-1 trigger, composed of the level-1.1 and level-1.2 triggers, operated on the events passing the level-0 trigger and involved partial processing of ADC and TD data. The level-1.1 trigger had a rejection factor of 12 after level-0, and introduced 10 to 20 μs of dead time per level-0 trigger. The level-1.2 trigger had a rejection factor of 2 after level-1.1 and introduced a dead time of up to 100 μs per level-1.1 trigger. The total rejection of these triggers reduced the 2.6×10^6 K^+ decays per spill to about 100 events.

2.7.1 Signal Triggers

Two signal triggers were used: $\pi\nu\bar{\nu}(1)$ and $\pi\nu\bar{\nu}(2)$ for the kinematic signal regions PNN1 and PNN2, respectively. The PNN1 analysis used only events passing the $\pi\nu\bar{\nu}(1)$ trigger as signal data while the PNN2 analysis used events passing either the $\pi\nu\bar{\nu}(1)$ or $\pi\nu\bar{\nu}(2)$

triggers. These triggers had the following requirements:

$$\pi\nu\bar{\nu}(1) \equiv \text{KB} \cdot \text{DC} \cdot \text{IC} \cdot (\text{T} \bullet 2) \cdot (6_{ct} + 7_{ct}) \cdot \overline{19_{ct}} \cdot \overline{(\text{BV} + \text{BVL} + \text{EC})} \cdot$$
$$\text{L0rr1} \cdot \overline{\text{zfrf}} \cdot \text{HEX} \cdot \text{L1.1} \cdot \text{L1.2}, \tag{2.3}$$

$$\pi\nu\bar{\nu}(2)_1 \equiv \text{KB} \cdot \text{DC} \cdot \text{IC} \cdot (\text{T} \bullet 2) \cdot 3_{ct} \cdot 4_{ct} \cdot 5_{ct} \cdot 6_{ct} \cdot \overline{(13_{ct} + \cdots + 18_{ct})} \cdot \overline{19_{ct}} \cdot$$
$$\overline{(\text{BV} + \text{BVL} + \text{EC})} \cdot \text{L0rr2} \cdot \text{HEX} \cdot \text{L1.1} \cdot \text{L1.2}, \tag{2.4}$$

$$\pi\nu\bar{\nu}(2)_2 \equiv \text{KB} \cdot \text{DC} \cdot \text{IC} \cdot (\text{T} \bullet 2) \cdot 3_{ct} \cdot 4_{ct} \cdot 5_{ct} \cdot 6_{ct} \cdot \overline{(13_{ct} + \cdots + 18_{ct})} \cdot \overline{19_{ct}} \cdot$$
$$\overline{(\text{BV} + \text{BVL} + \text{EC})} \cdot \text{L0rr2} \cdot \text{HEX} \cdot \text{L1.1} \cdot \text{L1.2} \cdot (\text{PS16} + \overline{C_\pi}), \tag{2.5}$$

which are explained in more detail below. In the trigger conditions described below, the designation "ct" refers to the Range-Stack sectors associated with the T$\bullet$2 hit plus the next two clockwise sectors, where clockwise was the direction that a positive particle moved in the magnetic field.

KB - The K^+ beam condition required a coincident hit in the kaon Čerenkov Counter (t_{CK}), the B4 Hodoscope, the AGS spill gate, and an analog sum of the energy of the hit fibers in the target of at least 20 MeV. This requirement ensured that the beam particle entering the target was a kaon and served as a beam strobe (BS) for the trigger. The AGS spill gate indicated the time in which the K^+s produced during the 2.2-s long AGS proton spill should have been arriving at the target.

T$\bullet$2 - A coincidence hit was required between the first two layers (T-Counter and layer 2) of the RS in the same sector. This condition required that a charged track from from the kaon decay entered the Range-Stack. This T$\bullet$2 time typically served as the detector strobe (DS) that gated all of the ADCs not associated with the beam system or target and provided a common stop for many of the TDCs.

43

IC - At least one of the hits in the I-Counter was required to be coincident with the T•2 time. This condition ensured that a charged track from the kaon decay entered the fiducial region of the detector.

DC - The online delayed coincidence condition (DC), was that the IC time (t_{IC}) was required to be at least 2 ns later than the time in the Kaon Čerenkov Counter (t_{CK}). This delayed coincidence requirement ensured that beam particle was a kaon that had decayed at rest rather than a beam pion that scattered into the active region of the detector or a kaon that decayed in flight.

$\overline{\text{zfrf}}$ - An additional requirement defining the active region of the detector was imposed for the $\pi\nu\bar{\nu}(1)$ trigger. This required the charged track to stop in the active region of the RS scintillators and not the second superlayer of the RSSCs (after RS layer 14). This condition did not need to be applied to the $\pi\nu\bar{\nu}(2)$ trigger since the range conditions of the $\pi\nu\bar{\nu}(2)$ trigger did not allow the pions to reach RS layer 13. It also removed long-range tracks with hits at large z-positions.

$6_{ct} + 7_{ct}$ - For the $\pi\nu\bar{\nu}(1)$ trigger, the charged track was required to reach RS layer 6 or 7. This condition suppressed the $K^+ \to \pi^+\pi^-\pi^+$ and $K^+ \to \pi^+\pi^0\pi^0$ backgrounds.

$3_{ct} \cdot 4_{ct} \cdot 5_{ct} \cdot 6_{ct}$ - For the $\pi\nu\bar{\nu}(2)$ trigger, the charged track (ct) was required to reach layer 6 and have hits in all previous layers. This condition suppressed backgrounds from 3 or more body decays such as $K^+ \to \pi^+\pi^-\pi^+$ and $K^+ \to \pi^+\pi^0\pi^0$.

$\overline{19_{ct}}$ - For the $\pi\nu\bar{\nu}(1)$ trigger, the $K_{\mu2}$ background was suppressed by requiring that the charged track did not reach the 19th layer of the RS.

$\overline{(13_{ct} + \cdots + 18_{ct})} \cdot \overline{19_{ct}}$ - For the $\pi\nu\bar{\nu}(2)$ trigger, the charged track was not allowed to reach Range-Stack layers 13 through 19. This condition suppressed the $K_{\mu2}$ background and other long-range charged tracks beyond the PNN2 kinematic region.

L0rr1, L0rr2 - These conditions were a refined calculation of the charged track range, which included the number of target fibers hit and the deepest layer of penetration of the track as corrected for polar angle by a measurement of the z-position of the track from flash TDCs on RS layers 3 and 11-13. The deepest later of penetration was determined by the online stopping-counter finder (SCF). The event was rejected if this calculated range was too long to be consistent with a charge track due to a π^+ in the kinematic region of interest (L0rr1 for PNN1 and L0rr2 for PNN2). For L0rr2, the only information used was the number of target fibers hit. These conditions suppressed the $K_{\mu 2}$ background and other long-range charged tracks beyond the kinematic region of interest.

$\overline{\textbf{BV} + \textbf{BVL} + \textbf{EC}}$ - Online photon veto in the BV, BVL and EC rejected events if there was activity coincident with the T•2 time. For each of the BV and BVL counters, digital mean-timers [100] were used to determine the mean time of the discriminated PMT signals from either end of the counter.

HEX - Only one RS hextant was allowed to have hits coincident with T•2, or two hextants if they were adjacent. This condition rejected events with multiple tracks and events with photon activity in the RS.

L1.1 - The level-1.1 trigger required a signature of $\pi^+ \to \mu^+$ decay in the online stopping counter. The height (PH) and the area (PA) of the pulse(s) as recorded by the TDs in the stopping counter were compared and the event was rejected if the ratio PH/PA was too large and there was no evidence of a detached pulse. This condition removed events without the $\pi^+ \to \mu^+$ decay signature as the ratio was smaller for double pulse activity than for single pulse. This decision was made by a control board with Application Specific Integrated Circuits (ASICs) on each TD board.

L1.2 - The level-1.2 trigger used data digitized by the ADCs and consisted of three con-

45

ditions. The first condition was the "L1.1 afterburner", which rejected events with accidental activity near the stopping counter. This rejected muon events that passed L1.1 due to accidental activity near the stopping counter and faked the double-pulse $\pi^+ \to \mu^+$ decay signature in the stopping counter. The second condition was the "HEX afterburner", which rejected events where one of the two adjacent hextant hits was not due to the charged track. This rejected events that passed the HEX trigger condition due to accidental activity. The third condition rejected events where the SCF assignment was not meaningful, such as finding a stopping layer beyond layer 19.

PS16+$\overline{C_\pi}$ - An online pion Čerenkov (C_π) veto was imposed during run 49151, when the beam separator broke down and the rate of beam pions was found to be too high. Approximately 39.4% of the data were taken before this condition became part of the trigger, changing the $\pi\nu\bar{\nu}(2)$ trigger from $\pi\nu\bar{\nu}(2)_1$ to $\pi\nu\bar{\nu}(2)_2$. In addition to events passing the C_π veto, 1/16th of the events were passed regardless of the C_π veto to allow measurement of the C_π veto performance.

2.7.2 Monitor Triggers

In addition to the $\pi\nu\bar{\nu}$ signal triggers, there were monitor triggers for calibration and normalization, as well as triggers for other physics modes. Only the monitor triggers used throughout the rest of this analysis are described here. A complete list of E949 triggers is available from [63]. The monitor triggers were prescaled to reduce the impact on the total dead time and the monitor trigger data were taken simultaneously with $\pi\nu\bar{\nu}$ signal data to ensure the experimental conditions were the same for all analyzed data.

$K_{\mu 2}$ Monitor Trigger

Since the final state of this decay contains no photons or additional charged particles, it was used for many of the acceptance measurements. This sample was used to determine the fraction of beam kaons coming to rest in the target by normalizing the measured $K_{\mu 2}$ branching ratio to the world average. This sample was also used to optimize the range-momentum consistency cut and the target quality cuts dealing with energy deposits. The $K_{\mu 2}$ trigger condition was defined as

$$K_{\mu 2} \equiv \mathrm{KB} \cdot (\mathrm{T} \bullet 2) \cdot (6_{ct} + 7_{ct}) \cdot (17_{ct} + 18_{ct} + 19_{ct}). \tag{2.6}$$

$K_{\pi 2}$ Monitor Trigger

The final state of this decay contained two photons from the π^0 decay and a mono-energetic π^+. The π^+ from this sample was used to check the measurement of the charged track momentum, energy and range, as well as to study particle identification in the Range-Stack. The photons were used to study the photon veto. The $K_{\pi 2}$ trigger condition was defined as

$$K_{\pi 2} \equiv \mathrm{KB} \cdot (\mathrm{T} \bullet 2) \cdot (6_{ct} + 7_{ct}) \cdot \overline{(19_{ct})}. \tag{2.7}$$

π_{scatter} Monitor Trigger

This sample contained beam pions that scattered into the fiducial volume of the RS. They were identified as beam pions by the πB trigger, which was the same as the KB trigger, except that a coincident hit was required in the Pion Čerenkov Counter instead of the Kaon Čerenkov Counter. Due to these pions not being mono-energetic, they were kinematically similar to $\pi\nu\bar{\nu}$ in the RS. This sample was used to calibrate the ionization energy loss of the pions and for studying the acceptance of many selection criteria applied

to the RS. The π_{scatter} trigger condition was defined as

$$\pi_{\text{scatter}} \equiv \pi\mathrm{B} \cdot \overline{\mathrm{DC}} \cdot (\mathrm{T} \bullet 2) \cdot \mathrm{IC} \cdot (6_{ct} + 7_{ct}) \cdot \overline{\mathrm{BV} + \mathrm{BVL} + \mathrm{EC}} \cdot \mathrm{HEX}. \qquad (2.8)$$

2.8 Summary of 2002 Data Collection

The physics run for the E949 experiment took place over 12 weeks from March to June of 2002. The data collected during this period corresponded to a total of 1.71×10^{12} K^+s that entered the target (KB$_{live}$). This total represents the total recorded by the scalers that counted the number of KB triggers for each spill for only "good runs". Various runs were discarded due to technical flaws known at the time of data collection or discovered during the analysis. Runs discarded in this way resulted in a lower overall KB$_{live}$, but did not introduce bias into the final measurement since monitor and $\pi\nu\bar{\nu}$ signal trigger data were discarded for all discarded runs. Figure 2.18 shows the accumulated KB$_{live}$ for the various running periods of E787 and E949. The proton intensity at the AGS for E949 was twice that of E787 and the total K^+ exposure for E949 was about 30% of that for E787 due to the significantly shorter running period.
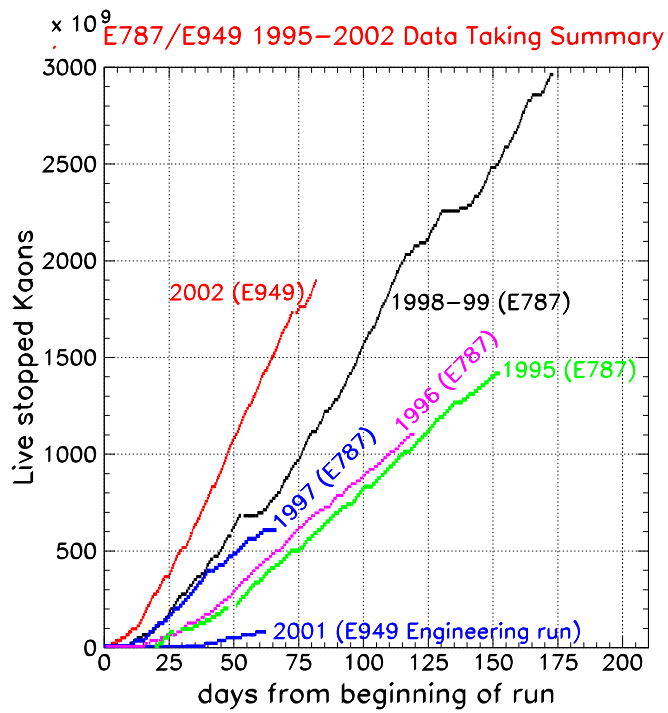
Figure 2.18: Number of accumulated K^+s that entered the target for E787 and E949 as a function of data-taking days. Figure reproduced from [37].

Chapter 3

Analysis Overview

This chapter discusses the key analysis methods and steps used to estimate the background level, measure the acceptance, and finally obtain the branching ratio for $K^+ \to \pi^+ \nu \bar{\nu}$.

The blind analysis technique [6, 7, 8, 11] was designed to avoid bias when creating the selection criteria ("cuts") used to suppress the backgrounds that could mimic the $K^+ \to \pi^+ \nu \bar{\nu}$ signal. This technique was based on identifying the competing background processes *a priori*. Knowing these competing background processes, two kinematic phase space regions having a high signal-to-background ratio were identified. The first region, known as PNN1, was above the $K^+ \to \pi^+ \pi^0$ ($K_{\pi 2}$) peak and covered the momentum region for the charged π^+ from 211 MeV/c to 229 MeV/c. The second region, known as PNN2, was below the $K_{\pi 2}$ peak and covered the momentum region from 140 MeV/c to 199 MeV/c. These two regions are shown in Figure 3.1 as part of the total momentum spectrum of the π^+ from the $K^+ \to \pi^+ \nu \bar{\nu}$ decay. This analysis was concerned with the PNN2 signal region and unless otherwise specified, all mentions of "the signal region" refer specifically to the PNN2 signal region.

To estimate the background level in the signal region for each type of background, a bifurcation method [6, 7, 8, 11] was used. This method relied on two uncorrelated sets of cuts suppressing each type of background. Multiple validity checks were performed to
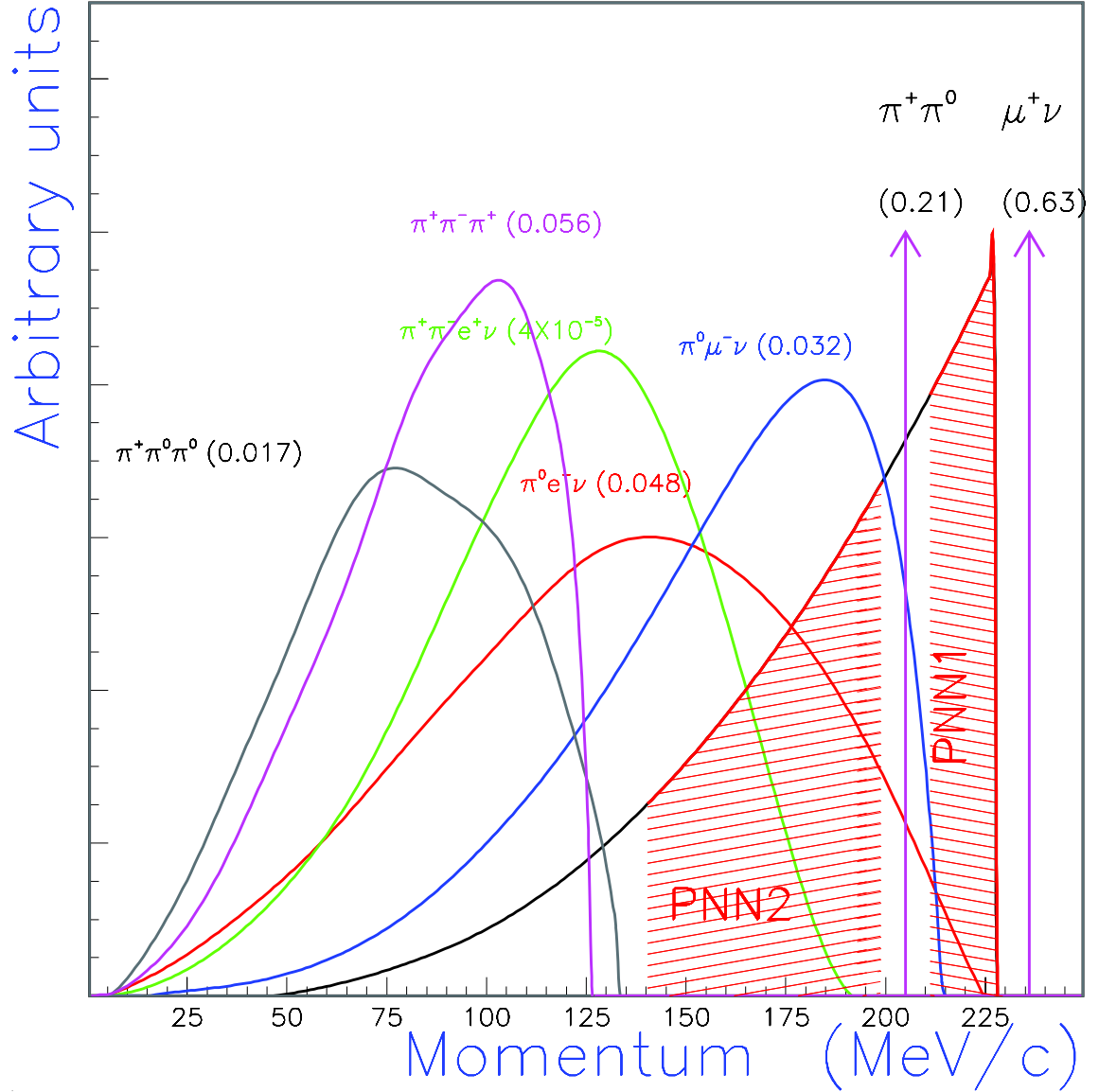
Figure 3.1: The momentum spectrum of the π^+ for the Standard Model $K^+ \to \pi^+ \nu \bar{\nu}$ process showing the PNN1 and PNN2 signal regions. Also shown are the charged product momentum spectra of the seven highest branching ratio K^+ decay modes along with their branching ratios in parentheses. The processes are not shown to scale. Figure modified from [37].

look for correlations between sets of bifurcation cuts, search for flaws in the analysis and check for cross-contamination in the background evaluations.

The components of acceptance were measured using monitor trigger data where possible, and Monte Carlo simulation data when appropriate samples could not be made using monitor trigger data. To validate the acceptance measurement, the $K_{\pi 2}$ branching ratio was measured. Based on the acceptance measurement and the total K^+ exposure, the single event sensitivity was determined, where the single event sensitivity was the branching ratio that would have corresponded to one candidate in the absence of background.

Once the background measurements were finalized and the acceptance measurements completed, the signal region was divided into nine cells whose relative signal-to-background varied by approximately a factor of four across the cells. The signal region was examined and all observed events in the signal region were considered signal candidates. Based on a likelihood analysis incorporating the acceptance, background and observed signal events in each cell, the branching ratio from this analysis was determined. Using the likelihood analysis, these results were combined with results from the previous E787 and E949 analyses [11, 6, 7] to obtain a combined E787/E949 branching ratio.

3.1   Overview of Backgrounds

Figure 3.2 shows the distribution of the range in plastic scintillator (`rtot`) versus momentum (`ptot`) of the outgoing charged particle for events that passed the $\pi\nu\bar{\nu}(1)$ or $\pi\nu\bar{\nu}(2)$ triggers. Events from competing background processes could mimic $K^+ \to \pi^+\nu\bar{\nu}$ and become background if they fell into the kinematic signal region PNN2BOX and passed all analysis cuts. These competing background processes could be misidentified as $K^+ \to \pi^+\nu\bar{\nu}$ decays when combinations of the following failure modes occurred: (1) photons and other particles escaped detection, (2) the pion was reconstructed incorrectly due to charged-particle scattering, (3) the overlapping tracks from different particles in-
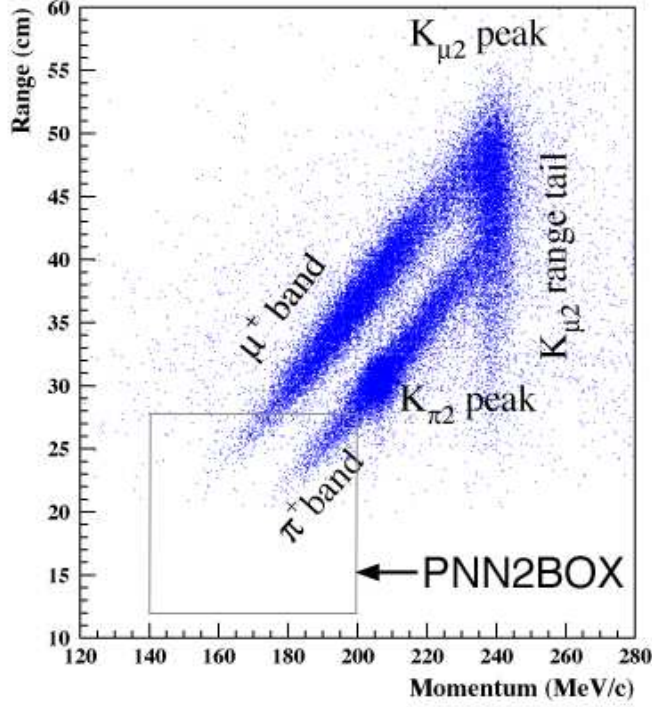
Figure 3.2: The range in plastic scintillator (`rtot`) versus momentum (`ptot`) distribution of the outgoing charged particle for events passing the $\pi\nu\bar{\nu}(1)$ or $\pi\nu\bar{\nu}(2)$ triggers. The momentum was determined assuming pion mass for all particles. The kinematic signal region is labeled "PNN2BOX". Figure reproduced from [72].

terfered with kinematic measurements or particle-identification cuts, or (4) beam particles emulated stopped-K^+ decays.

3.1.1 Stopped-K^+-Decay Backgrounds

The dominant background in this analysis was from $K_{\pi2}$ events where the photons escaped detection and the π^+ scattered in the target or Range-Stack such that the event fell into the kinematic signal region. The radiative $K_{\pi2}$ decay ($K_{\pi2\gamma}$) became a background when all three photons escaped detection. The $K^+ \to \mu^+\nu\gamma$ ($K_{\mu2\gamma}$) and $K^+ \to \mu^+\pi^0\nu$ ($K_{\mu3}$) processes were the primary source of muon-based backgrounds when the muon was misidentified as a pion and the photons escaped detection. The $K^+ \to \pi^+\pi^-e^+\nu$ (K_{e4}) decay became most problematic when the π^- and e^+ had low energies and escaped

detection.

3.1.2 Beam-Based Backgrounds

The beam-based backgrounds came from beam-pions scattering into the fiducial region of
the detector (π_{scatter}) or beam kaons decaying in flight.

The single-beam background originated from π_{scatter} and kaon decay-in-flight events
that passed the delayed coincidence requirement between the incoming beam particle and
the outgoing charged decay product due to incorrectly measured beam or Range-Stack
timing. For the π_{scatter} events, the beam pion also had to have been misidentified as a
kaon.

The double-beam background came from events where the decay products from an
initial kaon were missed, and a second beam particle was subsequently missed by the
beam-line detectors. This second particle could have been a π_{scatter} or kaon decay-in-
flight. This type of event satisfied the delayed coincidence requirement between incoming
beam kaon (the initial kaon) and outgoing decay product (the second beam particle)
times.

The charge-exchange (CEX) background came from the charge exchange interaction
$K^+n \to K^0p$ in the target. The most problematic decays that result from this charge ex-
change process were $K^0_L \to \pi^+e^-\nu_e$ and $K^0_L \to \pi^+\mu^-\nu_\mu$, both of which have π^+ kinematics
that overlap the kinematic signal region.

3.2 Analysis Strategy and Methods

3.2.1 Blind Analysis Method

A blind analysis method was developed to search for $K^+ \to \pi^+\nu\bar{\nu}$ signal candidates
amongst the many competing background processes. This method was based on (1) iden-

tifying the background sources *a priori*, and (2) keeping the signal region hidden until the background and acceptance analyses were completed. The signal region was defined by the application of all analysis cuts, thus, to avoid examining the signal region, two methods were used to create signal-like samples and samples rich in a specific type of background. The first was to use samples created from monitor triggers (see Section 2.7.2 for monitor trigger definitions). The second was to use events passing the PNN1 or PNN2 triggers and invert a cut that distinguished signal from background. By inverting a cut that suppressed a specific background, a sample of that background was created and the effectiveness of other cuts in suppressing that background could be measured. Depending on the circumstance, both of these methods could be used to create signal-like or background-like samples for use in developing cuts.

3.2.2 Bifurcation Method to Evaluate Backgrounds Using Data

Estimation of background levels in this analysis was performed using a bifurcation method in which each background was heavily suppressed by at least two sets of cuts designed to be generally uncorrelated. Studies such as the outside-the-box and the single-cut and double-cut failure studies, detailed in Chapter 5, were used to establish the level of correlation between these cuts.

For each source of background, a sample of that background was created by applying setup cuts that suppressed other background sources, leaving a sample made almost entirely of the desired background. Using this sample, the bifurcation method was used to estimate the number of events of that background that would remain in the signal region after all analysis cuts have been applied. Figure 3.3 illustrates the bifurcation method using the parameter space of the uncorrelated sets of bifurcation cuts, CUT1 and CUT2. The region "A" represents the signal region and contains A events from a sample which has passed both CUT1 and CUT2. Region "D" contains the D events which have failed

both CUT1 and CUT2. The total number of events in the sample is $A + B + C + D$. If the rejection of one of the cuts does not depend on the rejection of the other cut (they are uncorrelated), the ratios of the events in the four regions will be $A/B = C/D$. Rearranging this algebraic expression allows the number of background events in the signal region A to be estimated without being directly measured: $A = BC/D$.

In practice, the E949 bifurcation analysis was done through two branches: a normalization branch to measure B, and a rejection branch to determine the ratio $R = (C + D)/C$, where R was known as the rejection of CUT1. In this analysis, the convention was that the number of events in the region "B" was referred to as the normalization and assigned the notation N. Given these definitions, the number of background events in the signal region was estimated by

$$bg = \frac{N}{R - 1},$$ (3.1)

which is algebraically equivalent to $A = BC/D$.

3.2.3   Two Data Sets

After reconstructing events passing the $\pi\nu\bar{\nu}(1)$ or $\pi\nu\bar{\nu}(2)$ triggers and processing them to remove unreliable data, the data were divided into "1/3" and "2/3" data sets selected uniformly from the entire data set. The analysis cuts were developed and optimized using the 1/3 data set. Once the final cut positions were set, the 2/3 data set was used to evaluate the final background levels, removing potential bias introduced by optimizing the cuts on the 1/3 data set.

3.2.4   Validity Checks

This section briefly describes the validity checks performed to verify the reliability of the analysis strategy. The validity checks discussed are the single-cut and double-cut failure studies, the outside-the-box studies, and the contamination studies used to determine the
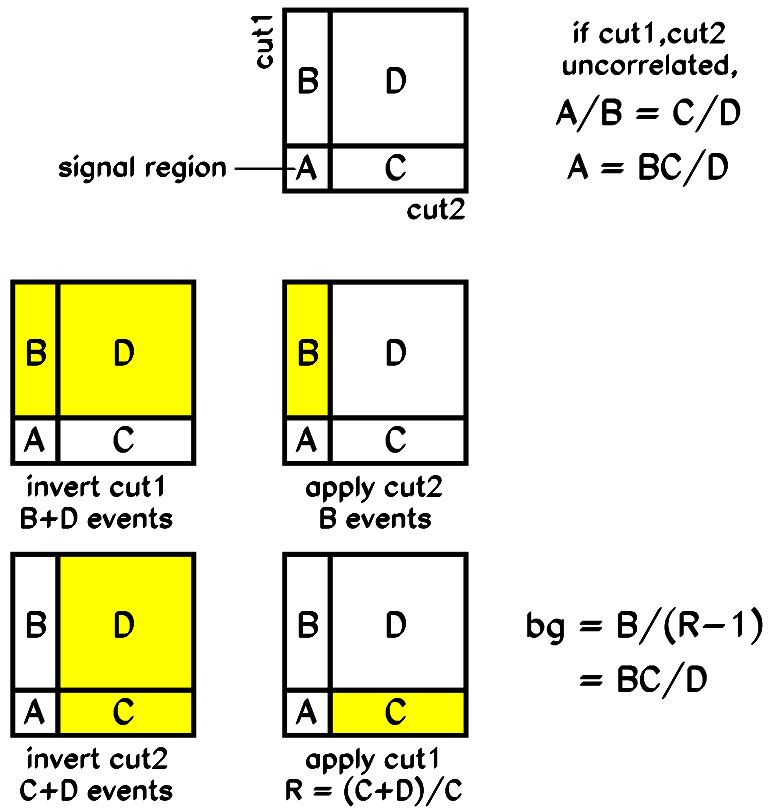
Figure 3.3: A schematic explanation of the bifurcation method. Figure reproduced from [37].
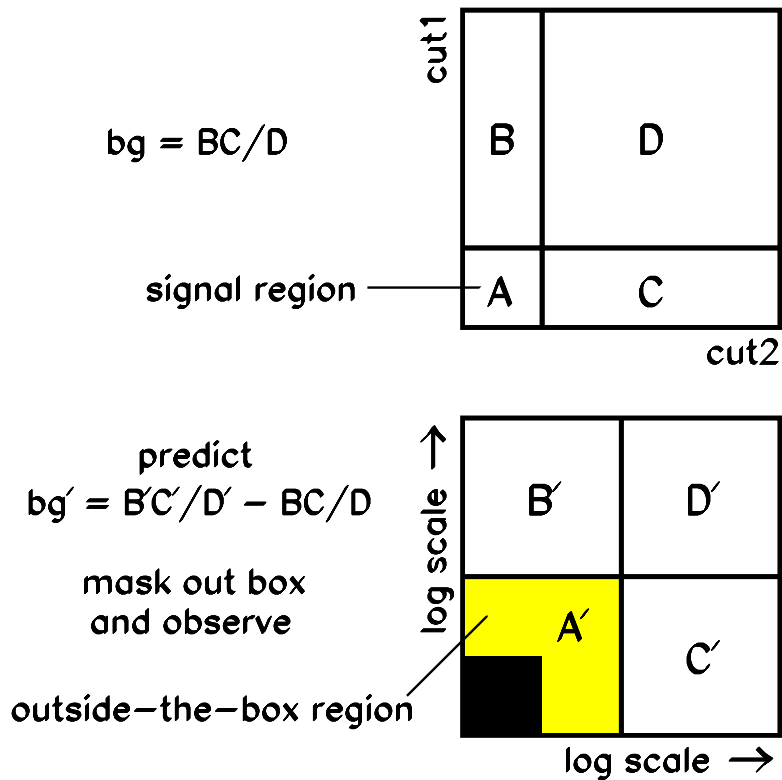
Figure 3.4: A schematic representation of the outside-the-box study. Figure reproduced from [37].

degree of contamination in a background estimate due to other background processes.

Outside-the-Box Studies

The "outside-the-box" studies tested the assumption that the cuts used in the bifurcation method were uncorrelated. This was done by simultaneously loosening the two bifurcation cuts CUT1 and CUT2 so that the four regions A, B, C and D became A', B', C' and D' as shown in Figure 3.4. The background study was performed in the same way as the standard background evaluations using the bifurcation method, except that the number of events in region A' was directly measured with the signal region masked out. This resulted in a region known as the "outside-the-box" region. The measured number of events in

the "outside-the-box" region was compared to the value $B'C'/D' - BC/D$. Correlations between the bifurcation cuts were present if the measured and predicted "outside-the-box" background levels did not agree. Significant correlations between bifurcation cuts would generally result in the background level being underestimated. The details of these studies are discussed in Section 5.1.

Single-Cut and Double-Cut Failure Studies

The single-cut and double-cut failure studies involved cataloging and examining events which failed only one or two sets of correlated cuts. Since the method used to estimate backgrounds depended on each background being suppressed by two uncorrelated sets of cuts, examining the events failing only a single set of correlated cuts provided a clear way to discover flaws in the analysis. Potential flaws included cuts not operating as designed to reject the appropriate background, new background processes not accounted for in the existing background estimates, and loop-holes by which a background event not accounted for in the background estimates could become a signal candidate. Analysis flaws discovered by examination of the single-cut and double-cut failure events were generally fixed by the modification of existing cuts or by the introduction of new safety cuts. Safety cuts are high acceptance cuts that target the specific analysis flaw. These studies were performed on both the 1/3 and 2/3 data sets, with consistency of the single-cut and double-cut failure rates between the two data sets providing a check for the potential bias introduced by optimizing the analysis cuts using the 1/3 data set. The details of these studies are discussed in Section 5.2.

Cross-Contamination in Background Estimates

The background contamination studies were designed to determine if contributions from any of the background processes were being double-counted by being included in more than one of the background estimates, causing the total background to be overestimated.

59

The details of these studies are discussed in Section 5.3.

3.3 Event Reconstruction

Reconstruction of each event was performed under the assumption that it was a $K^+ \rightarrow \pi^+ \nu \bar{\nu}$ event with only a single π^+ track in the detector. Background events with multiple charged decay tracks or multiple beam particles were greatly suppressed by this assumption as they typically failed one or more reconstruction steps. The reconstruction took place in a series steps, listed here and described in more detail in the rest of the section. These steps were as follows:

1. The initial time of the beam particle was determined from the beam instrumentation.

2. Clustering was performed in the Range-Stack providing track time, a guide for tracking in the UTC, and identification of the stopping counter.

3. The track was located in the UTC with based on the clustering information from the Range Stack.

4. In the target, K^+ and π^+ fibers were identified and clustered, and the fiber in which the K^+ decay occurred was identified.

5. Second iterations of both the UTC and target fitting were performed. The energy loss and range were found in the target.

6. Track fitting in the IC was used to find the energy loss and range in the IC.

7. Track fitting was performed in the RS. The energy loss and range in the RS were found.

8. The total range, energy and momentum were determined.

The x-y view of the results of a typical event reconstruction is shown in Figure 3.5.
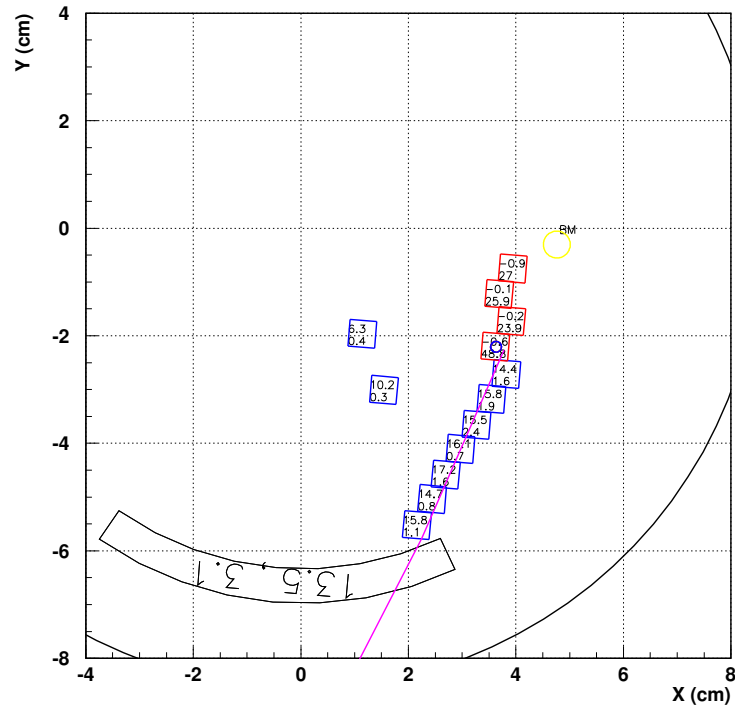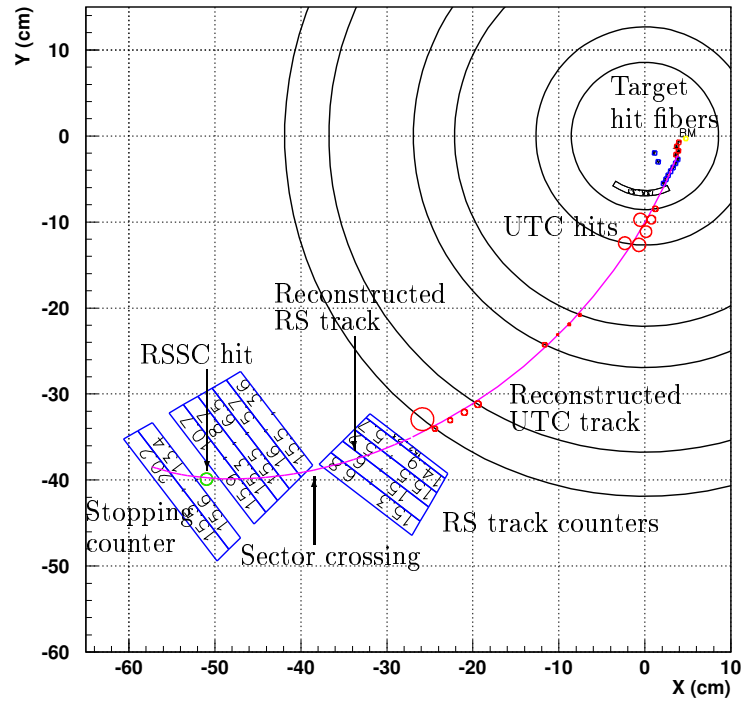
Figure 3.5: Reconstruction of an event in *x-y* view. The top figure shows reconstruction in the target, UTC and Range-Stack. The bottom shows an enlargement of reconstruction in the target. Figure reproduced from [37].

3.3.1 Beam Time Measurements

Beam times were found from TDC and CCD information for each of the C_K ($\mathtt{t_{CK}}$), C_π ($\mathtt{t_{C\pi}}$), BWPC ($\mathtt{t_{bw}}$), and B4 ($\mathtt{t_{bm}}$) detectors. Average TDC times from the clusters were used to determine these times with the CCD measurements being used to discriminate between beam particles close in time.

In the C_K and C_π counters, coincident TDC hits were clustered and the times averaged to find the time of the incoming particle. The same process was used for CCD hits.

In the BWPCs, hits from beam particles were reconstructed when two or three of the three planes had coincident TDC hits. The time of the incoming particles was taken from an average of the TDC hits.

In the B4 beam hodoscope, counters from the two layers were clustered based on coincident TDC or CCD hits. Energy-weighted averages were used to determine the time and x-y position of clusters. The measured energy deposits were used to differentiate between and identify beam kaons and beam pions.

3.3.2 Clustering in the Range Stack

Based on the coincidence with the online T•2 time ($\mathtt{t_{ds}}$), the offline T•2 sector was identified from TDC hits in the first two layers of the RS. Moving outward and clockwise from this T•2 sector, coincident hits within 10 ns of the T•2 time and with more than 0.5 MeV were included in the cluster. A good cluster involved at least six consecutive layers from inside to outside. The track time t_{rs} was determined from the average of all hit times in the good cluster. The outermost and most clockwise counter in the cluster was identified as the offline stopping counter.

3.3.3 Initial Track Finding in the UTC

Two separate fits were used to reconstruct the UTC track. The curvature of the fit in the x-y plane was used to determine the charged particle's transverse momentum. The fit in the r-z plane was used to determine the polar angle of the charged particle and the resulting slope was used to convert from the measured transverse momentum to the total momentum.

For the fit in the x-y plane, clusters in the hit wires were identified. A circle fit was performed using wire positions and drift distances with left-right ambiguity resolution.

For the fit in the r-z plane, the cathode foils from the clusters were used. A straight-line fit was performed, where the z position of the cluster was determined using a ratio method suggested in Reference [64]. This ratio method involved using the three cathode strips with the largest energy as measured by the ADCs and locating the centroid using an energy-weighted mean.

When more than one track pointed at the offline T•2 sector, the good UTC track was defined as the one closest to the first crossing point (from inward to outward) between RS sectors, or closest to the clockwise edge of the offline stopping counter otherwise.

3.3.4 Initial Target Reconstruction

The first step of the target reconstruction was to classify the hit target fibers into K^+, π^+, and γ fibers using their timing and energy information. Note that at the point of this initial classification, each fiber could fall into multiple categories. A fiber was classified as

- K^+ if it had an energy greater than 4 MeV and was coincident with the beam strobe $\mathtt{t_{bs}}$;

- Or π^+ if it had between 0.1 and 10.0 MeV of energy and was coincident with track time in the Range-Stack $\mathtt{t_{rs}}$;

- Or γ if it did not fall into the other two categories and had an energy above 0.1 MeV.

The fibers were clustered into K^+ and π^+ paths based on geometry. The π^+ fibers had to lie along a strip (typically 1 cm in width) along the UTC track extrapolated into the target.

The designation of each fiber as a π^+ or γ fiber could be be switched based on likelihood values calculated from energy, time and distance from the extrapolated UTC track. The event failed target reconstruction if there was more than one K^+ or more than one π^+ track, or if these two tracks were not geometrically adjacent in the x-y plane.

The decay vertex was identified in the K^+ fiber closest to the extrapolated UTC track and furthest away from the x-y position of the B4 hit. The position of the track exit from the target was identified. Fibers were reclassified from π^+ to opposite-side-π^+ fibers if they were located on the opposite side of the decay vertex as the track exit position. These hits were typically due to tracks from decays with multiple charged decay products. The average times of the K^+ and π^+ hits were defined as $\mathtt{t_K}$ and $\mathtt{t_{pi}}$, respectively. The sums of the K^+ and π^+ energies were defined as $\mathtt{E_K}$ and $\mathtt{E_{pi}}$, respectively.

This reconstruction process was performed as many as three times per event. For the first pass, the B4 position information was not used. After the first pass of target reconstruction, the B4 reconstruction was performed again with the hit closest to the average time of the kaon fiber hits being designated as that due to the K^+ beam particle. A second pass of the target reconstruction was then performed using this B4 information. Another round of B4 reconstruction followed by a third pass of the target reconstruction was performed if the solution found from the second pass was not satisfactory.

Further details on the target reconstruction can be found in [71].

64

3.3.5   Second Iteration of UTC Reconstruction

A second iteration of the UTC reconstruction was performed using the information from the first iteration of the target fitter as constraints.

3.3.6   Second Iteration Target Reconstruction

Then a second iteration of the target reconstruction was performed. In addition to the steps described for the first iteration of the target reconstruction, double-pulse fits were performed to search for π^+ or other energy hidden in the K^+ fibers using the CCD information from each of the K^+ fibers. The target pulse data fitter is discussed in more detail in Appendix C. In the case where the difference between $\mathtt{t_{pi}}$ and $\mathtt{t_K}$ was greater than 15 ns, any energy hidden in the second pulse of the vertex fiber was subtracted from $\mathtt{E_K}$ and assigned to $\mathtt{E_{pi}}$. The 15 ns threshold was the minimum time difference for which it was possible for the fitter to reliably identify the K^+ and π^+ pulses in a fiber. Figure 3.6 shows a double-pulse fit with hidden π^+ energy. The π^+ energy loss $\mathtt{E_{tg}}$ and range $\mathtt{r_{tg}}$ were found in the target based on the target reconstruction.

3.3.7   Track Fitting in the IC

A good track in the IC was one with hits in only one or two adjacent sectors. In the case of a sector crossing (two adjacent hits), the energy $\mathtt{E_{IC}}$ was the sum of the two energies and the time $\mathtt{t_{IC}}$ was the energy weighted sum of the times from the two sectors. The range $\mathtt{R_{IC}}$ was computed as the length of the extrapolated UTC track from the inner to the outer IC radius.

3.3.8   Reconstruction in the Range-Stack

The first step in RS reconstruction was to search for the $\pi^+ \to \mu^+ \to e^+$ decay signature by fitting the TD information in the stopping counter using single-, double- and triple-
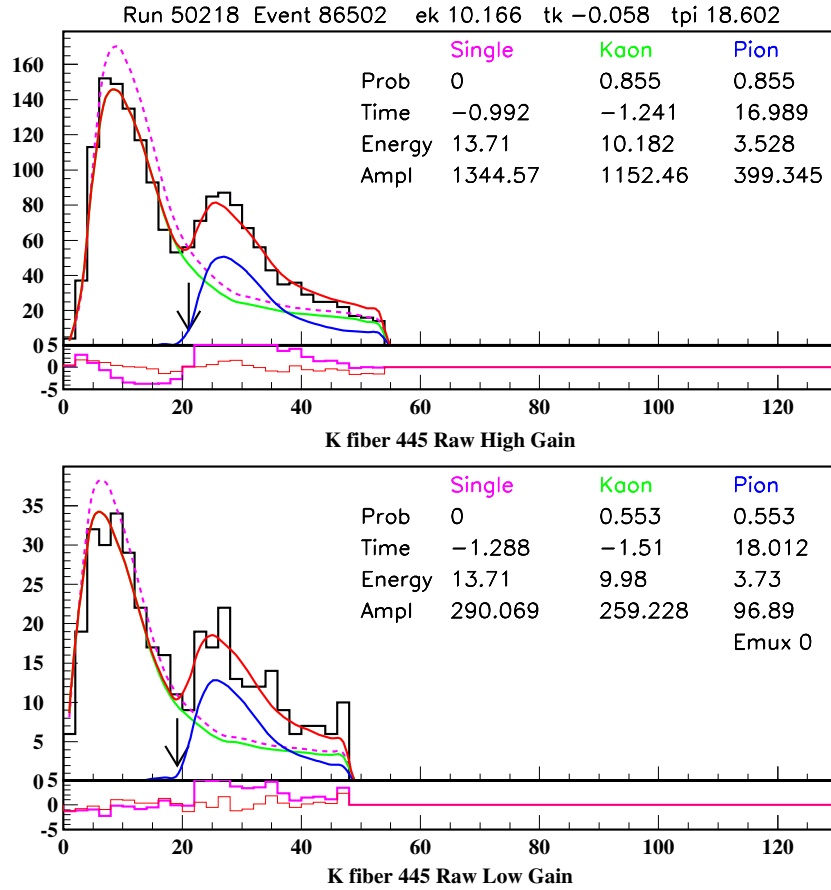
Figure 3.6: Double-pulse fit of the CCD information in the Kaon decay vertex for for the high-gain (top) and low-gain (bottom) CCDs. The energy of the second pulse was significantly higher than the expected 1 MeV energy from a pion headed directly toward the fiducial region of the detector and may have indicated a scatter.
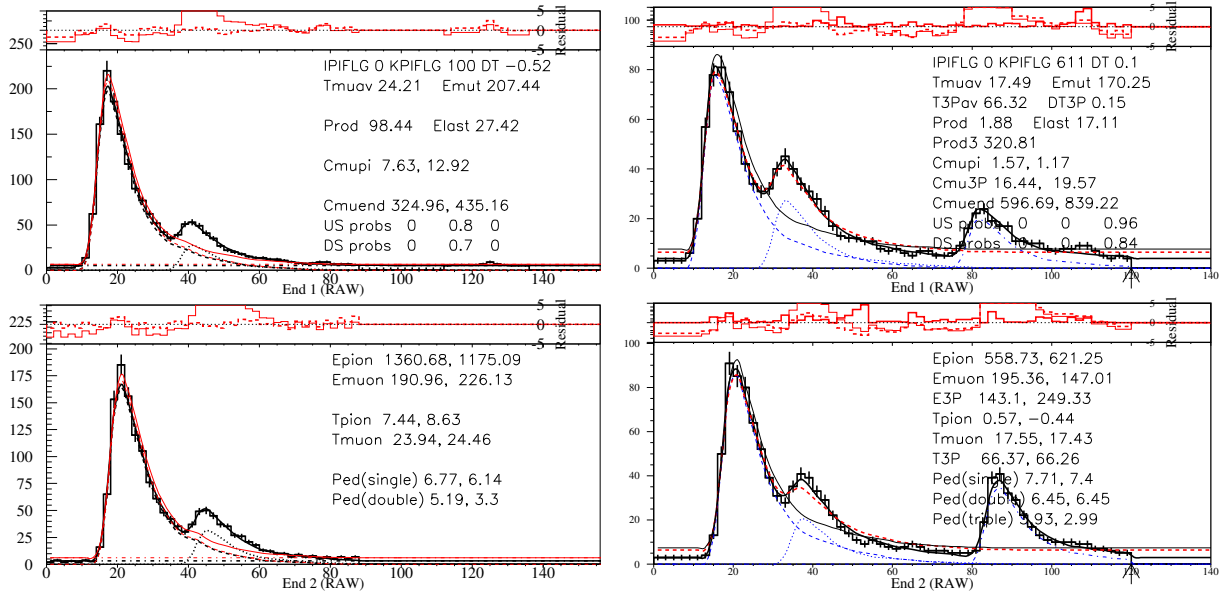
Figure 3.7: Double-pulse fit (left) to the TD pulse information in the RS stopping counter for the upstream (top) and downstream (bottom) readouts. Triple-pulse fit (right) to the TD pulse information in the RS stopping counter for the upstream (top) and downstream (bottom) readouts.

pulse assumptions. The fits were performed by varying the leading edges, heights and pedestals of template pulses, prepared for each individual counter using π_{scatter} monitor trigger data. Examples of double- and triple-pulse fits are shown in Figure 3.7 and further details on the TD fitter can be found in [57]. In addition to observation of the $\pi^+ \to \mu^+$ decay signature, these fits allowed the energy deposited by the muon E_μ in the stopping counter to be determined.

The RS track fit in the x-y plane was performed using (1) the entrance point provided by the UTC track extrapolation, (2) the sector crossing points, (3) the RSSC hit positions, and (4) the expected range predicted by energy losses in the RS layers. The χ^2 of the fitted track was minimized by changing the incident momentum and angle of entrance to the RS, with the shape of the track taking into account effects of energy loss in each counter as given by the Bethe-Bloch equation for a 1 T magnetic field. Due to this correlation between energy and range these quantities could not be treated as uncorrelated in the bifurcation analysis. Many of these quantities are labeled in Figure 3.5 and discussed in

67

more detail below.

Sector crossing points allowed for precise measurement of track positions in the x-y plane. Events were rejected if they had more than two sector crossings.

Hits in the RSSCs provided another precise position measurement in the x-y plane. Adjacent hits in Straw Chambers were formed into clusters and the track cluster was identified as that closest to the UTC track extrapolation. For each layer, the x-y position of the hit was taken from the average of the track hits and the time of the hit from the earliest hit.

The energy loss in each RS counter was determined using ADC information. A correction was applied to remove the additional energy recorded by the ADC from accidental activity by using the TD pulse height information. The total energy loss of the track in the RS (E_{rs}) was the sum of the energy losses in all the RS counters corrected for the the energy deposited by the μ^+ and e^+ in the stopping counter.

The polar angle in the RS was determined by a straight-line fit in the r-z plane. The z-positions in the RS counters and the Straw Chambers were determined from end-to-end time (and charge for the RS counters) differences, with average resolutions of 4-5 cm and 1.5 cm, respectively. The z-position of the extrapolated UTC track was also used in the fit. The range in the RS (R_{rs}) was calculated from the path length of the fitted track in the x-y plane, corrected for the polar angle.

3.3.9 Kinematic Measurements of the Track

The total range of the charged track (rtot) was the sum of R_{rs}, R_{IC} and R_{tg}. The total energy (etot) was the sum of E_{rs}, E_{IC} and E_{tg}. The total momentum (ptot) was obtained from the UTC with corrections from the range in the target and IC. Due to these corrections, there was some correlation between momentum and range and they could not be treated as uncorrelated in the bifurcation analysis. All three kinematic quantities were

corrected for tiny contributions due to inactive material in the UTC.

3.4   Selection Criteria

The cuts used to define the signal region and suppress backgrounds were optimized by maximizing their ability to suppress backgrounds while maximizing signal acceptance. The analysis was performed in three stages, called passes. The PASS1 cuts removed events which could not be reconstructed and obvious background events. The PASS2 cuts were a set of cuts which could be grouped into various combinations to enhance specific backgrounds. The PASS3 cuts were the final analysis cuts that were optimized to minimize the acceptance loss of signal events while maximizing their ability to reject the targeted background. The PASS3 cuts were grouped into categories of kinematic cuts, phase space cuts, delayed coincidence cuts, beam cuts, target quality cuts, $\pi^+ \to \mu^+ \to e^+$ decay-sequence cuts, and photon veto cuts.

3.4.1   Loose and Tight Cuts

The primary (loose) signal region was defined by the application of all of the analysis cuts described in this section. Four sets of analysis cuts were tightened and various combinations of these sets of cuts were used to divide the primary signal region into nine cells having varying levels of signal-to-background. The sets of cuts that were tightened were (1) the kinematic phase space cuts "PNN2BOX", (2) the delayed coincidence cuts "DELCO", (3) the $\pi^+ \to \mu^+ \to e^+$ decay-sequence cuts "$TDCUTS$", and (4) the photon veto "PVCUT". These cells were used in the likelihood method to determine the $K^+ \to \pi^+ \nu \bar{\nu}$ branching ratio from the observed candidates (Section 7.1). The cell having the highest signal-to-background was defined by the application of the tight versions of each of the four sets of cuts and is referred to as the "tight signal region" throughout the rest of this thesis.

3.4.2 PASS1 Cuts

The most basic analysis cuts were the PASS1 cuts. These loose cuts removed obvious $K_{\pi2}$, $K_{\mu2}$ and beam background events, as well as events which could not be reconstructed. Details of the PASS1 cuts are discussed further in Appendix D.1.

3.4.3 PASS2 Cuts

The PASS2 cuts consisted of looser versions of the final analysis cuts. The PASS2 cuts were applied in certain combinations to enhance specific backgrounds, reducing processing time when developing cuts and evaluating background levels. Details of the PASS2 cuts are discussed further in Appendix D.2.

3.4.4 PASS3 Cuts

The PASS3 cuts were the final analysis cuts, grouped into categories of kinematic cuts, phase space cuts, delayed coincidence cuts, beam cuts, target quality cuts, $\pi^+ \rightarrow \mu^+ \rightarrow e^+$ decay-sequence cuts, and photon veto cuts.

3.4.5 Kinematic Cuts

The kinematic cuts, collectively referred to as *KINCUTS*, were grouped into the following categories:

Fiducial cuts - These cuts ensured that the charged decay product passed only through and came to rest in the fiducial region of the detector, where the fiducial region was the active region of the detector in which events were accepted for further analysis. These cuts further tightened the conditions from the $\pi\nu\bar{\nu}(1)$ and $\pi\nu\bar{\nu}(2)$ triggers placed on the parts of the detector through which the charged decay product could travel or come to rest.

70

Track Reconstruction Cuts - These cuts required good track reconstruction in the UTC, and good matching between RS track reconstruction and UTC track extrapolation.

dE/dx Cuts in Range-Stack - These cuts removed events with energy deposits in the RS inconsistent with those of a π^+. These cuts removed events where a photon or extra track deposited energy that was measured by the ADCs. These cuts also removed events that scattered in the Range-Stack such as $K_{\pi2}$ Range-Stack scatter.

Range-Momentum Consistency Cut - Since muons typically had a longer range than pions for equivalent momenta, this cut suppressed muon backgrounds by requiring that the range of the charged track was consistent with that for pions.

Details of the kinematic cuts are discussed further in Appendix D.3.

3.4.6 Phase Space Cuts

To suppress $K_{\pi2}$ events, the upper limits on the phase space cut (PNN2BOX) were chosen to be below the $K_{\pi2}$ monochromatic peak (Figure 3.2) in momentum, energy and range. The upper bounds of this cut were located $2.5 \times \sigma_{\mathtt{ptot}}$ below the $K_{\pi2}$ momentum peak, $2.5 \times \sigma_{\mathtt{etot}}$ below the energy peak and $2.75 \times \sigma_{\mathtt{rtot}}$ below the range peak. The standard deviations on the measured kinematic quantities ($\sigma_{\mathtt{ptot}}$, $\sigma_{\mathtt{etot}}$, $\sigma_{\mathtt{rtot}}$) were measured using reconstructed $K_{\pi2}$ events. The lower bounds of this cut were chosen to suppress or kinematically exclude the troublesome many-body decays that could most easily mimic the $K^+ \to \pi^+ \nu \bar{\nu}$ decay. The acceptance conditions for the loose version of the phase space cut (BOXLOOSE) were:

$$140.0 \text{ MeV}/c \leq \quad \mathtt{ptot} \quad \leq 199.0 \text{ MeV}/c;$$
$$60.0 \text{ MeV} \leq \quad \mathtt{etot} \quad \leq 100.5 \text{ MeV};$$
$$12.0 \text{ cm} \leq \quad \mathtt{rtot} \quad \leq 28.0 \text{ cm}.$$

The phase space cut was one of the sets of cuts that was further tightened to define the tight signal region. The lower bounds of the tight phase space cut (BOXTIGHT) were raised to suppress the K_{e4} background, whose π^+ momentum peaked at around 160 MeV/c as shown in Figure 4.8. The lower momentum bound of 165 MeV/c was chosen to maximize K_{e4} suppression while minimizing the loss of signal acceptance. The upper momentum bound was lowered from 199 MeV/c to 197 MeV/c to increase $K_{\pi 2}$ suppression without having a significant impact on signal acceptance. The acceptance conditions for the tight version of the phase space cut (BOXTIGHT) were:

$$165.0 \text{ MeV}/c \leq \ \texttt{ptot} \ \leq 197.0 \text{ MeV}/c;$$
$$72.0 \text{ MeV} \leq \ \texttt{etot} \ \leq 100.0 \text{ MeV};$$
$$17.0 \text{ cm} \leq \ \texttt{rtot} \ \leq 28.0 \text{ cm}.$$

The optimization of BOXTIGHT is described in more detail in [55].

3.4.7 Beam Cuts

The beam cuts, collectively referred to as *BEAMCUTS*, were designed to suppress single-beam and double-beam backgrounds. Single-beam backgrounds were suppressed by a particle identification cut that ensured that the beam particle was a kaon based on its energy deposition in B4. Double-beam backgrounds were suppressed by searching for and removing events with extra beam particles in the beam instrumentation at track time ($\texttt{t}_{\texttt{rs}}$).

The beam cuts included cuts that (1) enforced timing consistency between CCD and TDC information in B4, between B4 and the average target K^+ fiber hit times, and between the track time in the Range-Stack and the average target π^+ fiber hit times, and (2) removed double-beam events with specific signatures known to cause the target reconstruction to find incorrect solutions. Details of the beam cuts are discussed further in Appendix D.5.

3.4.8　Delayed Coincidence Cuts

The delayed coincidence cuts suppressed single-beam backgrounds by enforcing a minimum time between the average time of the kaon fiber hits ($\mathtt{t_k}$) and the average time of the pion fiber hits ($\mathtt{t_{pi}}$). The delayed coincidence cuts were one of the sets of cuts that was further tightened to define the tight signal region. Details of the delayed coincidence cuts are discussed further in Appendix D.6.

3.4.9　Target Quality Cuts

The target quality cuts, collectively referred to as *TGCUTS*, were designed to select signal-like events based on quantities measured in the target. These cuts targeted specific backgrounds and/or event signatures. These cuts rejected events that fell into the following categories:

- Events where the energy deposited by a π^+ in a target fiber was larger than that expected for a π^+ traveling through the target along the extrapolated UTC track. This energy is a signature of π^+ scattering in the target, or could have been evidence of a photon in a π^+ fiber, or evidence of a photon or π^+ hidden in a K^+ fiber. These cuts suppressed the $K_{\pi2}$ target-scatter background, any backgrounds involving photons in the final state and events where a K^+ fiber was misidentified as a π^+ fiber.

- Events with poor agreement between the target π^+ track fitter and the target π^+ fibers as determined using χ^2-like quantities. These cuts suppressed events that scattered in the target.

- Events where the beam particle did not behave as a K^+. A likelihood function was constructed using the z-position of the kaon decay in the target as determined by UTC track extrapolation, the expected z-position of the kaon decay as determined

by the total energy deposited in target kaon fibers, and the energy deposited by the kaon in the B4 Hodoscope. These conditions suppressed the beam pion scatter single-beam background.

- Events where the π^+ cluster did not appear to originate from one of the K^+ cluster target fibers. This cut suppressed CEX and double-beam backgrounds.

- Events where there was a large uncertainty in the target pion path length from the target reconstruction. This suppressed double-beam and $K_{\pi 2}$ target scatter events.

- Events that did not meet consistency requirements for times or energies between the K^+ or π^+ tracks and those in other detector systems.

- Events with charged track dE/dx in the target inconsistent with that of a pion. This suppressed backgrounds where the charged track was due to a lepton, such as muon-based backgrounds.

- Events that did not meet position consistency requirements between the K^+ decay vertex, the beam particle in B4, and the target K^+ and π^+ clusters.

- Events with target π^+ fibers on both sides of the K^+ decay vertex as shown in Figure 4.7. This suppressed double-beam events and decays with multiple charged products, such as K_{e4}.

- Events that showed evidence of hidden energy as determined by likelihood functions comparing target π^+ fiber positions, times and energies to the extrapolated UTC track.

- Events that did not meet consistency requirements between the target K^+ fiber times and their distances to the vertex in the x-y plane or the z-positions of their hits as determined by the deposited energy.

- Events where the target pulse data fitter, described in Appendix E, failed to find acceptable solutions to both the single-pulse and double-pulse assumptions in any of the K^+ fibers having energy above a certain threshold.

- Events where there was coincident activity between the IC and a nearby K^+ fiber. This event signature was often an indication of double beam background.

Details of the target quality cuts are discussed further in Appendix D.7.

3.4.10 $\pi^+ \rightarrow \mu^+ \rightarrow e^+$ Decay-Sequence Cuts

The $\pi^+ \rightarrow \mu^+ \rightarrow e^+$ decay-sequence cuts, collectively referred to as *TDCUTS*, were designed to reject events in which a μ^+ caused the charged track. These cuts searched in and around the Range-Stack stopping counter for activity consistent with the observation of the $\pi^+ \rightarrow \mu^+ \rightarrow e^+$ decay sequence. The signature for this decay sequence, based on the pulse-shape information from the TDs, was

1. Three pulses were found in the stopping counter, corresponding to the π^+, μ^+ and e^+ of the $\pi^+ \rightarrow \mu^+ \nu_\mu$ and $\mu^+ \rightarrow e^+ \bar{\nu}_\mu \nu_e$ decays.

2. The 4.1 MeV of kinetic energy from the μ^+ was observed as about a 3 MeV pulse due to saturation [19]. Since the path length of a μ^+ coming from the decay of a π^+ at rest is approximately 1.4 mm in the RS scintillator counters, most of these muons did not exit the stopping counter.

3. Most of the positrons from the $\mu^+ \rightarrow e^+ \bar{\nu}_\mu \nu_e$ decays exited the stopping counter due to having up to 53 MeV of kinetic energy; thus the positron should be observed to deposit energy in and around the stopping counter.

Events were rejected if the above signatures were not observed or if it was determined that the observed signatures were faked by accidental activity.

The $\pi^+ \to \mu^+ \to e^+$ decay-sequence cuts were one of the sets of cuts that was further tightened to define the tight signal region. Details of these cuts are discussed further in Appendix D.8.

3.4.11 Photon Veto Cut

The photon veto cut (PVCUT) rejected events with activity above threshold in any of the photon veto subsystems coincident with Range-Stack track time $\mathtt{t_{rs}}$. These subsystems were the BV, BVL, RS, EC, target, IC, VC, CO, μCO, AD and DPV.

The photon veto cut was one of the sets of cuts that was further tightened to define the tight signal region. The photon veto cut was also loosened below the nominal level for some background and acceptance studies. The photon veto cut is discussed further in Appendix D.9.

3.5 Monte Carlo Simulation

Detector responses were modeled by a Monte Carlo simulation package, referred to internally as "UMC". The simulation modeled all detector systems other than the beam instrumentation upstream of the target. The simulation samples were generated with the same information and in the same format as data except that pulse-shape information from CCDs and TDs was not generated. The accuracy and performance of the simulation were verified by comparisons of kinematic variables between simulation and data for $K_{\pi 2}$ and $K_{\mu 2}$ decays [33].

3.5.1 Simulation of K^+ Propagation

A "beam file" was created from analysis of the K^+ stopping distribution using $K_{\mu 2}$ monitor trigger data. This file contained the B4 hit position; the K^+ stopping position and target

fiber element number; and the number of fiber hits, their time, energy and fiber element number for K^+ and accidental hits. The target patterns were the same in the simulation and the experimental data. Using this information, a simulated K^+ decay started from the stopping fiber at the given K^+ stopping position.

3.5.2   Simulation of K^+ Decay Products

A number of K^+ decays were simulated for various studies: $K^+ \rightarrow \pi^+ \nu \bar{\nu}$ signal, $K_{\mu 2}$, $K_{\pi 2}$, K_{e4}, $K_{\pi 2 \gamma}$, and a number of the CEX processes discussed in Section 4.8. Photon and electron interactions and their energy deposits were calculated using routines from the electromagnetic-shower simulation package EGS4 [86]. For other charged particles, the energy deposits were calculated by summing the energy losses of each ionization along the steps taken by the particles. Using the Bethe-Bloch formula, the total average energy deposited along each step was calculated. The multiple Coulomb scatterings of the charged particles with various nuclei in the detector were calculated according to the theory of Moliere [32], with corrections for the spin of the scattered particle and the form factor of the nucleus [79]. The hadronic interactions of positively charged pions in the plastic scintillators were calculated using a combination of data and phenomenological models [95]. The π^- absorption was modeled based on experimental data of stopped π^- in the Range Stack [97].

3.5.3   Simulation of Trigger

A comparison between simulated $K_{\mu 2}$ triggers and data was used to derive a weight function to correct for the trigger bias introduced by generating the beam file used in the simulation.

Chapter 4

Backgrounds

To obtain an unbiased estimate of the total background level, the data were split into two sets and the signal region was not examined until after the background evaluation studies were finalized. The "1/3 data set" was used to optimize the cuts and the resulting background levels. The final background levels were measured on the "2/3 data set". The process of creating the "1/3" and "2/3" data sets was described in Section 3.2.3. This chapter describes the background evaluation procedure and resulting background levels for each of the background categories described in Section 3.1. Throughout this chapter, results from the "1/3" and "2/3" data sets have been scaled by the appropriate factor to represent the background level for the entire data set. In cases where the background sample size was reduced to zero events due to high suppression of the given background, the calculation assumed one event remained.

Throughout this chapter, the backgrounds were estimated for both the loose and tight signal regions (Section 3.4.1). The estimates in the tight signal region were used as a validity check against the scaling method used to divide the signal region into nine cells as detailed in Section 7.1.

4.1 $K_{\pi 2}$ Target-Scatter Background

The decay $K^+ \to \pi^+ \pi^0$ ($K_{\pi 2}$) was responsible for the dominant background in this analysis. For this decay to become a background, the photons from the π^0 decay have to be missed and the π^+ has to lose some undetected energy, perhaps via nuclear interactions, such that it falls into the kinematic signal region (PNN2BOX). This scattering can happen in the target ($K_{\pi 2}$ target-scatter) or in the Range Stack ($K_{\pi 2}$ Range-Stack-scatter), but the target-scatter component dominates this background. The evaluation of the Range-Stack-scatter background is discussed in Section 4.2.

The topology of the most problematic type of $K_{\pi 2}$ target-scatter was that of a π^+ initially traveling along the kaon fibers and scattering into the active region of the detector. There were two reasons why this problematic type of target-scatter was difficult to reject. The first reason was that some energy deposited in the target by the scattering π^+ was hidden in a kaon fiber. The second reason was a consequence of the π^+ and π^0 emerging back-to-back. A π^+ initially traveling along the kaon fibers meant that the π^0 was also traveling parallel to the beam direction and the resulting photons from its decay were directed at the upstream or downstream ends of the detector. As can be seen in Figure 2.13, these small angles are where the photon veto is the weakest. Figure 4.1 contrasts this type of event with a regular $K_{\pi 2}$ event.

The $K_{\pi 2}$ target-scatters were classified into two non-exclusive categories. The first category, known as "z-scatters", occurred when the π^+ traveled in the beam direction, scattered in a kaon fiber and into the active region of the detector. The troublesome decay described above falls into this category. The second category, known as "xy-scatters", occurred when the π^+ scattered outside of the kaon fibers and the scatter was visible in the xy-plane. Section 4.1.3 describes how samples with varying degrees of "z-scatters" and "xy-scatters" were created to measure the photon veto rejection for these events in the rejection branch.
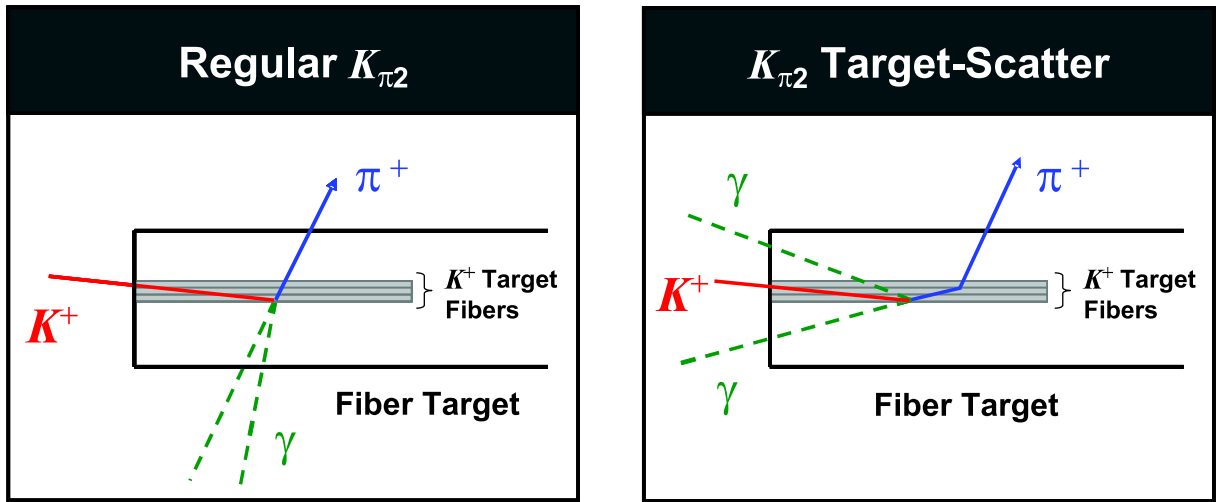
Figure 4.1: Schematic of the regular $K_{\pi 2}$ (left) and the $K_{\pi 2}$ target-scatter (right) processes. For a regular $K_{\pi 2}$ event (left), the back-to-back correlation between the directions of the π^+ and π^0 mean that a π^+ directed at the active region of the detector results in the photons from the π^0 being directed toward a region of the detector where the photon veto is strongest such as the Barrel Veto. For the most troublesome type of $K_{\pi 2}$ target-scatter event (right), a π^+ initially traveling along the kaon fibers and scattering toward the active region of the detector results in the π^0 also traveling parallel to the beam direction. The photons from the π^0 decay are then directed toward the upstream or downstream ends of the detector, where the photon veto is weakest.

The most effective methods of suppressing this background were the detection of the photons from the π^0 decay using the photon veto PVCUT and the detection of the elastic or inelastic scatter of the π^+ in the target using the target quality cuts $TGCUTS$, many of which suppress events with additional energy in the target thus suppressing π^+ scatters. The bifurcation cuts used for the $K_{\pi 2}$ target-scatter background evaluation were the photon veto PVCUT (CUT1) and the target quality cuts $TGCUTS$ (CUT2).

4.1.1 Potential Sources of Contamination

Since the photon veto was effective at suppressing all background process involving photons, a sample of $K_{\pi 2}$ target-scatter events created by inverting the photon veto was expected to have contamination from other background processes containing photons. It was also expected that other background processes could result in measurable and non-negligible amounts of contamination in both the normalization and rejection branches for the $K_{\pi 2}$ target-scatter background.

The $K_{\pi 2}$ target-scatter normalization branch was found to contain $K_{\pi 2}$ Range-Stack-scatter events and this contamination was exploited to estimate the $K_{\pi 2}$ Range-Stack scatter background (see Section 4.2). The $K_{\pi 2}$ target-scatter normalization branch was corrected for this Range-Stack-scatter contamination as is discussed in Section 4.1.2.

It was determined that the $K_{\pi 2}$ target-scatter normalization branch was likely to contain a large amount of contamination due to $K_{\pi 2\gamma}$ events due to the extra photon and decay-pion kinematics that fell mostly in the kinematic signal region. This contamination study is detailed in Section 5.3.4 and the resulting correction to the $K_{\pi 2}$ target-scatter background is discussed in Section 4.1.5.

Studies to measure the contamination due to muon and double-beam (Sections 5.3.2 and 5.3.3, respectively) events were performed and found negligible contamination in both the $K_{\pi 2}$ target-scatter normalization and rejection branches. Note that in the $K_{\pi 2}$ target-

81

scatter background studies, the setup cuts included the cuts designed to heavily suppress the muon and double-beam backgrounds thus the contamination due to the background processes was expected to be small.

Based on the bifurcation cuts used for the K_{e4} background normalization branch (Section 4.5.1), it can be argued that the number of K_{e4} events contaminating the $K_{\pi2}$ target-scatter normalization branch must have been less than the number of events that were in the K_{e4} normalization branch, and thus the K_{e4} contamination was negligible. The K_{e4} background normalization branch was created by inverting the combination of OPSVETO and TGPV and applying the remaining analysis cuts. For the 1/3 data set, the events remaining at the end of the K_{e4} normalization branch, before the application of CCDPUL, were visually examined and were found to be consistent with K_{e4} events. For the 1/3 (2/3) data set, there were 4 (7) events remaining at the end of this normalization branch. The $K_{\pi2}$ target-scatter normalization branch can be characterized as being selected by the application of OPSVETO, the inversion of the photon veto, and the application of all other analysis cuts. A sample of events chosen by OPSVETO and inverted TGPV is a subset of the $K_{\pi2}$ target-scatter normalization branch. Since OPSVETO rejects K_{e4} events, the number of K_{e4} events found in the sample chosen by OPSVETO and inverted TGPV will be less than those chosen by inverting the combination of OPSVETO and TGPV and thus the K_{e4} contamination in the $K_{\pi2}$ target-scatter normalization branch was negligible.

4.1.2 $K_{\pi2}$ Target-Scatter Normalization Branch

The $K_{\pi2}$ target-scatter normalization branch was created by inverting the loose photon veto PV60 (CUT1) and applying all the other analysis cuts. The "60" in PV60 refers to the fact that the parameters for the loose photon veto were optimized to accept approximately 60% of the signal-like events. The loose photon veto was inverted in the

$K_{\pi 2}$ Target-Scatter Bifurcations
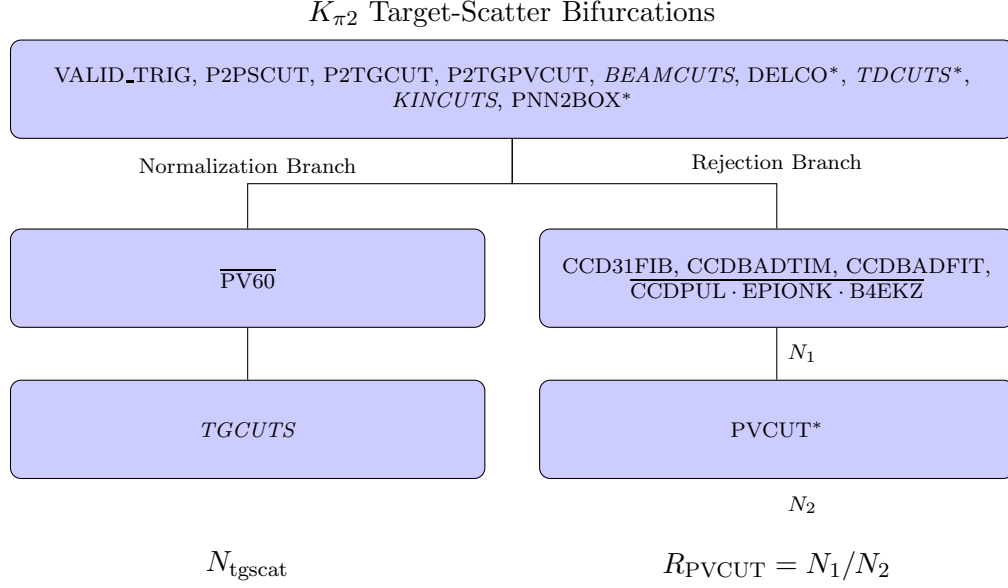
Figure 4.2: Flowchart showing the $K_{\pi 2}$ target-scatter bifurcations. Cuts in italics refer to named groups of cuts. Cuts denoted with an '*' indicate that the loose version of the cut was used for the background evaluation in the loose box and the tight version for the background evaluation in the tight box. The target quality cuts in the rejection branch are those for class 12.

normalization branches for both the loose and tight background evaluations because inverting the tight photon veto would have resulted in examining a portion of the loose signal region. Figure 4.2 shows a schematic representation of the normalization branch for the loose and tight $K_{\pi 2}$ target-scatter background evaluations.

The number of events remaining at the end of this normalization branch (N_{tgscat}) was corrected for the contamination due to n_{rsscat} $K_{\pi 2}$ Range-Stack-scatter events, the calculation of which is detailed in Section Section 4.2.1,

$$n_{\text{tgscat}} = N_{\text{tgscat}} - n_{\text{rsscat}}. \tag{4.1}$$

The resulting number of $K_{\pi 2}$ target-scatter normalization events are shown in Tables 4.4 and 4.5.

4.1.3 $K_{\pi 2}$ Target-Scatter Rejection Branch

Monte Carlo simulations [58] of $K_{\pi 2}$ decays have shown that for events where the π^+ enters the active region of the UTC and Range-Stack, the distribution of π^0 decay photons is much more uniform for events where the π^+ had scattered in the target than for events where the π^+ scatter had not occurred. In events where the π^+ scatter did not occur, the directions of the photons from the π^0 decay were strongly correlated to the direction of the π^+. When the π^+ scattered in the target, this correlation was obscured resulting in this more uniform distribution of photons from the π^+ scatter events. Due to the variation with polar angle of the total thickness of the photon veto (see Figure 2.13), the photon veto performance was not expected to be uniform in polar angle. As a result, the performance of the photon veto was expected to be different for the $K_{\pi 2}$ target-scatter events than for the $K_{\pi 2}$-peak events.

To measure the rejection of the photon veto for target-scatter events, 12 classes (classes 2-13 in Table 4.1) of $K_{\pi 2}$ target-scatter events were created by applying and inverting various combinations of the target quality cuts, creating samples with varying mixtures of "xy-scatter" and "z-scatter" events. Table 4.1 shows the cuts used to make the 12 classes and Figure 4.2 shows the rejection branch for class 12. Table 4.2 for each of the 12 classes for both the loose photon veto (PV60) and the tight photon veto (PV30). The directional correlation between the π^+ and the photons from the π^0 was obscured by using the given combinations of cuts to create classes of target-scatter samples, making classes 2-13 suitable for measuring the photon veto rejection of target-scatter events. Class 1 was not suited to measure the photon veto rejection of the target-scatter events since it consisted of events where the directional correlation between the π^+ and the photons from the π^0 was still present due the application of all $TGCUTS$ and the use of the kinematic region KP2BOX instead of the kinematic signal region PNN2BOX.

Class 12, considered to be the richest in z-scatters, was chosen to measure the photon

CLASS	Applied and Inverted *TGCUTS*
1	all *TGCUTS*, KP2BOX
2	$\overline{\text{CCDPUL} \cdot \text{EPIONK}}$
3	$\overline{\text{CCDPUL} \cdot \text{EPIONK}}$, all others
4	CCDPUL, EPIONK, TGZFOOL, EIC, OPSVETO, $\overline{\text{others}}$
5	$\overline{\text{CCDPUL} \cdot \text{EPIONK} \cdot \text{CHI567} \cdot \text{VERRNG}}$
6	$\overline{\text{CCDPUL} \cdot \text{EPIONK} \cdot \text{CHI567} \cdot \text{VERRNG}}$, all others
7	$\overline{\text{CHI567} \cdot \text{VERRNG}}$
8	$\overline{\text{CHI567} \cdot \text{VERRNG}}$, all others
9	$\overline{\text{CCDPUL} \cdot \text{EPIONK} \cdot \text{CHI567} \cdot \text{VERRNG}}$, KIC, PIGAP, TARGF, TPICS
10	$\overline{\text{B4EKZ}}$
11	$\overline{\text{B4EKZ}}$, all others
12	$\overline{\text{CCDPUL} \cdot \text{EPIONK} \cdot \text{B4EKZ}}$
13	$\overline{\text{CCDPUL} \cdot \text{EPIONK} \cdot \text{B4EKZ}}$, all others

Table 4.1: Definition of the classes of events used to measure the PV rejection of $K_{\pi 2}$ target-scatter events in the kinematic signal region. The notation "all others" refers to the remaining *TGCUTS* not applied in that class also being applied or inverted. All Classes that had either CCDPUL applied or CCDPUL inverted had the three associated safety cuts (CCDBADFIT, CCDBADTIM and CCD31FIB) applied. Class 1 was used to measure the PV rejection of $K_{\pi 2}$ Range-Stack-scatter events and not $K_{\pi 2}$ target-scatter events. Since class 1 used events from the $K_{\pi 2}$-peak instead of the kinematic signal region, all of the *TGCUTS* could be applied without examining the signal region.

| | Before | PV60 | | PV30 | |
CLASS	Photon Veto	After	Rejection	After	Rejection
1 1/3	61410	36	1706±284	13	4724±1310
2/3	122581	106	1156±112	44	2786±420
2 1/3	24396	9	2711±903	3	8132±4695
2/3	49032	21	2335±509	8	6129±2167
3 1/3	2776	3	925±534	1	2776±2776
2/3	5495	2	2748±1942	1	5495±5495
4 1/3	4159	3	1386±800	0	4159±4159
2/3	8092	1	8092±8092	1	8092±8092
5 1/3	29899	12	2492±719	4	7475±3737
2/3	59871	22	2721±580	8	7484±2646
6 1/3	4170	3	1390±802	1	4170±4170
2/3	8452	3	2817±1626	1	8452±8452
7 1/3	24574	6	4096±1672	1	24574±24574
2/3	49636	18	2758±650	7	7091±2680
8 1/3	353	0	353±353	0	353±353
2/3	644	0	644±644	0	644±644
9 1/3	23736	10	2374±750	3	7912±4568
2/3	47463	19	2498±573	7	6780±2563
10 1/3	11037	4	2759±1379	1	11037±11037
2/3	22037	10	2204±697	2	11019±7791
11 1/3	45	0	45±45	0	45±45
2/3	64	0	64±64	0	64±64
12 1/3	26317	10	2632±832	4	6579±3289
2/3	52621	22	2392±510	8	6578±2325
13 1/3	3319	3	1106±639	1	3319±3319
2/3	6503	2	3252±2299	1	6503±6503

Table 4.2: The rejection of loose photon veto (PV60) and tight photon veto (PV30) rejection for the $K_{\pi 2}$ target-scatter rejection branch. Class 1 was not considered as it used the KP2BOX kinematic box. For each class, the rejection "Rejection" of the photon veto was determined for each of PV30 and PV60. To determine the rejection, the number of events before the photon veto was applied "Before Photon Veto" was divided by the number of events remaining after the photon veto was applied "After". If zero events remained after the photon veto was applied, the calculation of the rejection assumed that one event remained. Only the classes having sufficient statistics for a meaningful measurement were considered.

veto rejection and the other classes having adequate statistics were used to determine the systematic uncertainty in this rejection. The inverted cuts (CCDPUL, EPIONK and B4EKZ) in class 12 rejected events with secondary energy deposits in target kaon fibers consistent with a scattered π^+. CCDPUL rejected events where a second pulse having more than 1.25 MeV of energy was found in a kaon fiber. EPIONK rejected events where a fiber classified as both a kaon and pion fiber had more than 1.25 MeV of pion energy. B4EKZ rejected events where the z-position of the decay vertex found by the UTC did not agree with the expected z-position as determined by the total energy deposited in the kaon fibers.

Due to the loss of statistics in the rejection branch for the background evaluation in the tight signal region, the rejection of the tight (PV30) photon veto was measured using a rejection branch that used the loose versions of PNN2BOX, $TDCUTS$ and DELCO. In doing this it was assumed that the rejections of the tight photon veto for each of the classes was the same when applying the loose and tight versions of PNN2BOX, $TDCUTS$ and DELCO. The "30" in PV30 refers to the fact that the parameters for the tight photon veto were optimized to accept approximately 30% of the signal-like events. Table 4.3 shows that the rejection of the tight photon veto did not change within statistical uncertainty when applying the tight versions of these cuts as compared to the loose versions of these cuts. When determining the systematic uncertainty of the tight photon veto rejection, the measurements using the tight kinematic box BOXTIGHT were treated as an additional class (called BOXTIGHT) and ended up being used to determine the lower bounds on the systematic uncertainty as shown in Table 4.5.

Tables 4.4 and 4.5 summarize the photon veto rejections and other values used in the background evaluation.

Setup Cuts	Events Before	Events After	PV30 Rejection
	1/3 Data Set		
All Loose	26317	4	6579±3289
BOXTIGHT	19741	4	4935±2467
DELCO6	22780	2	11390±8054
TDTIGHT	19624	2	9812±6938
All Tight	12725	1	12725±12725
	2/3 Data Set		
All Loose	52621	8	6578±2325
BOXTIGHT	39481	7	5640±2132
DELCO6	45574	6	7596±3101
TDTIGHT	39287	6	6548±2673
All Tight	25471	5	5094±2278

Table 4.3: Rejection of the tight photon veto cut PV30 for class 12 with various combinations of loose and tight versions of the setup cuts for the 1/3 sample and 2/3 sample. The columns "Events Before" and "Events After" show the number of events remaining before and after the application of PV30, respectively. The column "PV30 Rejection" is the rejection of the tight photon veto PV30, determined by taking the quotient of numbers found in the "Events Before" and "Events After" columns.

4.1.4 $K_{\pi 2}$ Target-Scatter Background Evaluation

Figure 4.3 shows the momentum distributions for the events remaining at various stages of performing the background estimate using the bifurcation method.

The loose $K_{\pi 2}$ target-scatter background was evaluated using the expression

$$bg_{\text{tgscat}}^{\text{loose}} = \frac{n_{\text{tgscat}}^{\text{loose}}}{R_{\text{PV60}} - 1}, \tag{4.2}$$

where $n_{\text{tgscat}}^{\text{loose}}$ was the number of events at the end of the loose normalization branch corrected for $K_{\pi 2}$ Range-Stack-scatter contamination as shown in Equation (4.1), and R_{PV60} was the rejection of the loose photon veto as measured on the loose rejection branch.

For the background evaluation in the tight signal region, the loose photon veto PV60 was inverted to avoid examining the signal region and the results of the entire background evaluation were scaled by the ratio of the loose and tight photon veto rejections. The $K_{\pi 2}$ target-scatter background in the tight signal region was evaluated using the expression

$$bg_{\text{tgscat}}^{\text{tight}} = \frac{n_{\text{tgscat}}^{\text{tight}}}{R_{\text{PV60}} - 1} \times \frac{R_{\text{PV60}}}{R_{\text{PV30}}}, \tag{4.3}$$

where $n_{\text{tgscat}}^{\text{tight}}$ was the number of events at the end of the tight normalization branch corrected for $K_{\pi 2}$ Range-Stack-scatter contamination, R_{PV60} was the rejection of the loose photon veto, and R_{PV30} was the rejection of the tight photon veto.

Tables 4.4 and 4.5 show the summary of all values used to determine the $K_{\pi 2}$ target-scatter background levels in the loose and tight signal regions, respectively. These background evaluations were scaled to the full data set for both the 1/3 and 2/3 data samples.
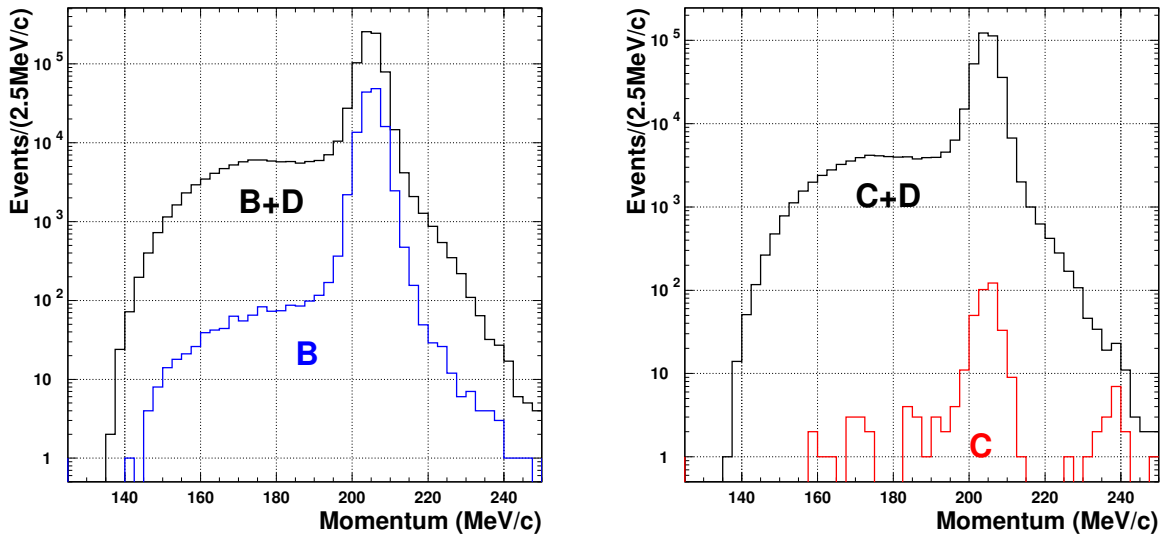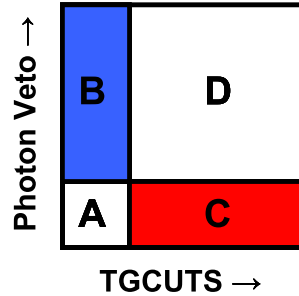
Figure 4.3: The bifurcation cuts used for the loose $K_{\pi 2}$ target-scatter background evaluation were the photon veto PV60 (CUT1) and the target quality cuts *TGCUTS* (CUT2). A schematic representation of the phase space of these two cuts after setup cuts to remove other backgrounds have been applied is shown on top with the arrows representing the cuts becoming increasingly loose. In the left plot, the momentum (`ptot`) distribution of the events remaining in the loose normalization branch after the inversion of the photon veto PV60 (black, regions B+D) and and after the application of all *TGCUTS* (blue, region B). In the right plot, the momentum (`ptot`) distribution of the events remaining in the loose rejection branch after class 12 has been chosen (black, regions C+D) and after the photon veto PV60 has been applied (red, region C). The estimate of the background events in the signal region "A" is given by "BC/D".

90

	1/3	2/3
	Normalization (Uncorrected)	
$N_{\text{tgscat}}^{\text{loose}}$	528	1131
	Normalization (Corrected for $K_{\pi 2}$ Range-Stack-scatter)	
$n_{\text{tgscat}}^{\text{loose}}$	$515.5 \pm 23.1\,{}^{+1.2}_{-1.1}$	$1107.7 \pm 33.8\,{}^{+2.9}_{-2.8}$
	Rejection	
$R_{\text{PV60}}(\text{CLASS12})$	2632 ± 832	2392 ± 510
$R_{\text{PV60}}(\text{max.})$	4096 ± 1672 (CLASS7)	2758 ± 650 (CLASS7)
$R_{\text{PV60}}(\text{min.})$	2374 ± 750 (CLASS9)	2204 ± 697 (CLASS10)
R_{PV60}	$2632 \pm 832\,{}^{+1464}_{-258}$	$2392 \pm 510\,{}^{+366}_{-188}$
	Background (Before correction for $K_{\pi 2\gamma}$)	
$bg_{\text{tgscat}}^{\text{loose}}(\text{uncorrected})$	$0.588 \pm 0.188\,{}^{+0.065}_{-0.211}$	$0.695 \pm 0.150\,{}^{+0.061}_{-0.094}$
	$K_{\pi 2\gamma}$ Background	
$bg_{K2\gamma}^{\text{loose}}$	$0.0514 \pm 0.0086\,{}^{+0.0042}_{-0.0038}$	$0.0757 \pm 0.0073\,{}^{+0.0062}_{-0.0056}$
	Background	
$bg_{\text{tgscat}}^{\text{loose}}$	$0.537 \pm 0.188\,{}^{+0.069}_{-0.215}$	$0.619 \pm 0.150\,{}^{+0.067}_{-0.100}$

Table 4.4: The summary of the loose $K_{\pi 2}$ target-scatter background evaluation. For the photon veto rejections R_{PV60} and background evaluations $bg_{\text{tgscat}}^{\text{loose}}$, the first uncertainty is statistical and the second uncertainty systematic. The maximum and minimum photon veto rejections are labeled to show which class was used to determine the systematic uncertainties in R_{PV60} and $bg_{\text{tgscat}}^{\text{loose}}$.

	1/3	2/3
	Normalization (Uncorrected)	
$N_{\text{tgscat}}^{\text{tight}}$	265	512
	Normalization (Corrected for $K_{\pi 2}$ Range-Stack-scatter)	
$n_{\text{tgscat}}^{\text{tight}}$	$259.1 \pm 16.4 {}^{+0.6}_{-0.7}$	$499.7 \pm 22.8 {}^{+1.1}_{-1.3}$
	Rejection (Tight Photon Veto)	
$R_{\text{PV30}}(\text{CLASS12})$	6579 ± 3289	6578 ± 3289
$R_{\text{PV30}}(\text{max.})$	8132 ± 4695 (CLASS2)	7484 ± 2646 (CLASS5)
$R_{\text{PV30}}(\text{min.})$	4935 ± 2467 (BOXTIGHT)	5640 ± 2132 (BOXTIGHT)
R_{PV30}	$6579 \pm 3289 {}^{+1553}_{-1644}$	$6578 \pm 2325 {}^{+906}_{-938}$
	Rejection (Loose Photon Veto)	
R_{PV60}	$2632 \pm 832 {}^{+1464}_{-258}$	$2392 \pm 510 {}^{+366}_{-188}$
	Background (Before correction for $K_{\pi 2\gamma}$)	
$bg_{\text{tgscat}}^{\text{tight}}(\text{uncorrected})$	$0.118 \pm 0.059 {}^{+0.075}_{-0.023}$	$0.114 \pm 0.041 {}^{+0.019}_{-0.014}$
	$K_{\pi 2\gamma}$ Background	
$bg_{K_{\pi 2\gamma}}^{\text{tight}}$	$0.0122 \pm 0.0038 {}^{+0.0010}_{-0.0010}$	$0.0188 \pm 0.0034 {}^{+0.0016}_{-0.0014}$
	Background	
$bg_{\text{tgscat}}^{\text{tight}}$	$0.106 \pm 0.059 {}^{+0.076}_{-0.024}$	$0.095 \pm 0.041 {}^{+0.020}_{-0.016}$

Table 4.5: The summary of the tight $K_{\pi 2}$ target-scatter background evaluation. For the photon veto rejections and background evaluations $bg_{\text{tgscat}}^{\text{loose}}$, the first uncertainty is statistical and the second uncertainty systematic. The maximum and minimum photon veto rejections are labeled to show which class was used to determine the systematic uncertainties in R_{PV30}, where the class called "BOXTIGHT" was described in Section 4.1.3. The rejection for the loose photon veto PV60 was taken from Table 4.4

4.1.5 Correction to Background for $K_{\pi 2 \gamma}$ Contamination

The contamination due to $K_{\pi 2 \gamma}$ events was only present in the normalization branch since any $K_{\pi 2 \gamma}$ contamination in the rejection branch was heavily suppressed by selecting events which scattered in the target. The $K_{\pi 2 \gamma}$ contamination in the normalization branch was enhanced by inverting the photon veto due to the presence of the additional photon in the $K_{\pi 2 \gamma}$ events. An upper limit of $30.0 \pm 7.5\%$ was found (Section 5.3.4) for the $K_{\pi 2 \gamma}$ contamination in the normalization branch using $K_{\pi 2}$ monitor trigger events under the assumption that all monitor trigger events found in the kinematic signal region were $K_{\pi 2 \gamma}$. Based on this upper limit and the fact that the size of the $K_{\pi 2 \gamma}$ background estimate was typically about 10% of the $K_{\pi 2}$ target-scatter background estimate or more, it was reasonable to conclude that the $K_{\pi 2 \gamma}$ background was being entirely double-counted between its own estimate and the $K_{\pi 2}$ target-scatter background estimate. To correct for this double-counting, the $K_{\pi 2 \gamma}$ background was subtracted from the $K_{\pi 2}$ target-scatter background as shown in Tables 4.4 and 4.5.

4.2 $K_{\pi 2}$ Range-Stack-Scatter Background

As was described in Section 4.1, there were two types of $K_{\pi 2}$ scatter backgrounds: target-scatter and Range-Stack-scatter. For $K_{\pi 2}$ scatters in the Range-Stack to become a background the momentum of the π^+ had to have been mis-measured in addition to the target-scatter conditions of the missing the energy lost in the scatter and the missing of the two photons from the π^0 decay. For this reason, the $K_{\pi 2}$ Range-Stack-scatter background was expected to be much smaller than the $K_{\pi 2}$ target-scatter background.

4.2.1 Range-Stack-Scatter Normalization Branch

The number of events N_{tgscat} left at the end of the target-scatter normalization branch actually consisted of n_{tgscat} target-scatter with contamination due to n_{rsscat} Range-Stack-scatter events:

$$N_{\text{tgscat}} = n_{\text{tgscat}} + n_{\text{rsscat}}. \tag{4.4}$$

As will be described in this section, the number of Range-Stack-scatter events n_{rsscat} was determined by studying the target-scatter and the Range-Stack-scatter normalization branches.

The most effective cuts against the $K_{\pi 2}$ Range-Stack-scatter background were the Range-Stack track quality cuts RSDEDX and PRRF, the PNN2BOX momentum cut (PNN2PBOX), and the photon veto. The cuts RSDEDX and PRRF were collectively referred to as *RSCT*. The Range-Stack normalization branch consisted of the same cuts as were used for the target-scatter normalization with *RSCT* inverted (see Figure 4.4). This sample was heavily contaminated with target-scatter events due to the inefficiency of the *RSCT* cuts.

The acceptance A_{RSCT} of *RSCT* for $K_{\pi 2}$ target-scatter events falling into the kinematic signal region was expected to be the same as for the signal. Thus the acceptance of these cuts was taken from the Range-Stack kinematic acceptance measurements found in

Section 6.2.2, with systematic uncertainties determined in the same way as described in that section.

The rejection R_{RSCT} of $RSCT$ was measured using events in the kinematic region known as the $K_{\pi2}$ range-tail. This region consisted of the $K_{\pi2}$-peak momentum region (KP2PBOX), but having a range and energy consistent with the signal region (PNN2REBOX). These were $K_{\pi2}$-peak events that did not scatter in the target and thus their momentum was still in the $K_{\pi2}$-peak region, but they scattered in the Range-Stack and their range and energy measurements fell into the range and energy of the signal region. Figure 4.4 shows the samples used to measure the rejection of the $RSCT$ cuts and Table 4.6 summarizes the results.

With the performance of the $RSCT$ cuts measured, it was possible to use equation 4.4 and the following equation for the number of events N_{rsscat} remaining at the end of the $K_{\pi2}$ Range-Stack-scatter normalization to determine the quantity n_{rsscat}:

$$\frac{1 - A_{RSCT}}{A_{RSCT}} \times n_{\mathrm{tgscat}} + (R_{RSCT} - 1) \times n_{\mathrm{rsscat}} = N_{\mathrm{rsscat}}. \qquad (4.5)$$

The n_{rsscat} values which resulted are shown in Table 4.6.

4.2.2 Range-Stack-Scatter Rejection Branch

The photon veto rejection of the Range-Stack-scatter events was assumed to be the same as for the $K_{\pi2}$-peak events since the distribution of photons coming from the π^0 for π^+ particles entering the fiducial region of the detector will be the same for the $K_{\pi2}$-peak and the $K_{\pi2}$ Range-Stack-scatter events. The $K_{\pi2}$-peak rejection branch from Figure 4.4 shows the sample used to measure this photon veto rejection $R_{\mathrm{PVCUT-KP2}}$ and Table 4.6 summarizes the results.

	Loose		Tight	
	1/3	2/3	1/3	2/3
		Acceptance of $RSCT$		
A_{RSCT}	$0.888 \pm 0.001 \pm 0.012$		$0.894 \pm 0.002\,^{+0.010}_{-0.012}$	
		Rejection of $RSCT$		
N_4	642	1355	307	739
N_5	80	192	44	118
R_{RSCT}	8.03 ± 0.84	7.06 ± 0.47	6.98 ± 0.97	6.26 ± 0.53
		Normalization Numbers		
N_{tgscat}	528	1131	265	512
N_{rsscat}	153	281	66	124
n_{rsscat}	$12.5 \pm 2.4^{+1.2}_{-1.2}$	$23.3 \pm 3.5^{+2.9}_{-3.0}$	$5.9 \pm 1.7^{+0.6}_{-0.7}$	$12.3 \pm 2.6^{+1.3}_{-1.5}$
		Photon Veto Rejection (K$_{\pi 2}$ peak)		
N_2	61410	122581	41103	82387
N_3	36	106	10	31
$R_{\mathrm{PVCUT-KP2}}$	1706 ± 184	1156 ± 112	4110 ± 1300	2658 ± 477
		Background		
$bg_{\mathrm{rsscat}}(1/3)$	$0.0220 \pm 0.0056\,^{+0.0021}_{-0.0021}$		$0.0043 \pm 0.0019\,^{+0.0004}_{-0.0005}$	
$bg_{\mathrm{rsscat}}(2/3)$	$0.0303 \pm 0.0054\,^{+0.0038}_{-0.0039}$		$0.0069 \pm 0.0019\,^{+0.0007}_{-0.0009}$	

Table 4.6: The summary of the $K_{\pi 2}$ Range-Stack-scatter background evaluation. For values having two sets of uncertainties, the first is statistical and the second systematic. See Figure 4.4 for definitions of N_2 - N_5.

4.2.3 Range-Stack-Scatter Background Evaluation

The final background level due from $K_{\pi 2}$ Range-Stack-scatter events was given by

$$bg_{\mathrm{rsscat}} = \frac{n_{\mathrm{rsscat}}}{R_{\mathrm{PVCUT-KP2}} - 1}, \qquad (4.6)$$

where the 1/3 and 2/3 data sets were normalized to the full data set. A summary of the $K_{\pi 2}$ Range-Stack-scatter background evaluation is found in Table 4.6.

$K_{\pi 2}$ Range-Stack Scatter Bifurcations

VALID_TRIG, P2PSCUT, P2TGCUT, P2TGPVCUT, *BEAMCUTS*, DELCO*, *TDCUTS**, *TGCUTS*

Normalization Branch

Rejection Branch

PNN2BOX

KP2BOX

KP2PBOX, PNN2REBOX

$\overline{\text{RSDEDX}}$ .OR. $\overline{\text{PRRF}}$

LAYER14, COS3D, LAYV4, ZFRF, ZUTOUT, UTCQUAL, RNGMOM

LAYER14, COS3D, LAYV4, ZFRF, ZUTOUT, UTCQUAL, RNGMOM

LAYER14, COS3D, LAYV4, ZFRF, ZUTOUT, UTCQUAL, RNGMOM

N_1

N_4

RSDEDX, PRRF

RSDEDX, PRRF

$\overline{\text{PV60}}$

N_2

N_5

PVCUT

$R_{RSCT} = N_4/N_5$

N_{rsscat}

N_3

$R_{\text{PVCUT}-\text{KP2}} = N_2/N_3$

Figure 4.4: Flowchart showing the $K_{\pi 2}$ Range-Stack-scatter bifurcations. Cuts in italics refer to named groups of cuts. Cuts denoted with an '*' indicate that the loose version of the cut was used for the background evaluation in the loose box and the tight version for the background evaluation in the tight box. The photon veto rejection $R_{\text{PVCUT}-\text{KP2}}$ is the photon veto rejection for events in the $K_{\pi 2}$ peak.

4.3 $K_{\pi 2 \gamma}$ Background

The background from the decay $K^+ \to \pi^+ \pi^0 \gamma$ ($K_{\pi 2 \gamma}$) was expected to be small relative to the $K^+ \to \pi^+ \pi^0$ ($K_{\pi 2}$) background due to (1) the smaller branching ratio and (2) the additional photon against which to veto.

The γ emitted in this decay can be produced by either direct emission (DE) or inner bremsstrahlung (IB). The inner bremsstrahlung process dominates these two γ emission processes with a branching ratio of $2.75 \pm 0.15 \times 10^{-4}$ for T_{π^+} in the range of 55 MeV to 90 MeV [99]. The direct emission process has a branching ratio of $4.3 \pm 0.7 \times 10^{-6}$ for the same T_{π^+} range [99].

Due to the difficulty of isolating a $K_{\pi 2 \gamma}$ sample in data, evaluation of this background was performed using a combination of data and Monte Carlo simulation. The simulation was used to predict the number of $K_{\pi 2 \gamma}$ events that would be found in the signal region given a certain number of $K_{\pi 2}$ events found in the $K_{\pi 2}$-peak kinematic box KP2BOX using data. This was done by determining the relative acceptance of the π^+ from $K_{\pi 2}$ and $K_{\pi 2 \gamma}$ events, and determining the extra rejection from the photon veto due to the additional photon.

4.3.1 Relative Rate of π^+ Acceptance for $K_{\pi 2}$ and $K_{\pi 2 \gamma}$ Events

The quantity κ represents the relative rate of acceptance of the π^+ for $K_{\pi 2}$ and $K_{\pi 2 \gamma}$ events given (1) the acceptance A of the events generated in Monte Carlo for passing the trigger conditions and offline cuts, and (2) the branching ratio $\mathcal{B}$ of the process. The following expression is used for κ,

$$\kappa = \frac{\mathcal{B}\left(K_{\pi 2}\right) \times A(K_{\pi 2})}{\mathcal{B}\left(K_{\pi 2 \gamma}\right) \times A(K_{\pi 2 \gamma})}. \tag{4.7}$$

To determine the acceptances A, about 2×10^5 $K_{\pi 2}$ and 5×10^5 $K_{\pi 2 \gamma}$ Monte Carlo

events were generated. The events were required to pass either the PNN1 or PNN2 trigger conditions in simulation without the online photon veto, L1.1, L1.2 or L0rr2 triggers. The events were then required to pass all available offline cuts including the appropriate kinematic region cuts, but excluding the photon veto. The kinematic boxes used were the $K_{\pi 2}$-peak kinematic box KP2BOX for the $K_{\pi 2}$ events and the PNN2 kinematic box PNN2BOX for the $K_{\pi 2\gamma}$ events. The numbers of events used to determine the acceptance values are shown in Table 4.7.

Also needed to determine κ were the branching ratios of $K_{\pi 2}$ and $K_{\pi 2\gamma}$. The branching ratio of the direct emission $K_{\pi 2\gamma}$ process was ignored since it is known to be two orders of magnitude smaller than the inner bremsstrahlung $K_{\pi 2\gamma}$ process. The branching ratio for the inner bremsstrahlung $K_{\pi 2\gamma}$ process was only given over the π^+ energy range of 55 - 90 MeV. To extrapolate this branching ratio to the full energy spectrum available to the decay π^+, the Monte Carlo simulation was used to determine this energy spectrum available to the π^+ as shown in Figure 4.5. Using this spectrum, the effective branching ratio $\mathcal{B}(K_{\pi 2\gamma})$ for T_{π^+} between 0 and 106 MeV was calculated,

$$\mathcal{B}(K_{\pi 2\gamma}) = \frac{\int_0^{106} dN}{\int_{55}^{90} dN} \times (2.75 \pm 0.15) \times 10^{-4} = (1.11 \pm 0.06) \times 10^{-3}. \qquad (4.8)$$

The branching ratio for $K_{\pi 2}$ was 0.2092 ± 0.0012 [99].

The resulting values for κ in the loose and tight signal regions are shown in Table 4.7. It was found that κ was fairly insensitive to the applied cuts and was determined mainly from the relative branching ratios.

4.3.2 Additional Photon Veto Rejection

The performance of the photon veto in rejecting events based on the photons from the π_0 decay was expected to be the same for both $K_{\pi 2}$ and $K_{\pi 2\gamma}$ events. However due to
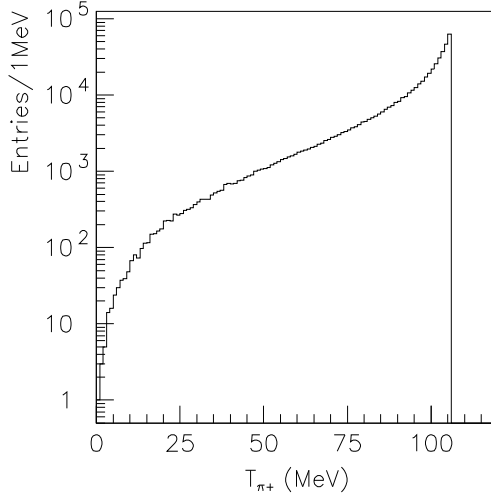
Figure 4.5: Kinetic energy distribution of the π^+ from $K_{\pi2\gamma}$ events in Monte Carlo. Figure reproduced from [55].

the third decay photon, $K_{\pi2\gamma}$ events had additional photon veto rejection above that for $K_{\pi2}$ events. A single photon rejection function was created by convolving the spatial and energy distribution of the third photon (from the simulation) with the detector detection inefficiency for a single photon (from data [83]). The additional photon veto rejection factor (R_γ) was determined by applying this single photon rejection function to the 11,305 $K_{\pi2\gamma}$ events remaining after the loose offline cuts and 7,409 $K_{\pi2\gamma}$ events remaining after the tight offline cuts, respectively. The resulting rejection factors, taken from [55], were

$$R_\gamma^{\text{loose}} = 5.04 \pm 0.10. \tag{4.9}$$

and

$$R_\gamma^{\text{tight}} = 5.11 \pm 0.11 \tag{4.10}$$

4.3.3 $K_{\pi2\gamma}$ Background Evaluation

To evaluate the background level bg from the $K_{\pi2\gamma}$ process, the number of $K_{\pi2}$ events ($N_{K_{\pi2}-\text{peak}}$) found in the $K_{\pi2}$-peak kinematic box KP2BOX was used to predict the num-

Number of Events	$N_{K_{\pi 2}}$	$N_{K_{\pi 2\gamma}}$
N_1: Total events produced	199986	499973
N_2: Passed PNN1 or PNN2 trigger	30625	64217
N_3: Passed loose offline cuts	9776	11035
N_4: Passed tight offline cuts	7608	7409
$A_{\text{loose}} = N_3/N_1$	0.0489±0.0005	0.0221±0.0002
$A_{\text{tight}} = N_4/N_1$	0.0380±0.0004	0.0148±0.0002
κ_{loose}	417 ± 24	
κ_{tight}	483 ± 28	

Table 4.7: Summary of Monte Carlo simulation events produced and remaining after various cuts have been applied as were used to determine $A(K_{\pi 2})$ and $A(K_{\pi 2\gamma})$. The cuts tightened for the tight offline cuts measurement N_4 were DELCO for both types of events, and the PNN2BOX for $K_{\pi 2\gamma}$ events. Table reproduced from [55].

ber of $K_{\pi 2\gamma}$ events that would have been found in the signal region. This prediction was done by using the simulation to determine κ, the relative rate of π^+ acceptance for $K_{\pi 2}$ and $K_{\pi 2\gamma}$ events, and by using a combination of simulation and photon veto data to determine R_γ, the additional rejection due to the third photon from the $K_{\pi 2\gamma}$ events. The following expression was used to evaluate the background level due to the $K_{\pi 2\gamma}$ process:

$$bg = \frac{N_{K_{\pi 2}-\text{peak}}}{\kappa \cdot R_\gamma}, \tag{4.11}$$

where $N_{K_{\pi 2}-\text{peak}}$ was the value N_3 from Figure 4.4 and Table 4.6, and the other terms were determined previously in this section. This background was normalized to the full data set for the 1/3 and 2/3 data sets. Table 4.8 summarizes the results of the $K_{\pi 2\gamma}$ background evaluation.

	Loose	Tight
	Normalization	
$N_{K_{\pi 2}-\text{peak}}(1/3)$	36	10
$N_{K_{\pi 2}-\text{peak}}(2/3)$	106	31
	Relative Rate of π^+ Acceptance	
κ	417±24	483±28
	Additional PV Rejection	
R_γ	5.04±0.10	5.11±0.11
	Background	
$bg(1/3)$	$0.0514 \pm 0.0086\,^{+0.0042}_{-0.0038}$	$0.0121 \pm 0.0038\,^{+0.0010}_{-0.0010}$
$bg(2/3)$	$0.0757 \pm 0.0073\,^{+0.0062}_{-0.0056}$	$0.0188 \pm 0.0034\,^{+0.0016}_{-0.0014}$

Table 4.8: Summary of the $K_{\pi 2\gamma}$ background evaluation. The relative rate of π^+ acceptance "κ" for $K_{\pi 2}$ and $K_{\pi 2\gamma}$ events and the additional photon veto rejection "R_γ" are defined in the text. The first uncertainty in the background bg is statistical (from $N_{K_{\pi 2}-\text{peak}}$) and the second is systematic (from κ and R_γ). The background bg was normalized to the full data set for the 1/3 and 2/3 data sets. The values for κ and R_γ were taken from [55].

4.4 Muon Background

The decay $K^+ \rightarrow \mu^+ \nu_\mu$ ($K_{\mu2}$) has a very high branching ratio, but due to the μ^+ momentum of 236 MeV/c, it would need to lose a large amount of undetected energy to simulate $K^+ \rightarrow \pi^+ \nu \bar{\nu}$ in the PNN2 kinematic region, and therefore it was highly suppressed. The muon background came primarily from the $K^+ \rightarrow \mu^+ \nu \gamma$ ($K_{\mu2\gamma}$) and $K^+ \rightarrow \mu^+ \pi^0 \nu$ ($K_{\mu3}$) decays, each of which have a μ^+ momentum spectrum that extends into the kinematic signal region. For these decays to be backgrounds, the muon had to be misidentified as a pion and the photon(s) must have escaped detection.

The main cuts used to suppress muon backgrounds are the particle identification cuts in the Range-Stack and the photon veto. The bifurcation cuts used for the muon background evaluation were the loose $\pi^+ \rightarrow \mu^+ \rightarrow e^+$ decay sequence cuts *TDLOOSE* (CUT1) and the range-momentum consistency cut RNGMOM (CUT2). The RNGMOM cut required that the measured range of the charged decay particle was consistent with that predicted for a π^+ given the measured momentum.

4.4.1 Muon Normalization Branch

The muon normalization branch was created by inverting the loose $\pi^+ \rightarrow \mu^+ \rightarrow e^+$ decay sequence cuts *TDLOOSE* (CUT1) and applying all other analysis cuts. The loose version of the $\pi^+ \rightarrow \mu^+ \rightarrow e^+$ decay sequence cuts was inverted in the normalization branches for both the loose and tight background evaluations since inverting the tight version *TDTIGHT* would have resulted in examining a portion of the loose signal region. Inverting *TDLOOSE* resulted in a sample rich in K^+ decays with muons since these cuts were designed to strongly suppress events having muon-like signatures in detector subsystems outside the target. Figure 4.6 shows a schematic representation of the normalization branch used for the loose and tight muon background evaluations.

4.4.2 Muon Rejection Branch

To create the sample upon which the rejection of *TDLOOSE* (CUT1) was measured, RNGMOM (CUT2) was inverted. Setup cuts were applied to this sample to remove $K_{\pi 2}$ decays and beam backgrounds. Figure 4.6 shows a schematic representation of the rejection branch used for the loose and tight muon background evaluations.

Muon Bifurcations

VALID_TRIG, P2TGCUT, P2PSCUT, *BEAMCUTS*, *DELCO**, P2TGPVCUT

Normalization Branch | Rejection Branch

$\overline{TDLOOSE}$

$\overline{RNGMOM}$

PNN2BOX*, *KINCUTS*, *TGCUTS*, PVCUT*

PNN2BOX*, *KINCUTS* (excluding RNGMOM), *TGCUTS* (excluding CHI567 & CHI5MAX), PVPNN1

N_1

N_{muon}

TDCUTS*

N_2

$$R_{TDCUTS} = N_1/N_2$$
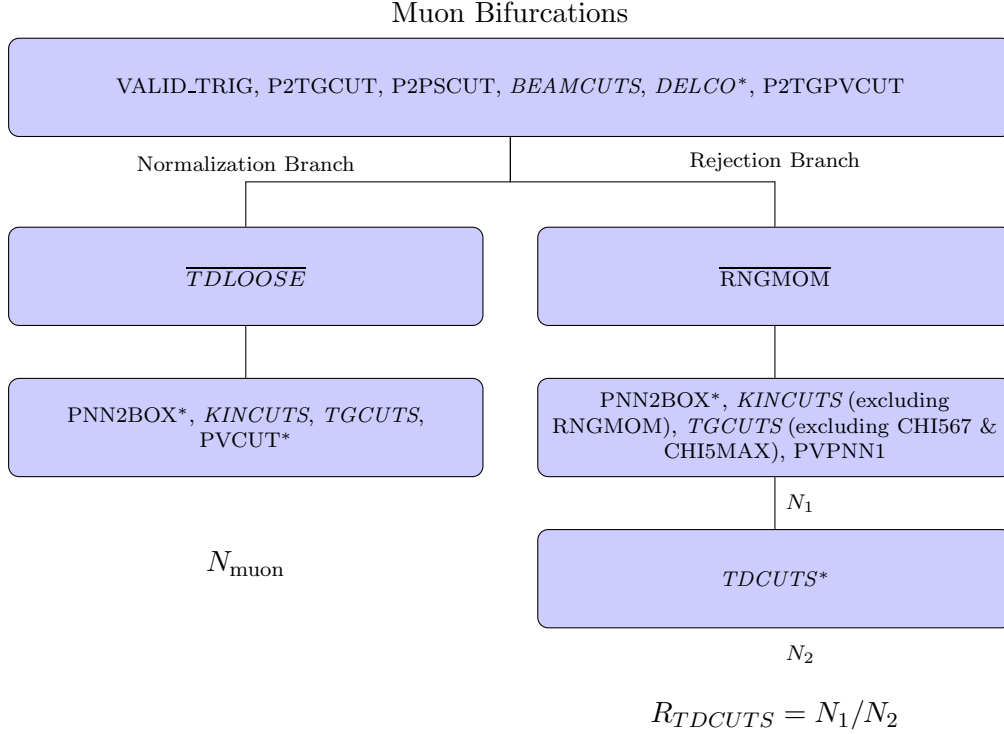
Figure 4.6: Flowchart showing the muon bifurcation branches. Cuts in italics refer to named groups of cuts. Cuts denoted with an '*' indicate that the loose version of the cut was used for the background evaluation in the loose box and the tight version for the background evaluation in the tight box.

4.4.3 Muon Background Evaluation

The loose muon background $bg_{\mathrm{muon}}^{\mathrm{loose}}$ was evaluated using the expression

$$bg_{\mathrm{muon}}^{\mathrm{loose}} = \frac{N_{\mathrm{muon}}^{\mathrm{loose}}}{R_{TDLOOSE} - 1}, \tag{4.12}$$

where $N_{\mathrm{muon}}^{\mathrm{loose}}$ was the number of events at the end of the loose muon normalization branch and $R_{TDLOOSE}$ was the rejection of *TDLOOSE*. This background was scaled to the full data set from the 1/3 or 2/3 data samples.

For the background evaluation in the tight signal region, *TDLOOSE* was inverted in order to not examine the signal region and the results of the entire background evaluation scaled by the ratio of the rejections of *TDLOOSE* and *TDTIGHT*. The tight muon background $bg_{\mathrm{muon}}^{\mathrm{tight}}$ was evaluated using the expression

$$bg_{\mathrm{muon}}^{\mathrm{tight}} = \frac{N_{\mathrm{beam}}^{\mathrm{tight}}}{R_{TDLOOSE} - 1} \times \frac{R_{TDLOOSE}}{R_{TDTIGHT}}, \tag{4.13}$$

where N_{muon}^{tight} was the number of events at the end of the tight muon normalization branch, and $R_{TDLOOSE}$ and $R_{TDTIGHT}$ were the rejection of *TDLOOSE* and *TDTIGHT*, respectively. This background estimate was scaled to the full data set for the 1/3 and 2/3 data samples.

Table 4.9 summarizes the muon background evaluations.

Muon Background Summary		
	1/3	2/3
Normalization		
$N_{\text{muon}}^{\text{loose}}$	0	1
$N_{\text{muon}}^{\text{tight}}$	0	1
Rejection ($TDLOOSE$)		
N_1	10328	20488
N_2	84	154
$R_{TDLOOSE}$	123.0 ± 13.4	133.0 ± 10.7
Rejection ($TDTIGHT$)		
N_1	9277	18411
N_2	17	45
$R_{TDTIGHT}$	546 ± 132	409 ± 61
Background		
$bg_{\text{muon}}^{\text{loose}}$	0.0246 ± 0.0246	0.0114 ± 0.0114
$bg_{\text{muon}}^{\text{tight}}$	0.0055 ± 0.0055	0.0037 ± 0.0037

Table 4.9: Summary of the muon background evaluation. See Figure 4.6 for definitions of N_1 and N_2 for $R_{TDLOOSE}$ and $R_{TDTIGHT}$.

4.5 K_{e4} Background

The $K^+ \to \pi^+\pi^- e^+ \nu$ (K_{e4}) decay has a branching ratio of approximately 4×10^{-5} and could be a serious background due to the lack of photons to veto and a substantial fraction of the decay π^+ phase-space falling in the kinematic signal region. The target event display of a typical K_{e4} event is shown in Figure 4.7.
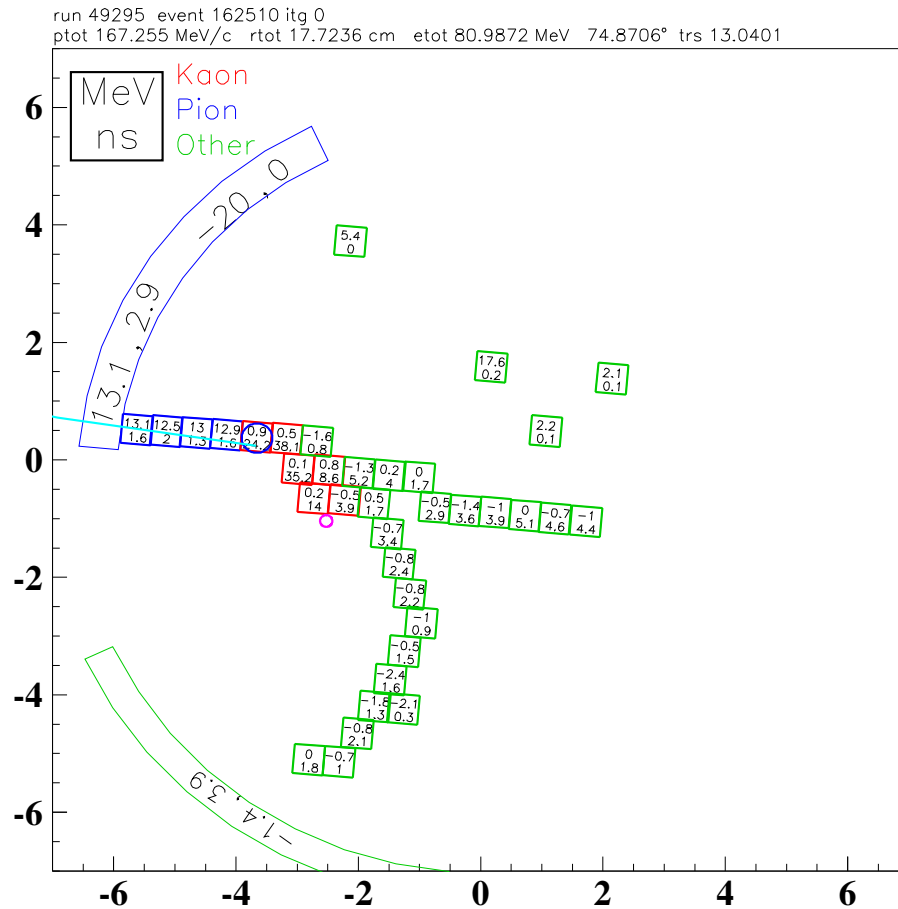
Figure 4.7: The target event display of a typical K_{e4} event. Red squares indicate the K^+ fibers, blue squares the π^+ fibers, and green the opposite-side-π^+ and γ fibers. The two green tracks to the right of the decay vertex (blue circle) show the tracks of the π^- and e^+. The top number shown in each fiber is the time of the hit and the bottom number is the energy deposited.

This background was most problematic when the low-energy π^- and e^+ did not leave the target and escaped detection by depositing all their energy in kaon fibers or insensitive

materials. For a combined total kinetic energy (T_2) of the π^- and e^+ below 100 MeV, the π^+ momentum peaked at around 160 MeV/c (see Figure 4.8), which was in the loose kinematic signal region. As is described in Appendix D.4, the tight kinematic signal region was chosen to kinematically exclude most of the K_{e4} background while minimizing the acceptance loss of signal events.
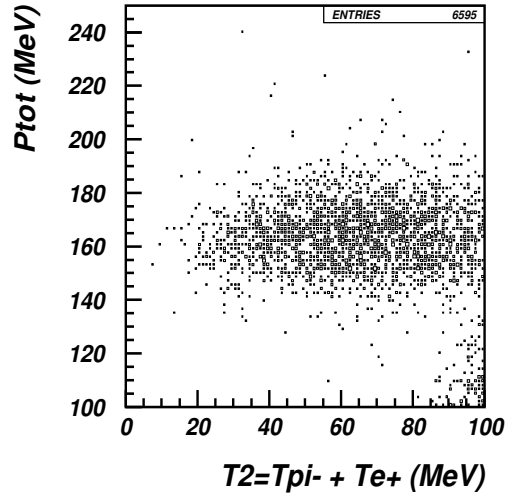
Figure 4.8: Total kinetic energy (T_2) of the π^- and the e^+ versus π^+ momentum (P_{tot}) for Monte Carlo K_{e4} events that pass the trigger conditions. Figure reproduced from [55].

The most effective cuts in finding the additional energy deposited in the target from the low-energy π^- and e^+ were the target sub-system of the photon veto (TGPV), the opposite side pion-fiber veto (OPSVETO) and the pion-energy cut from target-CCD pulse fitting (CCDPUL). After inverting the combination of OPSVETO and TGPV to create the normalization branch, there remained no set of cuts with which to create a K_{e4}-rich data sample to measure the rejection of OPSVETO and TGPV so Monte Carlo simulation was used.

4.5.1 Normalization Branch Using Data

The K_{e4} normalization branch used data and was created by inverting the combination of the TGPV and OPSVETO cuts (CUT1), such that an event failing either of these cuts

108

remained in the normalization branch. All other analysis cuts other than TGGEO were applied. TGGEO was highly correlated with the inverted cuts and was thus excluded from the normalization branch. Figure 4.9 shows all the cuts applied in the normalization branch.

K_{e4} Normalization Branch

VALID_TRIG, P2TGCUT, P2PSCUT, *KINCUTS*, PNN2BOX*, *BEAMCUTS* (excluding TGGEO), DELCO*, *TDCUTS*, PVCUT* (excluding TGPV)
$\overline{\text{TGPV} \cdot \text{OPSVETO}}$
TGCUTS (excluding OPSVETO)

N_{Ke4}
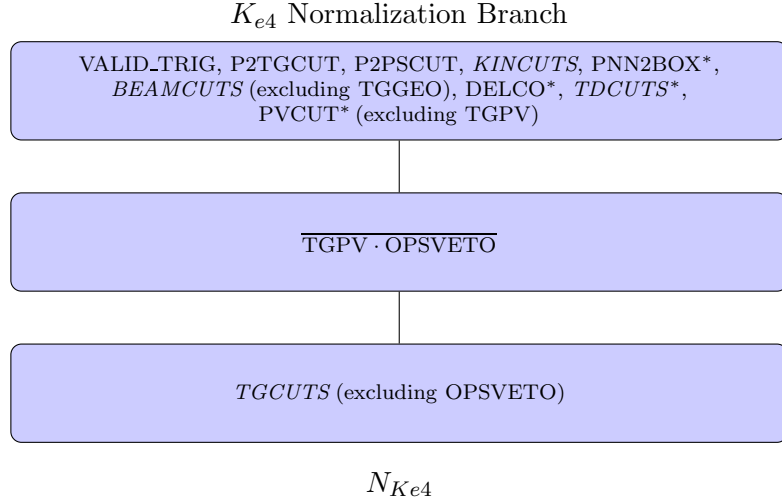
Figure 4.9: Flowchart showing the K_{e4} normalization branch. Cuts in italics refer to named groups of cuts. Cuts denoted with an '*' indicate that the loose version of the cut was used for the background evaluation in the loose box and the tight version for the background evaluation in the tight box. The loose version of TGPV was inverted for both the loose and tight normalization branches. Table 4.12 shows the number of events left at the end of this normalization branch.

4.5.2 Rejection Branch Using Monte Carlo

Monte Carlo simulation was used to determine the total rejection of the combination of the TGPV and OPSVETO cuts for K_{e4} events. A total of approximately 2×10^8 K_{e4} events with $\text{T}_2 < 50$ MeV were produced, where T_2 was the combined kinetic energy of the π^- and the e^+ from the K_{e4} decay. This constraint on T_2 was used to enhance the statistical power of the simulation by concentrating on the most troublesome phase space of the K_{e4} decay. Before measuring the rejection of the combination of the TGPV and OPSVETO cuts, these events were required to pass all possible cuts in simulation.

The Monte Carlo simulation used two different measures of energy deposited in target

fibers to reproduce the effects of OPSVETO, TGPV and CCDPUL. The first quantity $\texttt{T}_{\texttt{xtg}}$ was the total energy deposited in all fibers not classified as kaon or pion fibers by the reconstruction algorithm. This represented the energy available to the TGPV and OPSVETO cuts. The second quantity $\texttt{E}_{\texttt{hide}}$ was the total energy deposited in kaon fibers by the π^- and e^+. This represented the energy available to the CCDPUL cut.

The main source of uncertainty in the simulation for this study was from the energy of absorbed π^- particles. The π^- absorption was modeled based on experimental data of stopped π^- in the Range Stack [97]. The absorption of the π^- by carbon dominated and the excited nucleus de-excited by gamma emission or particle evaporation. The resulting gammas and neutrons were likely to escape the target and were not simulated in the Monte Carlo simulation. Since the charged particles resulting from particle evaporation had a short range, they were treated in Monte Carlo as having deposited all their energy in the same fiber as the original π^- absorption. Figure 4.10 shows the additional absorption energy of the π^- which was determined experimentally by taking the difference between the measured absorption energy in the Range Stack and the π^- energy as determined from its momentum. Due to the resolution of the two measurements used to determine the total π^- absorption energy, it was expected that a small number of events would have a negative energy. This distribution was sampled in Monte Carlo to determine the total π^- absorption energy with energies below zero being treated as zero.

Since the correlation between the energy deposited by particles in the simulation and in the data was not precisely known, the rejection thresholds for the quantities $\texttt{T}_{\texttt{xtg}}$ and $\texttt{E}_{\texttt{hide}}$ were independently varied over a range of energies as shown in Tables 4.10 and 4.11. The rejection of the combined TGPV and OPSVETO cuts (represented by the quantity $\texttt{T}_{\texttt{xtg}}$) was determined based on events above the $\texttt{E}_{\texttt{hide}}$ threshold. The central value for this rejection was used for the background estimation while the variations based on $\texttt{T}_{\texttt{xtg}}$ and $\texttt{E}_{\texttt{hide}}$ provided the systematic uncertainty. The K_{e4} background summary table (Table 4.12) shows the values for the rejection as used in the background estimate.

110
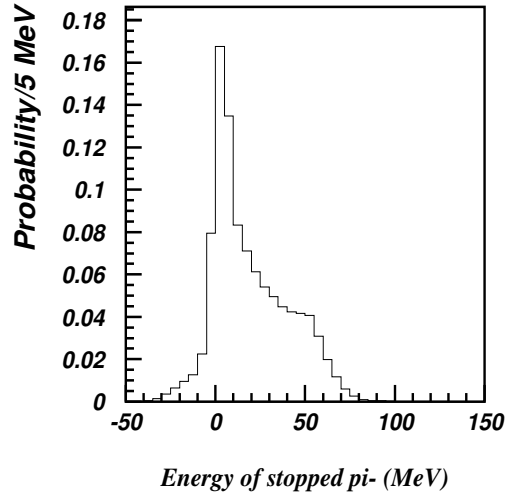
Figure 4.10: Observable absorption energy of π^- stopped in the Range Stack as used by the Monte Carlo simulation. This is the additional energy observed from a stopped π^- beyond that expected from the energy of the π^- as determined by momentum. Figure reproduced from [37].

4.5.3 K_{e4} Background Evaluation

The K_{e4} background was evaluated using the expression

$$bg_{K_{e4}} = \frac{N_{K_{e4}}}{R_{\text{TGPV·OPSVETO}} - 1}, \tag{4.14}$$

where N_{Ke4} was the number of events at the end of the K_{e4} normalization branch and $R_{\text{TGPV·OPSVETO}}$ was the rejection of TGPV and OPSVETO as measured using Monte Carlo. The results are summarized in Table 4.12.

	$T_{xtg} < 0.6$ MeV	$T_{xtg} < 1.2$ MeV	$T_{xtg} < 1.8$ MeV
$E_{hide} < 1.6$ MeV	$2250/66 = 34$	$2250/86 = 26$	$2250/98 = 23$
$E_{hide} < 2.5$ MeV	$6769/100 = 68$	$6769/129 = 52$	$6769/149 = 45$
$E_{hide} < 4.0$ MeV	$34992/202 = 173$	$34992/288 = 122$	$34992/335 = 104$
$E_{hide} < 10.0$ MeV	$97100/627 = 155$	$97100/888 = 109$	$97100/1105 = 88$

Table 4.10: Rejection of $R_{\text{TGPV·OPSVETO}}$ as a function of E_{hide} for the loose rejection branch. In a given cell, the first number shows the number of events remaining after the E_{hide} condition was applied, and the second number shows the number of events remaining after the T_{xtg} condition was applied. The T_{xtg} condition represented the cuts TGPV and OPSVETO within the simulation. Table reproduced from [55].

	$T_{xtg} < 0.6$ MeV	$T_{xtg} < 1.2$ MeV	$T_{xtg} < 1.8$ MeV
$E_{hide} < 1.6$	$389/18 = 22$	$389/20 = 19$	$389/22 = 18$
$E_{hide} < 2.5$	$2282/23 = 99$	$2282/26 = 88$	$2282/31 = 74$
$E_{hide} < 4.0$	$15105/43 = 351$	$15105/53 = 285$	$15105/65 = 232$
$E_{hide} < 10.0$	$37174/160 = 232$	$37174/206 = 180$	$37174/269 = 138$

Table 4.11: Rejection of $R_{\text{TGPV·OPSVETO}}$ as a function of E_{hide} for the tight rejection branch. In a given cell, the first number shows the number of events remaining after the E_{hide} condition was applied, and the second number shows the number of events remaining after the T_{xtg} condition was applied. The T_{xtg} condition represented the cuts TGPV and OPSVETO within the simulation. Table reproduced from [55].

	Loose		Tight	
	1/3	2/3	1/3	2/3
	Normalization			
$N_{K_{e4}}$	4	6	1	0
	Rejection			
$R_{\text{TGPV·OPSVETO}}$	52^{+121}_{-29}		88^{+263}_{-70}	
	Background			
$bg_{K_{e4}}(1/3)$	$0.235 \pm 0.118^{+0.310}_{-0.166}$		$0.034 \pm 0.034^{+0.142}_{-0.026}$	
$bg_{K_{e4}}(2/3)$	$0.176 \pm 0.072^{+0.233}_{-0.124}$		$0.017 \pm 0.017^{+0.071}_{-0.013}$	

Table 4.12: The values used for the K_{e4} background evaluation are shown with the results from the 1/3 and 2/3 data samples normalized to the full data set. The first uncertainty of bg_{Ke4} is statistical from $N_{K_{e4}}$ and the second uncertainty is the systematic uncertainty determined from the range of values found for $R_{\text{TGPV·OPSVETO}}$. The values for $R_{\text{TGPV·OPSVETO}}$ were taken from [55].
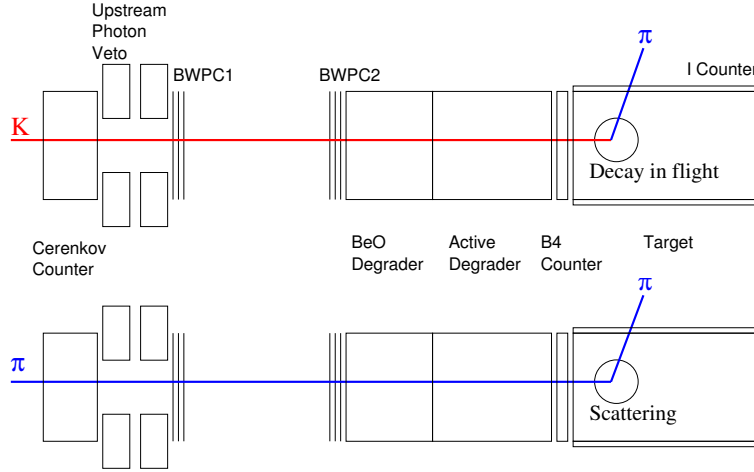
Figure 4.11: A schematic of the single-beam background processes. The top figure shows a kaon decay-in-flight and the bottom a beam pion scattering into the fiducial region of the detector. Figure reproduced from [37].

4.6 Single-Beam Background

The beam backgrounds were a collection of backgrounds due to beam pions scattering into the fiducial region of the detector or beam kaons decaying in flight.

For events having only a single beam particle, the delayed coincidence cuts (DELC3 for the loose box and DELC6 for the tight box) removed all properly reconstructed events of this type. DELC3 (DELC6) required that the kaon decayed at least 3 ns (6 ns) after entering the target. Both the scattered pion and the kaon decay-in-flight failed this minimum time difference condition between outgoing particles from the target and incoming particles from the beam. These types of events could imitate $K^+ \to \pi^+ \nu \bar{\nu}$ if the event was poorly reconstructed such that the beam and/or RS timing wasn't measured correctly and the event passed the delayed coincidence requirements. This type of background was referred to as single-beam background and schematic representations of these two single-beam background processes are shown in Figure 4.11.

A kaon decay-in-flight looked like a regular kaon-stop to the beam-line detectors and the decay products looked like any other kaon stop decay to rest of the detector. As a result the cuts designed to suppress stopped-kaon background were also effective against

decay-in-flight kaon events. The kinematic box provided additional suppression due to the Lorentz boost of the π^+ resulting from the K^+ decaying in flight.

The scattered beam pions were heavily suppressed by the high efficiency Čerenkov and B4 counters that could distinguish between K^+ and π^+ in the beam. Scattered beam pions that were not suppressed by the beam-line counters and delayed coincidence cuts could simulate $K^+ \rightarrow \pi^+ \nu \bar{\nu}$ when scattering into the fiducial region of the detector if the kinematics of the π^+ were the same as a signal π^+ since there were no photons against which to veto.

4.6.1 Single-Beam Normalization Branch

For the single-beam background evaluation, the normalization branch bifurcation cut (CUT1) was the delayed coincidence cut DELC3. To avoid examining the signal region for the background evaluation in the tight signal region, only the loose cut DELC3 was inverted and the results of the background evaluation scaled to take into account the additional rejection of the tight version (DELC6) of the cut. Figure 4.12 shows the normalization branch and Table 4.13 the resulting event counts.

4.6.2 Single-Beam Rejection Branch

To create the sample used to measure the rejection of DELC3, a loose version of the B4DEDX cut was inverted. Inverting this cut demanded that the beam particle was a pion by requiring that the energy `b4abm_atc` in the B4 at beam time was less than 1.0 MeV. Figure 4.12 shows the rejection branch and Table 4.13 the resulting event counts. It was assumed that the rejections of the delayed coincidence cuts DELC3 and DELC6 were the same for scattered beam pions as for decay-in-flight kaons. To preserve statistics in the single-beam background study, the very loose photon veto PV90 was applied in the rejection branch. The Active Degrader and target photon veto subsystems were excluded

from this photon veto as indicated by the notation "noTG, noAD".

4.6.3 Single-Beam Background Evaluation

The loose single-beam background bg_{1bm}^{loose} was written as

$$bg_{1bm}^{loose} = \frac{N_{1bm}^{loose}}{R_{DELC3} - 1},$$
(4.15)

where N_{1bm}^{loose} was the number of events at the end of the loose single-beam normalization branch and R_{DELC3} was the rejection of DELC3. These values are summarized in Table 4.13. This background was scaled to the full data set for the 1/3 and 2/3 data samples.

The expression used to evaluate the tight single-beam background was

$$bg_{1bm}^{tight} = \frac{N_{1bm}^{tight}}{R_{DELC3} - 1} \times \frac{R_{DELC3}}{R_{DELC6}},$$
(4.16)

where N_{1bm}^{tight} was the number of events at the end of the tight single-beam normalization branch, R_{DELC3} and R_{DELC6} were the rejections of DELC3 and DELC6, respectively as measured on the loose rejection branch. The scaling by the ratios of the rejections of DELC3 and DELC6 was required because DELC3 was inverted in the tight single-beam normalization branch in order to not look in the loose signal region and this scaling results in a normalization value that would have been measured had DELC6 been inverted. This expression simplifies for the 1/3 data set since the rejection of DELC3 was used for both DELC3 and DELC6 due to statistical limitations.

Table 4.13 summarizes the results of the single-beam background evaluation.

	1/3	2/3
	Normalization	
$N_{\text{1bm}}^{\text{loose}}$	1	0
$N_{\text{1bm}}^{\text{tight}}$	1	0
	Rejection (DELC3)	
N_1	6483	12850
N_2	0	2
R_{DELC3}	6483 ± 6483	6425 ± 4543
	Rejection (DELC6)	
N_1	3913	7780
N_2	0	1
R_{DELC6}	3913 ± 3913	7780 ± 7780
	Background	
$bg_{\text{1bm}}^{\text{loose}}$	0.00046 ± 0.00046	0.00023 ± 0.00023
$bg_{\text{1bm}}^{\text{tight}}$	0.00046 ± 0.00046	0.00019 ± 0.00019

Table 4.13: Summary of the single-beam background evaluation. Note that for the 1/3 data set, the rejection of DELC6 was lower than DELC3 due to statistical limitations. For this reason, the rejection of DELC3 from the 1/3 data set was used when determining $bg_{\text{1bm}}^{\text{tight}}$. See Figure 4.12 for definitions of N_1 and N_2 for R_{DELC3} and R_{DELC6}. Table reproduced from [56].

Single-Beam Bifurcations

VALID_TRIG, P2TGCUT, B4CCD, B4TRS, BWTRS, UPVTRS, RVTRS, B4ETCON, TGGEO, TGQUALT, TIMCON, TGTCON, PNN2BOX*, *TDCUTS**

Normalization Branch

Rejection Branch

$\overline{\text{DELC3}}$

b4abm_atc < 1.0

B4DEDX, CKTRS, CKTAIL, CPITRS, CPITAIL, PVCUT*, *TGCUTS*

EPITG, TGER, TARGF, TIC, DTGTTP, RTDIF, EPIMAXK, DRP, PHIVTX, EIC, OPSVETO, KIC, TGEDGE, TGZFOOL, TGDEDX, TGLIKE, TGB4, PIGAP, PV90(noTG,noAD)

$N_{1\text{bm}}$

N_1

DELCO*

N_2

$$R_{DELCO^*} = N_1/N_2$$

Figure 4.12: Flowchart showing the single-beam bifurcation branches. Cuts in italics refer to named groups of cuts. Cuts denoted with an '*' indicate that the loose version of the cut was used for the background evaluation in the loose box and the tight version for the background evaluation in the tight box.
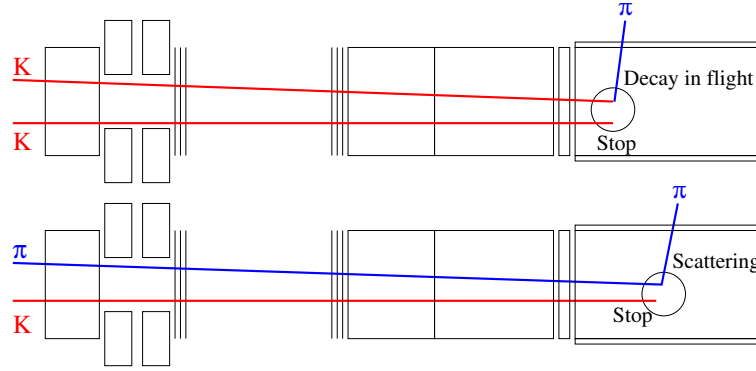
Figure 4.13: A schematic of the double-beam background processes. The top figure shows the *KK* class (kaon-kaon) and the bottom figure the *KP* class (kaon-pion). Figure reproduced from [37].

4.7 Double-Beam Background

Section 4.6 discussed how a single beam pion or decay-in-flight kaon could become single-beam background. The other way that a scattered beam pion or decay-in-flight kaon could become background was if it was missed by the beam-line detectors and an earlier beam kaon satisfied the kaon requirements in the beam-line detectors. For this type of event to become background, the decay products of the early kaon had to be missed and the scattered beam pion or decay-in-flight kaon had to be missed by the beam-line detectors. This type of background was referred to as double-beam background and was subdivided into two classes. The first class, *KK*, was an early kaon followed by a decay-in-flight kaon. The second class, *KP*, was an early kaon followed by a scattered beam pion. Schematic representations of these two double-beam background processes are shown in Figure 4.13. The discrimination between pions and kaons by the Čerenkov counters allowed the two classes of double-beam background, *KK* and *KP*, to be evaluated separately.

4.7.1 Double-Beam Normalization Branch

The bifurcation cut (CUT1$_{KK}$) for the *KK* double-beam normalization branch, used to select events with an early kaon followed by a decay-in-flight kaon, was the collection of

cuts CKTRS, CKTAIL and BWTRS. For the KP double-beam normalization branch, the bifurcation cut (CUT1$_{KP}$) used to select events with an early kaon followed by a scattered beam pion, was the collection of cuts CPITRS, CPITAIL and BWTRS. The Active Degrader (ADPV) and target photon veto (TGPV) subsystems were excluded from the initial application of the photon veto in these normalization branches as indicated by the notation "noTG, noAD". Both of these subsystems were applied as part of the secondary bifurcations of these normalization branches.

Due to low statistics, each of the normalization branches were bifurcated into two branches containing uncorrelated sets of cuts. The notation is shown for the KK class, but this can be replaced with KP for the early kaon followed by a scattered beam pion class of double-beam background. The first branch consisted of B4TRS, B4CCD, TGGEO, B4DEDX, the target photon veto TGPV, and the target-quality cuts $TGCUTS$ excluding EPITG, DTGTTP, RTDIF, DRP, EIC, TIC, TGER and KIC. The number of events remaining after these cuts were applied was called n_{KK}. The second branch measured the rejection r_{KK} of the active degrader ADPV. The final normalization N_{KK} was then defined as

$$N_{KK} = \frac{n_{KK}}{r_{KK}}. \tag{4.17}$$

Figure 4.14 shows the schematic representation of the double-beam normalization branches and the results for the measurements on this normalization branch are shown in Tables 4.14 and 4.15.

4.7.2 Double-Beam Rejection Branch

For both the KK and KP classes of double-beam background, the bifurcation cut used to create the rejection sample (CUT2) was the pair of cuts B4TRS and B4CCD. It was assumed that the B4 counters used for CUT2 were uncorrelated with the beam wire chambers and Čerenkov counters used for CUT1 due to the multiple scattering that

occurred in the degraders between the two sets of systems. Inverting CUT2 selected events that had activity in the B4 counters at $\mathtt{t_{rs}}$, the time of the charged track in the Range-Stack. The sample of events created by inverting CUT2 was contaminated by decays from stopped kaons where one of the decay products was directed upstream and detected by the B4 counters. To correctly measure the rejections of CUT1$_{KK}$ and CUT1$_{KP}$, a sample of pure double-beam events was desired so KPIGAP was applied after CUT2 was inverted to remove the contamination due to stopped kaon decays in the rejection sample. The cut KPIGAP required that kaon and pion clusters in the target were spatially disconnected, thus applying this cut selected events that were geometrically inconsistent with the decay of a single stopped K^+. The rejection of CUT1$_{KK}$ and CUT1$_{KP}$ for this subset of spatially disconnected double-beam events was expected to be consistent with the rejection of these cuts for all double-beam events since there was no significant correlation of these cuts with the proximity of the double-beam particles.

To select the KK class of events in the rejection branch, the Čerenkov pion-veto cuts CPITRS and CPITAIL were applied. This sample of KK events was further purified by requiring that the energy deposited in the B4 by the second beam particle at Range-Stack time $\mathtt{b4ars}$ was consistent with the energy deposited by a kaon (between 1.1 and 5.0 MeV).

To select KP events in the rejection branch, the Čerenkov kaon-veto cuts CKTRS and CKTAIL were applied. This sample of KP events was further purified by requiring that $\mathtt{b4ars}$ was consistent with the energy deposited by a pion (less than 1.1 MeV).

After each of the KK and KP rejection branch samples were purified, the rejections of CUT1$_{KK}$ and CUT1$_{KP}$ were measured. Figure 4.15 shows the schematic representation of the double-beam rejection branches and the results for the measurements on this rejection branch are shown in Tables 4.14 and 4.15.

Double-Beam Normalization Branches

VALID_TRIG, P2TGCUT, PNN2BOX*, *KINCUTS*, DELCO*, TGQUALT, TIMCON, UPVTRS, RVTRS, TGTCON, B4ETCON

PVCUT*(noTG,noAD), *TDCUTS**, EPITG, DTGTTP, RTDIF, DRP, EIC, TIC, TGER, KIC

KK Branch

KP Branch (early runs only)

CPITRS, CPITAIL

CKTRS, CKTAIL

$\overline{\text{CKTRS} \cdot \text{CKTAIL} \cdot \text{BWTRS}}$

$\overline{\text{CPITRS} \cdot \text{CPITAIL} \cdot \text{BWTRS}}$

B4TRS, B4CCD, TGGEO, B4DEDX, TGPV*, *TGCUTS* (excluding EPITG, DTGTTP, RTDIF, DRP, EIC, TIC, TGER, KIC)

N_1

ADPV

N_2

B4TRS, B4CCD, TGGEO, B4DEDX, TGPV*, *TGCUTS* (excluding EPITG, DTGTTP, RTDIF, DRP, EIC, TIC, TGER, KIC)

N_3

ADPV

N_4

n_{KK} $r_{KK} = N_1/N_2$ n_{KP} $r_{KP} = N_3/N_4$

Figure 4.14: Flowchart showing the double-beam normalization branches Cuts in italics refer to named groups of cuts. Cuts denoted with an '*' indicate that the loose version of the cut was used for the background evaluation in the loose box and the tight version for the background evaluation in the tight box.

4.7.3   Double-Beam Background Evaluation

The *KP* background evaluation had an additional complication due to the addition of the Čerenkov pion-veto to the PNN2 trigger part of the way through data collection (see Section 2.7.1). Due to the lack of statistics for *KP*-type events after this trigger change, the *KP* background was evaluated using events before the trigger change and scaled to represent the entire run. This scaling was done using the inverse of the fraction of the

total KB_{live} before the trigger change $f_{KB_{live}}^{before}$,

$$f_{scale} = 1/f_{KB_{live}}^{before}$$
$$= 1/0.394 \tag{4.18}$$
$$= 2.54,$$

where the value for $f_{KB_{live}}^{before}$ was taken from [72]. To verify the method of applying the scaling factor to a subset of the run for the KP double-beam background evaluation, two additional measurements were performed to show that these backgrounds were consistent before and after the trigger change, as detailed in [72]. The first was to use only the PNN1 trigger to evaluate the KP double-beam background before and after the PNN2 trigger change. The second was to evaluate the KK double-beam before and after the PNN2 trigger change. When scaling each of these measurements to the full run, each of these measurements found the backgrounds to be consistent before and after the PNN2 trigger change. Figure 4.15 shows the schematic representation of the double-beam bifurcations and Table 4.15 the results for the measurements on this rejection branch.

The KK double-beam background bg_{KK} was written as

$$bg_{KK} = \frac{N_{KK}}{R_{KK} - 1}, \tag{4.19}$$

where N_{KK} was the number of events left at the end of the KK class double-beam normalization branch and R_{KK} was the rejection of $CUT1_{KK}$ (BWTRS, CKTRS and CKTAIL). The KP double-beam background bg_{KP} was written as

$$bg_{KP} = f_{scale} \times \frac{N_{KP}}{R_{KP} - 1}, \tag{4.20}$$

where N_{KP} was the number of events left at the end of the KP class double-beam normalization branch, R_{KP} was the rejection of $CUT1_{KP}$ (BWTRS, CPITRS and CPITAIL),

123

	Loose		Tight	
	1/3	2/3	1/3	2/3
Normalization				
n_{KK}	0	0	0	0
N_1	1363	2699	212	462
N_2	182	325	22	48
r_{KK}	7.49±0.52	8.30±0.43	9.64±1.94	9.62±1.32
N_{KK}	0.134±0.134	0.120±0.120	0.104±0.104	0.104±0.104
Rejection				
N_5	790	1576	148	269
N_6	7	4	1	1
R_{KK}	113±43	394±197	148±148	269±269
Background				
	1/3		2/3	
bg_{KK}^{loose}	0.00359±0.00359		0.00046±0.00046	
bg_{KK}^{tight}	0.00212±0.00212		0.00058±0.00058	

Table 4.14: The summary of the double-beam KK-background evaluation. See Figures 4.14 and 4.15 for definitions of the normalization and rejection quantities, respectively. Table reproduced from [56].

and f_{scale} was the scaling factor applied so that the background evaluation as measured before the trigger change represented the entire run. These expressions describe both the loose and tight background evaluations for both double-beam classes.

	Loose		Tight	
	1/3	2/3	1/3	2/3
	Normalization			
n_{KP}	0	0	0	0
N_3	2289	4435	494	939
N_4	221	464	36	92
r_{KP}	10.36±0.66	9.56±0.42	13.72±2.20	10.21±1.01
N_{KP}	0.097±0.097	0.105±0.105	0.073±0.073	0.098±0.098
	Rejection			
N_7	1179	2467	261	541
N_8	2	4	0	0
R_{KP}	590±417	617±308	261±261	541±541
	Background			
	1/3		2/3	
bg_{KP}^{loose}	0.00126±0.00126		0.00065±0.00065	
bg_{KP}^{tight}	0.00095±0.00095		0.00069±0.00069	

Table 4.15: The summary of the double-beam KP-background evaluation. See Figures 4.14 and 4.15 for definitions of the normalization and rejection quantities, respectively. Table reproduced from [56].

	Loose		Tight	
	1/3	2/3	1/3	2/3
bg_{KK}	0.00359±0.00359	0.00046±0.00046	0.00212±0.00212	0.00058±0.00058
bg_{KP}	0.00126±0.00126	0.00065±0.00065	0.00095±0.00095	0.00069±0.00069
$bg_{\text{2bm}}(\text{total})$	0.00485±0.00380	0.00111±0.00080	0.00307±0.00232	0.00127±0.00090

Table 4.16: The summary of the total expected double-beam background.
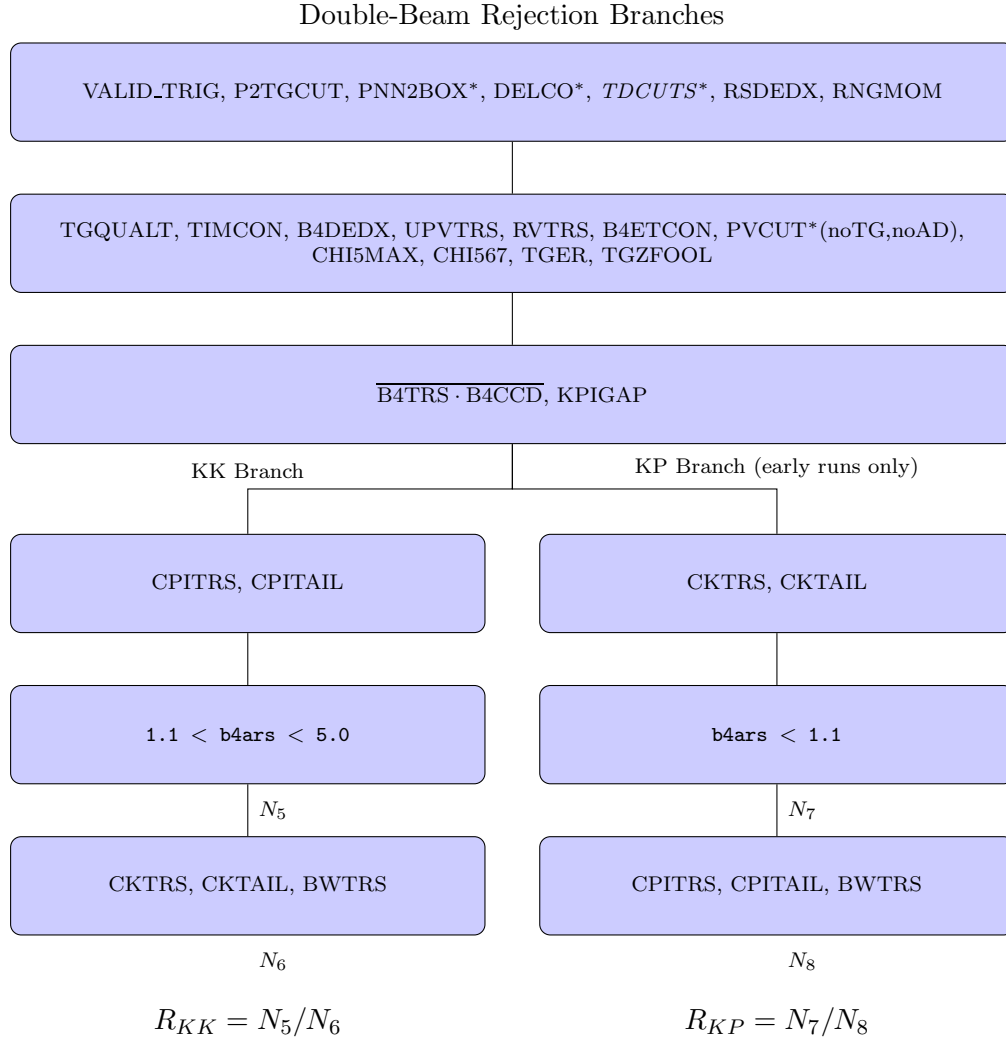
Figure 4.15: Flowchart showing the double-beam rejection branches. Cuts in italics refer to named groups of cuts. Cuts denoted with an '*' indicate that the loose version of the cut was used for the background evaluation in the loose box and the tight version for the background evaluation in the tight box.
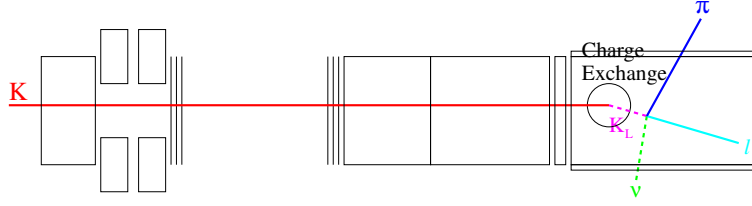
Figure 4.16: A schematic of the problematic semileptonic charge-exchange background processes $K_L^0 \to \pi^+ e^- \nu_e$ and $K_L^0 \to \pi^+ \mu^- \nu_\mu$. Figure reproduced from [37].

4.8 Charge Exchange Background

The charge-exchange (CEX) background came from the charge exchange interaction $K^+ n \to K^0 p$. The K^0 could be either the shorter lifetime K_S^0 state (0.1 ns) or the longer lifetime K_L^0 state (51 ns). Through oscillation of the K^0 to $\bar{K}^0$, it is also possible for hyperon (a strange baryon) production to become another charge exchange background source. This mode is discussed in more detail in Section 4.8.4.

The main K_S^0 decay channel that could simulate $K^+ \to \pi^+ \nu \bar{\nu}$ was $K_S^0 \to \pi^+ \pi^-$. Since it is such a prompt decay, it was very heavily suppressed by the delayed coincidence cut DELCO and any contributions to background from these K_S^0 decays were determined as part of the single-beam background estimation (see Section 4.6).

The more problematic K_L^0 decay modes were the semileptonic decays $K_L^0 \to \pi^+ e^- \nu_e$ and $K_L^0 \to \pi^+ \mu^- \nu_\mu$ with branching ratios of 40.56% and 27.05%, respectively [99], where these branching ratios are for the sum of the possible charge states for each decay mode. The kinematics of the decay π^+ from these decay modes fell inside the kinematic signal region used for this analysis. A schematic representation of these semileptonic decays is shown in Figure 4.16.

The two main methods of suppressing the problematic K_L^0 decay modes were (1) detection of the excess energy deposited in the target from the negatively charged lepton, and (2) identification of gaps between the incoming kaon and outgoing pion tracks in the target. Due to the longer life (51 ns) and non-interacting nature of the K_L^0, there was a gap between where the kaon track ended and where the outgoing (daughter) pion track

127

began.

4.8.1 Method Used to Evaluate CEX Background

To effectively use the bifurcation method on data, two uncorrelated sets of inverted cuts need to be able to isolate the background in question. The only cut that was capable of isolating this background was TARGF, which identified gaps greater than one fiber width (0.6 cm) between the kaon and pion fiber clusters. Any cuts that detected the excess energy deposited in the target suppressed many different backgrounds and could not have been inverted to isolate only the CEX background.

The background evaluation for CEX varied slightly from the bifurcation method used for most of the other backgrounds (see Section 3.2.2), but it also relied on geometric arguments to determine the number of background events without examining the signal region. A schematic representation of this background evaluation is shown in Figure 4.17.

The normalization branch was created by applying KPIGAP (a tighter version of $\overline{\text{TARGF}}$) using data with N_{KPIGAP} events left at the end of the branch. Using Monte Carlo, the normalization branch was reproduced using the cuts available to Monte Carlo with M_{KPIGAP} events remaining at the end of the branch. A similar branch was created in Monte Carlo using the TARGF cut instead of KPIGAP, with M_{TARGF} events remaining after TARGF has been applied. Measurement of the number of events N_{TARGF} that would remain in the data study if TARGF were applied instead of KPIGAP was forbidden since it would have involved examining the signal region. Instead geometric arguments were used to show that the following ratios were equal for the number of events remaining after each of TARGF or KPIGAP were applied in the data and Monte Carlo studies:

$$\frac{N_{\text{TARGF}}}{N_{\text{KPIGAP}}} = \frac{M_{\text{TARGF}}}{M_{\text{KPIGAP}}}. \tag{4.21}$$

To retain statistics in measuring N_{KPIGAP}, two groups of cuts were excluded from this

128
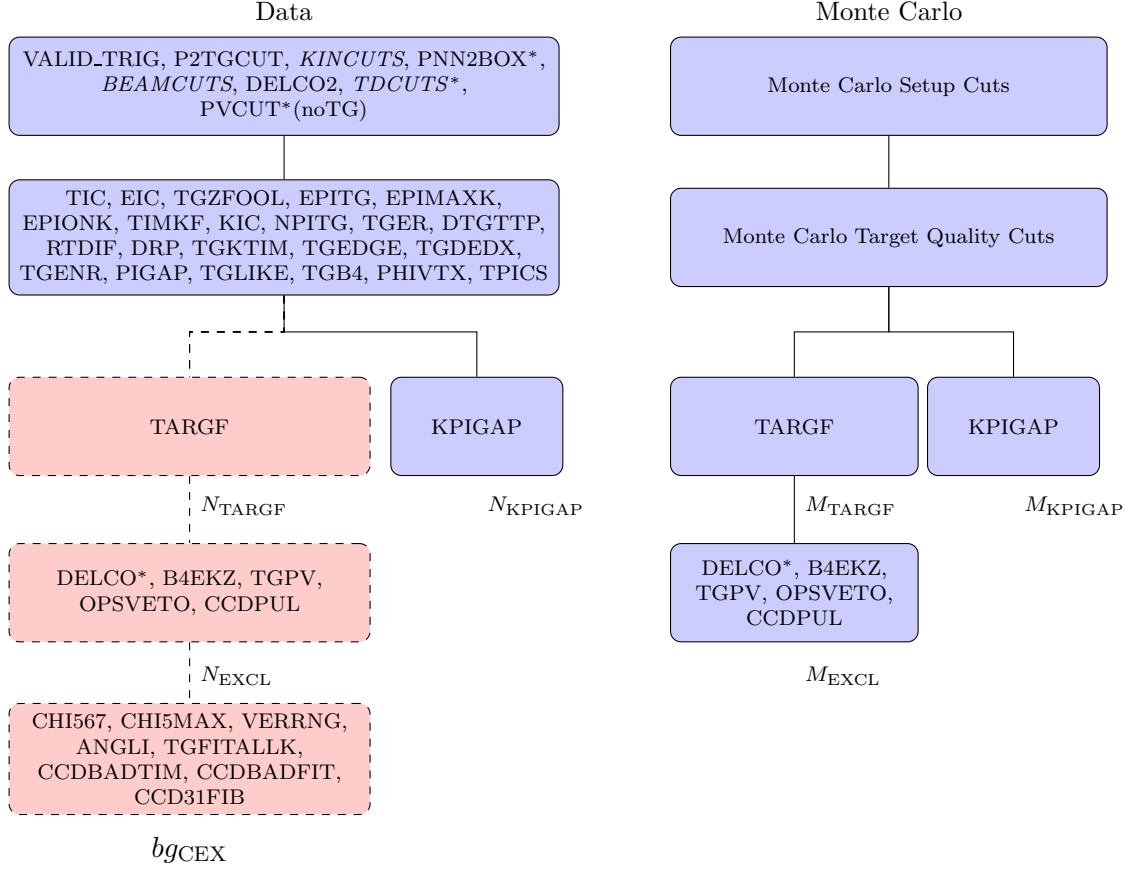
Figure 4.17: Flowchart showing the charge-exchange data and Monte Carlo branches. Cuts in italics refer to named groups of cuts. Cuts denoted with an '*' indicate that the loose version of the cut was used for the background evaluation in the loose box and the tight version for the background evaluation in the tight box. The dashed boxes indicate a branch inaccessible to data due to being in the signal region. Instead the measurements were performed on an equivalent branch using Monte Carlo.

normalization branch. The first group consisted of cuts where CEX events were expected to have rejection above the acceptance loss of signal-like events: DELCO, B4EKZ, TGPV, OPSVETO and CCDPUL. The rejection of these cuts was measured on the M_{TARGF} events remaining after TARGF was applied in the Monte Carlo study:

$$R_{\mathrm{EXCL}} = \frac{M_{\mathrm{TARGF}}}{M_{\mathrm{EXCL}}}. \tag{4.22}$$

The second group consisted of cuts where the CEX events were expected to behave like

signal events and thus the measured acceptance losses of these cuts (Section 6.1.3) were used. These cuts were CHI567, CHI5MAX, VERRNG, ANGLI, TGFITALLK, CCD-BADTIM, CCDBADFIT and CCD31FIB, and their combined acceptance will be referred to as A_{loss}. The background level bg_{CEX} in the signal region was determined by correcting the calculated number of events N_{TARGF} for the performance of the cuts excluded from the normalization branch,

$$bg_{\text{CEX}} = \frac{A_{\text{loss}}}{R_{\text{EXCL}}} \times N_{\text{TARGF}}. \tag{4.23}$$

Combining the expressions from Equations (4.21), (4.22) and (4.23) the expression for the background can be written as

$$bg_{\text{CEX}} = N_{\text{KPIGAP}} \times \frac{M_{\text{EXCL}}}{M_{\text{KPIGAP}}} \times A_{\text{loss}}. \tag{4.24}$$

4.8.2 The CEX Monte Carlo Study

The branches of the CEX Monte Carlo study were evaluated using approximately 3.42×10^8 $K_L^0 \to \pi^+ \mu^- \bar{\nu}_\mu$ events in Monte Carlo. These events were generated with production points, momentum distributions, and corresponding B4 and kaon fiber information from $K_S^0 \to \pi^+\pi^-$ data [92]. Figure 4.17 shows the cuts applied to measure the quantities M_{KPIGAP} and M_{EXCL}.

The measurement of the quantity M_{EXCL} involved simulating the performance of the cuts TGPV, OPSVETO and CCDPUL. The same method as described for the K_{e4} background (Section 4.5.2) was used to determine the systematic uncertainty associated with the possible mismatch between the target-fiber energy scale in Monte Carlo and data. The Monte Carlo simulation energy T_{xtg} was the total energy deposited in photon veto and opposite-side pion fibers and was varied over the range of 0.6 to 1.8 MeV. This energy was used to simulate the performance of TGPV and OPSVETO. The Monte Carlo simulation energy E_{hide} was the total energy deposited in the kaon fibers from the K_L^0 decay

130

	Loose	Tight
	Data	
$N_{\mathrm{KPIGAP}}(1/3)$	3	1
$N_{\mathrm{KPIGAP}}(2/3)$	0	0
	Monte Carlo	
M_{EXCL}	50^{+33}_{-10}	6^{+6}_{-2}
M_{KPIGAP}	4136	3332
	Acceptance Loss	
A_{loss}	0.687 ± 0.001	0.687 ± 0.001
	Background	
$bg(1/3)$	$0.076 \pm 0.044^{+0.058}_{-0.015}$	$0.0038 \pm 0.0038^{+0.0038}_{-0.0013}$
$bg(2/3)$	$0.013 \pm 0.013^{+0.010}_{-0.003}$	$0.0019 \pm 0.0019^{+0.0019}_{-0.0006}$

Table 4.17: The summary of the charge-exchange background evaluation. Values for M_{EXCL} and M_{KPIGAP} taken from [55]. See Figure 4.17 for definitions of the measured quantities N_{KPIGAP}, M_{EXCL} and M_{KPIGAP}.

products and was varied over the range of 1.5 to 5.0 MeV. The values of "$\mathtt{T_{xtg}} = 1.2$ MeV" and "$\mathtt{E_{hide}} = 2.5$ MeV" were used to determine the mean number of events M_{EXCL} and the variations due to the ranges of $\mathtt{T_{xtg}}$ and $\mathtt{E_{hide}}$ were used to determine the systematic uncertainty. Table 4.17 shows a summary of results of these measurements made on the KPIGAP and TARGF branches using Monte Carlo.

4.8.3   CEX Background Evaluation

Equation (4.24) shows the expression used to evaluate the CEX background level using a combination of data and Monte Carlo. Table 4.17 summarizes the results of this background evaluation, where the results for the 1/3 and 2/3 data sets are scaled to represent the entire data set.

4.8.4 Hyperon Background

This section discusses the method by which hyperon production can become a background process and presents arguments as to why the existing charge exchange background estimate takes hyperon production into account.

The production of hyperons is a multi-stage process. First, a K^0 is produced via the charge exchange interaction $K^+ n \rightarrow K^0 p$. Next, the K^0 oscillates to $\bar{K}^0$ [49], which contains a strange quark. The $\bar{K}^0$ can then interact with a nucleon (N), producing a hyperon (Y) and pion:

$$\bar{K}^0 + N \rightarrow Y + \pi. \tag{4.25}$$

There are a number of processes by which a π^+ having a momentum which overlaps the PNN2 region can be produced:

$$
\begin{aligned}
\overline{K^0} + p &\rightarrow \pi^0 + \Sigma^+ \rightarrow \pi^0 + (p^+\pi^0 \text{ or } n\pi^+), \\
\dots &\rightarrow \pi^+ + \Sigma^0 \rightarrow \pi^+ + (\Lambda^0\gamma) \rightarrow \pi^+ + ((p^+\pi^- \text{ or } n\pi^0)\gamma), \\
\dots &\rightarrow \pi^+ + \ \Lambda \ \rightarrow \pi^+ + (p^+\pi^- \text{ or } n\pi^0), \\
\overline{K^0} + n &\rightarrow \pi^0 + \Sigma^0 \ \rightarrow \pi^0 + (\Lambda^0\gamma) \rightarrow \pi^+ + ((p^+\pi^- \text{ or } n\pi^0)\gamma), \\
\dots &\rightarrow \pi^- + \Sigma^+ \rightarrow \pi^- + (p^+\pi^0 \text{ or } n\pi^+), \\
\dots &\rightarrow \pi^+ + \Sigma^- \rightarrow \pi^+ + (n\pi^-),
\end{aligned}
\tag{4.26}
$$

where the Σ and Λ particles are hyperons.

The cross-sections for hyperon production are not well determined. At a K_L^0 momentum of 168 MeV/c, the total cross-section is 481 mb/(carbon nucleus) and 70 mb/H [91]. This agrees well with a total hyperon production cross-section of 90 mb per proton for K^- at 160 MeV/c [75], where the K^- and K_L^0 cross-sections are expected to have only small differences due to isospin differences and electromagnetic effects. According to [75], the K_L^0 cross-sections should approximately double in the lower momentum region of 0 to 100

MeV/c. Based on this information and an assumption of an entirely polystyrene target, the mean free path of the $\bar{K}^0$ in the target was estimated to be between 37.3 and 75.6 cm, which corresponds to a survival probability of 73% to 85% after the $\bar{K}^0$ travels 6 cm in the target [56]. As a result the KPIGAP cut, which selected events with a gap between the incoming kaon and outgoing pion tracks, should have been effective at selecting both the semi-leptonic K_L^0 and hyperon production events. Thus the charge exchange normalization branch should have consisted of both these types of events. Similar to the K^0 case, only the long-lived component of the $\bar{K}^0$ results in potential background processes due to the delayed coincidence cut DELCO removing the short-lived component.

The rejection of TGPV, CCDPUL and OPSVETO was estimated using the semi-leptonic K_L^0 decays in simulation. For the hyperon production events, particles such as π^-, Σ and Λ were also produced. Due to their relatively short lifetimes, it is expected that they would deposit their energy in the target and thus be rejected by TGPV, CCDPUL and OPSVETO. Thus the rejection of TGPV, CCDPUL and OPSVETO for charge exchange events, determined in Section 4.8.2, should underestimate the rejection power of these cuts on hyperon events. Based on the above arguments and the large systematic error associated with the rejection of TGPV, CCDPUL and OPSVETO, it was decided that the estimation of the charge exchange background presented in this section also takes hyperon production into account.

4.9 Other Backgrounds

The previous sections in this chapter discussed the backgrounds which were identified as being significant sources of background for this analysis. Table 4.18 shows a list of K^+ decays which could have contributed to backgrounds in the PNN2 region. This list contains both decays which were considered in background studies earlier in the chapter and decays which were considered to have negligible contributions to the background due to the following reasons:

- Many decay modes were excluded due to the charged products being kinematically excluded from the signal region by having kinematic quantities lower than the ranges covered by the kinematic signal region PNN2BOX. Products from K^+ decays-in-flight could have been boosted into the kinematic signal region, but these types of events were accounted for in the single- and double-beam studies.

- Decays having three or more photons and no π^+ had small branching ratios. The combination of photon veto and $\pi^+ \rightarrow \mu^+ \rightarrow e^+$ particle identification suppressed these backgrounds to a level where they were not considered significant sources of background.

- Decay modes having only an e^+ and no π^+ or μ^+ were highly suppressed by the $\pi^+ \rightarrow \mu^+ \rightarrow e^+$ decay sequence conditions and dE/dx measurements.

- The remaining decay modes were heavily suppressed by having a combination of multiple charged products, photons against which to veto, $\pi^+ \rightarrow \mu^+ \rightarrow e^+$ particle identification where no decay π^+ was present, and very small branching ratios.

Background	Branching Ratio	Kinematically Excluded	Extra TG Energy	Fails π^+ ID	Number of Photons
$K^+ \to \mu^+\nu$	0.6344	✓		✓	
$K^+ \to \pi^+\pi^0$	0.2092	✓			2
$K^+ \to \pi^+\pi^+\pi^-$	0.0559	✓	✓		
$K^+ \to \pi^0 e^+\nu$	0.0498			✓	2
$K^+ \to \pi^0 \mu^+\nu$	0.0332			✓	2
$K^+ \to \pi^+\pi^0\pi^0$	0.01757	✓			4
$K^+ \to \mu^+\nu\gamma$	0.0062			✓	1
$K^+ \to \pi^+\pi^0\gamma$	0.000275				3
$K^+ \to \pi^0 e^+\nu\gamma$	0.000269			✓	3
$K^+ \to \pi^+\pi^+\pi^-\gamma$	0.000104	✓	✓		1
$K^+ \to \pi^+ 3\gamma$	< 0.0001				3
$K^+ \to e^+\nu\nu\bar{\nu}$	< 0.00006			✓	
$K^+ \to \pi^+\pi^- e^+\nu$	0.0000409		✓		
$K^+ \to \pi^0 \mu^+\nu\gamma$	0.000024			✓	3
$K^+ \to \pi^0\pi^0 e^+\nu$	0.000022			✓	4
$K^+ \to e^+\nu$	0.0000155	✓		✓	
$K^+ \to e^+\nu\gamma$	0.0000152			✓	1
$K^+ \to \pi^+\pi^- \mu^+\nu$	0.000014		✓		
$K^+ \to \pi^+\pi^0\pi^0\gamma$	0.0000076	✓			5
$K^+ \to \mu^+\nu\nu\bar{\nu}$	< 0.000006			✓	
$K^+ \to \pi^0\pi^0 e^+\nu\gamma$	< 0.000005			✓	4
$K^+ \to \pi^0\pi^0\pi^0 e^+\nu$	< 0.0000035	✓		✓	6
$K^+ \to \pi^+\gamma\gamma$	0.00000110				2
$K^+ \to \mu^+\nu e^+ e^-$	0.000000071		✓	✓	
$K^+ \to \mu^+\nu\mu^+\mu^-$	< 0.00000041		✓	✓	
$K^+ \to e^+\nu e^+ e^-$	0.000000025		✓	✓	
$K^+ \to e^+\nu\mu^+\mu^-$	0.000000017		✓	✓	

Table 4.18: Various K^+ decays with their branching ratios [99]. A ✓ in the column "Kinematically Excluded" indicates that the process is kinematically excluded from the PNN2 signal region. A ✓ in the column "Extra TG Energy" indicates that the decay is suppressed by cuts that reject events with additional energy in the target. A ✓ in the column "Fails π^+ ID" that there is no π^+ in the final state and thus is suppressed by the $\pi^+ \to \mu^+ \to e^+$ decay-sequence cuts. The right-most column indicates the number of photons in the final state.

Loose	1/3			2/3		
$K_{\pi 2}$ TG-scatter	0.537	± 0.188	$^{+0.069}_{-0.215}$	0.619	± 0.150	$^{+0.067}_{-0.100}$
$K_{\pi 2}$ RS-scatter	0.0220	± 0.0056	$^{+0.0021}_{-0.0021}$	0.0303	± 0.0054	$^{+0.0038}_{-0.0039}$
$K_{\pi 2\gamma}$	0.0514	± 0.0086	$^{+0.0042}_{-0.0038}$	0.0757	± 0.0073	$^{+0.0062}_{-0.0056}$
Muon	0.0246	± 0.0246		0.0114	± 0.0114	
K_{e4}	0.235	± 0.118	$^{+0.310}_{-0.166}$	0.176	± 0.072	$^{+0.233}_{-0.124}$
Single-Beam	0.00046	± 0.00046		0.00023	± 0.00023	
Double-Beam	0.00485	± 0.00380		0.00111	± 0.00080	
CEX	0.076	± 0.044	$^{+0.058}_{-0.015}$	0.013	± 0.013	$^{+0.010}_{-0.003}$
Total	0.951	± 0.228	$^{+0.443}_{-0.402}$	0.927	± 0.168	$^{+0.320}_{-0.237}$

Table 4.19: The summary of the total expected background in the loose signal region from the various components.

4.10 Background Summary

The evaluation of the final background levels came from the 2/3 sample with the results from the 1/3 sample providing a check against large biases introduced when tuning the cuts. The total background level in the loose signal region was estimated to be $0.927 \pm 0.168\,^{+0.320}_{-0.237}$ and in the tight signal region $0.144 \pm 0.045\,^{+0.095}_{-0.032}$, where the first uncertainty is statistical and the second systematic. Recall that the signal region was divided into nine cells (see Section 7.1) and the cell designed to have the highest signal-to-background was designated the tight signal region. Tables 4.19 and 4.20 summarize the background levels for both data sets in the loose and tight signal regions, respectively. Results from both data sets were scaled to represent the entire data set. The individual and total background levels were statistically consistent between the 1/3 and 2/3 data sets.

Tight	1/3			2/3		
$K_{\pi2}$ TG-scatter	0.106	±0.059	$^{+0.076}_{-0.024}$	0.095	±0.041	$^{+0.020}_{-0.016}$
$K_{\pi2}$ RS-scatter	0.0043	±0.0019	$^{+0.0004}_{-0.0005}$	0.0069	±0.0019	$^{+0.0007}_{-0.0009}$
$K_{\pi2\gamma}$	0.0121	±0.0038	$^{+0.0010}_{-0.0010}$	0.0188	±0.0034	$^{+0.0016}_{-0.0014}$
Muon	0.0055	±0.0055		0.0037	±0.0037	
K_{e4}	0.034	±0.034	$^{+0.142}_{-0.026}$	0.017	±0.017	$^{+0.071}_{-0.013}$
Single-Beam	0.00046$\pm$0.00046			0.00019$\pm$0.00019		
Double-Beam	0.00212$\pm$0.00212			0.00058$\pm$0.00058		
CEX	0.0038	±0.0038	$^{+0.0038}_{-0.0013}$	0.0019	±0.0019	$^{+0.0019}_{-0.0006}$
Total	0.177	±0.069	$^{+0.223}_{-0.053}$	0.144	±0.045	$^{+0.095}_{-0.032}$

Table 4.20: The summary of the total expected background in the tight signal region from the various components.

Chapter 5

Validity Checks

The validity studies detailed in this chapter were used to verify the reliability of the analysis strategy as motivated in Section 3.2.4.

5.1 Outside-the-Box Studies

The general method used to evaluate the number of events in the outside-the-box region is described here, with the details of each individual outside-the-box study described in its own respective section. These outside-the-box studies tested the assumption that the bifurcation cuts, used to estimate a given background, were uncorrelated.

The outside-the-box studies involved loosening either set of bifurcation cuts used for the $K_{\pi2}$ target-scatter background evaluation: the photon veto or the "EPI" cuts collection of cuts: CCDBADFIT, CCDBADTIM, CCDPUL and EPIONK. With the cuts loosened, the $K_{\pi2}$ target-scatter, Range-Stack-scatter and $K_{\pi2\gamma}$ backgrounds were re-evaluated. The remaining backgrounds were scaled using appropriate acceptance loss factors from the loosened and nominal levels of the cuts.

The estimate of the total background level in the outside-the-box region was taken as the difference between the total background level evaluated with the loosened cuts and

the total background level in the signal region. The 2/3 data set was used for all outside-the-box background evaluations. The number of events in the outside the box region was measured directly using the full data set and compared to the outside-the-box estimate.

Three outside-the-box studies were performed, examining the following regions:

- **PV1** - Between the loose photon veto PV60 and the very loose photon veto PV90, where the "60" or "90" refers to the fact that the parameters for the photon veto were optimized to accept approximately 60% or 90% of the signal-like events;

- **PV2** - Between the very loose photon veto PV90 and the even looser PNN1-level photon veto PVPNN1;

- **EPI** - Between the pion energy thresholds of 1.25 MeV and 2.5 MeV for the cuts CCDBADFIT, CCDBADTIM, CCDPUL and EPIONK.

Note that for all of these studies, the $K_{\pi 2\gamma}$ background contributed only to the uncertainty and not the central value of the total outside-the-box background estimates due to the way the correction to the $K_{\pi 2}$ target-scatter background due to $K_{\pi 2\gamma}$ contamination was applied (see Section 4.1.5).

5.1.1 PV1 Region

For many of the backgrounds, loosening the photon veto increased the background by the ratio of the acceptance of PV90 to PV60. These backgrounds were K_{e4}, CEX, muon and beam and the scaling factor was given by

$$\frac{A(\text{PV90})}{A(\text{PV60})} = \frac{0.8855}{0.6199} = 1.428. \tag{5.1}$$

For the remaining backgrounds, the new background level due to loosening of the photon veto was evaluated using PV90 instead of PV60. Table 5.1 shows the backgrounds due to PV60, PV90 and the resulting PV1 outside-the-box background.

Background	PV60	PV90	OTB (PV1)
$K_{\pi 2}$-tgscat	$0.695 \pm 0.150\,^{+0.061}_{-0.094}$	$9.58 \pm 0.63\,^{+1.13}_{-1.00}$	$8.89 \pm 0.64\,^{+1.23}_{-1.06}$
$K_{\pi 2}$-rsscat	$0.030 \pm 0.005\,^{+0.004}_{-0.004}$	$0.143 \pm 0.022\,^{+0.018}_{-0.018}$	$0.113 \pm 0.023\,^{+0.022}_{-0.022}$
$K_{\pi 2\gamma}$	$0.076 \pm 0.007\,^{+0.006}_{-0.006}$	$0.357 \pm 0.016\,^{+0.029}_{-0.026}$	$0.281 \pm 0.018\,^{+0.023}_{-0.020}$
K_{e4}	$0.176 \pm 0.072\,^{+0.233}_{-0.124}$	$0.251 \pm 0.103\,^{+0.333}_{-0.177}$	$0.075 \pm 0.031\,^{+0.100}_{-0.053}$
CEX	$0.013 \pm 0.013\,^{+0.010}_{-0.003}$	$0.019 \pm 0.019\,^{+0.014}_{-0.004}$	$0.006 \pm 0.006\,^{+0.004}_{-0.001}$
Muon	0.0114 ± 0.0114	0.0163 ± 0.0163	0.0049 ± 0.0049
1bm	0.00023 ± 0.00023	0.00033 ± 0.00033	0.00010 ± 0.00010
2bm-KK	0.00046 ± 0.00046	0.00065 ± 0.00065	0.00020 ± 0.00020
2bm-KP	0.00065 ± 0.00065	0.00093 ± 0.00093	0.00028 ± 0.00028
Total	$0.93 \pm 0.17\,^{+0.31}_{-0.23}$	$10.02 \pm 0.64\,^{+1.53}_{-1.23}$	$9.09 \pm 0.65\,^{+1.38}_{-1.15}$

Table 5.1: Summary of the PV1 Outside-the-Box Study. Scaling by a factor of $A(\text{PV90})/A(\text{PV60}) = 0.8855/0.6199 = 1.428$ was used for the K_{e4}, CEX, muon and beam backgrounds. The remaining backgrounds were re-evaluated using PV90. For values having two sets of uncertainties, the first is statistical and the second systematic. The central value for $K_{\pi 2\gamma}$ was treated as zero as the contribution due to this background was included in the $K_{\pi 2}$ target-scatter value.

The total number of background events predicted in the PV1 outside-the-box study was $N_{pred} = 9.09 \pm 0.65(stat.)\,^{+1.38}_{-1.15}(sys.)$. When the number of events in this region was measured directly, 3 events were found. Treating the central value of 9.09 events as the mean of a Poisson distribution gave a probability of 0.02 of observing 3 or less events. When this probability was re-evaluated at the upper and lower bounds of the total uncertainty of N_{pred}, the probability range was $[0.01, 0.05]$.

To help determine if this lower than expected number of events was a statistical anomaly or an indication of anti-correlation between the photon veto and EPI cuts, this outside-the-box study was repeated looking at the region between the PV90 and the PNN1-level photon veto PVPNN1.

5.1.2 PV2 Region

This study examined the outside-the-box region between PV90 and PVPNN1. Scaling was used to determine the background level in the expanded box for K_{e4}, CEX, muon and beam. The scaling factor was

$$\frac{A(\text{PVPNN1})}{A(\text{PV60})} - \frac{A(\text{PV90})}{A(\text{PV60})} = \frac{0.9248}{0.6199} - \frac{0.8855}{0.6199} = 0.064. \tag{5.2}$$

As with the PV1 outside-the-box study, the $K_{\pi2}$-scatter and $K_{\pi2\gamma}$ backgrounds were re-evaluated for the expanded regions. Table 5.2 shows the backgrounds due to PV90, PVPNN1 and the resulting PV2 outside-the-box background.

Background	PV90	PVPNN1	OTB (PV2)
$K_{\pi2}$-tgscat	$9.584 \pm 0.626 \, ^{+1.133}_{-1.000}$	$41.63 \pm 1.74 \, ^{+12.09}_{-6.65}$	$32.04 \pm 1.85 \, ^{+13.09}_{-7.78}$
$K_{\pi2}$-rsscat	$0.143 \pm 0.022 \, ^{+0.018}_{-0.018}$	$0.449 \pm 0.067 \, ^{+0.054}_{-0.056}$	$0.305 \pm 0.070 \, ^{+0.073}_{-0.074}$
$K_{\pi2\gamma}$	$0.357 \pm 0.016 \, ^{+0.029}_{-0.026}$	$1.091 \pm 0.028 \, ^{+0.090}_{-0.079}$	$0.734 \pm 0.018 \, ^{+0.061}_{-0.053}$
K_{e4}	$0.251 \pm 0.103 \, ^{+0.333}_{-0.177}$	$0.266 \pm 0.107 \, ^{+0.348}_{-0.185}$	$0.011 \pm 0.005 \, ^{+0.015}_{-0.008}$
CEX	$0.019 \pm 0.019 \, ^{+0.014}_{-0.004}$	$0.019 \pm 0.019 \, ^{+0.015}_{-0.005}$	$0.0008 \pm 0.0008 \, ^{+0.0006}_{-0.0002}$
Muon	0.0163 ± 0.0163	0.0170 ± 0.0170	0.0007 ± 0.0007
1bm	0.00033 ± 0.00033	0.00034 ± 0.00034	0.00001 ± 0.00001
2bm-KK	0.00065 ± 0.00065	0.00068 ± 0.00068	0.00003 ± 0.00003
2bm-KP	0.00093 ± 0.00093	0.00097 ± 0.00097	0.00004 ± 0.00004
Total	$10.02 \pm 0.64 \, ^{+1.53}_{-1.23}$	$42.38 \pm 1.75 \, ^{+12.60}_{-6.98}$	$32.36 \pm 1.85 \, ^{+13.24}_{-7.92}$

Table 5.2: Summary of the PV2 Outside-the-Box Study. Scaling was used for the K_{e4}, CEX, muon and beam backgrounds. The remaining backgrounds were re-evaluated in both the PVPNN1 and PV90 regions. For values having two sets of uncertainties, the first is statistical and the second systematic. The central value for $K_{\pi2\gamma}$ was treated as zero since the contribution due to this background was included in the $K_{\pi2}$ target-scatter value.

The total number of background events predicted in the PV2 outside-the-box study was $N_{pred} = 32.36 \pm 1.85(stat.) \, ^{+13.24}_{-7.92}(sys.)$. When the number of events in this region was

measured directly, 34 events were found. This number of observed events agrees with the predicted number within statistical uncertainty. Assuming a Poisson distribution of mean 32.36 can be approximated by a Gaussian of mean 32.36 and $\sigma = \sqrt{32.36}$, the probability of observing 34 or fewer events was 0.61. When this probability was re-evaluated at the upper and lower bounds of the total uncertainty of N_{pred}, the probability range was $[0.05, 0.98]$.

5.1.3 EPI Region

For the purpose of this study, the cuts CCDBADFIT, CCDBADTIM, CCDPUL and EPIONK will be called "EPI" cuts. The pion energy threshold for these cuts was loosened from 1.25 MeV ("EPI=1.25") to 2.5 MeV ("EPI=2.5") for this outside-the-box study. Scaling by a factor of

$$\frac{A(\text{EPI} = 2.5)}{A(\text{EPI} = 1.25)} = \frac{0.6862}{0.4576} = 1.4995 \tag{5.3}$$

was used to determine the K_{e4}, CEX, muon and beam backgrounds in the expanded box. The normalization branch for $K_{\pi 2\gamma}$ was re-evaluated and the $K_{\pi 2}$-scatter backgrounds completely re-evaluated to determine the background levels in the expanded box.

Table 5.3 shows the backgrounds due to EPI=1.25, EPI=2.5 and the resulting EPI outside-the-box background.

The total number of background events predicted by the EPI outside-the-box study was $N_{pred} = 0.79 \pm 0.35(stat.)\,^{+0.30}_{-0.37}(sys.)$. When the number of events in this region was measured directly, 0 events were found. Treating the central value of 0.79 events as the mean of a Poisson distribution gave a probability of 0.45 of observing 0 events. When this probability was re-evaluated at the upper and lower bounds of the total uncertainty of N_{pred}, the probability range was $[0.29, 0.62]$.

Background	EPI=1.25	EPI=2.5	OTB (EPI)
$K_{\pi2}$-tgscat	$0.695 \pm 0.150 \,^{+0.061}_{-0.094}$	$1.361 \pm 0.314 \,^{+0.066}_{-0.229}$	$0.666 \pm 0.348 \,^{+0.160}_{-0.290}$
$K_{\pi2}$-rsscat	$0.030 \pm 0.005 \,^{+0.004}_{-0.004}$	$0.057 \pm 0.008 \,^{+0.008}_{-0.008}$	$0.026 \pm 0.009 \,^{+0.011}_{-0.011}$
$K_{\pi2\gamma}$	$0.076 \pm 0.007 \,^{+0.006}_{-0.006}$	$0.121 \pm 0.009 \,^{+0.010}_{-0.009}$	$0.045 \pm 0.012 \,^{+0.004}_{-0.003}$
K_{e4}	$0.176 \pm 0.072 \,^{+0.233}_{-0.124}$	$0.264 \pm 0.108 \,^{+0.349}_{-0.186}$	$0.088 \pm 0.036 \,^{+0.116}_{-0.062}$
CEX	$0.013 \pm 0.013 \,^{+0.010}_{-0.003}$	$0.019 \pm 0.019 \,^{+0.015}_{-0.005}$	$0.006 \pm 0.006 \,^{+0.005}_{-0.002}$
Muon	0.0114 ± 0.0114	0.0171 ± 0.0171	0.0057 ± 0.0057
1bm	0.00023 ± 0.00023	0.00034 ± 0.00034	0.00011 ± 0.00011
2bm-KK	0.00046 ± 0.00046	0.00069 ± 0.00069	0.00023 ± 0.00023
2bm-KP	0.00065 ± 0.00065	0.00097 ± 0.00097	0.00032 ± 0.00032
Total	$0.93 \pm 0.17 \,^{+0.31}_{-0.23}$	$1.72 \pm 0.33 \,^{+0.45}_{-0.44}$	$0.79 \pm 0.35 \,^{+0.30}_{-0.37}$

Table 5.3: Summary of the EPI outside-the-box study. Scaling by a factor of $A(\text{EPI-2.5})/A(\text{EPI-1.25}) = 1.499$ was used for the K_{e4}, CEX, muon and beam backgrounds. The remaining backgrounds were re-evaluated using the loosened CCDPUL, CCDBADFIT, CCDBADTIM and EPIONK cuts. For values having two sets of uncertainties, the first is statistical and the second systematic. The central value for $K_{\pi2\gamma}$ was treated as zero as the contribution due to this background was included in the $K_{\pi2}$ target-scatter value.

5.1.4 Consistency of the Outside-the-Box Studies

The purpose of the outside-the-box was to look for correlations between the bifurcation cuts used for the largest background, $K_{\pi2}$ target-scatter. This section discusses the combined probabilities of the observed number of events from each study given the predictions.

Given the probabilities of the observed number of events from two outside-the-box studies p_1 and p_2, the combined probability of the two observations is given by [39]

$$p_{12} = p_1 p_2 \left(1 - \ln p_1 p_2\right). \tag{5.4}$$

Combining the probabilities of the observations from the three outside-the-box studies (0.02, 0.61 and 0.45) gave a combined probability of 0.14. When this combined probability was re-evaluated at the upper and lower bounds of the constituent probabilities, the

probability range was $[0.01, 0.40]$. These probabilities indicated that the observed and predicted number of events in the outside-the-box studies were generally consistent, giving confidence in the background estimates and their associated systematic uncertainties.

5.2   Single-Cut and Double-Cut Failure Studies

For the single-cut and double-cut failure studies, the cuts were were divided into 13 groups based on correlations. The cuts contained in each group are listed below:

1. **BOX** - This group of cuts, known as PNN2BOX, defined the kinematic signal region with cuts on the π^+ momentum (*ptot*), energy (*etot*) and range in plastic scintillator (*rtot*).

2. **PV** - This group was a single cut, the standard loose photon veto (PV60) including neither the target photon veto (TGPV) nor the active degrader (ADPV).

3. **ADPV** - This group was a single cut, the active degrader (ADPV).

4. **DELC3** - This group was a single cut, the loose delayed coincidence (DELC3).

5. **B4EKZ** - This group was a single cut, the beam likelihood cut (B4EKZ).

6. **TGZ** - This group was a single cut, the target fiducial region cut (TGZFOOL) which demanded that the K^+-decay vertex was within the target fiducial volume.

7. **ETG** - This group of cuts removed events that had extra energy in the target: TGPV, OPSVETO.

8. **EKAON** - This group of cuts removed events that had large pion energy in kaon fibers: CCDPUL, CCDBADFIT, CCDBADTIM, CCD31FIB, EPIONK, TIMKF.

9. **ICGEO** - This group of cuts removed events that had beam-particle activity in the I-Counters: TGGEO, KIC

10. **TD** - This group of cuts was used for particle identification in the Range-Stack counters: PIFLG, ELVETO, TDFOOL, TDNN, RSHEX, RSHEX2.

11. **KIN** - This group of cuts was a collection of cuts based on kinematic constraints in various detector sub-systems: COS3D, ZFRF, ZUTOUT, UTCQUAL, TICCON, EICCON, RNGMOM, PRRF, RSDEDX, LAYER14.

12. **BEAM** - This group of cuts removed single- and double-beam events: BWTRS, CKTRS, CKTAIL, CPITRS, CPITAIL, B4DEDX, B4TRS, B4CCD, TIMCON, UPVTRS, RVTRS.

13. **OTHER** - This group of cuts was a large group of cuts that didn't fit into any of the first 12 groups: TGQUALT, NPITG, EPITG, EPIMAXK, TGER, TARGF, DTGTTP, RTDIF, TGKTIM, TGEDGE, TGDEDX, TGENR, PIGAP, TGLIKE, TGB4, PHIVTX, CHI567, CHI5MAX, ALLKFIT, TPICS, TGTCON, B4ETCON, DRP.

5.2.1 Single-Cut Failures

The single-cut failure study consisted of examining the signal data for events failing only one of the 13 groups of cuts detailed above. Examination of these events provided a clear way to discover flaws in the analysis. Events were classified as "true" single-cut failures if they were classified as single-cut failures and failed only a single cut within that group.

The single-cut study was performed twice. The initial study was performed only on the 1/3 signal data. All events, other than those that failed multiple photon veto cuts, were visually inspected. Two events exposing potential analysis flaws were found in this initial study, prompting the creation of the CCDBADTIM and early BVL safety cuts as discussed in Section 5.2.3. A third event was found in this initial study, exposing an error in the way energy de-multiplexing was being handled in the low-gain target fiber

Group	1/3	2/3
BOX	41 (0)	114 (0)
PV	221 (22)	494 (38)
ADPV	0 (0)	2 (2)
DELC3	0 (0)	0 (0)
B4EKZ	0 (0)	0 (0)
TGZ	0 (0)	0 (0)
ETG	1 (0)	3 (0)
EKAON	3 (2)	3 (3)
ICGEO	1 (1)	0 (0)
TD	0 (0)	1 (1)
KIN	3 (2)	1 (0)
BEAM	0 (0)	0 (0)
OTHER	3 (1)	1 (1)
Total	273 (28)	619 (45)

Table 5.4: The number of single-cut failures listed by group. For each data set, the first number is the number of events which fail only cuts the given group. The numbers in parenthesis are the "true" single-cut failures, events which fail only one of the individual cuts within the given group. The numbers shown for the "true" PVCUT group do not include the pass 2 photon veto P2PVCUT since this cut was composed of multiple subsystems: EC, RD and BV. When P2PVCUT was included in the "true" single-cut failures, there was only 1 event in this group for the 1/3 data set and 6 for the 2/3 data set. Table was reproduced from [56].

CCDs. Appendix E.6 details the way in which this error was fixed and the subsequent improvements that were made to the de-multiplexing algorithm.

The second study was performed on both the 1/3 and 2/3 signal data sets after the final cut positions were set and the 2/3 data set was used to evaluate the final background levels. The results of this study are found in Table 5.4 and show that the rate of single-cut failures was consistent between the 1/3 and 2/3 data sets. The single-cut failures, other than those failing multiple photon veto cuts, were visually inspected. It was concluded from the visual inspection of the "true" photon veto failure events, that these events were $K_{\pi 2}$ decays where one or two very energetic photons were converted and contained within a single photon detector.

Group	1.	2.	3.	4.	5.	6.	7.	8.	9.	10.	11.	12.	13.
1. BOX	-	47518	61	2	3	1	176	79	11	353	934	3	26
2. PV	47518	-	233	39	17	8	93	1328	30	48	179	37	808
3. ADPV	61	233	-	1			3	9		2	2		2
4. DELC3	2	39	1	-							1		2
5. B4EKZ	3	17			-						1		
6. TGZ	1	8				-							
7. ETG	176	93	3				-	36	3		1		19
8. EKAON	79	1328	9				36	-			1		5
9. ICGEO	11	30					3		-				1
10. TD	353	48	2							-	121		1
11. KIN	934	179	2	1	1		1	1		121	-		1
12. BEAM	3	37										-	1
13. OTHER	26	808	2	2			19	5	1	1	1	1	-
Total	49167	50338	313	45	21	9	331	1458	45	525	1241	41	866

Table 5.5: The number of double-cut failures listed by group for the 1/3 sample. All blank entries represent zero events failing that combination of groups. Table was reproduced from [56].

5.2.2 Double-Cut Failures

The double-cut failure study consisted of examining the signal data for events failing cuts in exactly two of the 13 groups of cuts detailed above. The results for the 1/3 data set are shown in Table 5.5 and for the 2/3 data set in Table 5.6. As with the single-cut failures, it was found that the rate of double-cut failures was consistent between the 1/3 and 2/3 data sets.

5.2.3 Safety Cuts

Two events exposing potential analysis flaws were found when examining events from the initial single-cut failure study on the 1/3 data set. These events prompted the creation of two safety cuts: CCDBADTIM and the early BVL. These cuts had minimal acceptance loss and were devised to target the signatures of the two events.

The first event was an ADPV single-cut failure. From reconstruction, the event was

147

Group	1.	2.	3.	4.	5.	6.	7.	8.	9.	10.	11.	12.	13.
1. BOX	-	94557	141	9	6	2	352	187	23	731	1885	16	95
2. PV	94557	-	533	96	32	4	182	2557	82	113	372	60	1575
3. ADPV	141	533	-					6			8		7
4. DELC3	9	96		-	1			1				2	8
5. B4EKZ	6	32		1	-			1			2		
6. TGZ	2	4				-							
7. ETG	352	182					-	56	3	2	1	1	30
8. EKAON	187	2557	6	1	1		56	-	2	3	4	2	25
9. ICGEO	23	82					3	2	-				2
10. TD	731	113					2	3		-	268		
11. KIN	1885	372	8		2		1	4		268	-	1	4
12. BEAM	16	60		2			1	2			1	-	2
13. OTHER	95	1575	7	8			30	25	2		4	2	-
Total	98004	100163	695	117	42	6	627	2844	112	1117	2545	84	1748

Table 5.6: The number of double-cut failures listed by group for the 2/3 sample. All blank entries represent zero events failing that combination of groups. Table was reproduced from [56].

identified as a $K_{\pi 2}$ target-scatter with one of the photons being detected in the Active Degrader. Comparisons between the raw target-CCD data and the solutions found by the target CCD fitter revealed a large second pulse (~ 8 MeV) in one of the kaon fibers that was not found by the fitter. Subsequent studies found common incorrect target CCD fitter solutions that could be found when checking for consistency between the pulse times found using the target CCD fitter and those expected from target reconstruction. The cut CCDBADTIM was created to remove these types of events and is discussed in more detail in Appendix E.

The second event was a PV single-cut failure in the BVL. Examination of this event and data from previous studies [92] revealed that two photons from a single π^0 decay converting in the same BVL element caused the timing of these photon hits to be mismeasured. The "early BVL" cut was added to the photon veto, removing events having a mean time in the BVL between -5.0 and -2.0 ns, a time difference between the hits on each end of less than 4.0 ns, and energy of the hit of greater than 10.0 MeV.

5.3   Background Cross-Contamination Studies

As discussed in 4.1.1, a number of contamination studies were performed on the $K_{\pi 2}$ target-scatter background. This section details data-driven studies that found negligible contamination due to muon and double-beam events in the $K_{\pi 2}$ target-scatter background estimate. Also found in this section are the details of a study used to determine the upper-limit of $K_{\pi 2 \gamma}$ contamination in the $K_{\pi 2}$ target-scatter normalization branch, supporting the method used to correct for $K_{\pi 2 \gamma}$ contamination in the $K_{\pi 2}$ target-scatter background discussed in Section 4.1.5. Details of the contamination due to $K_{\pi 2}$ Range-Stack-scatter in the $K_{\pi 2}$ target-scatter normalization branch were previously discussed in Sections 4.1.2 and 4.2.1 and are not discussed further in this section. The subject of contamination due to K_{e4} in the $K_{\pi 2}$ target-scatter normalization branch, which was argued to be negligible in Section 4.1.2, is also not discussed further in this section.

5.3.1   Effects of Contamination Background Estimates

The method used to quantify the muon and double-beam contamination in the $K_{\pi 2}$ target-scatter background is discussed in this section and the calculations detailed in the two subsequent sections.

For the $K_{\pi 2}$ target-scatter background, estimated using the bifurcation method, the effects of a generic contamination were as follows. The number of events remaining at the end of the normalization branch N_{tgscat} was inflated due to contamination events in addition the target-scatter events. The effect on the rejection of CUT1 (R_{PV60}) varied depending on whether or not the rejection of the contamination events was higher or lower than that of the target-scatter events. If the rejection of the contamination events was higher (lower) than that of the target-scatter events, the rejection was overestimated (underestimated). The typical effect of these mis-measurements of the normalization and rejection was that the $K_{\pi 2}$ target-scatter background was overestimated, but a sufficiently

overestimated rejection could have caused the background to be underestimated.

5.3.2   Muon Contamination

The bifurcation cuts used to evaluate the muon background were used to estimate the contamination of muon events in the $K_{\pi 2}$ target-scatter normalization and rejection branches and thus the effect of this contamination on the background evaluation. These cuts were the loose TD cuts *TDLOOSE* (CUT1) and the range-momentum consistency cut RNG-MOM (CUT2).

Acceptance and Rejection of the Muon Bifurcation Cuts

To perform a data-driven estimate of the muon contamination in the $K_{\pi 2}$ target-scatter normalization and rejection branches, the acceptance of these cuts on $K_{\pi 2}$ target-scatter events (A_π) and the rejection of these cuts on muon events (R_μ) had to be evaluated.

The rejection of RNGMOM (R_{RNGMOM}) for muon events was measured on the muon background normalization branch (Figure 4.6) after setup cuts and the inversion of *TD-LOOSE*. The rejection of *TDLOOSE* (R_{TDCUT02}) for muon events was measured in the muon background rejection branch by inverting RNGMOM (Table 4.9). The combined rejection of these cuts R_μ was

$$
\begin{aligned}
R_\mu &= R_{\mathrm{RNGMOM}} \times R_{TDLOOSE}, \\
&= (28.29 \pm 1.06) \times (133.0 \pm 10.7), \\
&= 3764 \pm 333.
\end{aligned}
\tag{5.5}
$$

The acceptance of these cuts (A_π) was measured using a modified version of the rejection branch used in the $K_{\pi 2}$ target-scatter background estimate. The modifications were that *TDLOOSE* and RNGMOM were removed from the setup cuts and the kinematic box was changed from PNN2BOX box to the $K_{\pi 2}$-peak kinematic box KP2BOX.

After the setup cuts were applied, the 12 classes (2-13) described in Table 4.1 were applied and the performance of RNGMOM and *TDLOOSE* was measured before and after application of the photon veto PV60 as shown in Table 5.7. Ignoring the classes with very low statistics, the measured acceptance of these muon bifurcation cuts were equal before and after the application of the photon veto cut within statistical uncertainty. The acceptance A_π was taken as the average of the highest and lowest acceptance values measured before the application of PV60 with the difference between these extreme values setting the bounds for the uncertainty:

$$A_\pi = 0.809 \pm 0.030. \tag{5.6}$$

CLASS	BEFORE PV60	AFTER PV60
2	$293455/363196 = 0.808 \pm 0.001$	$280/343 = 0.816 \pm 0.021$
3	$120164/148540 = 0.809 \pm 0.001$	$115/140 = 0.821 \pm 0.032$
4	$120568/149124 = 0.809 \pm 0.001$	$109/138 = 0.790 \pm 0.035$
5	$364667/451267 = 0.808 \pm 0.001$	$346/428 = 0.808 \pm 0.019$
6	$175663/217075 = 0.809 \pm 0.001$	$159/199 = 0.799 \pm 0.028$
7	$179337/222017 = 0.808 \pm 0.001$	$166/214 = 0.776 \pm 0.029$
8	$27644/34214 = 0.808 \pm 0.002$	$16/25 = 0.640 \pm 0.096$
9	$343309/424682 = 0.808 \pm 0.001$	$331/412 = 0.803 \pm 0.020$
10	$59863/74471 = 0.804 \pm 0.002$	$58/72 = 0.806 \pm 0.047$
11	$5883/7383 = 0.797 \pm 0.005$	$5/5 = 1.000 \pm 0.000$
12	$316971/392405 = 0.808 \pm 0.001$	$303/368 = 0.823 \pm 0.020$
13	$132619/164163 = 0.808 \pm 0.001$	$127/152 = 0.836 \pm 0.030$

Table 5.7: The acceptance of RNGMOM×TDCUT02 measured on $K_{\pi 2}$-peak events before and after the application of the photon veto cut PV60 for each of the 12 classes (2-13) from the $K_{\pi 2}$ target-scatter rejection branch.

Muon Contamination in the Normalization Branch

To determine the amount of muon contamination in the $K_{\pi 2}$ target-scatter normalization branch, the number of events N left at the end of the normalization branch was treated

as being made up of either muon (N_μ) or pion (N_π) events,

$$N = N_\pi + N_\mu. \tag{5.7}$$

With the performance known for the muon bifurcation cuts (RNGMOM and *TD-LOOSE*) with respect to pions (A_π) and muons (R_μ), these cuts were moved to the bottom of the $K_{\pi 2}$ target-scatter normalization branch. The number of events remaining before RNGMOM and *TDLOOSE* were applied was denoted M. These M events were also made up of pion or muon events as given by

$$M = \frac{N_\pi}{A_\pi} + N_\mu R_\mu. \tag{5.8}$$

The amount of muon contamination left at the end of the normalization branch was represented by the quantity f,

$$\begin{aligned} f &= \frac{N_\mu}{N}, \\ &= \frac{A_\pi \frac{M}{N} - 1}{A_\pi R_\mu - 1}. \end{aligned} \tag{5.9}$$

Taking the acceptance ($A_\pi = 0.809 \pm 0.030$), rejection ($R_\mu = 3764 \pm 333$), and measured values $N = 1131$ and $M = 12980$, the value of f was determined,

$$f = (2.72 \pm 0.26) \times 10^{-3}. \tag{5.10}$$

After being corrected for muon contamination, the number of events at the end of the $K_{\pi 2}$ target-scatter normalization branch was given by

$$\begin{aligned} N' &= N(1 - f), \\ &= 1128 \pm 34. \end{aligned} \tag{5.11}$$

This was corrected for Range-Stack contamination n_{rs}, which gave the final corrected normalization:

$$
\begin{aligned}
n'_{\text{tgscat}} &= N' - n_{rs} \\
&= (1128 \pm 34) - (23.3 \pm 3.5) \\
&= 1105 \pm 34.
\end{aligned}
\tag{5.12}
$$

Muon Contamination in the Rejection Branch

The method used to determine the amount of muon contamination in the rejection branch was very similar to that for the normalization branch except the amount of contamination had to be measured before and after the $K_{\pi 2}$ target-scatter bifurcation cut PV60.

The number of events left at the end of the $K_{\pi 2}$ target-scatter rejection branch (Figure 4.2) was denoted N_2 where only the results for CLASS12 were used for this part of the study. The number of events before the photon veto was applied was denoted N_1 and the photon veto rejection R_{PV} given by

$$
R_{\text{PV}} = \frac{N_1}{N_2}
\tag{5.13}
$$

It was possible to examine the amount of muon contamination both before and after the photon veto was applied by treating N_1 and N_2 as being made up of muon and pion events as with the normalization branch method:

$$
\begin{aligned}
N_1 &= N_{\pi 1} + N_{\mu 1}, \\
N_2 &= N_{\pi 2} + N_{\mu 2}.
\end{aligned}
\tag{5.14}
$$

Again, the performances of the muon bifurcation cuts (RNGMOM and *TDLOOSE*) with respect to pions (A_π) and muons (R_μ) were used to solve for the fraction of the events which were contamination muons.
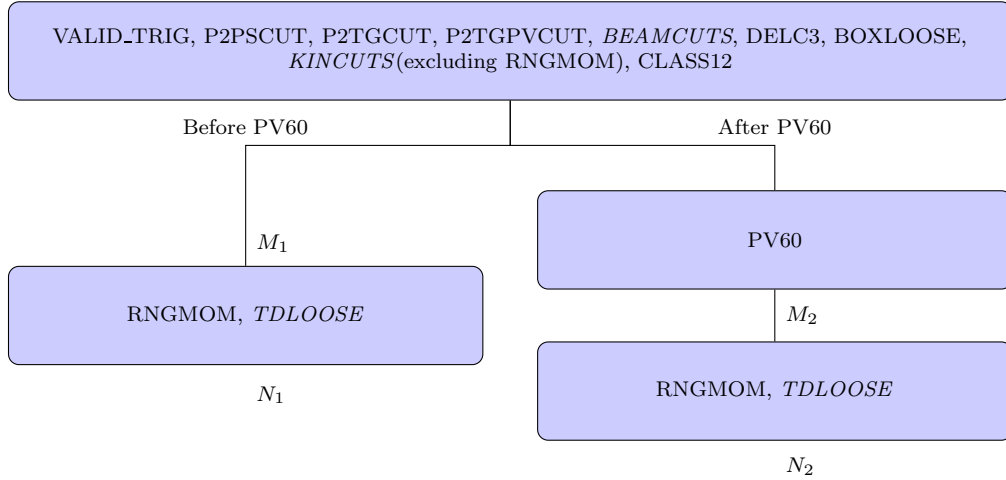
Figure 5.1: Flowchart showing the muon contamination study in the $K_{\pi 2}$ target-scatter rejection branch. Cuts in italics refer to named groups of cuts.

Figure 5.1 shows a flowchart with the cuts applied and the quantities measured for this part of the contamination study. To determine the muon contamination remaining before the photon veto was applied, the number of events remaining before the application of PV60 was measured with (N_1) and without (M_1) the muon bifurcation cuts applied. The same was done to determine the muon contamination present after the application of PV60 by measuring the events remaining at the end of the rejection branch with (N_2) and without (M_2) the muon bifurcation cuts applied.

The following equations show the breakdown of pion and muon events in the quantities M_1 and M_2:

$$
\begin{aligned}
M_1 &= \frac{N_{\pi 1}}{A_\pi} + N_{\mu 1} R_\mu, \\
M_2 &= \frac{N_{\pi 2}}{A_\pi} + N_{\mu 2} R_\mu.
\end{aligned}
\tag{5.15}
$$

The amounts of muon contamination before and after PV60 was applied were represented

154

by the quantities f_1 and f_2, respectively,

$$
\begin{aligned}
f_1 &= \frac{A_\pi \frac{M_1}{N_1} - 1}{A_\pi R_\mu - 1}, \\
f_2 &= \frac{A_\pi \frac{M_2}{N_2} - 1}{A_\pi R_\mu - 1}.
\end{aligned}
\tag{5.16}
$$

Using the measured values summarized in Table 5.8, The corrected photon veto rejection was given by

$$
\begin{aligned}
R'_{\text{PV60}} &= \frac{N_1(1 - f_1)}{N_2(1 - f_2)} \\
&= 2666 \pm 843
\end{aligned}
\tag{5.17}
$$

Quantity	Before PV60	After PV60
Muon bifurcation cuts not applied	$M_1 = 94424$	$M_2 = 652$
Muon bifurcation cuts applied	$N_1 = 52621$	$N_2 = 22$
f-value	$f_1 = (1.76 \pm 0.16) \times 10^{-4}$	$f_2 = (7.63 \pm 1.80) \times 10^{-3}$
Corrected value	$N'_1 = N_1(1 - f_1)$ $= 52612 \pm 229$	$N'_2 = N_2(1 - f_2)$ $= 21.8 \pm 4.7$
$R'_{\text{PV60}} = N'_1/N'_2$	2410 ± 518	

Table 5.8: Table showing the values used to arrive at the $K_{\pi 2}$ target-scatter photon veto rejection after the effects of muon contamination were removed.

Background Estimate Corrected for Muon Contamination

The numbers from the contamination study in the normalization and rejection branches were used to estimate the background with the effects of muon contamination removed,

$$
\begin{aligned}
bg'_{\text{tgscat}} &= \frac{3}{2} \times \frac{n'_{tgscat}}{R'_{\text{PV}} - 1}, \\
&= \frac{3}{2} \times \frac{1105 \pm 34}{(2410 \pm 518) - 1}, \\
&= 0.688 \pm 0.150.
\end{aligned}
\tag{5.18}
$$

Since the central value of the nominal $K_{\pi2}$ target-scatter background evaluation ($0.695 \pm 0.150 \, ^{+0.061}_{-0.094}$) and this value agree to approximately 1%, the muon contamination in the $K_{\pi2}$ target-scatter background was considered to be negligible. Note that the values used for this $K_{\pi2}$ target-scatter background comparison were both values without the corrections for $K_{\pi2\gamma}$ contamination applied.

5.3.3 Double-Beam Contamination

Due to a lack of acceptance and rejection information for the rejection branch bifurcation cuts (CUT2) for double-beam background, only the normalization branch bifurcation cuts (CUT1) were used in this study.

The rejection of CKTRS, CKTAIL and BWTRS for KK-type events will be denoted R_{KK} and the rejection of CPITRS, CPITAIL and BWTRS for KP-type events will be denoted R_{KP}. These rejections were taken from the double-beam rejection branches: Table 4.14 for R_{KK} and Table 4.15 for R_{KP}. The combined acceptance of these groups of cuts for pion events, denoted A_{KK} and A_{KP}, were taken from the beam acceptance measurement (Table 6.4). The sample used for that measurement used $K_{\mu2}$ monitor trigger data with cuts applied to ensure the event looks like a single K^+ decay with no photons. These values are summarized in Table 5.9.

156

	KK Branch	KP Branch
Cuts	CKTRS·CKTAIL·BWTRS	CPITRS·CPITAIL·BWTRS
Acceptance	$A_{KK} = 0.8973 \pm 0.0002$	$A_{KP} = 0.9159 \pm 0.0002$
Rejection	$R_{KK} = 394 \pm 197$	$R_{KP} = 617 \pm 308$

Table 5.9: Acceptance of pion events and rejection of double-beam events for the double-beam bifurcation cuts.

Double-Beam Contamination in the Normalization Branch

The method for determining the double-beam contamination in the $K_{\pi 2}$ target-scatter normalization branch was the same as that described for muon contamination, but with a different set of cuts for each the KK and KP double-beam contaminations. Since the contamination due to each of these backgrounds was expected to be very small, the KK contamination was ignored for the KP contamination study and the KP contamination ignored for the KK contamination study.

The following discussion lays out the equations used to determine the amount of KK double-beam contamination, but the same equations all apply for the KP double-beam contamination with the KP notation replacing the KK notation. To determine the amount of KK contamination in the normalization branch, the number of events N left at the end of the normalization branch was treated as being made up of N_π pion events and N_{KK} KK double-beam events. Written in equation form, this looks like:

$$N = N_\pi + N_{KK}. \tag{5.19}$$

With the performance known for the KK double-beam rejection branch bifurcation cuts (CKTRS, CKTAIL and BWTRS) with respect to $K_{\pi 2}$ target-scatter events (A_{KK}) and KK double-beam events (R_{KK}), these cuts were moved to the bottom of the $K_{\pi 2}$ target-scatter normalization branch. The number of events remaining before these cuts were applied was denoted M. These M events were made up of pion and KK double-beam

157

events as given by

$$M = \frac{N_\pi}{A_{KK}} + R_{KK}N_{KK}.$$

(5.20)

The amount of KK contamination left at the end of the normalization branch was represented by the quantity f, given by the expression

$$f = \frac{A_{KK}\frac{n}{N} - 1}{A_{KK}R_{KK} - 1}.$$

(5.21)

Table 5.10 shows the values used to determine the fractional contamination due to KK and KP double-beam events in the $K_{\pi 2}$ target-scatter normalization branch. Note that the final corrected normalization n'_{tgscat} was corrected for both the given double-beam contamination and the range-stack scatter component n_{rs}.

	KK Branch	KP Branch
M	1186	1160
N	1131	1131
f-value	$f_{KK} = -0.00017 \pm 0.00009$	$f_{KP} = -0.00011 \pm 0.00005$
TG-Scatter Normalization corrected for f-value and n_{rs}		
$n'_{\text{tgscat}} = N(1 - f) - n_{rs}$	$n'_{\text{tgscat}} = 1108 \pm 23$	$n'_{\text{tgscat}} = 1108 \pm 34$

Table 5.10: Correcting for double-beam contamination in the $K_{\pi 2}$ target-scatter normalization branch.

Double-Beam Contamination in the Rejection Branch

The method used to determine the double-beam contamination in the $K_{\pi 2}$ target-scatter rejection branch was also similar to that described for muon contamination with the KK or KP double-beam bifurcation cuts replacing the muon bifurcation cuts. As with the double-beam contamination in the normalization branch study, contamination due to one type of double-beam process (KK or KP) was ignored when studying the other.

The following discussion lays out the equations used to determine the amount of KK double-beam contamination, but the same equations all apply for the KP double-beam contamination with the KP notation replacing the KK notation. As with the muon contamination in the rejection branch, the amount of contamination was measured before and after the photon veto was applied.

The amount of KK double-beam contamination, both before and after the photon veto was applied, was examined by treating the N_1 events before the application of PV60 and the N_2 events after the application of PV60 as being made up of double-beam and pion events as was done for the normalization branch:

$$N_1 = N_{\pi 1} + N_{KK1},$$
$$N_2 = N_{\pi 2} + N_{KK2}. \tag{5.22}$$

These KK double-beam bifurcation cuts were applied immediately before the end of the branch (after the photon veto) which gave M_2 events before the KK double-beam bifurcation cuts and N_2 after. The same was done by applying these KK double-beam bifurcation cuts immediately before the photon veto which gave M_1 events before the KK double-beam bifurcation cuts and N_1 after. The breakdown of pion and double-beam events in the quantities M_1 and M_2 was as follows:

$$M_1 = \frac{N_{\pi 1}}{A_{KK}} + N_{KK1}R_{KK},$$
$$M_2 = \frac{N_{\pi 2}}{A_{KK}} + N_{KK2}R_{KK}. \tag{5.23}$$

The amount of KK double-beam contamination before and after the photon veto was applied was represented by the quantities f_M and f_N, respectively, using the same definition as introduced for muons (Section 5.3.2). Tables 5.11 and 5.12 show the values used to arrive at values for the PV60 rejection after being corrected for each of the double-beam processes.

Quantity	Before PV60	After PV60
Double-beam bifurcation cuts not applied	$M_1 = 55873$	$M_2 = 25$
Double-beam bifurcation cuts applied	$N_1 = 52621$	$N_2 = 22$
f-value	$f_1 = (-13.3 \pm 6.7) \times 10^{-5}$	$f_2 = (5.48 \pm 2.16) \times 10^{-5}$
Corrected value	$N_1' = N_1(1 - f_1)$ $= 52628 \pm 230$	$N_2' = N_2(1 - f_2)$ $= 22.0 \pm 4.7$
$R'_{\mathrm{PV60}}(KK) = N_1'/N_2'$	2392 ± 510	

Table 5.11: The KK Double-Beam Contamination in the $K_{\pi 2}$ target-scatter rejection branch. This table shows the values used to arrive at the photon veto rejection after the effects of KK double-beam contamination were removed.

Quantity	Before PV60	After PV60
Double-beam bifurcation cuts not applied	$M_1 = 54563$	$M_2 = 25$
Double-beam bifurcation cuts applied	$N_1 = 52621$	$N_2 = 22$
f-value	$f_1 = (-8.90 \pm 4.46) \times 10^{-5}$	$f_2 = (-7.18 \pm 14.11) \times 10^{-5}$
Corrected value	$N_1' = N_1(1 - f_1)$ $= 52626 \pm 229$	$N_2' = N_2(1 - f_2)$ $= 22.0 \pm 4.7$
$R'_{\mathrm{PV60}}(KP) = N_1'/N_2'$	2392 ± 510	

Table 5.12: KP Double-Beam Contamination in the $K_{\pi 2}$ target-scatter rejection branch. This table shows the values used to arrive at the photon veto rejection after the effects of KP double-beam contamination were removed.

Background Estimates Corrected for Double-Beam Contamination

The numbers from the double-beam contamination studies in the normalization and rejection branches were used to estimate the backgrounds with the effects of each of the studied double-beam processes removed:

$$
\begin{aligned}
bg'_{KK} &= \frac{3}{2} \times \frac{n'_{\text{tgscat}}}{R'_{\text{PV60}} - 1}, \\
&= \frac{3}{2} \times \frac{1108 \pm 34}{(2392 \pm 510) - 1}, \\
&= 0.695 \pm 0.150;
\end{aligned} \tag{5.24}
$$

and

$$
\begin{aligned}
bg'_{KP} &= \frac{3}{2} \times \frac{n'_{\text{tgscat}}}{R'_{\text{PV60}} - 1}, \\
&= \frac{3}{2} \times \frac{1108 \pm 34}{(2392 \pm 510) - 1}, \\
&= 0.695 \pm 0.150.
\end{aligned} \tag{5.25}
$$

Since the central values of each of these corrected backgrounds agreed to better than 1% with the nominal value of 0.695 ± 0.150, the contamination due to both types of double-beam contamination was considered negligible. Note that the values used for this $K_{\pi 2}$ target-scatter background comparison were both values without the corrections for $K_{\pi 2\gamma}$ contamination applied.

Double-Beam Contamination Follow-Up Study

A follow-up study was performed to test the assumption that the KP contamination could be ignored for the KK contamination study and vice versa. In this study, Equations (5.19)

and (5.20) were replaced with a set of 3 equations,

$$N = N_\pi + N_{KK} + N_{KP},$$

$$M_{KK} = \frac{N_\pi}{A_{KK}} + N_{KK}R_{KK} + \frac{N_{KP}}{A'_{KK}}, \qquad (5.26)$$

$$M_{KP} = \frac{N_\pi}{A_{KP}} + \frac{N_{KK}}{A'_{KP}} + N_{KP}R_{KP}.$$

For these equations M_{KK} and M_{KP} were the M-values from Table 5.10 for the KK and KP branches, respectively. The definitions of the combined acceptances A'_{KK} and A'_{KP} were the same as A_{KK} and A_{KP} except the acceptance of BWTRS was replaced with the inverse of the rejection for BWTRS for that specific background, from the double-beam rejection branch. To determine the amount of KK and KP contamination, the values N_{KK} and N_{KP} were determined from the above set of 3 equations and the f-values determined as

$$f_{KK} = \frac{N_{KK}}{N},$$

$$f_{KP} = \frac{N_{KP}}{N}. \qquad (5.27)$$

The results from this follow-up study were consistent with the original double-beam contamination studies, showing it was reasonable to assume that at the given levels of contamination, the KP contamination could be ignored for the KK contamination study and vice versa.

5.3.4 Upper Limit of $K_{\pi2\gamma}$ Contamination

This study was performed to estimate the upper limit of $K_{\pi2\gamma}$ contamination in the $K_{\pi2}$ target-scatter normalization branch using $K_{\pi2}$ monitor trigger data. This study involved two kinematic regions, the $K_{\pi2}$-peak region KP2BOX and the kinematic signal region PNN2BOX. The L1.1 and L1.2 triggers and all analysis cuts other than the photon

veto $PVCUT$ were applied to the sample, leaving n_{peak} events in the KP2BOX and n_{tail} events in the PNN2BOX. After applying all analysis cuts, these samples should have been dominated by events where a beam K^+ decayed into a π^+ and any number of photons since the photon veto was not applied. Due to the high branching ratio and pion identification cuts, the n_{peak} events should have been made up entirely of $K_{\pi2}$ events. The n_{tail} events should have been a mixture of $K_{\pi2}$-scatter and $K_{\pi2\gamma}$ events. For the purpose of an upper limit study, it was assumed that the $K_{\pi2\gamma}$ contamination in the $K_{\pi2}$ monitor trigger data was large enough that n_{tail} was made up entirely of $K_{\pi2\gamma}$ events.

The fraction of $K_{\pi2\gamma}$ events in the $K_{\pi2}$ target-scatter normalization branch was expressed as

$$g = \frac{N_g}{N_s + N_g}, \tag{5.28}$$

where N_g was the number of $K_{\pi2\gamma}$ events in the $K_{\pi2}$ target-scatter normalization branch and N_s was the number of $K_{\pi2}$-scatter events in the $K_{\pi2}$ target-scatter normalization branch. The value for $N_s + N_g$ was $N_{\text{tgscat}} = 1131$, taken from Table 4.4.

The relative rate of n_{tail} to n_{peak} from this study was given by

$$f = \frac{n_{\text{tail}}}{n_{\text{peak}}},$$
$$f = \frac{16}{5778}, \tag{5.29}$$
$$f = 0.00277 \pm 0.00069.$$

Next, the $K_{\pi2}$ target-scatter normalization branch (Figure 4.2) was reproduced using the kinematic region KP2BOX instead of PNN2BOX, leaving $N_p = 122473$ events at the end of that normalization branch. Based on the relative rate f determined above, the upper limit on the number of $K_{\pi2\gamma}$ events (N_g) in the $K_{\pi2}$ target-scatter normalization branch was

$$N_g = f \times N_p. \tag{5.30}$$

Finally, Equation (5.28) was rewritten as

$$
\begin{aligned}
g &= \frac{N_g}{N_s + N_g}, \\
&= \frac{f \times N_p}{N_{\text{tgscat}}}, \\
&= \frac{(0.00277 \pm 0.00069) \times 122473}{1131}, \\
&= 0.300 \pm 0.075,
\end{aligned}
\tag{5.31}
$$

which was the upper limit on $K_{\pi2\gamma}$ contamination in the $K_{\pi2}$ target-scatter normalization branch. Section 4.1.5 details how this upper limit contributed to the process of correcting the $K_{\pi2}$ target-scatter background for $K_{\pi2\gamma}$ contamination.

Chapter 6

Signal Acceptance and Sensitivity

To accurately measure the branching ratio of $K^+ \to \pi^+ \nu \bar{\nu}$, the components of acceptance of the many cuts applied to the signal data needed to be carefully measured. As with the rest of this analysis, experimental data were used instead of Monte Carlo simulation wherever possible. The $K_{\pi 2}$, $K_{\mu 2}$ and π_{scatter} monitor trigger data were used to measure the components of acceptance of most of the cuts, with the Monte Carlo simulation being used to measure primarily those cuts involving decay phase space and trigger efficiencies. Since the monitor trigger data was collected in parallel with the signal data, effects due to running conditions such as rate effects were automatically taken into account.

To measure the acceptance "acc" of a cut, the cut is applied to a sample of N events, leaving n events that survive the cut. Thus the acceptance is defined as

$$acc = \frac{n}{N}. \tag{6.1}$$

The acceptance is the probability of success of a cut and is thus described by a binomial distribution. The uncertainty on the acceptance measurement is then given by the

standard deviation on a measurement of N trials,

$$\begin{aligned}
\sigma_{acc} &= \frac{1}{N}\sqrt{N \cdot acc \cdot (1 - acc)}, \\
&= \sqrt{\frac{acc \cdot (1 - acc)}{N}}.
\end{aligned} \tag{6.2}$$

6.1 Acceptance Factors from $K_{\mu 2}$ Monitor Trigger Events

With a single charged track, and no photons or other activity in the detector, $K_{\mu 2}$ and $K^+ \to \pi^+ \nu \bar{\nu}$ events were topologically very similar with respect to event reconstruction and hit patterns in many subsystems. The $K_{\mu 2}$ monitor trigger events were used to measure the acceptance of event reconstruction cuts in the Range-Stack (A_{RS}), event reconstruction cuts in the target and UTC (A_{recon}), and the acceptance of the photon veto (A_{PV}). These monitor trigger events were also used to measure the beam cuts and the target-quality cuts that did not involve pion energies (A_{beam}). Table 6.1 shows the setup cuts applied to create the samples used for each of these categories of cuts.

6.1.1 Range-Stack Tracking Acceptance

To measure the acceptance A_{RS} (Table 6.2) of the Range-Stack tracking, the setup cuts $Setup_{\mathrm{RS}}$ were used to create a sample consisting of good tracks arriving at the Range-Stack. This was done by ensuring successful reconstruction in the target (TRIGGER, ICBIT) and UTC (UTC, UTC_QUAL), both of which are independent of Range-Stack reconstruction. To ensure it was a stopped K^+ decay, B4DEDX made sure that the beam particle had an energy consistent with a K^+, and a modified delayed-coincidence condition ($\mathtt{t_{IC}} - \mathtt{t_{CK}} > 5\mathrm{ns}$) ensured that the kaon did not decay in flight. The modified delayed coincidence condition, using the kaon time in the Čerenkov counters and the hit

$K_{\mu 2}$ Setup Categories	Measured Quantities	Setup Cuts
$Setup_{\mathrm{RS}}$	A_{RS}	TRIGGER, ICBIT, $\mathtt{t_{IC}} - \mathtt{t_{CK}} > 5$ns, B4DEDX, UTC, UTC_QUAL
$Setup_{\mathrm{recon}}$	A_{recon}	TRIGGER, ICBIT, $\mathtt{t_{IC}} - \mathtt{t_{CK}} > 5$ns, B4DEDX, CPITRS, CPITAIL, CKTRS, CKTAIL, BWTRS, RDTRK, TRKTIM, $\|\mathtt{t_{IC}} - \mathtt{t_{RS}}\| < 5$ns, PVCUT(noBV,noBVL)
$Setup_{\mathrm{beam}}$	A_{beam}	TRIGGER, ICBIT, RDTRK, TRKTIM, RDUTM, KM2PBOX, COS3D
$Setup_{\mathrm{PV}}$	A_{PV}	$Setup_{\mathrm{beam}}$, A_{beam} cuts, stopping layer < 19

Table 6.1: The setup cuts applied for the $K_{\mu 2}$-based acceptance measurements. The notation "A_{beam} cuts" means that all the cuts whose acceptance were measured to determine the quantity A_{beam} were applied as setup cuts. KM2PBOX selected events in the momentum range 226 MeV/c < $\mathtt{ptot}$ < 246 MeV/c. The photon veto "PVCUT(noBV,noBVL)" was applied with the Barrel-Veto and Barrel-Veto Liner subsystems excluded. Table reproduced from [56].

time in the IC, was used because the standard delayed coincidence cut DELC3 indirectly required a reconstructed track in the Range-Stack.

6.1.2   Target and UTC Reconstruction Efficiency

To measure the reconstruction efficiency A_{recon} (Table 6.3) of the target and UTC, the setup cuts $Setup_{\mathrm{recon}}$ were applied to create a sample which required a K^+ decay (B4DEDX, $\mathtt{t_{IC}} - \mathtt{t_{CK}} > 5$ns) without beam contamination (CPITRS, CPITAIL, CKTRS, CKTAIL,

Cut	Loose		Tight	
	Events	Acceptance	Events	Acceptance
$Setup_{\mathrm{RS}}$	2967140		2967140	
RD_TRK	2967140	1.0000 ± 0.0000	2967140	1.0000 ± 0.0000
TRKTIM	2966943	0.9999 ± 0.0000	2966943	0.9999 ± 0.0000
A_{RS}		0.9999 ± 0.0000		0.9999 ± 0.0000

Table 6.2: The acceptance of the range-stack-reconstruction cuts using $K_{\mu 2}$ monitor trigger events. Table reproduced from [56].

Cut	Loose		Tight	
	Events	Acceptance	Events	Acceptance
$Setup_{\mathrm{recon}}$	1542443		759060	
RDUTM	1541571	0.9994 ± 0.0000	758792	0.9996 ± 0.0000
TARGET	1541571	1.0000 ± 0.0000	758792	1.0000 ± 0.0000
A_{recon}		0.9994 ± 0.0000		0.9996 ± 0.0000

Table 6.3: The acceptance of the target and UTC reconstruction cuts using $K_{\mu 2}$ monitor trigger events. Table reproduced from [56].

BWTRS). The sample also required that a good track crossed through the UTC to the Range-Stack ($|\mathtt{t_{IC}} - \mathtt{t_{RS}}| < 5$ns, RD_TRK, TRKTIM), and required no photons in order to avoid possible contamination from $K_{\mu 2 \gamma}$. To avoid self-vetoing from events where the μ^+ passed through the Range-Stack and into the Barrel-Veto and Barrel-Veto Liner, these subsystems were excluded from the photon veto applied to this sample as indicated by the notation "PVCUT(noBV,noBVL)".

6.1.3 Beam and Target-Quality Acceptance

To measure the acceptance A_{beam} (Table 6.4) of the beam and selected target-quality cuts, the setup cuts $Setup_{\mathrm{beam}}$ were applied to select K^+ decays with a single charged track, no photons, no beam contamination and no other activity in the detector. Successfully reconstructed $K_{\mu 2}$ events were chosen by restricting the momentum to the $K_{\mu 2}$-peak (KM2PBOX), ensuring the charged track entered the active region of the detector (COS3D), and ensuring the quality of the track (RD_TRK, TRKTIM, RDUTM). The cuts measured by this sample were ordered to obtain the most meaningful acceptance for each individual cut. For example, most of the target-quality cuts requires a successful target reconstruction, so TGQUALT was applied before any of the other cuts.

Cut	Loose		Tight	
	Events	Acceptance	Events	Acceptance
$Setup_\text{beam}$	3824854		3824854	
TGCUT	3741291	0.9782 ± 0.0001	3741291	0.9782 ± 0.0001
TGQUALT	3610937	0.9652 ± 0.0001	3610937	0.9652 ± 0.0001
NPITG	3610937	1.0000 ± 0.0000	3610937	1.0000 ± 0.0000
TIMCON	3605667	0.9985 ± 0.0000	3605667	0.9985 ± 0.0000
TGTCON	3566647	0.9892 ± 0.0001	3566647	0.9892 ± 0.0001
B4ETCON	3531329	0.9901 ± 0.0001	3531329	0.9901 ± 0.0001
DCBIT	3110649	0.8809 ± 0.0002	3110649	0.8809 ± 0.0002
DELCO	2665661	0.8569 ± 0.0002	2191189	0.7044 ± 0.0002
PSCUT	2528550	0.9486 ± 0.0001	2074552	0.9468 ± 0.0001
B4DEDX	2514694	0.9945 ± 0.0001	2063095	0.9945 ± 0.0001
BWTRS	2308180	0.9179 ± 0.0002	1892260	0.9172 ± 0.0002
CPITRS	2304287	0.9983 ± 0.0000	1889137	0.9983 ± 0.0000
CPITAIL	2303213	0.9995 ± 0.0000	1888271	0.9995 ± 0.0000
CKTRS	2288540	0.9936 ± 0.0001	1878953	0.9951 ± 0.0001
CKTAIL	2251649	0.9839 ± 0.0001	1867769	0.9940 ± 0.0001
B4TRS	2193877	0.9743 ± 0.0001	1818255	0.9735 ± 0.0001
B4CCD	2164219	0.9865 ± 0.0001	1798933	0.9894 ± 0.0001
UPVTRS	2128633	0.9836 ± 0.0001	1770430	0.9842 ± 0.0001
RVTRS	2126603	0.9990 ± 0.0000	1768838	0.9991 ± 0.0000
TGGEO	2041316	0.9599 ± 0.0001	1696457	0.9591 ± 0.0001
B4EKZ	1861055	0.9117 ± 0.0002	1544226	0.9103 ± 0.0002
TGZFOOL	1838070	0.9876 ± 0.0001	1525163	0.9877 ± 0.0001
TARGF	1778937	0.9678 ± 0.0001	1475963	0.9677 ± 0.0001
DTGTTP	1778930	1.0000 ± 0.0000	1475956	1.0000 ± 0.0000
RTDIF	1761888	0.9904 ± 0.0001	1461737	0.9904 ± 0.0001
TGKTIM	1744527	0.9901 ± 0.0001	1456412	0.9964 ± 0.0001
EICCON	1697720	0.9732 ± 0.0001	1417410	0.9732 ± 0.0001
TICCON	1697716	1.0000 ± 0.0000	1417407	1.0000 ± 0.0000
PIGAP	1682926	0.9913 ± 0.0001	1405081	0.9913 ± 0.0001
TGB4	1588984	0.9442 ± 0.0002	1327709	0.9449 ± 0.0002
PHIVTX	1541372	0.9700 ± 0.0001	1283527	0.9667 ± 0.0001
CCDPUL	694731	0.4507 ± 0.0004	633868	0.4938 ± 0.0004
EPIONK	691595	0.9955 ± 0.0001	630732	0.9951 ± 0.0001
CCDBADTIM	684667	0.9900 ± 0.0001	624344	0.9899 ± 0.0001
CCD31FIB	684658	1.0000 ± 0.0000	624335	1.0000 ± 0.0000
TIMKF	628179	0.9175 ± 0.0003	572339	0.9167 ± 0.0004
VERRNG	585499	0.9321 ± 0.0003	533386	0.9319 ± 0.0003
ANGLI	585135	0.9994 ± 0.0000	533050	0.9994 ± 0.0000
ALLKFIT	577756	0.9874 ± 0.0002	526144	0.9870 ± 0.0002
TPICS	577003	0.9987 ± 0.0001	525413	0.9986 ± 0.0001
KIC	576825	0.9997 ± 0.0000	525245	0.9997 ± 0.0000
A_beam	0.1508 ± 0.0002		0.1373 ± 0.0002	

Table 6.4: The acceptance of the target and beam cuts using $K_{\mu 2}$ monitor trigger events. Table reproduced from [56].

6.1.4 Photon Veto Acceptance

To measure the acceptance A_{PV} (Table 6.5) of the photon veto cuts, the setup cuts $Setup_{\mathrm{PV}}$ were applied to create a sample of successfully reconstructed $K_{\mu 2}$ events without additional beam particles at decay time. To measure the acceptance of the photon veto, the same conditions as used for measuring A_{beam} were needed, but an even cleaner sample was created by also applying all the cuts measured for A_{beam}. Additionally, the requirement that the muon stopped prior to the 19th Range-Stack layer (stopping layer < 19) was imposed so that muons penetrating into the BVL and BV were not used for the measurement. Since the $K_{\mu 2}$ monitor trigger had no online PV requirement, it was possible to measure the acceptance of online and offline photon veto cuts with this sample.

6.1.5 $K_{\mu 2}$-Based Acceptance Summary

The total acceptance $A_{K_{\mu 2}}$ was the product of the four categories of components of acceptance measured using $K_{\mu 2}$ monitor trigger events:

$$A_{K_{\mu 2}} = A_{\mathrm{RS}} \times A_{\mathrm{recon}} \times A_{\mathrm{beam}} \times A_{\mathrm{PV}}. \tag{6.3}$$

Table 6.6 summarizes the results.

6.2 Acceptance Factors from π_{scatter} Monitor Trigger Events

The π_{scatter} monitor trigger selected beam pions that scattered into the active region of the detector. These events were similar to $K^+ \to \pi^+ \nu \bar{\nu}$ in that the π_{scatter} events covered the entire phase space of the kinematic signal region PNN2BOX and they provided a single π^+ in the Range-Stack with a continuous stopping layer distribution. The π_{scatter}

Cut	Loose		Tight	
	Events	Acceptance	Events	Acceptance
$Setup_{\mathrm{PV}}$	62556		56294	
LHEX	58388	0.9334 ± 0.0010	52530	0.9331 ± 0.0011
HEXAFTER	56244	0.9633 ± 0.0008	50621	0.9637 ± 0.0008
PVONLINE	53832	0.9571 ± 0.0009	48449	0.9571 ± 0.0009
LAY20or21	53413	0.9922 ± 0.0004	48069	0.9922 ± 0.0004
STLAY	52910	0.9906 ± 0.0004	47609	0.9904 ± 0.0004
RSHEX	50992	0.9637 ± 0.0008	45855	0.9632 ± 0.0009
PVCUT	49039	0.9617 ± 0.0009	44092	0.9616 ± 0.0009
TGPVCUT	48558	0.9902 ± 0.0005	43661	0.9902 ± 0.0005
TGPVTR	48558	1.0000 ± 0.0000	43661	1.0000 ± 0.0000
TGPV	47044	0.9688 ± 0.0008	40121	0.9189 ± 0.0013
ICPV	46996	0.9990 ± 0.0002	40007	0.9972 ± 0.0003
VCPV	46966	0.9994 ± 0.0001	39933	0.9981 ± 0.0002
COPV	46707	0.9945 ± 0.0003	39778	0.9961 ± 0.0003
MCPV	46702	0.9999 ± 0.0001	39768	0.9997 ± 0.0001
ECinner	43191	0.9248 ± 0.0012	31655	0.7960 ± 0.0020
ECouter	37652	0.8718 ± 0.0016	25258	0.7979 ± 0.0023
EC 2nd	37390	0.9930 ± 0.0004	23395	0.9262 ± 0.0016
RSPV	34680	0.9275 ± 0.0013	16681	0.7130 ± 0.0030
BVPV	32182	0.9280 ± 0.0014	15318	0.9183 ± 0.0021
BVLPV	31668	0.9840 ± 0.0007	15108	0.9863 ± 0.0009
ADPV	30132	0.9515 ± 0.0012	14439	0.9557 ± 0.0017
$EARLY_{BV}$	30106	0.9991 ± 0.0002	14433	0.9996 ± 0.0002
DPV	30103	0.9999 ± 0.0001	14432	0.9999 ± 0.0001
$EARLY_{BVL}$	30103	1.0000 ± 0.0000	14432	1.0000 ± 0.0000
PV60	-	-	14120	0.9784 ± 0.0021
A_{PVCUT}	0.6199 ± 0.0022		0.3234 ± 0.0022	
A_{PVALL}	0.4812 ± 0.0020		0.2508 ± 0.0018	

Table 6.5: The online and offline acceptance of the photon veto cuts using $K_{\mu2}$ monitor trigger events. The acceptance A_{PVCUT} refers specifically to the acceptance of the cut PV60 (loose) or PV30 (tight). The component of acceptance A_{PVALL} is the product of all components of acceptance measured in this table. Table reproduced from [56].

	Loose	Tight
A_{RS}	0.9999 ± 0.0000	0.9999 ± 0.0000
A_{recon}	0.9994 ± 0.0000	0.9996 ± 0.0000
A_{beam}	0.1508 ± 0.0002	0.1373 ± 0.0002
A_{PVALL}	0.4812 ± 0.0020	0.2508 ± 0.0018
$A_{K_{\mu 2}}$	0.0725 ± 0.0003	0.0344 ± 0.0003

Table 6.6: The $K_{\mu 2}$-based acceptance summary Table reproduced from [56].

π_{scatter} Setup Categories	Measured Quantities	Setup Cuts
$Setup_{\mathrm{BAD\_STC}}$	A_{BADSTC}	RD_TRK, TRKTIM, STLAY, UTC, RDUTM, PDC, ICBIT, `b4abm2` < 1.3MeV, $\lvert \mathtt{t_{pi}} - \mathtt{t_{RS}} \rvert < 5$ns, $\lvert \mathtt{t_{IC}} - \mathtt{t_{RS}} \rvert < 5$ns, TARGF, DTGTTP, RTDIF, TGQUALT, TGZFOOL, CKTRS, CKTAIL, PVCUT(onlyRS), COS3D, LAYV4, BOXLOOSE
$Setup_{\mathrm{RS-kin}}$	$A_{\mathrm{RS-kin}}$, $A_{\mathrm{RS-kin}}^{\mathrm{small}}$, $A_{\mathrm{RS-kin}}^{\mathrm{large}}$	$Setup_{\mathrm{BAD\_STC}}$, BAD_STC, *TDCUTS*
$Setup_{\mu \to \pi \to e}$	A_{TD1}, A_{TD2}	$Setup_{\mathrm{BAD\_STC}}$, BAD_STC, RNGMOM, ZFRF, ZUTOUT, LAYER14, UTCQUAL, EIC

Table 6.7: The setup cuts applied for the π_{scatter}-based acceptance measurements. The quantity `b4abm2` is the energy deposited in the B4 near beam time. Table reproduced from [56].

monitor trigger events were used to measure the acceptance of Range-Stack stopping counter reliability (A_{BADSTC}), kinematic and quality cuts in the UTC and Range-Stack ($A_{\mathrm{RS-kin}}$), and particle identification in the Range-Stack ($A_{\pi \to \mu \to e}$). Table 6.7 shows the setup cuts applied for each of these categories of cuts.

6.2.1 Range-Stack Stopping Counter Reliability

The setup cuts $Setup_{\mathrm{BADSTC}}$ were applied to create the sample used to measure the acceptance A_{BADSTC} (Table 6.8) of BAD_STC, a cut that removed events when the TD in the Range-Stack stopping counter was not working properly. This sample required that

Cut	Loose		Tight	
	Events	Acceptance	Events	Acceptance
$Setup_{\text{BAD\_STC}}$	153716		74214	
BAD_STC	153474	0.9984 ± 0.0001	74093	0.9984 ± 0.0001
A_{BADSTC}		0.9984 ± 0.0001		0.9984 ± 0.0001

Table 6.8: The acceptance of BAD_STC using π_{scatter} monitor trigger events. Table reproduced from [56].

the events had a single beam π^+ that scattered in the target and entered the Range-Stack. For this sample, beam kaons were removed (`b4abm2` < 1.3MeV, CKTRS, CKTAIL), the tracks in the target and Range-Stack were required to be created from the same particle ($|\text{t}_{\text{pi}} - \text{t}_{\text{RS}}|$ < 5ns, $|\text{t}_{\text{IC}} - \text{t}_{\text{RS}}|$ < 5ns), the loose kinematic signal region was chosen (BOXLOOSE), and a well reconstructed track was required (the remaining cuts). Additionally, the Range-Stack subsystems of the photon veto "PVCUT(onlyRS)" were applied to remove coincident activity in the Range-Stack.

6.2.2 Range-Stack-Kinematic Acceptance

To measure the acceptance $A_{\text{RS-kin}}$ (Table 6.10) of the kinematic and quality cuts in the UTC and Range-Stack, the setup cuts $Setup_{\text{RS-kin}}$ were applied to create a sample of events that had a single beam π^+ that scattered in the target and decayed at rest in the Range-Stack. In addition to the setup cuts $Setup_{\text{BADSTC}}$, the $\pi^+ \to \mu^+ \to e^+$ decay-sequence cuts $TDCUTS$ were applied to remove events where the π^+ decayed in flight in the Range-Stack.

Good target reconstruction required good classification of the kaon and pion fibers, but since the incoming particle was a beam pion and not a kaon, the clustering based on times and energies was not as reliable as for a stopped-kaon decay. This poor target reconstruction led to less well-measured momentum (`ptot`), range (`rtot`) and energy (`etot`) of the outgoing particle. To determine the systematic uncertainty associated with

these larger uncertainties in momentum, range and energy, the kinematic signal region cuts (BOXLOOSE) were all loosened and tightened by one standard deviation to create small and large kinematic boxes, respectively.

The relative resolutions of the reconstructed π^+ mass,

$$\mathtt{m}_\pi = \frac{\mathtt{ptot}^2 - \mathtt{etot}^2}{2 \cdot \mathtt{etot}}, \tag{6.4}$$

from π_{scatter} and $K_{\pi 2}$ events were used to determine the size of the shifts to the kinematic signal region. The distributions of $\mathtt{m}_\pi$ for these events are shown in Figure 6.1, where $\sigma_{\pi_{\mathrm{scatter}}}$ was 13.8 MeV and $\sigma_{K_{\pi 2}}$ was 8.4 MeV. Taking the mean reconstructed mass from the $K_{\pi 2}$ events as 139.4 MeV, the relative uncertainty in the reconstructed mass of these two types events was determined,

$$\frac{\sqrt{13.8^2 - 8.4^2}}{139.4} = 7.8\%. \tag{6.5}$$

The contributions to the resolution of the reconstructed mass from the momentum and energy were roughly the same, so the uncertainties in each were taken as $7.8\%/\sqrt{2} = 5.5\%$. Additionally, the range scaled with energy so the uncertainty in $\mathtt{rtot}$ was also taken as 5.5%. The boundaries of the nominal loose kinematic signal region (BOXLOOSE) were loosened and tightened by 5.5% to create BOXSMALL and BOXLARGE as shown in Table 6.9. These loosened and tightened kinematic signal regions were applied in $Setup_{\mathrm{RS-kin}}$ to measure $A_{\mathrm{RS-kin}}^{\mathrm{small}}$ (Table 6.11) and $A_{\mathrm{RS-kin}}^{\mathrm{large}}$ (Table 6.12), respectively. The variations between the components of acceptance $A_{\mathrm{RS-kin}}^{\mathrm{small}}$ and $A_{\mathrm{RS-kin}}^{\mathrm{large}}$ were used to determine the systematic uncertainty for the measurement $A_{\mathrm{RS-kin}}$. The final values for $A_{\mathrm{RS-kin}}$ are shown in Table 6.15.
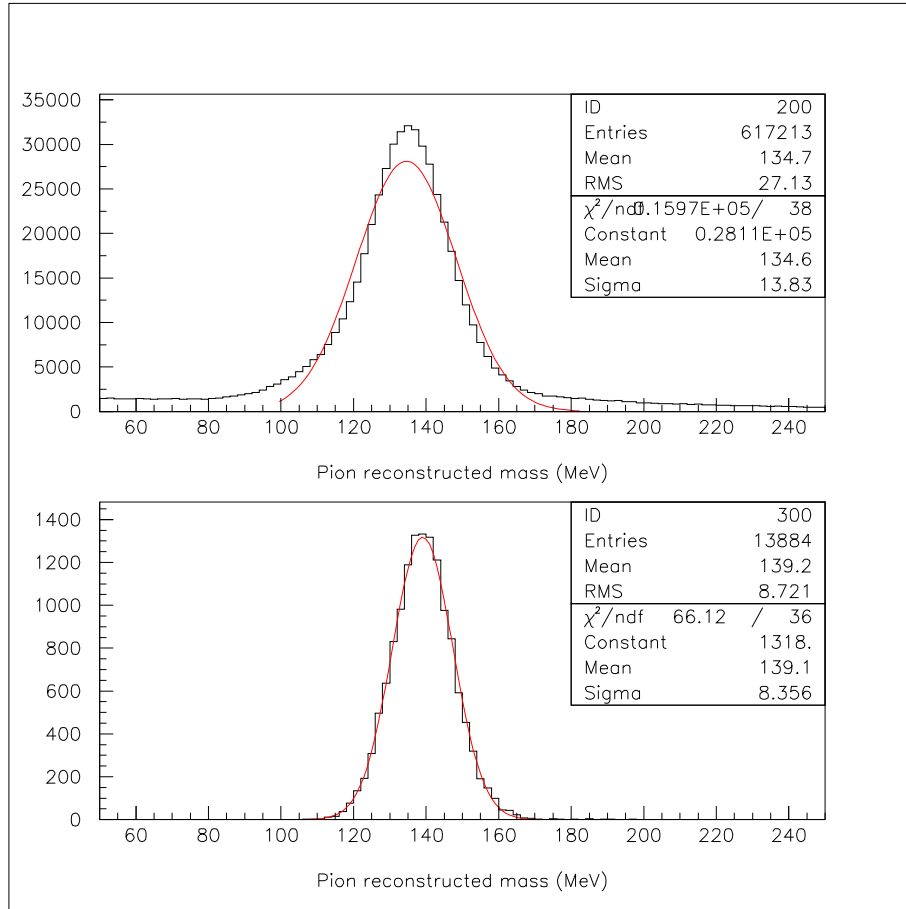
Figure 6.1: Distributions of the reconstructed π^+ mass from π_{scatter} (top) and $K_{\pi 2}$ events (bottom). Figure reproduced from [56].

	Momentum ptot (MeV/c)	Energy etot (MeV)	Range rtot (cm)
BOXLOOSE	$140 - 199$	$60.0 - 100.5$	$12 - 28$
BOXSMALL	$147.7 - 188.1$	$63.3 - 95.0$	$12.7 - 26.5$
BOXLARGE	$132.3 - 209.9$	$56.7 - 106.7$	$11.3 - 29.5$

Table 6.9: The "small" and "large" versions of the loose kinematic signal regions as created by loosening and tightening the nominal PNN2BOX by one standard deviation (5.5%). Table reproduced from [56].

Cut	Loose		Tight	
	Events	Acceptance	Events	Acceptance
$Setup_{\mathrm{RS-kin}}$	88719		32932	
UTCQUAL	84373	0.9510 ± 0.0007	31672	0.9617 ± 0.0011
RNGMOM	82845	0.9819 ± 0.0005	31161	0.9839 ± 0.0007
RSDEDXMAX	80449	0.9711 ± 0.0006	30355	0.9741 ± 0.0009
RSDEDXCL	76828	0.9550 ± 0.0007	29048	0.9569 ± 0.0012
RSLIKE	76828	1.0000 ± 0.0000	29048	1.0000 ± 0.0000
PRRF1	76196	0.9918 ± 0.0003	28841	0.9929 ± 0.0005
PRRFZ	73596	0.9659 ± 0.0007	27862	0.9661 ± 0.0011
$A_{\mathrm{RS-kin}}$	0.8295 ± 0.0013		0.8461 ± 0.0020	

Table 6.10: The acceptance of the Range-Stack-kinematic cuts using π_{scatter} monitor trigger events. The "Tight" label indicates the tightening of *TDCUTS* and PVCUT(onlyRS). Table reproduced from [56].

Cut	Loose		Tight	
	Events	Acceptance	Events	Acceptance
$Setup_{\mathrm{RS-kin}}^{\mathrm{small}}$	63400		29195	
UTCQUAL	60350	0.9519 ± 0.0009	27906	0.9558 ± 0.0012
RNGMOM	59251	0.9818 ± 0.0005	27396	0.9817 ± 0.0008
RSDEDXMAX	57778	0.9751 ± 0.0006	26746	0.9763 ± 0.0009
RSDEDXCL	55375	0.9584 ± 0.0008	25685	0.9603 ± 0.0012
RSLIKE	55375	1.0000 ± 0.0000	25685	1.0000 ± 0.0000
PRRF1	55017	0.9935 ± 0.0003	25548	0.9947 ± 0.0005
PRRFZ	53324	0.9692 ± 0.0007	24778	0.9699 ± 0.0011
LAYER14	53324	1.0000 ± 0.0000	24778	1.0000 ± 0.0000
$A_{\mathrm{RS-kin}}^{\mathrm{small}}$	0.8411 ± 0.0015		0.8487 ± 0.0021	

Table 6.11: The acceptance of the Range-Stack-kinematic cuts in the small version of the loose kinematic box BOXSMALL using π_{scatter} monitor trigger events. The "Tight" label indicates the tightening of *TDCUTS* and PVCUT(onlyRS). Table reproduced from [56].

Cut	Loose		Tight	
	Events	Acceptance	Events	Acceptance
$Setup_{\text{RS}-\text{kin}}^{\text{large}}$	110317		51078	
UTCQUAL	104830	0.9503 ± 0.0007	48730	0.9540 ± 0.0009
RNGMOM	102909	0.9817 ± 0.0004	47846	0.9819 ± 0.0006
RSDEDXMAX	99517	0.9670 ± 0.0006	46347	0.9687 ± 0.0008
RSDEDXCL	94726	0.9519 ± 0.0007	44201	0.9537 ± 0.0010
RSLIKE	94726	1.0000 ± 0.0000	44201	1.0000 ± 0.0000
PRRF1	93737	0.9896 ± 0.0003	43806	0.9911 ± 0.0005
PRRFZ	90176	0.9620 ± 0.0006	42205	0.9635 ± 0.0009
LAYER14	90176	1.0000 ± 0.0000	42205	1.0000 ± 0.0000
$A_{\text{RS}-\text{kin}}^{\text{large}}$	0.8174 ± 0.0012		0.8263 ± 0.0017	

Table 6.12: The acceptance of the Range-Stack-kinematic cuts in the large version of the loose kinematic box BOXLARGE using π_{scatter} monitor trigger events. The "Tight" label indicates the tightening of *TDCUTS* and PVCUT(onlyRS). Table reproduced from [56].

6.2.3 $\pi^+ \to \mu^+ \to e^+$ Identification Acceptance

To measure the acceptance $A_{\pi \to \mu \to e}$ (Tables 6.13 and 6.14) of the Range-Stack particle identification cuts, the setup cuts $Setup_{\pi \to \mu \to e}$ were applied to create a sample of events that had a single beam π^+ that scattered in the target and entered the Range-Stack. In addition to the setup cuts $Setup_{\text{BADSTC}}$, the Range-Stack kinematic cuts were applied to ensure that the track in the Range-Stack was due to a π^+. Since the π_{scatter} monitor trigger did not include the online L1.1 and L1.2 triggers, the components of acceptance of these online cuts were also measured with this sample.

Some small correlations existed between some of the cuts measured in $A_{\text{RS}-\text{kin}}$ and $A_{\pi \to \mu \to e}$. A μ^+ accidental along the Range-Stack track could have been rejected by both the dE/dx condition of RSDEDX and by the $\mu^+ \to e^+$ decay requirement of EV5. The other correlation was between the dependence of the Range-Stack stopping-counter energy in PRRF and the TD-pulse fitting information used by TDNN. To examine the effects of these correlations, the cuts measured for $A_{\pi \to \mu \to e}$ were measured without (A_{TD1}, Table 6.13) and with (A_{TD2}, Table 6.14) RSDEDX and PRRF applied as setup cuts. The

Cut	Loose		Tight	
	Events	Acceptance	Events	Acceptance
$Setup_{\pi \to \mu \to e}$	126239		64210	
PIFLG	104055	0.8243 ± 0.0011	53280	0.8298 ± 0.0015
RSHEX2	102123	0.9814 ± 0.0004	52271	0.9811 ± 0.0006
LEV1.1	82659	0.8094 ± 0.0012	42382	0.8108 ± 0.0017
LEV1.2	69374	0.8393 ± 0.0013	38160	0.9004 ± 0.0015
TDCUT	65186	0.9396 ± 0.0009	35907	0.9410 ± 0.0012
ELVETO	62425	0.9576 ± 0.0008	34453	0.9595 ± 0.0010
TDFOOL	62208	0.9965 ± 0.0002	34343	0.9968 ± 0.0003
TDNN	58607	0.9421 ± 0.0009	29016	0.8449 ± 0.0020
EV5	58607	1.0000 ± 0.0000	24264	0.8362 ± 0.0022
A_{TD1}	0.4643 ± 0.0014		0.3779 ± 0.0019	

Table 6.13: The acceptance of the $\pi^+ \to \mu^+ \to e^+$ cuts using π_{scatter} monitor trigger events. Table reproduced from [56].

measurement for A_{TD2} included additional acceptance loss due to π^+ absorption and π^+ decay-in-flight for which a 1.4% correction factor was estimated using Monte Carlo [55] and applied to A_{TD2}. The value for $A_{\pi \to \mu \to e}$ was taken as the average of A_{TD1} and A_{TD2}, with the systematic uncertainty taken from the difference.

6.2.4 π_{scatter}-Based Acceptance Summary

The total acceptance $A_{\pi_{\text{scatter}}}$ was the product of the three categories of components of acceptance measured using π_{scatter} monitor trigger events:

$$A_{\pi_{\text{scatter}}} = A_{\text{BADSTC}} \times A_{\text{RS-kin}} \times A_{\pi \to \mu \to e}. \qquad (6.6)$$

Table 6.15 summarizes the results.

Cut	Loose		Tight	
	Events	Acceptance	Events	Acceptance
$Setup_{\pi\to\mu\to e}$	107124		55113	
RSDEDX, PRRF	107124		55113	
PIFLG	90161	0.8417 ± 0.0011	46466	0.8431 ± 0.0016
RSHEX2	88616	0.9829 ± 0.0004	45640	0.9822 ± 0.0006
L1.1	72545	0.8186 ± 0.0013	37347	0.8183 ± 0.0018
L1.2	61913	0.8534 ± 0.0013	34125	0.9137 ± 0.0015
TDCUT	58288	0.9415 ± 0.0009	32155	0.9423 ± 0.0013
ELVETO	55833	0.9579 ± 0.0008	30859	0.9597 ± 0.0011
TDFOOL	55655	0.9968 ± 0.0002	30774	0.9972 ± 0.0003
TDNN	52472	0.9428 ± 0.0010	26060	0.8468 ± 0.0021
EV5	52472	1.0000 ± 0.0000	21820	0.8373 ± 0.0023
A_{TD2}(uncorrected)	0.4898 ± 0.0015		0.3959 ± 0.0021	
A_{TD2}	0.4967 ± 0.0015		0.4015 ± 0.0021	

Table 6.14: The acceptance of the $\pi^+ \to \mu^+ \to e^+$ cuts using π_{scatter} monitor trigger events. The acceptance A_{TD2}(uncorrected) was the acceptance before the correction factor of 1.014 was applied. This correction factor corrected for π^+ decay-in-flight and π^+ absorption in the stopping counter. Table reproduced from [56].

	Loose	Tight
A_{BADSTC}	0.9984 ± 0.0001	0.9984 ± 0.0001
$A_{\mathrm{RS-kin}}$	$0.8295 \pm 0.0013 \pm 0.012$	$0.8461 \pm 0.0020^{+0.003}_{-0.020}$
$A_{\pi\to\mu\to e}$	$0.4805 \pm 0.0015 \pm 0.016$	$0.3897 \pm 0.0021 \pm 0.012$
$A_{\pi_{\mathrm{scat}}}$	$0.3980 \pm 0.0014 \pm 0.014$	$0.3292 \pm 0.002 \ ^{+0.010}_{-0.013}$

Table 6.15: The π_{scatter}-based acceptance summary Table reproduced from [56].

$K_{\pi 2}$ Setup Categories	Measured Quantities	Setup Cuts
$Setup_{\mathrm{utc}}$	A_{utc}	TRIGGER, RD_TRK, TRKTIM, STLAY, BAD_STC
$Setup_{\mathrm{opsveto}}$	A_{opsveto}	$Setup_{\mathrm{utc}}$, UTC, RDUTM, PDC, *BEAMCUTS*, DELCO, *KINCUTS*, *TGCUTS* (excluding $A_{\mathrm{TG-kin}}$ and OPSVETO), *TDCUTS*, KP2BOX
$Setup_{\mathrm{TG-kin}}$	$A_{\mathrm{TG-kin}}$	$Setup_{\mathrm{opsveto}}$, OPSVETO, TGPVCUT

Table 6.16: The setup cuts applied for the $K_{\pi 2}$-based acceptance measurements. The notation "A_{opsveto} cuts" means that all the cuts whose acceptance were measured to determine the quantity A_{opsveto} were applied as setup cuts. Table reproduced from [56].

6.3   Acceptance Factors from $K_{\pi 2}$ Monitor Trigger Events

The $K_{\pi 2}$ monitor trigger events were similar to $K^+ \to \pi^+ \nu \bar{\nu}$ in that they both had a single outgoing π^+ coming from the incoming K^+, thus $K_{\pi 2}$ monitor trigger events were used to measure the acceptance of cuts requiring good decay-vertex determination in the target. The $K_{\pi 2}$ monitor trigger events were used to measure the acceptance of the PASS1 UTC cut (A_{UTC}), OPSVETO (A_{opsveto}), and the target kinematic cuts ($A_{\mathrm{TG-kin}}$). Table 6.16 shows the setup cuts applied for each of these categories of cuts.

6.3.1   UTC Acceptance

To measure the acceptance A_{utc} (Table 6.17) of the PASS1 UTC cut, the setup cuts $Setup_{\mathrm{utc}}$ were applied to create a sample with valid reconstruction of events in the target and Range-Stack.

Cut	Events	Acceptance
$Setup_{\text{utc}}$	1502895	
UTC	1417906	0.9435 ± 0.0002
A_{UTC}		0.9435 ± 0.0002

Table 6.17: The acceptance of UTC using $K_{\pi 2}$ monitor trigger events. Table reproduced from [56].

Cut	Events	Acceptance
$Setup_{\text{opsveto}}$	64024	
OPSVETO	62370	0.9742 ± 0.0006
A_{opsveto}		0.9742 ± 0.0006

Table 6.18: The acceptance of OPSVETO using $K_{\pi 2}$ monitor trigger events. Table reproduced from [56].

6.3.2 OPSVETO Acceptance

To measure the acceptance A_{opsveto} (Table 6.18) of OPSVETO, the setup cuts $Setup_{\text{opsveto}}$ were applied to create a sample of events with valid reconstruction in the target, UTC and Range-Stack, along with the requirement of no secondary beam particles. These setup cuts consisted of all analysis cuts other than the photon veto PVCUT, OPSVETO and the target quality cuts $TGCUTS$ measured in $A_{\text{TG-kin}}$. The group of cuts $BEAMCUTS$ was applied to remove secondary beam particles. The kinematic box cut KP2BOX and the rest of the listed cuts were applied to ensure good $K_{\pi 2}$ decays.

6.3.3 Target Kinematic Acceptance

The cuts measured in the acceptance $A_{\text{TG-Kin}}$ (Table 6.19) were target-kinematic cuts that required valid reconstruction in the target, UTC and Range-Stack along with the requirements of no secondary beam particles and the decay product to be a π^+. The setup cuts $Setup_{\text{TG-kin}}$ were applied to create a sample similar to that used for A_{opsveto}, with the additional application of OPSVETO and the online target photon veto TGPVCUT

181

Cut	Loose		Tight	
	Events	Acceptance	Events	Acceptance
$Setup_{\text{TG−kin}}$	61687		37295	
TGDEDX	61017	0.9891 ± 0.0004	36883	0.9890 ± 0.0005
TGER	61000	0.9997 ± 0.0001	36873	0.9997 ± 0.0001
TGENR	58984	0.9670 ± 0.0007	35594	0.9653 ± 0.0010
TGLIKE1	57931	0.9821 ± 0.0006	34946	0.9818 ± 0.0007
TGLIKE2	57005	0.9840 ± 0.0005	34381	0.9838 ± 0.0007
EPITG	51086	0.8962 ± 0.0013	30874	0.8980 ± 0.0016
EPIMAXK	51086	1.0000 ± 0.0000	30874	1.0000 ± 0.0000
TGEDGE	50802	0.9944 ± 0.0003	30715	0.9949 ± 0.0004
DRP	50716	0.9983 ± 0.0002	30658	0.9981 ± 0.0003
CHI567	44324	0.8740 ± 0.0015	26823	0.8749 ± 0.0019
CHI5MAX	44323	1.0000 ± 0.0000	26822	1.0000 ± 0.0000
$A_{\text{TG−kin}}$	0.7185 ± 0.0018		0.7192 ± 0.0023	

Table 6.19: The acceptance of the target kinematic cuts using $K_{\pi 2}$ monitor trigger events. Table reproduced from [56].

to remove additional activity in the target.

6.3.4 $K_{\pi 2}$ -Based Acceptance Summary

The total acceptance $A_{K_{\pi 2}}$ was the product of the three categories of components of acceptance measured using $K_{\pi 2}$ monitor trigger events:

$$A_{K_{\pi 2}} = A_{\text{utc}} \times A_{\text{opsveto}} \times A_{\text{TG−kin}}. \tag{6.7}$$

Table 6.20 summarizes the results.

6.4   Acceptance Factors Using Monte Carlo

The acceptance losses of the online trigger (A_{trigger}), and the phase space and solid angle cuts (A_{box}) were measured using approximately 10^5 $K^+ \rightarrow \pi^+ \nu \bar{\nu}$ Monte Carlo events.

	Loose	Tight
A_{utc}	0.9435 ± 0.0002	0.9435 ± 0.0002
A_{opsveto}	0.9742 ± 0.0006	0.9735 ± 0.0008
$A_{\text{TG}-\text{kin}}$	0.7185 ± 0.00181	0.7192 ± 0.0023
$A_{K_{\pi2}}$	0.6604 ± 0.0018	0.6606 ± 0.0023

Table 6.20: The $K_{\pi2}$-based acceptance summary Table reproduced from [56].

The acceptance losses due to pion decay-in-flight and pion nuclear interactions were also measured due to the inclusion of these processes in Monte Carlo. The cut UFATE required that the pion stopped without decay or interaction. The cut USTMED required that the pion stopped in a scintillator counter in the Range-Stack. The cut USTOP_HEX required that the offline reconstructed stopping counter agreed with the true stopping counter. These three cuts used information taken directly from the Monte Carlo event and not the subsequent reconstruction. The cut SETUP was a requirement that the reconstructed momentum `ptot` was less than 300 MeV.

6.5   Acceptance Summary

The total acceptance A_{total} of signal events due to all analysis cuts was the product of the components of acceptance from each of the monitor trigger data and Monte Carlo:

$$A_{\text{total}} = A_{K_{\mu2}} \times A_{\pi_{\text{scatter}}} \times A_{K_{\pi2}} \times A_{\text{MC}}. \tag{6.8}$$

These values are summarized in Table 6.22.

6.6   Correction to T•2 Trigger Acceptance

A correction factor was determined to account for the fact that the simulated T•2 trigger in Monte Carlo did not include acceptance losses due to the geometric (ϵ_{geom}) and counter

Cut	
	99999
T●2	39227
$3_{ct} \cdot 4_{ct} \cdot 5_{ct} \cdot 6_{ct}$	27575
Trigger $(\pi\nu\bar{\nu}(1)$ or $\pi\nu\bar{\nu}(2))$	26288
A_{trigger}	0.2629 ± 0.0014
SETUP	25793
UFATE	22688
USTMED	22517
USTOP_HEX	21743
COS3D	20870
LAYER14	20838
ZFRF	20175
ZUTOUT	20148
BOXLOOSE	9552
$A_{\text{box}}^{\text{loose}}$	0.3703 ± 0.0030
$A_{\text{MC}}^{\text{loose}}$	0.0974 ± 0.0009
BOXTIGHT	7758
$A_{\text{box}}^{\text{tight}}$	0.3008 ± 0.0029
$A_{\text{MC}}^{\text{tight}}$	0.0791 ± 0.0009

Table 6.21: The acceptance of the online trigger, phase space and solid angle cuts using Monte Carlo. Table reproduced from [56].

	Loose	Tight
$A_{K_{\mu 2}}$	0.0725 ± 0.0003	0.0344 ± 0.0003
$A_{\pi_{\text{scatter}}}$	$0.3980 \pm 0.0014 \pm 0.014$	$0.3292 \pm 0.0020^{+0.010}_{-0.013}$
$A_{K_{\pi 2}}$	0.6604 ± 0.0018	0.6606 ± 0.0023
A_{MC}	0.0974 ± 0.0009	0.0791 ± 0.0009
A_{total}	$(1.857 \pm 0.021 \pm 0.065) \times 10^{-3}$	$(0.592 \pm 0.009^{+0.018}_{-0.024}) \times 10^{-3}$

Table 6.22: The total acceptance of all online and offline cuts. Table reproduced from [56].

184

($\epsilon_{\text{counter}}$) inefficiencies of the T-Counters. The T•2 trigger was a coincidence between the first two layers of the RS (T-Counter and layer 2) in the same sector. The geometric inefficiency was due to tracks passing through the azimuthal gap between two adjacent T-Counters. The counter inefficiency was due to events that did not produce a large enough signal to pass our threshold. The counter inefficiency was expressed as

$$\epsilon_{\text{counter}} = e^{-kE}, \tag{6.9}$$

where k was the number of photoelectrons produced per MeV and E was the mean energy deposited in the T-counters.

Both inefficiencies were originally determined in [33] using $K_{\pi 2}$ and $K_{\mu 2}$ events from KB monitor trigger data (see Section 2.7 for trigger definitions). The KB monitor trigger data were used since the $K_{\pi 2}$ and $K_{\mu 2}$ triggers contain the T•2 trigger as one of their conditions. Reconstructed events pointing at the T-Counters were checked against their T•2 online trigger state to determine the inefficiencies. The values corresponding to the $K_{\pi 2}$ monitor trigger data were used for the T•2 trigger inefficiencies in this analysis due to their similarity to $K^+ \to \pi^+ \nu \bar{\nu}$ PNN2 pions. The geometric inefficiency was found to be $\epsilon_{\text{geom}} = 0.0286 \pm 0.0027$.

For the counter inefficiency, k values of 1.74 and 1.62 photoelectrons per MeV were found. The first value was for all sectors apart from two that had hardware problems for which the second value applied. Monte Carlo $K^+ \to \pi^+ \nu \bar{\nu}$ events in the PNN2 kinematic signal region were used to determine the mean energy deposited in the T-counters as a function of momentum, giving a counter inefficiency of $\epsilon_{\text{counter}} = 0.0210 \pm 0.0027$ [37].

Subtracting the two inefficiencies from unity gave a T•2 trigger efficiency of

$$\epsilon_{\text{T•2}} = 0.9505 \pm 0.0012_{stat.} \pm 0.0143_{sys.}, \tag{6.10}$$

where the 1.5% systematic uncertainty accounted for the variation observed when further constraining the z-position requirement of the reconstructed track passing through the T-counters as detailed in [33].

6.7 K^+ Stopping Fraction

The K^+ stopping fraction quantified the number of beam kaons that decayed in the target relative to the number of kaons that satisfied the KB trigger requirement. These kaons decayed after the Čerenkov counter with the daughter satisfying the B4 and target requirements of the KB trigger or they deposited some energy in the target and exited without decaying. This fraction was obtained as part of the E949 PNN1 analysis [33] by normalizing the total kaon exposure to the $K_{\mu 2}$ branching ratio using $K_{\mu 2}$ monitor trigger events. The stopping fraction was found to be

$$f_s = 0.7740 \pm 0.0011. \tag{6.11}$$

6.8 Measurement of the $K_{\pi 2}$ Branching Ratio

The measurement of the $K_{\pi 2}$ branching ratio served as a consistency check of the acceptance measurements detailed earlier in this chapter. The $K_{\pi 2}$ monitor trigger data were used for this measurement. The online prescale factor for these monitor trigger data was 163840 for runs earlier than and including run 48045. For runs after 48045, the prescale factor was 131072. The total number of stopped $K_{\pi 2}$ events in the monitor trigger data ($N_{K_{\pi 2}}$) was measured by applying the cuts shown in Figure 6.2. Acceptance measurements were performed for all the triggers and cuts applied to make the $N_{K_{\pi 2}}$ measurement. Details of the acceptance measurements used to determine the total acceptance $A_{K_{\pi 2}}$ are found in Appendix F.

186

$$N_{K_{\pi 2}}$$
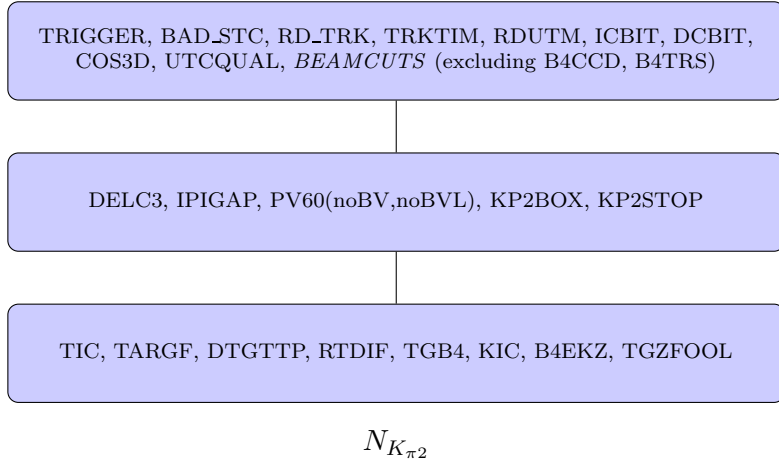
Figure 6.2: The cuts applied to measure $N_{K_{\pi 2}}$.

	All Runs	Prescale 163840	Prescale 131072
$N_{K_{\pi 2}}$	144989	2973	141926
Prescale Factor	131926	163840	131072
KB_{live}	1.792×10^{12}	0.052×10^{12}	1.740×10^{12}
$A_{K_{\pi 2}}$	0.04833 ± 0.00047	0.04921 ± 0.00084	0.04830 ± 0.00047
$\mathcal{B}(K_{\pi 2})$	0.2213 ± 0.0022	0.1905 ± 0.0051	0.2216 ± 0.0016

Table 6.23: The summary of the $K_{\pi 2}$ branching ratio measurements for all runs and for the two different prescale factors. Details for the constituent components of acceptance making up the total acceptance $A_{K_{\pi 2}}$ are given in Appendix F. Table reproduced from [55].

The $K_{\pi 2}$ branching ratio was measured using

$$\mathcal{B}\left(K^+ \to \pi^+\pi^0\right) = \frac{PRESCALE \cdot N_{K_{\pi 2}}}{\text{KB}_{\text{live}} \cdot A_{K_{\pi 2}}}, \tag{6.12}$$

where $PRESCALE$ was the prescale factor and KB_{live} was the total number of K^+ decays. Table 6.23 summarizes the results of this calculation for all runs (weighted average) and for the two different prescale factors. The average measured branching ratio of 0.2213 ± 0.0022 overestimates the world average value of 0.2092 ± 0.0012 [99] by approximately 5.8%.

It was also observed that the range of variation in the average measured branching ratio was approximately 4.4% as a function of rate as shown in Figure 6.3.
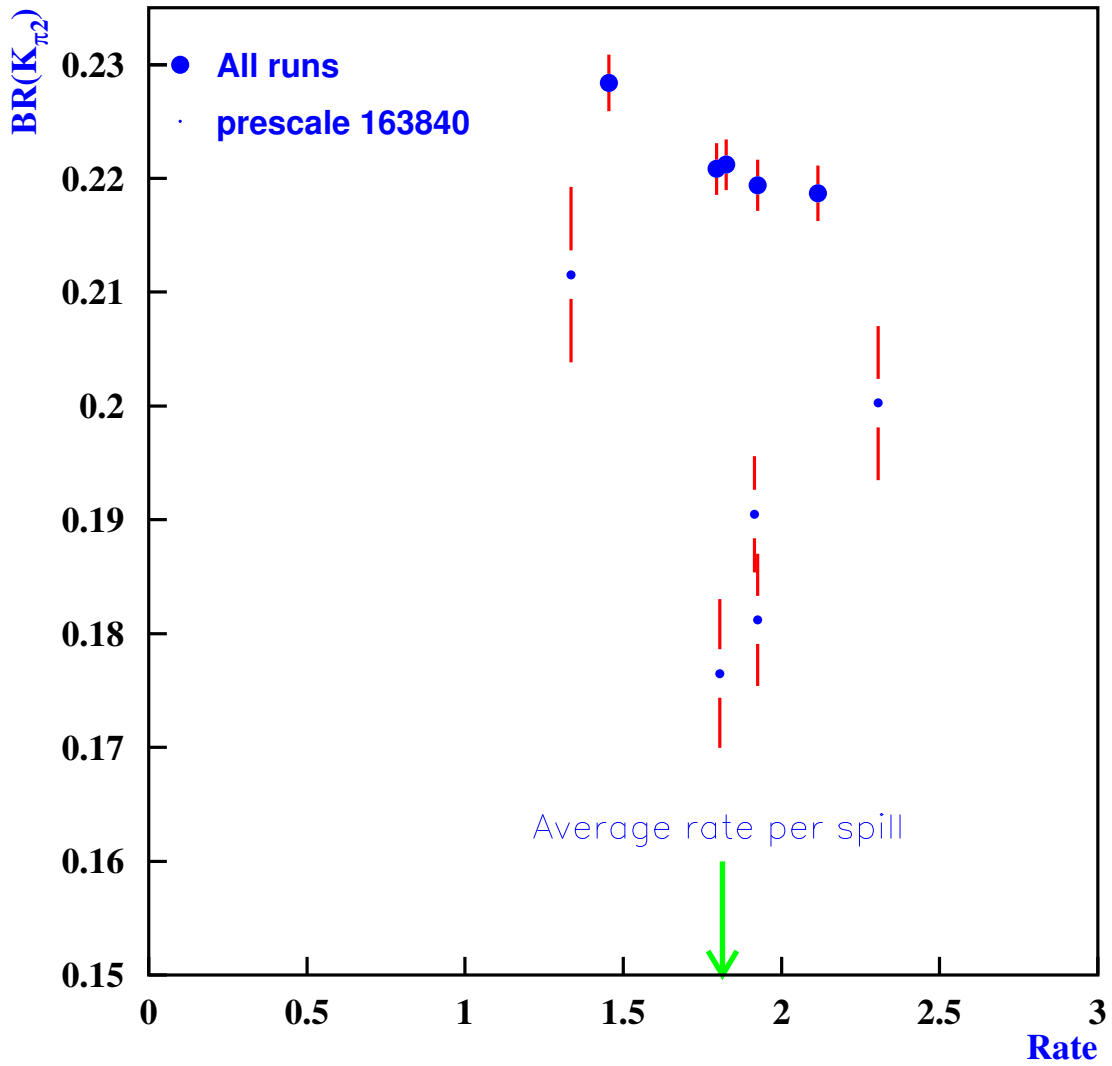
Figure 6.3: The $K_{\pi 2}$ branching fraction versus rate for all runs (large points) and for runs with prescaler 163840 (small points). Rate is measured in 10^6 KB_{live} per second during the spill. The arrow shows the average rate. Figure modified from [55].

	Loose	Tight	Source
A_{total}	$(1.857 \pm 0.021 \pm 0.065) \times 10^{-3}$	$\left(0.592 \pm 0.009\,{}^{+0.018}_{-0.024}\right) \times 10^{-3}$	Table 6.22
$\epsilon_{T\bullet 2}$	$0.9505 \pm 0.0012 \pm 0.0143$		Section 6.6
f_s	0.7740 ± 0.0011		Ref. [92]
KB_{live}	1.7096×10^{12}		Section 2.8
SES	$(4.28 \pm 0.43) \times 10^{-10}$	$(13.13 \pm 1.31) \times 10^{-10}$	

Table 6.24: The summary of the values used to determine the single event sensitivity. For values with two sets of uncertainties, the first uncertainty is statistical and the second systematic. The total uncertainties of SES reflect the 10% total uncertainty applied to the acceptance due to consistency issues when measuring $\mathcal{B}\left(K^+ \to \pi^+\pi^0\right)$. Table reproduced from [55].

A relative systematic uncertainty of 10% was assigned to the total signal acceptance to account for the concerns discussed above and the inconsistencies in the measured branching ratios for the two different prescale factors.

6.9   Single-Event Sensitivity

The single event sensitivity (SES) was the branching ratio that would have corresponded to one candidate in the absence of background. It was determined by

$$SES^{-1} = A_{\text{total}} \times \epsilon_{\text{T}\bullet 2} \times f_s \times KB_{\text{live}}, \tag{6.13}$$

where A_{total} was the total acceptance of all online and offline cuts, $\epsilon_{\text{T}\bullet 2}$ was the T$\bullet$2 trigger efficiency, f_s was the fraction of beam kaons stopping in the target, and KB_{live} was the total number of K^+ decays in the detector for the full data set. Table 6.24 summarizes SES for the loose and tight signal regions.

The relative uncertainty associated with the single event sensitivity was conservatively set to 10% based on the uncertainties in the total acceptance and the discrepancy between the measured $K_{\pi 2}$ branching fraction and the world average (Section 6.8).

Chapter 7

Results

7.1 Cell Definitions

The signal region was divided into nine cells using the loose and tight versions of the kinematic phase space cuts (PNN2BOX), the delayed coincidence cuts (DELC), the $\pi^+ \to \mu^+ \to e^+$ decay-sequence cuts ($TDCUTS$), and the photon veto (PVCUT). Each of these cuts was used to divide the signal region into two, with the first region being defined by the application of the tight version of the cut and the second region being the rest of the signal region outside of the region defined by the tight version of the cut:

$$\begin{aligned}
\text{KIN}_1 &\equiv \text{BOXTIGHT}, & \text{KIN}_2 &\equiv \overline{\text{BOXTIGHT}} \cdot \text{BOXLOOSE}, \\
\text{DC}_1 &\equiv \text{DELC6}, & \text{DC}_2 &\equiv \overline{\text{DELC6}} \cdot \text{DELC3}, \\
\text{TD}_1 &\equiv \text{TDTIGHT}, & \text{TD}_2 &\equiv \overline{\text{TDTIGHT}} \cdot \text{TDLOOSE}, \\
\text{PV}_1 &\equiv \text{PV30}, & \text{PV}_2 &\equiv \overline{\text{PV30}} \cdot \text{PV60}.
\end{aligned}$$

Based on these regions, the signal region was first divided into two major regions defined by KIN_1 and KIN_2. The major region defined by KIN_1 was sub-divided into 8 cells based on all possible permutations of the regions defined by the other three cuts. The cell defined by the application of the tight version of each of the four cuts (cell 1) was the tight signal region and had the highest signal-to-background ratio of all the cells.

Cell Number	Cuts	Acc.	Total Background	S/B
1	$KIN_1 \cdot TD_1 \cdot DC_1 \cdot PV_1$	0.314	$0.152 \pm 0.027\,^{+0.047}_{-0.035}$	0.84
2*	$KIN_1 \cdot TD_1 \cdot DC_1 \cdot PV_2$	0.287	$0.243 \pm 0.044\,^{+0.054}_{-0.047}$	0.47
3	$KIN_1 \cdot TD_1 \cdot DC_2 \cdot PV_1$	0.031	$0.019 \pm 0.005\,^{+0.007}_{-0.004}$	0.66
4*	$KIN_1 \cdot TD_1 \cdot DC_2 \cdot PV_2$	0.028	$0.027 \pm 0.006\,^{+0.008}_{-0.005}$	0.42
5	$KIN_1 \cdot TD_2 \cdot DC_1 \cdot PV_1$	0.073	$0.038 \pm 0.007\,^{+0.011}_{-0.008}$	0.78
6	$KIN_1 \cdot TD_2 \cdot DC_1 \cdot PV_2$	0.066	$0.059 \pm 0.011\,^{+0.012}_{-0.011}$	0.45
7	$KIN_1 \cdot TD_2 \cdot DC_2 \cdot PV_1$	0.007	$0.005 \pm 0.001\,^{+0.002}_{-0.001}$	0.57
8	$KIN_1 \cdot TD_2 \cdot DC_2 \cdot PV_2$	0.006	$0.007 \pm 0.001\,^{+0.002}_{-0.001}$	0.35
9*	KIN_2	0.188	$0.379 \pm 0.074\,^{+0.177}_{-0.120}$	0.20

Table 7.1: Relative acceptance and background summary of each cell. The components of acceptance ("Acc.") were normalized such that the entire signal region was normalized to have an acceptance equal to one. The signal-to-background ratios ("S/B") were calculated assuming $\mathcal{B}\left(K^+ \to \pi^+ \nu \bar{\nu}\right) = 1.73 \times 10^{-10}$. The cells denoted with an '*' were the cells within which the candidate events were observed. Table modified from [56].

The ninth cell was the major region defined by KIN_2, and it had the lowest signal-to-background ratio. These cell definitions are shown in Table 7.1.

7.1.1 Acceptance of Each Cell

For each of the four cuts used to define the cells, the additional acceptance loss when tightening a cut was defined as the ratio of the acceptance of the tight version of the cut to the acceptance of the loose version of the cut as determined in Chapter 6. These acceptance losses are summarized in Table 7.2.

The relative acceptance of each cell was then calculated by the product of the appropriate acceptance losses for the cuts used to define the cell. For example, cell 2 was defined by the tight versions of each of PNN2BOX, *TDCUTS* and DELCO, and by the

Background	PNN2BOX	*TDCUTS*	DELC	PVCUT
		Acceptance Loss		
	0.812	0.812	0.911	0.522
	Rejection Above Acceptance Loss			
$K_{\pi 2}$-tgscat	1.63	-	-	2.75
$K_{\pi 2}$-rsscat	1.63	-	-	2.75
$K_{\pi 2\gamma}$	1.20	-	-	2.75
K_{e4}	2.70	-	-	-
CEX	-	-	6.7	-
Muon	-	3.08	-	-
Beam	-	-	1.0	-

Table 7.2: Summary of the additional rejection above the acceptance loss for each background when tightening the kinematic phase space cuts (PNN2BOX), the delayed coincidence cuts (DELC), the $\pi^+ \to \mu^+ \to e^+$ decay-sequence cuts (*TDCUTS*), and the photon veto (PVCUT). Blank entries indicate that there was no rejection above the acceptance loss indicated in the "Acc. Loss" row. Table modified from [56].

region between the loose and tight versions of PVCUT, so the acceptance of that cell was

$$A(\text{cell } 2) = A(\text{KIN}_1) \times A(\text{TD}_1) \times A(\text{DC}_1) \times A(\text{PV}_2),$$

$$= 0.812 \times 0.812 \times 0.911 \times (1 - 0.522), \tag{7.1}$$

$$= 0.287.$$

Using these relative components of acceptance, the entire signal region had a relative acceptance of one. The relative components of acceptance of each of the nine cells are summarized in Table 7.1.

7.1.2 Background Levels in Each Cell

In Chapter 4, the bifurcation method was used to estimate the backgrounds in the two signal regions known as the "loose" and the "tight" signal regions. In the context of the discussion of dividing the signal region into cells, the "loose" signal region was the

entire signal region which was divided into the nine cells. The "tight" signal region was equivalent to cell number 1, which was defined by the application of the tightened versions of each the cuts used to define the cells. What follows is a discussion of the scaling method used to estimate the background levels in each of the nine cells. The scaling method was verified by comparing the scaled result in cell number 1 to that found using the bifurcation method to directly estimate the background level in the "tight" signal region from Chapter 4.

Using the scaling method, the total background level in each cell was calculated by estimating the contribution of each type of background to the total in that cell. For each of the tightened cuts, additional rejection above the acceptance loss was gained for some of the backgrounds, as summarized in Table 7.2.

When evaluating the background level in each of the cells, the single- and double-beam backgrounds were treated as a single background called "Beam". This simplification was possible due to the tiny contribution to the total background from the "Beam" background.

Tightening the kinematic phase space cuts from BOXLOOSE to BOXTIGHT resulted in rejection above the acceptance loss for the $K_{\pi 2}$-scatter and K_{e4} backgrounds. The lower bounds of BOXTIGHT were chosen to heavily suppress K_{e4} and this additional rejection was determined using the Monte Carlo simulation. The additional rejection for the $K_{\pi 2}$ target-scatter and $K_{\pi 2}$ Range-Stack-scatter backgrounds was determined using the loose and tight $K_{\pi 2}$ target-scatter normalization branches (Section 4.1.2) while taking into account the additional acceptance loss of the DELCO and *TDCUTS* between the two branches. It was assumed that the rejection of the photon veto for $K_{\pi 2}$-scatter events was not correlated with PNN2BOX as discussed in Section 4.1.3. For the remaining backgrounds, the additional acceptance loss of BOXTIGHT above that of BOXLOOSE was used.

Tightening the $\pi^+ \to \mu^+ \to e^+$ decay-sequence cuts from *TDLOOSE* to *TDTIGHT*

resulted in rejection above the acceptance loss only for the muon background. The additional rejection on the muon background was taken from Table 4.9. For the remaining backgrounds, the additional acceptance loss of *TDLOOSE* above that of *TDCUTS* was used.

Tightening the delayed coincidence cut from DELC3 to DELC6 resulted in rejection above the acceptance loss for the charge exchange background, measured using the Monte Carlo simulation. This cut should also have heavily suppressed the single-beam background, but the statistical limitations on the background estimate of this very tiny background resulted in no significant rejection above the acceptance loss being measured when tightening DELCO. Since the contributions of the single-beam background were very small, it was treated in the same way as the remaining backgrounds, where the change in background level was accounted for by the additional acceptance loss of DELC6 above that of DELC3.

Tightening the photon veto from PV60 to PV30 resulted in rejection above the acceptance loss for the $K_{\pi2}$-scatter and $K_{\pi2\gamma}$ backgrounds. This additional rejection was determined from Table 4.5. For the remaining backgrounds, the additional acceptance loss of PV30 above that of PV60 was used.

Using the scaling method the total background in cell number 1, which was equivalent to the "tight" signal region, was $0.152 \pm 0.027 \, {}^{+0.047}_{-0.035}$. Using the bifurcation method to directly estimate the background in the "tight" signal region, the total background was $0.1441 \pm 0.0448 \, {}^{+0.0952}_{-0.0319}$. These two values were consistent.

7.2 Examination of the Signal Region

Examination of the signal region revealed three candidate events. The kinematics of these events, along with the four previous E787/E949 $K^+ \rightarrow \pi^+\nu\bar{\nu}$ candidates, are shown in Figure 7.1 and summarized in Table 7.3. Displays of various event parameters for the

	ptot (MeV/c)	etot (MeV)	rtot (cm)	S/B	Ref.
Candidate A	161.4	76.1	17.3	0.20	Cell 9
Candidate B	188.4	95.6	24.2	0.47	Cell 2
Candidate C	191.3	98.0	26.1	0.42	Cell 4
95A (E787-PNN1)	218.2	117.7	34.7	59	[11]
96B (E787-PNN2)	180.7	86.3	22.1	0.17	[6]
98C (E787-PNN1)	213.8	117.1	33.9	8	[11]
02A (E949-PNN1)	227.3	128.9	39.2	1.1	[7]

Table 7.3: Summary of the π^+ kinematics and signal-to-background ratio (S/B) for all $K^+ \to \pi^+\nu\bar{\nu}$ candidates. The signal-to-background ratios were calculated assuming $\mathcal{B}(K^+ \to \pi^+\nu\bar{\nu}) = 1.73 \times 10^{-10}$. Table reproduced from [56].

	ptot (MeV/c)	etot (MeV)	rtot (cm)
Candidate A	204.3 ± 2.2	110.3 ± 3.2	30.6 ± 1.5
Candidate B	205.2 ± 2.4	108.1 ± 3.0	30.3 ± 0.9
Candidate C	205.3 ± 2.3	108.8 ± 3.3	30.4 ± 0.8
All E949 Data	204.9 ± 2.3	108.8 ± 3.0	30.3 ± 0.9

Table 7.4: Summary of momentum (ptot), energy (etot) and range (rtot) measurements for $K_{\pi 2}$ events in the runs containing candidates. Table reproduced from [56].

three candidates are found in Figures 7.2, 7.3, and 7.4. The three candidates were found in cells 2, 4 and 9 as indicated by the '*' adjacent to these cell numbers in Table 7.1.

7.2.1 Consistency of $K_{\pi 2}$ Kinematics

For each of the runs containing an E949 PNN2 candidate, the momentum, energy and range of the π^+ from the $K_{\pi 2}$ events were compared to those found for the entire data set as shown in Table 7.4. For each of the runs these quantities were found to be consistent with those found for the entire data set.
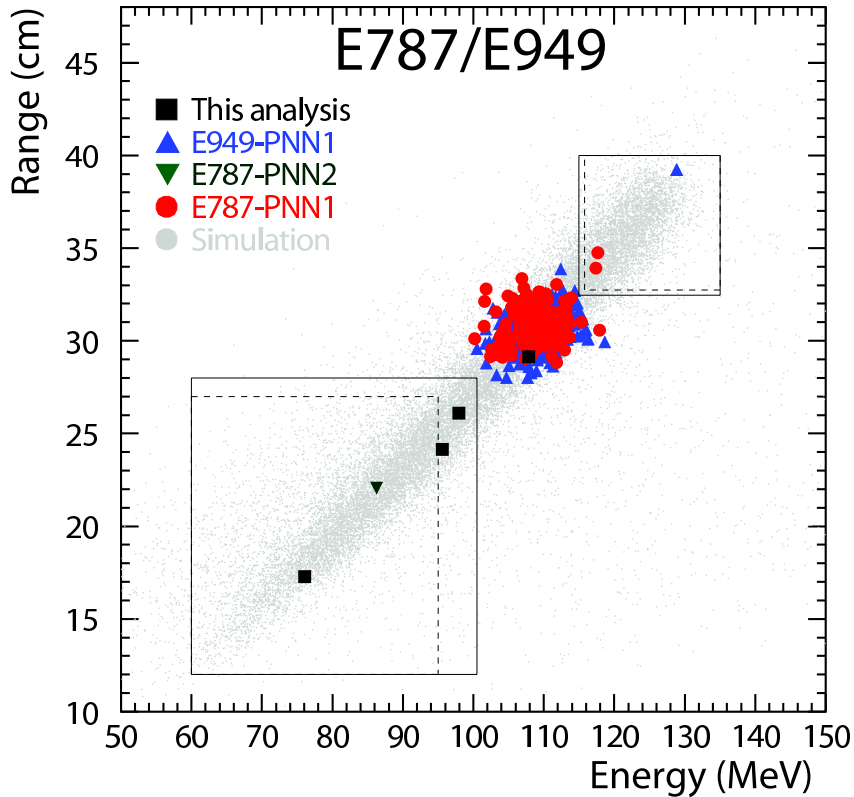
Figure 7.1: Energy (etot) vs. range (rtot) of all candidate events passing all other cuts. The squares represent the events selected by this analysis. The circles and upward-pointing triangles represent the events selected by the E787 and E949 PNN1 analyses, respectively. The downward-pointing triangles represent the events selected by the E787 PNN2 analysis. The solid (dashed) lines represent the limits of the PNN1 and PNN2 signal regions for the E949 (E787) analyses. No kinematic cuts were applied to the simulated $K^+ \rightarrow \pi^+ \nu \bar{\nu}$ events (light gray). Despite the smaller signal region displayed in this figure, the PNN1 analyses were 4.2 times more sensitive than the PNN2 analyses. The events shown near Energy = 108 MeV were $K_{\pi 2}$ events that survived the photon veto. These events were predominantly events from the PNN1 analyses due to the higher sensitivity and less stringent photon veto cuts. The light gray points are simulated $K^+ \rightarrow \pi^+ \nu \bar{\nu}$ events that would be accepted by the $\pi \nu \bar{\nu}(1)$ or $\pi \nu \bar{\nu}(2)$ triggers.
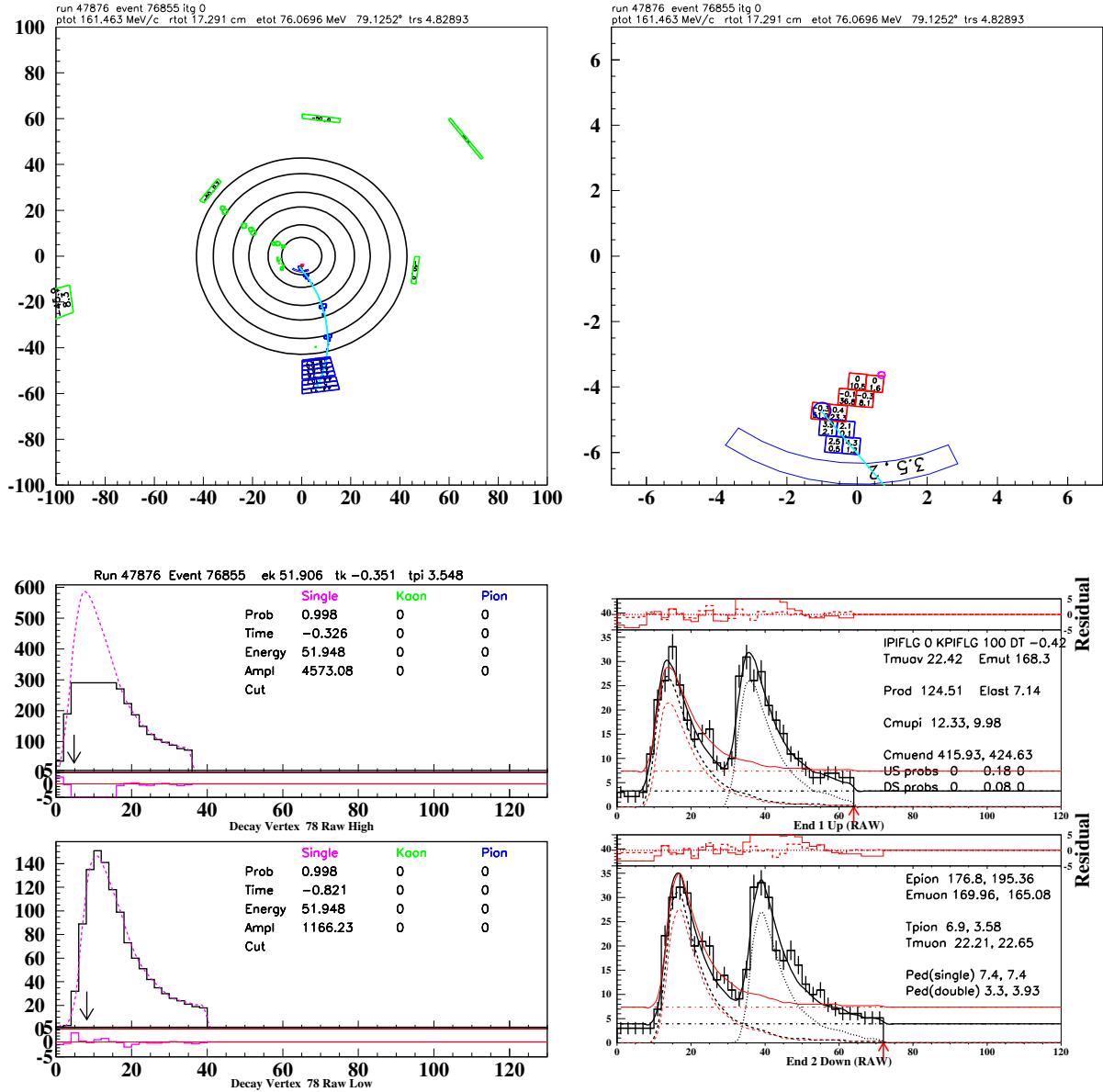
Figure 7.2: Some event parameter displays for Candidate A. Top-left is the end-view showing the UTC track fit where the circles along the track show the hits in the UTC. The layers hit in the RS and RSSC are shown outside the UTC. Additional hits shown in green show hits that were out of time with the event, in this case they were at least 40 ns before the K^+ entered the target. Top-right shows a magnification of the target where the red squares are the K^+ fibers and the blue ones are the π^+ fibers. Bottom-left shows the target CCD data for the vertex fiber where the upper plot is the "high-gain" CCD and the lower plot is the "low-gain". The x-axis shows time in ns and the y-axis shows the pulse-height. The purple dashed line shows the result of the single-pulse fit for each of the CCD channels. Bottom-right shows the TD data in the π^+ stopping counter. The x-axis shows time in ns and the y-axis shows the pulse-height. The solid red line shows the result of the fit for the single-pulse assumption and the solid black line shows the result of the fit for the double-pulse assumption. Figures reproduced from [56].

Figure 7.3: Some event parameter displays for Candidate B. Top-left is the end-view showing the UTC track fit where the circles along the track show the hits in the UTC. The layers hit in the RS and RSSC are shown outside the UTC. Additional hits shown in green show hits that were out of time with the event, in this case they were at least 50 ns before or 40 ns after the K^+ entered the target. Top-right shows a magnification of the target where the red squares are the K^+ fibers, the blue ones are the π^+ fibers and the green ones are the γ fiber. The energies in each of these γ fibers were significantly below the target photon veto threshold. Bottom-left shows the target CCD data for the vertex fiber where the upper plot is the "high-gain" CCD and the lower plot is the "low-gain". The x-axis shows time in ns and the y-axis shows the pulse-height. The purple dashed line shows the result of the single-pulse fit for each of the CCD channels. Bottom-right shows the TD data in the π^+ stopping counter. The x-axis shows time in ns and the y-axis shows the pulse-height. The solid red line shows the result of the fit for the single-pulse assumption and the solid black line shows the result of the fit for the double-pulse assumption. Figures reproduced from [56].

198
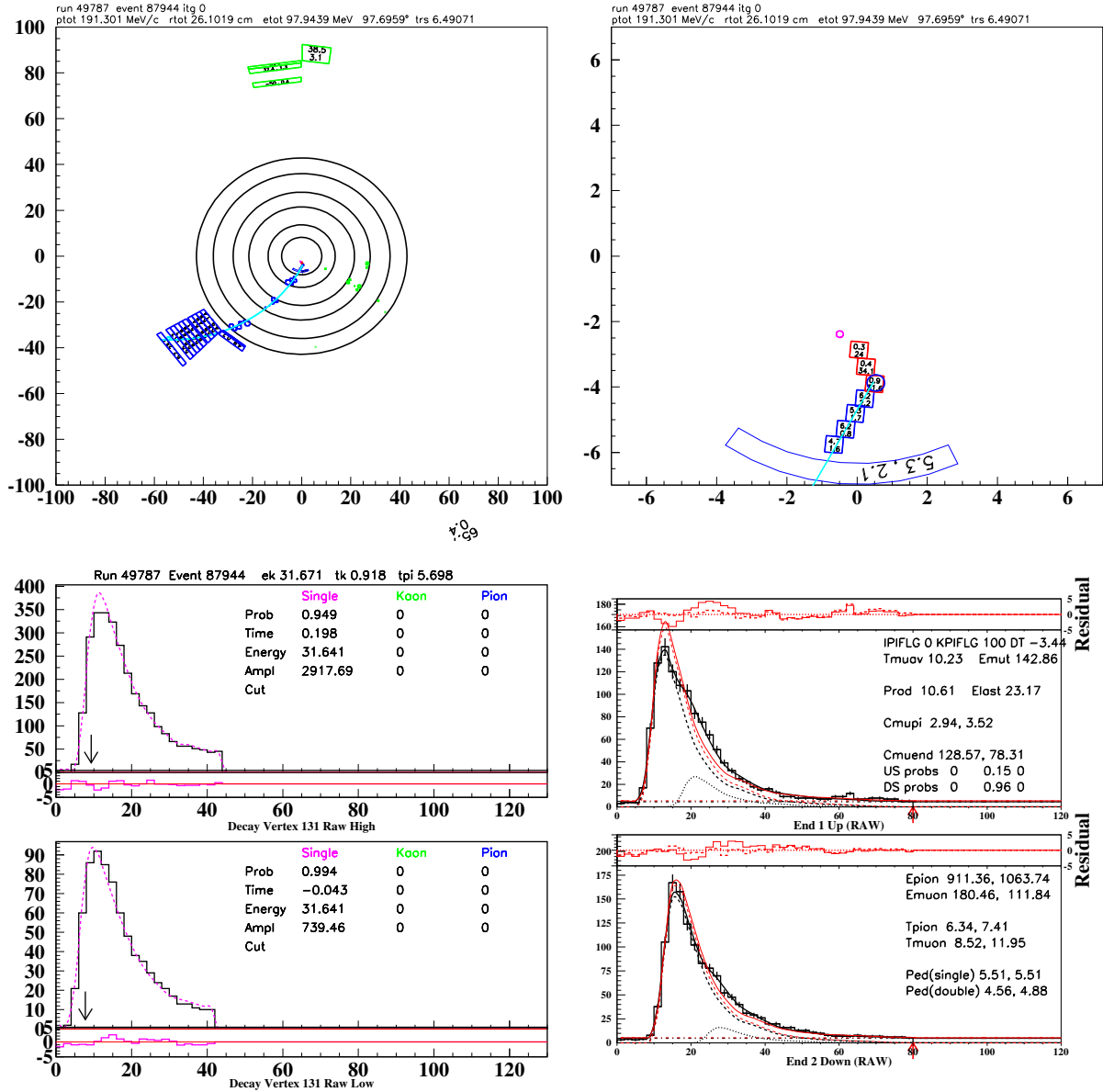
Figure 7.4: Some event parameter displays for Candidate C. Top-left is the end-view showing the UTC track fit where the circles along the track show the hits in the UTC. The layers hit in the RS and RSSC are shown outside the UTC. Additional hits shown in green show hits that were out of time with the event, in this case they were at least 50 ns before or 35 ns after the K^+ entered the target. Top-right shows a magnification of the target where the red squares are the K^+ fibers and the blue ones are the π^+ fibers. Bottom-left shows the target CCD data for the vertex fiber where the upper plot is the "high-gain" CCD and the lower plot is the "low-gain". The x-axis shows time in ns and the y-axis shows the pulse-height. The purple dashed line shows the result of the single-pulse fit for each of the CCD channels. Bottom-right shows the TD data in the π^+ stopping counter. The x-axis shows time in ns and the y-axis shows the pulse-height. The solid red line shows the result of the fit for the single-pulse assumption and the solid black line shows the result of the fit for the double-pulse assumption. Figures reproduced from [56].

199

7.2.2 Signal Probability Analysis

To verify that the properties of each of the candidates were consistent with signal, quantities classified into four categories were checked: reconstruction quality, kaon identification quality, pion identification quality and single particle quality. For each cut, distributions of the important quantities used to discriminate signal from background were generated for signal-like events and the properties of each of the candidate events compared to these distributions. For each cut, the same sample that was used to measure the acceptance of the cut in Chapter 6 was also used to generate the reference distributions due to signal-like events. The expectation was that an event which was consistent with a signal would have a fairly flat distribution when the probabilities due to each quantity were compared together. Figures 7.5 through 7.13 show the comparisons between the quantities from the candidate events and the reference distributions. For many of the cuts that target only a single specific background, a reference distribution for background-like events is also included.

Reconstruction quality

To make sure the candidates were of good reconstruction quality the quantities checked fell into the categories of timing consistency (Figure 7.5), target reconstruction (Figure 7.6), and UTC reconstruction (Figure 7.7).

Kaon identification quality

To make sure the beam particle in the candidate events was a kaon the quantities checked involved the B4 counters, Čerenkov hits at beam time and some target quantities (Figure 7.8).
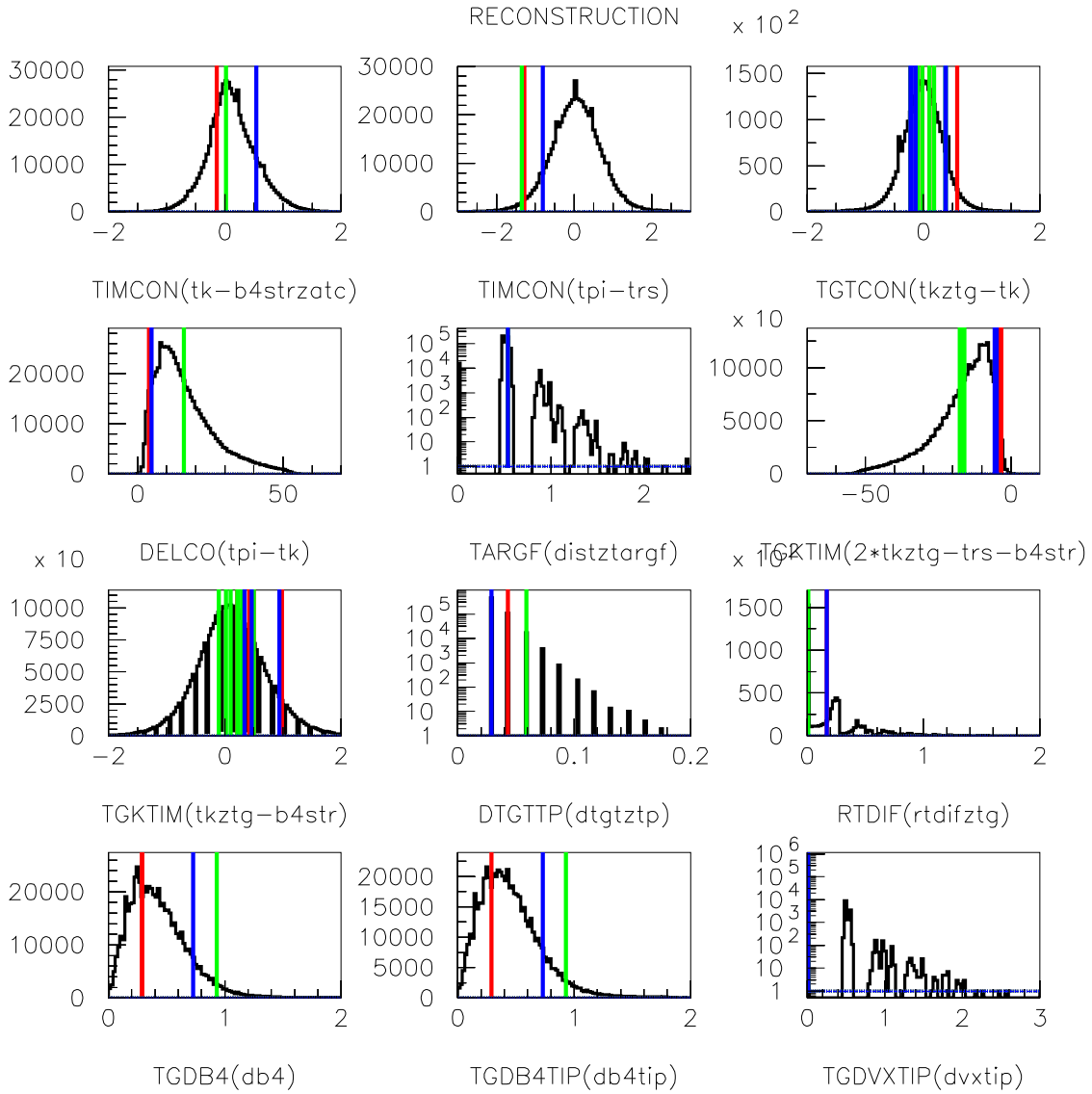
Figure 7.5: Quantities related to timing consistency in reconstruction cuts. The abscissa label contains the quantity plotted in lowercase and the cut from which that quantity is plotted in uppercase. For the reference signal-like distribution (black), the ordinate axis shows the number of events per abscissa bin. The measured quantity for each candidate is shown as a colour-coded vertical line: candidate A in red, candidate B in green and candidate C in blue. Note that for some quantities a candidate has multiple entries and that when multiple quantities fell in the same abscissa bin, information from only one candidate was displayed. Sample for the signal-like distribution was from $K_{\mu2}$ monitor trigger data.
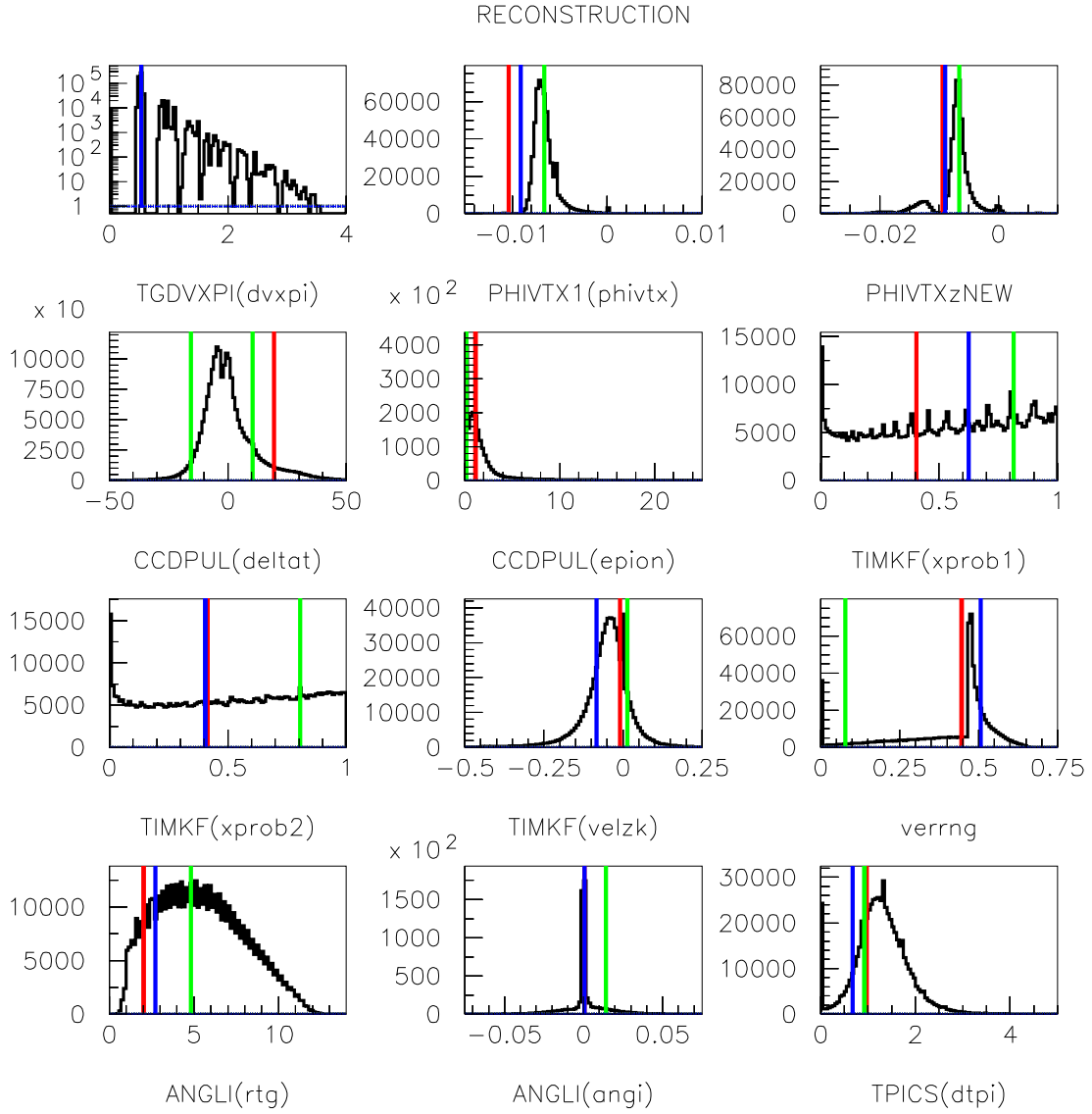
Figure 7.6: Quantities related to reconstruction cuts in the target. The abscissa label contains the quantity plotted in lowercase and the cut from which that quantity is plotted in uppercase. For the reference signal-like distribution (black), the ordinate axis shows the number of events per abscissa bin. The measured quantity for each candidate is shown as a colour-coded vertical line: candidate A in red, candidate B in green and candidate C in blue. Note that for some quantities a candidate has multiple entries and that when multiple quantities fell in the same abscissa bin, information from only one candidate was displayed. Sample for the signal-like distribution was from $K_{\mu 2}$ monitor trigger data.
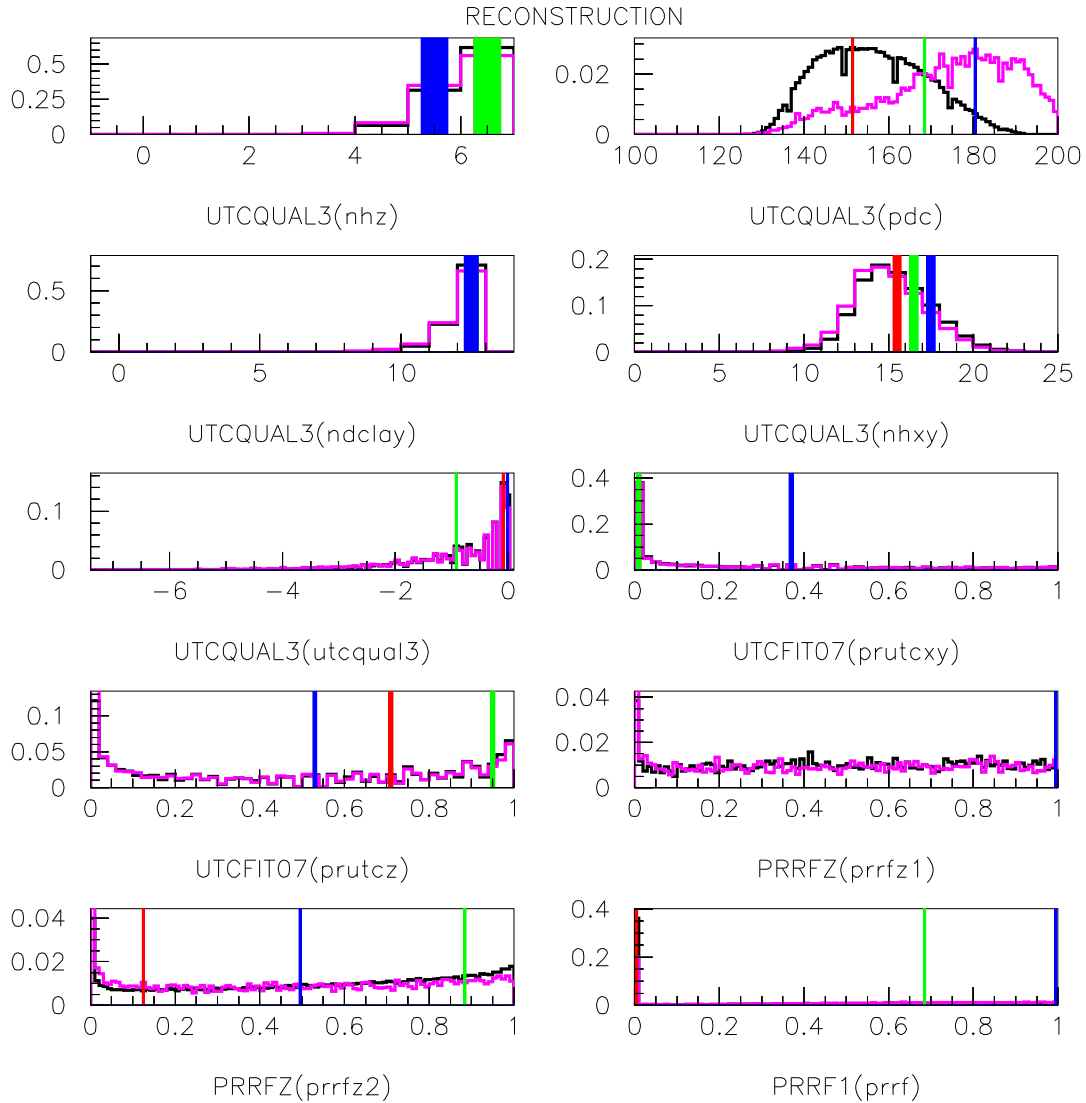
Figure 7.7: Quantities related to UTC and Range Stack reconstruction. The abscissa label contains the quantity plotted in lowercase and the cut from which that quantity is plotted in uppercase. The reference signal-like (black) and background-like (purple) distributions were each normalized to an area equal to one, thus the ordinate axis shows the normalized number of events per abscissa bin. The measured quantity for each candidate is shown as a colour-coded vertical line: candidate A in red, candidate B in green and candidate C in blue. Note that for some quantities a candidate has multiple entries and that when multiple quantities fell in the same abscissa bin, information from only one candidate was displayed. The sample for the reference signal-like distribution was from $\pi_{scatter}$ monitor trigger data in PNN2BOX and the sample for the reference background-like distribution was from $K_{\pi 2}$ monitor trigger data in KP2BOX.

KAON ID

Figure 7.8: Quantities related to target kaon reconstruction. The abscissa label contains the quantity plotted in lowercase and the cut from which that quantity is plotted in uppercase. For the reference signal-like distribution (black), the ordinate axis shows the number of events per abscissa bin. The measured quantity for each candidate is shown as a colour-coded vertical line: candidate A in red, candidate B in green and candidate C in blue. Note that for some quantities a candidate has multiple entries and that when multiple quantities fell in the same abscissa bin, information from only one candidate was displayed. Sample for the signal-like distribution was from $K_{\mu 2}$ monitor trigger data.

204

Pion identification quality

To make sure the charged track in the candidate events was due to a pion the quantities checked fell into the categories of energy deposited in the IC counters (Figure 7.9), Range-Stack kinematics (Figure 7.10), Range-Stack TD variables (Figure 7.11), and kinematics from Monte Carlo $\pi^+\nu\bar{\nu}$ events (Figure 7.12).

Single particle quality

To make sure there was only a single decay particle in the candidate events the quantities checked were related to beam detectors at track time in the Range-Stack (Figures 7.9 and 7.13).

Signal-like Probability

Based on the reference distributions, the signal-like probability was computed for each candidate for each of the quantities as summarized in Figure 7.14. These probabilities were determined using a cumulative integral for each of the reference distributions and were formed such that low probability corresponded to more background-like and high probability corresponded to more signal-like quantities.

For distributions where one side was signal-like and the other side background-like, the probability distribution was built going from low probability on the background-like side to high probability on the signal-like side. For quantities where extreme values were background-like and median values were signal-like, the probability distribution was constructed to be very low for extreme values and high for median values. For quantities where extreme values were signal-like and median values were background-like, the probability distribution was constructed to be very high for extreme values and low for median values.

Figure 7.14 shows the probabilities of each component of reconstruction quality, single
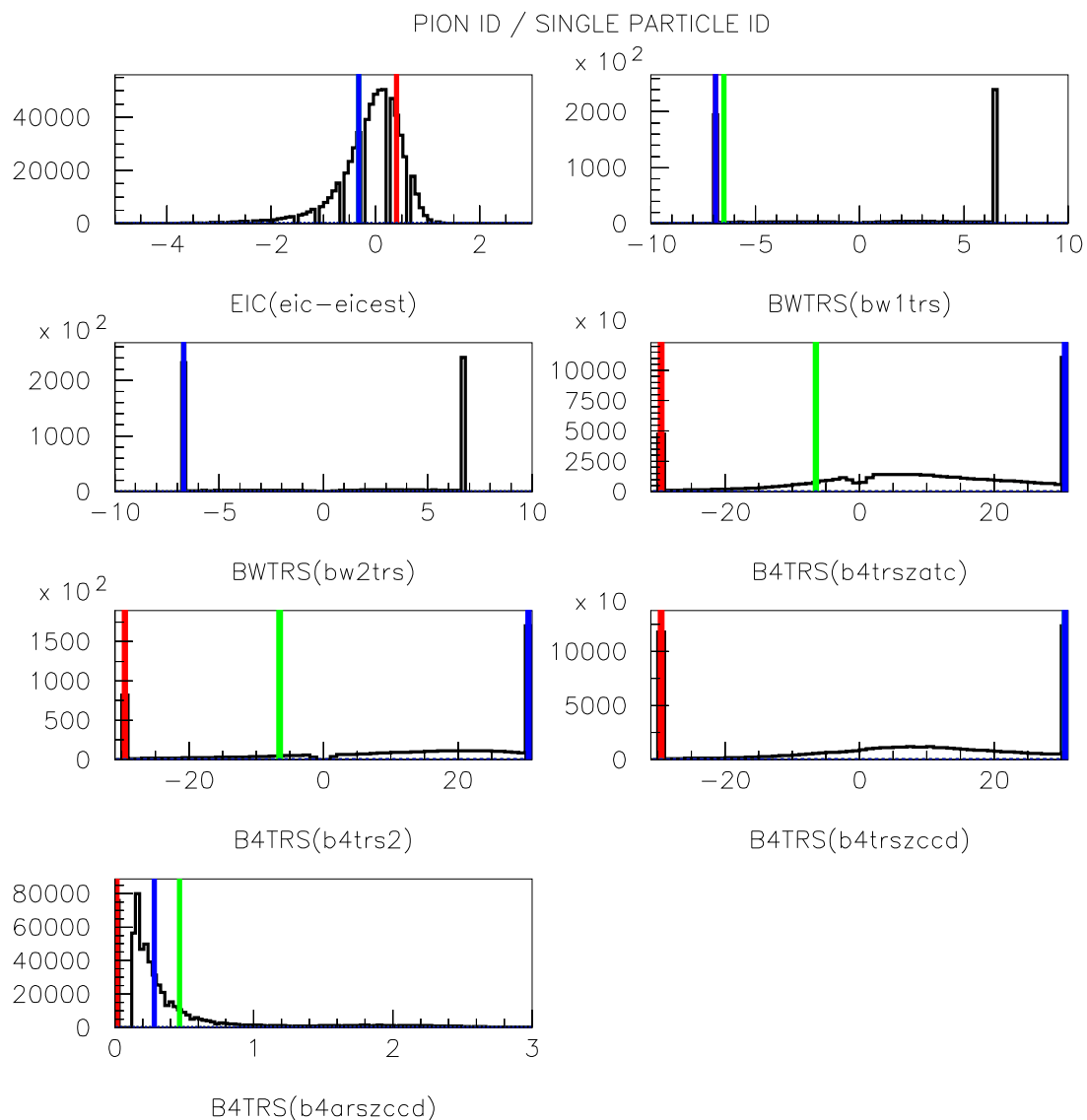
Figure 7.9: Quantities related to pion identification, single beam detection and photon veto. The top-left plot is related to pion identification and the rest of the plots to single beam detection and photon veto. The abscissa label contains the quantity plotted in lowercase and the cut from which that quantity is plotted in uppercase. For the reference signal-like distribution (black), the ordinate axis shows the number of events per abscissa bin. The measured quantity for each candidate is shown as a colour-coded vertical line: candidate A in red, candidate B in green and candidate C in blue. Note that for some quantities a candidate has multiple entries and that when multiple quantities fell in the same abscissa bin, information from only one candidate was displayed. Sample for the signal-like distribution was from $K_{\mu2}$ monitor trigger data. Overflow channels correspond to no hits or hits that are very far out of time with the quantity being checked.

Figure 7.10: Quantities related to pion identification by Range Stack kinematics. The abscissa label contains the quantity plotted in lowercase and the cut from which that quantity is plotted in uppercase. The reference signal-like (black) and background-like (purple) distributions were each normalized to an area equal to one, thus the ordinate axis shows the normalized number of events per abscissa bin. The measured quantity for each candidate is shown as a colour-coded vertical line: candidate A in red, candidate B in green and candidate C in blue. Note that for some quantities a candidate has multiple entries and that when multiple quantities fell in the same abscissa bin, information from only one candidate was displayed. The sample for the reference signal-like distribution was from $\pi_{scatter}$ monitor trigger data in PNN2BOX and the sample for the reference background-like distribution was from $K_{\pi 2}$ monitor trigger data in KP2BOX.

Figure 7.11: Quantities related to pion particle identification from TD variables. The abscissa label contains the quantity plotted in lowercase and the cut from which that quantity is plotted in uppercase. The reference signal-like (black) and background-like (purple) distributions were each normalized to an area equal to one, thus the ordinate axis shows the normalized number of events per abscissa bin. The measured quantity for each candidate is shown as a colour-coded vertical line: candidate A in red, candidate B in green and candidate C in blue. Note that for some quantities a candidate has multiple entries and that when multiple quantities fell in the same abscissa bin, information from only one candidate was displayed. The sample for the reference signal-like distribution was from $\pi_{scatter}$ monitor trigger data in PNN2BOX and the sample for the reference background-like distribution was from $K_{\mu 2}$ monitor trigger data since these cuts were designed to suppress muon-based backgrounds.
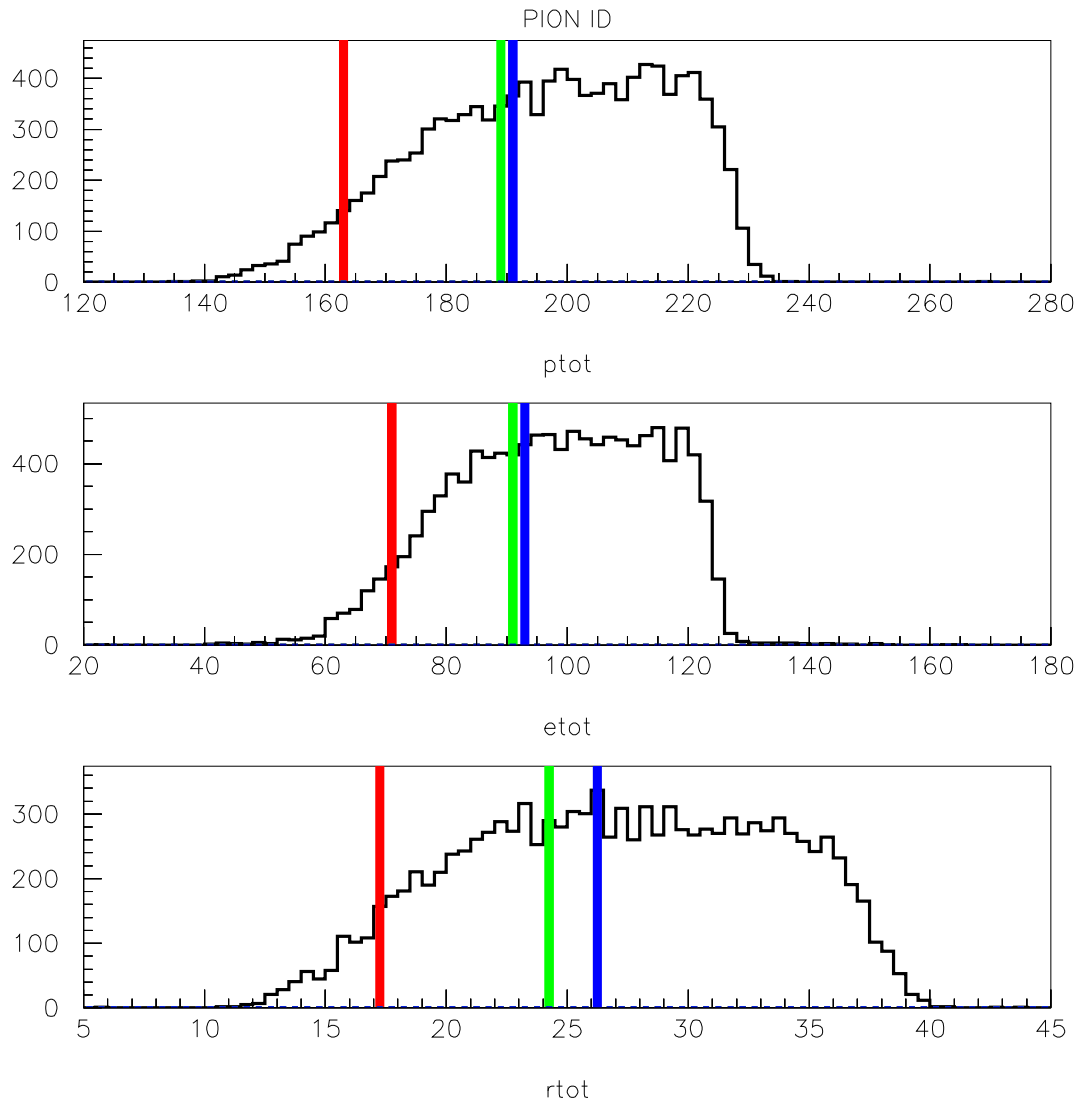
Figure 7.12: Quantities related to pion particle identification from kinematic variables. The abscissa label contains the quantity plotted in lowercase and the cut from which that quantity is plotted in uppercase. For the reference signal-like distribution (black), the ordinate axis shows the number of events per abscissa bin. The measured quantity for each candidate is shown as a colour-coded vertical line: candidate A in red, candidate B in green and candidate C in blue. Note that for some quantities a candidate has multiple entries and that when multiple quantities fell in the same abscissa bin, information from only one candidate was displayed. Sample for the signal-like distribution was from UMC $K^+ \to \pi^+ \nu \bar{\nu}$ events passing $\pi \nu \bar{\nu}(1)$ or $\pi \nu \bar{\nu}(2)$ triggers.

209

SINGLE PARTICLE ID
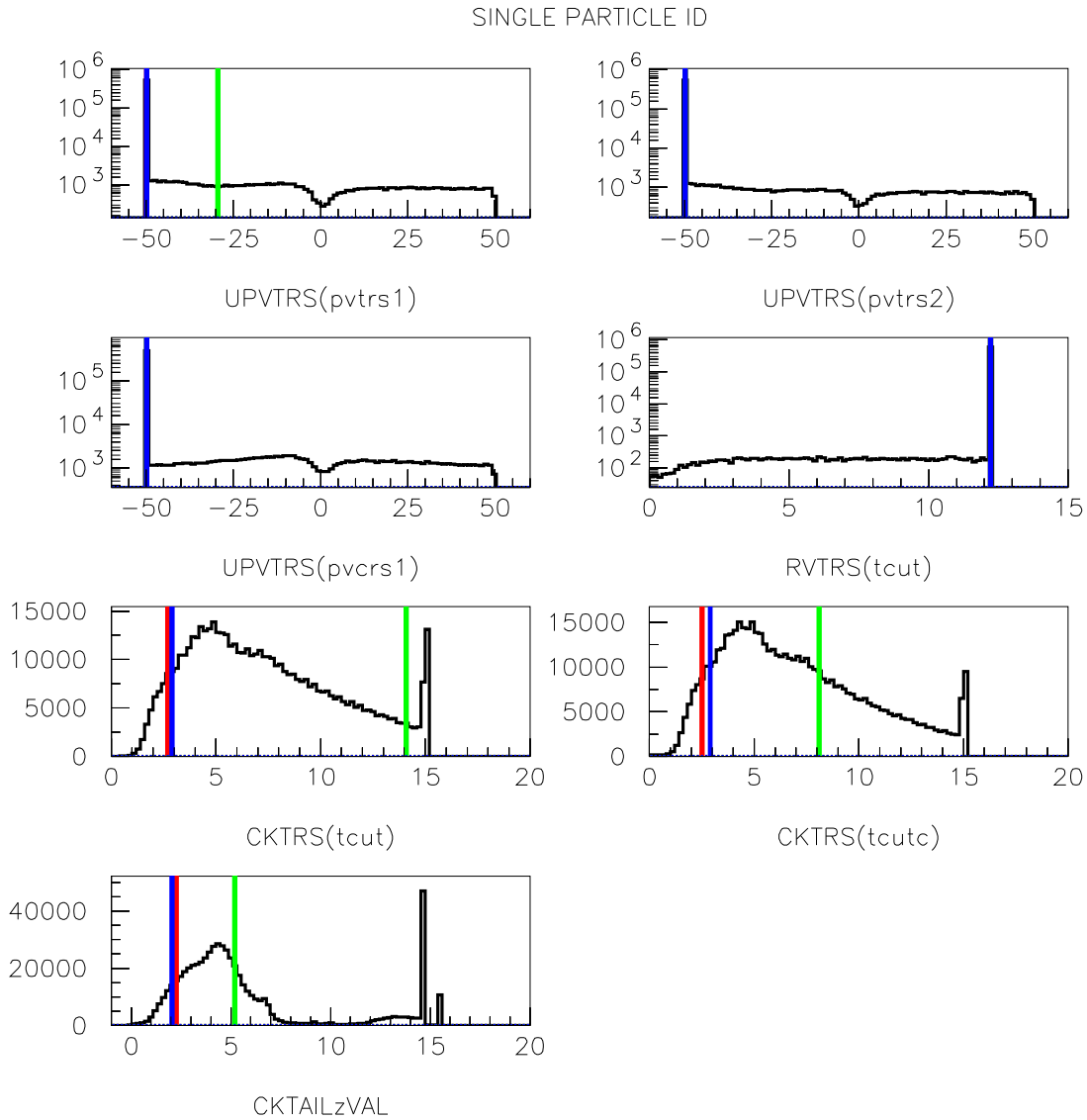
Figure 7.13: More quantities related to single beam detection and photon veto. The abscissa label contains the quantity plotted in lowercase and the cut from which that quantity is plotted in uppercase. For the reference signal-like distribution (black), the ordinate axis shows the number of events per abscissa bin. The measured quantity for each candidate is shown as a colour-coded vertical line: candidate A in red, candidate B in green and candidate C in blue. Note that for some quantities a candidate has multiple entries and that when multiple quantities fell in the same abscissa bin, information from only one candidate was displayed. Sample for the signal-like distribution was from $K_{\mu2}$ monitor trigger data. Overflow channels correspond to no hits or hits that are very far out of time with the quantity being checked.

beam K^+ requirements, decay π^+ requirements and single decay product requirements. These probabilities, other than the "single particle quality", showed fairly flat distributions for each candidate, which was consistent with the expected signal distributions. The quantities from the "single particle quality" were typically associated with particle vetoes where probabilities being peaked at 1 was expected due to the binary nature of the quantities used.

7.2.3 Background and Signal Fluctuation Probabilities

Based on the signal acceptance and the estimated background in each cell, the probability that the three observed candidates were due to background only was 3.7% and the probability that the three observed candidates were due to a combination of background processes and SM predicted signal was 5.7%. The probability that all seven E949 and E787 $K^+ \to \pi^+ \nu \bar{\nu}$ candidates (Table 7.3) were due to background was 0.1%.

7.3 Calculation of $K^+ \to \pi^+ \nu \bar{\nu}$ Branching Ratio

This section describes the likelihood analysis used to measure the branching ratio $\mathcal{B}(K^+ \to \pi^+ \nu \bar{\nu})$ based on the method described in [60].

7.3.1 Branching Ratio Using Maximum Likelihood

Assuming the signal and background processes obeyed Poisson statistics, the probability of observing exactly d_i events in the ith cell having an estimated background level of b_i and expected signal level of s_i was

$$P(d_i | s_i + b_i) = e^{-(b_i + s_i)} \frac{(b_i + s_i)^{d_i}}{d_i!}. \tag{7.2}$$
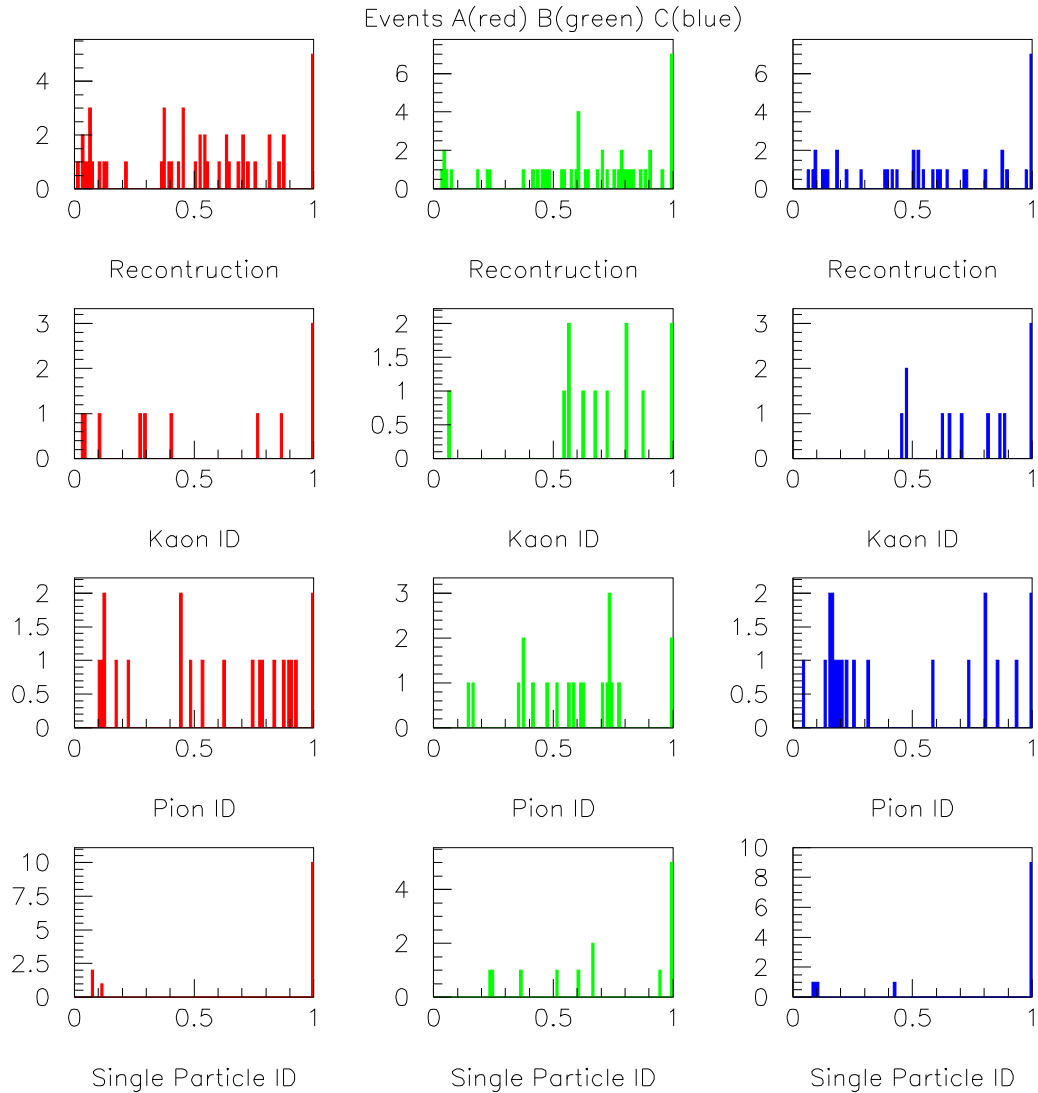
Figure 7.14: Signal-like probabilities (abscissa) for the three candidates. The ordinate axis shows the number of events per abscissa bin. The probabilities were calculated for each candidate for each of the entries appearing in Figures 7.5 through 7.13 and classified into the four categories defined in the text: reconstruction quality ("Reconstruction"), single beam K^+ requirements ("Kaon ID"), decay π^+ requirements ("Pion ID") and single decay product requirements ("Single Particle ID"). Candidates are colour coded: candidate A in red (column 1), candidate B in green (column 2), and candidate C in blue (column 3).

212

For a background only assumption, the probability was

$$P(d_i|b_i) = e^{-b_i} \frac{b^{d_i}}{d_i!}. \tag{7.3}$$

For m cells, a combination of d_i events in each of the i cells was given the index α. Given the assumption of signal and background, the probability of observing the exact combination α was

$$
\begin{aligned}
P_\alpha(s+b) &= \prod_{i=1}^{m} P(d_i|s_i + b_i) \\
&= \prod_{i=1}^{m} e^{-(b_i+s_i)} \frac{(b_i + s_i)^{d_i}}{d_i!}.
\end{aligned} \tag{7.4}
$$

The probability of the same combination given the assumption of background only was

$$
\begin{aligned}
P_\alpha(b) &= \prod_{i=1}^{m} P(d_i|b_i) \\
&= \prod_{i=1}^{m} e^{-b_i} \frac{b_i^{d_i}}{d_i!}.
\end{aligned} \tag{7.5}
$$

A likelihood ratio X_α, defined as

$$
\begin{aligned}
X_\alpha &\equiv \prod_{i=1}^{m} X_i, \\
&\equiv \prod_{i=1}^{m} \frac{e^{-(b_i+s_i)} \dfrac{(b_i + s_i)^{d_i}}{d_i!}}{e^{-b_i} \dfrac{b_i^{d_i}}{d_i!}}, \\
&= \prod_{i=1}^{m} e^{-s_i} (1 + \frac{s_i}{b_i})^{d_i},
\end{aligned} \tag{7.6}
$$

was used to compare the probability of the signal and background assumption to the background-only assumption for a combination α.

The likelihood ratio for the distribution of the 3 candidates in the 9 cells of this analysis

213

was denoted X_{obs}. To determine $\mathcal{B}(K^+ \to \pi^+ \nu\bar{\nu})$, $\mathcal{B}$ was varied to maximize X_{obs} given the following relationship between $\mathcal{B}$ and the expected signal in each cell s_i:

$$s_i = A_i \times \frac{\mathcal{B}}{SES}, \tag{7.7}$$

where SES was the single event sensitivity in the loose signal region from Table 6.24 and A_i was the fraction of the total acceptance of the ith cell from Table 7.1. The value of $\mathcal{B}$ that maximized X_{obs} was taken as the branching ratio.

Thus far in the discussion of the likelihood analysis, uncertainties in the signal and background levels have not been discussed. Based on [60], the uncertainties on the background (σ_{b_i}) and signal (σ_{s_i}) levels were taken into account using a gaussian convolution, and the likelihood ratio was replaced with

$$X = \prod_{i=1}^{m} \frac{\int_0^\infty \int_0^\infty \dfrac{e^{-\left(\frac{(s'-s_i)^2}{2\sigma_{s_i}^2} + \frac{(b'-b_i)^2}{2\sigma_{b_i}^2}\right)}}{2\pi\sigma_{s_i}^2 \sigma_{b_i}^2} X_i \, ds' db'}{\int_0^\infty \int_0^\infty \dfrac{e^{-\left(\frac{(s'-s_i)^2}{2\sigma_{s_i}^2} + \frac{(b'-b_i)^2}{2\sigma_{b_i}^2}\right)}}{2\pi\sigma_{s_i}^2 \sigma_{b_i}^2} \, ds' db'}. \tag{7.8}$$

The resulting curve for X_{obs} as a function of $\mathcal{B}$ is shown in the top plot of Figure 7.15. The value of $\mathcal{B}$ that maximized X_{obs}, 7.89×10^{-10}, was the branching ratio based on the candidates observed in this analysis. The next section discusses the method used to determine the uncertainty of this branching ratio.
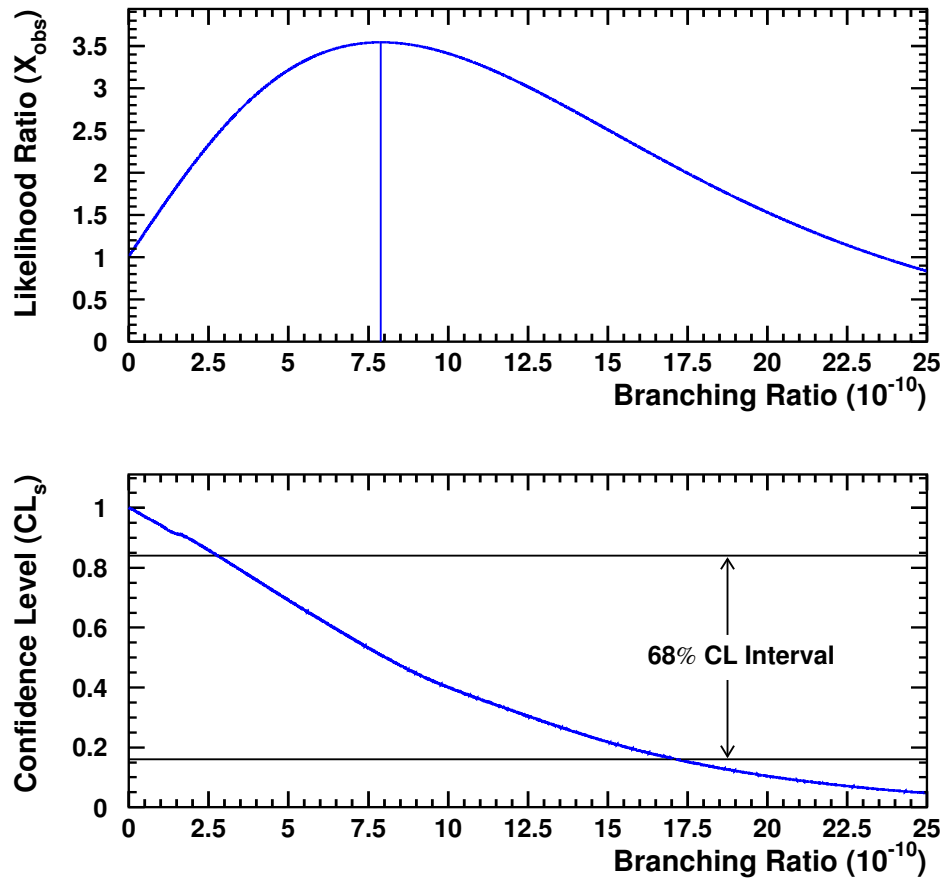
Figure 7.15: Likelihood ratio X_{obs} (top) and confidence level CL_s (bottom) for the three candidates from the E949-PNN2 analysis. The value of $\mathcal{B}$ (7.89×10^{-10}) that maximized X_{obs} is indicated with a vertical line (top).

7.3.2 Branching Ratio Uncertainty Using Confidence Level Interval

The sum of all probabilities P_{s+b} which had a likelihood ratio X_α less than or equal to X_{obs} gives the confidence level for the signal plus background assumption,

$$CL_{s+b} \equiv P_{s+b}(X_\alpha < X_{\text{obs}}) = \sum_{X_\alpha < X_{\text{obs}}} \left(\prod_{i=1}^{m} e^{-(b_i+s_i)} \frac{(b_i + s_i)^{d_i}}{d_i!} \right). \tag{7.9}$$

The confidence level for the background-only assumption was

$$CL_b \equiv P_b(X_\alpha < X_{\text{obs}}) = \sum_{X_\alpha < X_{\text{obs}}} \left(\prod_{i=1}^{m} e^{-b_i} \frac{b_i^{d_i}}{d_i!} \right). \tag{7.10}$$

Based on these two confidence levels, the confidence level for the signal was defined as

$$CL_s \equiv \frac{CL_{s+b}}{CL_b}. \tag{7.11}$$

Again the branching ratio $\mathcal{B}$ was treated as a parameter and varied, with the resulting curve for the quantity CL_s shown in the bottom plot of Figure 7.15. The 68% confidence level interval (equivalent to $\pm\sigma$) was taken as the interval corresponding to the branching ratios at CL_s values equal to 0.84 and 0.16. The branching ratio determined by maximizing X_{obs} was taken as the central value and the resulting branching ratio for the three observed candidates in this analysis was

$$\mathcal{B}(K^+ \to \pi^+\nu\bar{\nu}) = \left(7.89^{+9.26}_{-5.10} \right) \times 10^{-10}. \tag{7.12}$$

7.3.3 Combined E787/E949 Branching Ratio

For the combined E787 and E949 result (all candidates shown in Table 7.3), the d_i, b_i and s_i information was determined for each cell of each analysis and information was treated

as one large data set. The resulting X_{obs} and CL_s plots are shown in Figure 7.16, which gives a final branching ratio due to all $K^+ \to \pi^+ \nu \bar{\nu}$ candidates of

$$\mathcal{B}(K^+ \to \pi^+ \nu \bar{\nu}) = \left(1.73^{+1.15}_{-1.05}\right) \times 10^{-10}. \tag{7.13}$$

The CL_s plot was also used to get the 90% confidence level limit of $\mathcal{B}(K^+ \to \pi^+ \nu \bar{\nu}) < 3.35 \times 10^{-10}$. This result was consistent with the standard model prediction of $\mathcal{B}^{SM}(K^+ \to \pi^+ \nu \bar{\nu}) = (0.85 \pm 0.07) \times 10^{-10}$ [25].
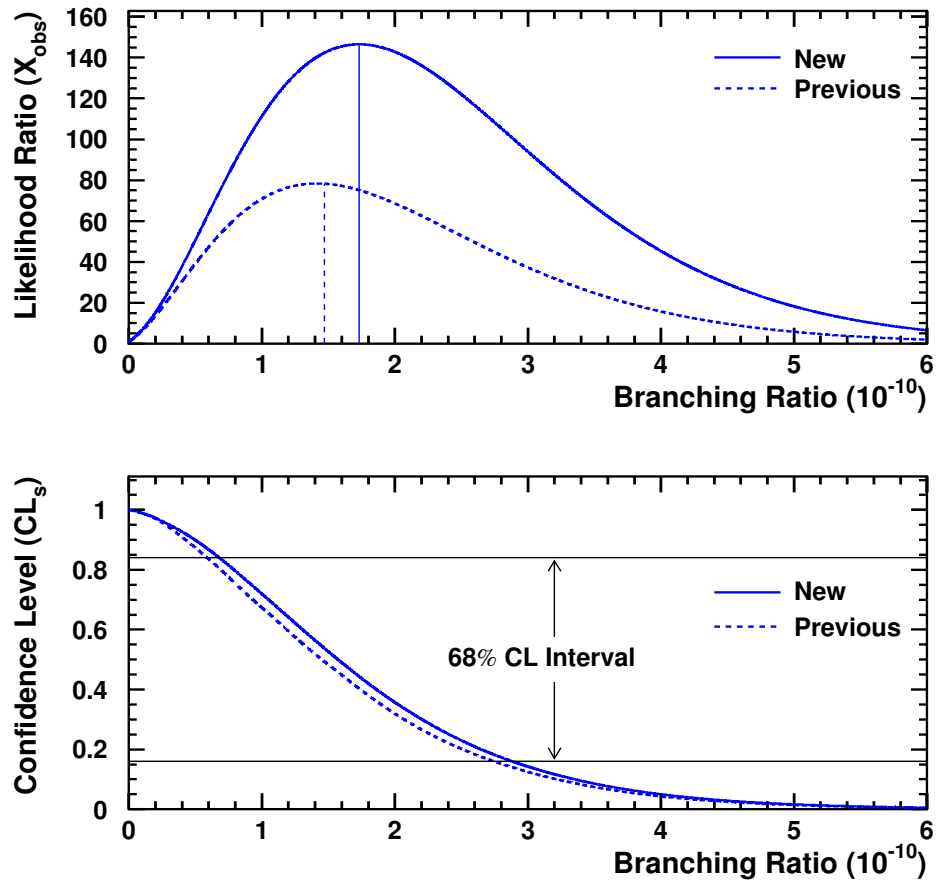
Figure 7.16: Likelihood ratio X_{obs} (top) and confidence level CL_s (bottom) for the new and previously published [11] combined results for all E787 and E949 analyses. analysis. The values of $\mathcal{B}$ that maximized X_{obs} for the respective results are indicated with vertical lines (top).
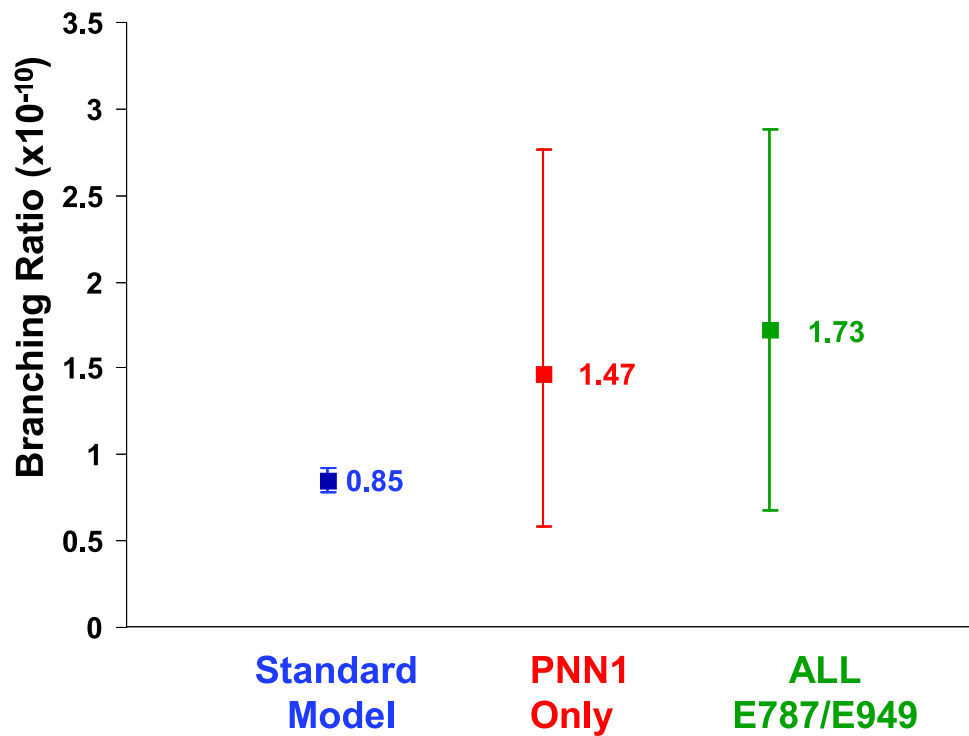
Figure 7.17: Comparison of the Standard Model ($0.85 \pm 0.07 \times 10^{-10}$), previous PNN1 only ($1.47^{+1.30}_{-0.89} \times 10^{-10}$ [11]), and final E787/E949 ($1.73^{+1.15}_{-1.05} \times 10^{-10}$) branching ratios.

Chapter 8

Conclusion

BNL experiment E949 was an upgrade of the E787 experiment, designed to measure the rare $K^+ \rightarrow \pi^+ \nu \bar{\nu}$ decay. The search took place in the π^+ momentum region of 140 to 199 MeV/c for this analysis. A blind analysis technique was used to analyze the 1.71×10^{12} stopped K^+ decays collected in the E949 detector. This technique was based on keeping the signal region hidden until all selection criteria for signal had been finalized, estimates of all background levels completed, and the acceptance of the signal region determined. The background levels were estimated from data using a bifurcation method, where two uncorrelated cuts with significant rejection of a specific background were used to estimate the background level in the signal region using measurements outside of the signal region. The signal region was divided into nine cells, whose relative signal-to-background levels varied by a factor of 4.

The estimated background was $0.927 \pm 0.168(stat.)\,^{+0.320}_{-0.237}(sys.)$ events. Based on acceptance measurements, the single event sensitivity was $(4.28 \pm 0.43) \times 10^{-10}$.

Examination of the signal region yielded 3 candidate events. Based on these 3 candidates a likelihood analysis was used to determine the branching ratio, $\mathcal{B}(K^+ \rightarrow \pi^+ \nu \bar{\nu}) = (7.89^{+9.26}_{-5.10}) \times 10^{-10}$ at 68% confidence level. Based on the signal acceptance and the estimated background in each cell, the probability that these three events were due to

background only was 3.7% and the probability that the three observed candidates were due to a combination of background processes and SM predicted signal was 5.7%.

Using the likelihood analysis, all E787 and E949 results were combined to give a branching ratio of $\left(1.73^{+1.15}_{-1.05}\right) \times 10^{-10}$ at 68% confidence level. This branching ratio is consistent with the Standard Model prediction of $(0.85 \pm 0.07) \times 10^{-10}$. The probability that all observed E787 and E949 candidates were due to background only was 0.1%.

E949 has made a significant step in confirming the SM's detailed predictions involving second-order weak interactions, and it has advanced the state-of-the art in the experimental technique of measuring small effects. However, given the level of statistical uncertainty associated with this $\mathcal{B}(K^+ \to \pi^+ \nu \bar{\nu})$ measurement, it was not possible to make any definitive conclusions regarding physics beyond the SM. It was very unfortunate that an executive decision by the Department of Energy (DOE) resulted in the E949 experiment being terminated after only 20% of the approved beam time as the potential for strong hints of physics beyond the SM were within reach. Future measurements of $\mathcal{B}(K^+ \to \pi^+ \nu \bar{\nu})$ are being planned. The NA62 experiment, currently in preparation at CERN, aims to collect 65 $K^+ \to \pi^+ \nu \bar{\nu}$ events over two years of data-taking using a decay-in-flight experiment [10]. A letter of intent for a decay-at-rest experiment similar to E949 was presented at J-PARC [69]. These experiments should be able to make definitive conclusions regarding the presence or absence of new physics contributions to this decay if the branching ratio is comparable to the central value found by E949.

Bibliography

[1] K. Abe *et al.* (Belle Collaboration), Phys. Rev. Lett. **87** 091802 (2001).

[2] S. Adler *et al.* (E787 Collaboration), Phys. Rev. Lett. **76** 1421 (1996).

[3] S. Adler *et al.* (E787 Collaboration), Phys. Rev. Lett. **79** 2204 (1996).

[4] S. Adler *et al.* (E787 Collaboration), Phys. Rev. Lett. **84** 3768 (2000).

[5] S. Adler *et al.* (E787 Collaboration), Phys. Rev. Lett. **88** 041803 (2002).

[6] S. Adler *et al.* (E787 Collaboration), Phys. Lett. B **537** 211 (2002).

[7] S. Adler *et al.* (E787 Collaboration), Phys. Rev. D **70** 037102 (2004).

[8] S. Adler *et al.* (E949 Collaboration), Phys. Rev. D **77** 052003 (2008).

[9] J.K. Ahn *et al.* (E391a Collaboration), Phys. Rev. Lett. **100**, 201802 (2008).

[10] F. Ambrosino *et al.* (NA62 Collaboration), "Proposal to Measure the Rare Decay $K^+ \rightarrow \pi^+ \nu \bar{\nu}$ at the CERN SPS", (2005). http://na48.web.cern.ch/NA48/NA48-3/Documents/P326.pdf

[11] V.V. Anisimovsky *et al.* (E949 Collaboration), Phys. Rev. Lett. **93** 031801 (2004).

[12] A.V. Artamonov *et al.* (E949 Collaboration), (2008), arXiv:0808.2459v1 [hep-ex].

[13] Y. Asano *et al.*, Phys. Lett. B **107**, 159 (1981).

[14] M. Atiya *et al.*, Nucl. Instrum. Methods Phys. Res., Sect. A **279**, 180 (1989).

[15] M. Atiya *et al.* (E787 Collaboration), Nucl. Instrum. Methods Phys. Res., Sect. A **321**, 129 (1992).

[16] M. Atiya *et al.* (E787 Collaboration), Phys. Rev. D **48**, R1 (1993).

[17] B. Aubert *et al.* (BABAR Collaboration), Phys. Rev. Lett. **87** 091801 (2001).

[18] B. Basseleck *et al.* (E949 Collaboration), BNL Report No. BNL-67247, TRIUMF Report No. TRI-PP-00-06 (1999). http://www.phy.bnl.gov/e949/

[19] J. B. Birks, Proc. Phys. Soc. **A64**, 874 (1951).

[20] B. Bhuyan, "Search for the rare decay $K^+ \to \pi^+ \nu \bar{\nu}$", Ph.D. thesis (2003).

[21] B. Bhuyan, "Analysis of 1997 data in the pnn2 region", E787 Technical Note **391** (2003), Unpublished.

[22] E.W. Blackmore *et al.*, Nucl. Instr. Meth. **A404**, 295 (1998).

[23] M. Blanke *et al.*, J. High Energy Phys. **0701**, 066 (2007).

[24] H. Brafman *et al.*, IEEE Trans. Nucl. Sci. **32**, 336 (1985).

[25] J. Brod & M. Gorbahn (2008), arXiv:0805.4119 [hep-ph].

[26] D.A. Bryman *et al.*, Nucl. Instrum. Methods Phys. Res., Sect. A **396**, 394 (1997).

[27] A.J. Buras, M.E. Lautenbacher, and G. Ostermaier, Phys. Rev. D **50**, 3433 (1994).

[28] A.J. Buras, F. Schwab, and S. Uhlig (2007), arXiv:hep-ph/0405132v3.

[29] N. Cabibbo, Phys. Rev. Lett. **10**, 531 (1963).

[30] G.D. Cable *et al.*, Phys. Rev. D **8**. 3807 (1973).

[31] U. Camenrini *et al.*, Phys. Rev. Lett. **23**. 326, (1969).

[32] C. Caso *et al.*, European Physical Journal **C3**, 1 (1998).

[33] S. Chen *et al.*, "2002 $\pi\nu\bar{\nu}(1)$ Data Analysis", E949 Technical Notes **K-034** and **K-038** (2003), Unpublished.

[34] H. C. Cheng and I. Low, JHEP **0309**, 051 (2003).

[35] I.H. Chiang *et al.*, IEEE Trans. Nucl. Sci. **42**, 394 (1995).

[36] J.H. Christienson *et al.*, Phys. Rev. Lett. **13** 138 (1964).

[37] I. Christidi, "Search for the rare decay $K^+ \to \pi^+ \nu \bar{\nu}$ with $p_{\pi^+} < 199$ MeV/c", Ph.D. thesis (2006).

[38] M. Diwan, J. Frank and V. Jain, "An algorithm to fit pulses in target CCD data", E787 Technical Note **374** (1999), Unpublished.

[39] W.T. Eadie, D. Drijard, F.E. James, M. Roos and B. Sadoulet, Statistical Methods in Experimental Physics, North-Holland (1971), pp.292-283.

[40] J. Doornbos *et al.*, Nucl. Instr. Meth. **A444**, 546 (2000).

[41] Dow Corning Corporation, South Saginaw Road, Midland, Michigan 48686, United States.

[42] The reference manual can be found at http://ppd.fnal.gov/elec/dyc3.

[43] Electron Tubes Inc., 100 Forge Way, Unit F, Rockaway, New Jersey 07866, United States.

[44] The original figure can be found at http://www.phy.bnl.gov/e949/detector/photon_veto/.

[45] J.S. Frank, "Study of the target CCD pulse fitting analysis", E949 Technical Note **K-045** (2005), Unpublished.

[46] Results from bench tests of the target can be found at http://www.phy.bnl.gov/e949/detector/tracking/tt/general/general.html.

[47] S.L. Glashow, J. Iliopoulos, and L. Maiani, Phys. Rev. **D1** 1585 (1970).

[48] Personal communication with Martin Gorbahn.

[49] D. Griffiths, "Introduction to Elementary Particles", John Wiley & Sons Inc. (1987).

[50] Y. Grossman and Y. Nir, Phys. Lett. **B398**, 163 (1997).

[51] J.S. Hagelin and L.S. Littenberg, Prog. Part. Nucl. Phys **23**, 1 (1989).

[52] Hamamatsu Photonics K.K., 312-5, Shimokanzo, Iwata City, Shizuoka Pref., 438-0193, Japan.

[53] G. Isidori, F. Mescia, and C. Smith, Nucl. Phys. **B718**, 319 (2005).

[54] G. Isidori *et al.*, J. High Energy Phys. **0608**, 064 (2006).

[55] J. Ives *et al.*, "Analysis of the 1/3 E949 pnn2 data", E949 Technical Note **K-073** (6 December 2007), Unpublished. Note that this work is cited to attribute to a co-author the reproduced results or figure.

[56] J. Ives *et al.*, "Analysis of the 2/3 E949 pnn2 data", E949 Technical Note **K-074** (24 April 2008), Unpublished. Note that this work is cited to attribute to a co-author the reproduced results or figure.

[57] D. Jaffe, "FITPI: Triple-pulse fitting and other modifications", E949 Technical Note **K-029** (2002), Unpublished.

[58] V. Jain, "Simulation of elastic scatters of π^+ in the target from Kp2 decays", E787 Technical Note **375** (1999), Unpublished.

[59] C. Jarlskog and R.Stora, Phys. Lett. **B208**, 268 (1988).

[60] T. Junk, Nucl. Instr. Meth. Phys. Res. **A434**, 435 (1999).

[61] K. Mizouchi, "Experimental Search for the Decay $\pi^0 \to \nu\bar{\nu}$ ", Ph.D. thesis (2006).

[62] M. Aoki *et al.*, "An experiment to measure the branching ratio $B(K^+ \to \pi^+\nu\bar{\nu}$", E949 Technical Note **K-001** (1998), Unpublished.

[63] S. Kettel, T. Yoshioka, "Trigger definitions - (2002)", E949 Technical Note **K-030** (2002), Unpublished.

[64] N. Khovansky *et al.*, Nucl. Instr. Meth. **A351**, 317 (1994).

[65] J.H. Klems, R.H. Hiledebrand, and R. Steining, Phys. Rev. D **4**, 66 (1971).

[66] M. Kobayashi & T. Maskawa, *Prog. Theor. Phys.* **49**, 652 (1973).

[67] T. Komatsubara, "Brief Summary of The Status of Upgraded-E787 in 1995", E787 Technical Note 305 (1995), Unpublished.

[68] T.K. Komatsubara *et al.* (E787 Collaboration), Nucl. Instr. Meth. **A404**, 315 (1998).

[69] T.K. Komatsubara, T. Nakano and T. Nomura, "Letter of Intent for Study of the Rare Decay $K^+ \to \pi^+\nu\bar{\nu}$ with Stopped Kaon Beam at J-PARC" (2002). http://www-ps.kek.jp/jhf-np/LOIlist/pdf/L04.pdf

[70] LeCroy Corporation, 700 Chestnut Ridge Road, Chestnut Ridge, NY 10977-6499, United States.

[71] B. Lewis, "A new Target Reconstruction and Target Scatter Algorithm", E949 Technical Note **K-063** (2006), Unpublished.

[72] B. Lewis, "The Quest for the Rare Decay $K^+ \to \pi^+\nu\bar{\nu}$", Ph.D. thesis (2008).

[73] X. Li *et al.*, "Improvement to the Range Stack Straw Chamber Electronics", E949 Technical Note **K-023** (2002), Unpublished.

[74] D. Ljung and D. Cline, Phys. Rev. D **8**, 1307 (1973).

[75] A.D. Martin, Nucl. Phys. **B179**, 33 (1981).

[76] W.J. Marciano and Z. Pars, Phys. Rev. D **53**, R1 (1996).

[77] R.A. McPherson, "Chasing the Rare Decay $K^+ \to \pi^+\nu\bar{\nu}$", Ph.D. Thesis (1995).

[78] F. Mescia and C. Smith, Phys. Rev. D **76** 034017 (2007)

[79] P. Meyers, "A modified Version of the UMC Multiple Scattering Routine MSCAT1", E787 Technical Note **77** (1985), Unpublished.

[80] The reference manual can be found at http://midas.triumf.ca.

[81] The reference manual can be found at wwwinfo.cern.ch/asdoc/minuit/minmain.html.

[82] O. Mineev *et al.* (E949 Collaboration), Nucl. Instrum. Methods Phys. Res., Sect. A **494**, 362 (2002).

[83] K. Mizouchi, "Experimental Search for the Decay $\pi^0 \to \nu\bar{\nu}$", Ph.D. thesis (2006).

[84] T. Morii, C.S. Lim, and S.M. Mukherjee, "The Physics of the Standard Model and Beyond", World Scientific Co. Pte. Ltd. (2004).

[85] Motorola Inc., 1303 E. Algonquin Road, Schaumburg, Illinois 60196, United States.

[86] W.R. Nelson *et al.*, "The EGS4 Code System", SLAC Report No. **265** (1985).

[87] The reference manual can be found at wwwinfo.cern.ch/asd/paw/reference_manual/index.html.

[88] C. Promberger, S. Schatt, and F. Schwab, Phys. Rev. D **75**, 115007 (2007).

[89] Compagnie de Saint-Gobain, Les Miroirs, 18, avenue d'Alsace, 92400 Courbevoie, France.

[90] A.D. Sakharov, JETP Lett 5 (1967) 24.

[91] G.A. Sayer *et al.*, Physical Review **169**, 1045 (1968).

[92] T. Sekiguchi, "Measurement of the $K^+ \to \pi^+ \nu \bar{\nu}$ Branching Ratio", Ph.D. thesis (2004).

[93] SGI, 1140 E. Arques Ave., Sunnyvale, CA 94085, United States.

[94] C. Smith (2007), arXiv:0710.2883v2 [hep-ph].

[95] A.J. Stevens, "Nuclear Interactions in CH revisited", E787 Technical Note **140** (1987), Unpublished.

[96] Struck Innovative Systeme, Harksheider Str. 102A, 22399 Hamburg, Germany.

[97] C. Witzig, "Pi- Absorption in the Range Stack", E787 Technical Note **278** (1994), Unpublished.

[98] L. Wolfenstein, Phys. Rev. Lett. **51**, 1945 (1983).

[99] W.-M. Yao *et al.* (Particle Data Group), Journal of Physics G **33**, 1 (2003).

[100] T. Yoshika *et al.* (E949 Collaboration), IEEE Trans. Nucl. Sci. **51**, 199 (2004).

Appendix A

E787 to E949 Upgrades

The E949 experiment was a successor to experiment E787 at BNL [15], whose data taking was completed in 1998. The experiment was quite similar to E787, with the following upgrades to the beam and detector [18], and to the trigger and data acquisition [100].

A.1   Beam Upgrades

The proton intensity at the production target was increased by a factor of two, resulting in about twice the beam rate as E787. The mean K^+ momentum was 710 MeV/c throughout E949 data collection. For E787 the mean K^+ momentum ranged from 670 to 790 MeV/c [62] over the entire life of the experiment.

A.2   Detector Upgrades

The detector upgrades were as follows:

- The two outer-most layers of the Range-Stack were replaced by the Barrel Veto Liner (BVL), adding 2.3 radiation lengths to the photon veto. The BVL was a lead/scintillator sandwich sampling calorimeter like the Barrel Veto.

- The Active Degrader (AD), Upstream Photon Veto (UPV), and Downstream Photon Veto (DPV) were installed to add photon veto coverage at small polar angle (θ).

- One third of the RS scintillation counters were replaced to increase the light output.

- A gain monitor system was installed in the RS, operated by blue LED flashers. This allowed changes in the gains of the PMTs to be tracked on a spill by spill basis and even within a spill, improving energy calibration.

- The UTC read-out electronics were upgraded to operate in the higher rate environment.

- The RSSC read-out electronics were upgraded to improve resolution of z-position measurements.

A.3   Trigger and DAQ Upgrades

The trigger and DAQ upgrades were as follows:

- The level 0 trigger board was upgraded [100].

- Digital mean-timer modules were installed to improve the performance of the online photon rejection [100].

Appendix B

Data Acquisition, Storage, and Processing

The E949 experiment collected its physics data for 12 weeks from March through June of 2002.

B.1   Data Acquisition

Detector analog and discriminated signals were digitized by ADC, TDC, TD and CCD systems. The ADCs and TDCs were commercial units, and the TD and CCD waveform digitizers (WFD) were custom built. Data from a triggered event was digitized and stored in a buffer module or local crate controller. At the end of the spill, all buffered data from the spill were transferred to the host computer. Table B.1 shows a summary of the digitizing electronics that were used.

For the Fastbus systems, SLAC Scanner Processor (SSP) modules [24] served as crate controllers as well as performing the tasks of reading out, reformatting and buffering the data from the front end after each trigger were accepted. The CAMAC ADCs were readout through the FERA bus by a Fastbus Struck [96] 370 QDP DSP module. The

Type	Model	Standard	Resolution	Subsystems
ADC	LRS 4300B	CAMAC	10 bits	RS,BV,BVL,EC,beam
	LRS 1881	Fastbus	13 bits	target, UTC
TDC	LRS 3377	CAMAC	0.5 ns	RS, BVL
	LRS 1879	Fastbus	2 ns	UTC,BV,target
	LRS 1876	Fastbus	1 ns	EC,RSSC,beam
WFD	TD	Fastbus	500 MHz sampling 8 bits, 10 μs depth	RS,BVL,IC
	CCD	Fastbus	500 MHz sampling 8 bits, 256 ns depth	beam, target, EC

Table B.1: Digitizing electronics for E949. The ADCs and TDCs were commercial units (LeCroy [70]), and TD and CCD waveform digitizers (WFD) were custom built. Reprinted table with permission from S. Adler *et al.* (E949 Collaboration), Phys. Rev. D **77** 052003 (2008), http://link.aps.org/abstract/PRD/v77/e052003. Copyright 2008 by the American Physical Society.

CAMAC TDCs were readout by custom-built DYC3 modules [42] which pushed the data into VME memory boards. The readout time per event, as determined by the slowest crate, was typically 850 μs.

At the end of each spill, the data from the Fastbus buffer memories were readout via the cable segment (12-15 MB/s) by Struck 340 SFI modules, each controlled by a Motorola [85] VME 2604 single-board computer (SBC) running VxWorks. The VME memory boards were readout by a separate SBC. Data were transferred from the SBCs to the host computer (SGI [93] Origin 200, designated bnlku9) via 9 MB/s per link ethernet through a simple network switch. Event fragments from the readout segments were combined by event builder processes running on the host computer. The $\pi\nu\bar{\nu}$ triggers were written to two DLT-7000 drives at 5 MB/s per drive; a third DLT drive was used to log monitor triggers.

Under typical running conditions, 300 events were written per spill with a typical event size of 80 kB. This was well within the maximum possible throughput of the system

of about 50 MB per spill. The DAQ dead time was due entirely to the speed of the event-by-event readout of the front-end electronics at the crate level. The total dead time introduced by the trigger and DAQ was typically 26%.

A slow control system, based on the MIDAS [80] framework, ran independently of the main DAQ system, and was used to monitor a variety of experiment conditions, including crate voltages and temperatures.

B.2   PASS0

After the 12 week physics data run had completed, PASS0 processing was performed. For each monitor trigger, the data were staged, sorted and written to dedicated DLT tapes.

B.3   PASS1 and PASS2 Processing

PASS1 and PASS2 processing were performed in sequence on the various monitor and signal trigger data by first staging raw data from DLT tapes to hard-drive disks. Next, the data were unpacked and event reconstruction was performed using a cluster of 25 Linux-based computers. Fortran routines and shell scripts were used to decode the raw digitized information written to tape, run event processing and create PAW [87] ntuples containing event information.

B.4   PASS3 Analysis

Subsequent analysis of the PAW ntuples employed PAW comis functions and kumac scripts to apply the desired cuts to the event ntuples. The output from this stage typically took the form of histograms of the desired quantities. The ntuples and cut functions were available in public areas such that data analysis could be performed by multiple analyzers in parallel.

Appendix C

Target Pulse Data Analysis

The implementation of the target pulse data analysis, known as the "target CCD fitter", for the analysis of experimental data from the E787 experiment is described in [38] with improvements to the fitter described in [21]. Further improvements were made to the fitter for the E949 analysis as described in [45]. This appendix describes the target CCD fitter and details the modifications and improvements made to the fitter for this analysis, summarized as follows:

- The uncertainties associated with the first bin and with bins containing less than ten counts were increased to de-weight these bins in the fit.

- Bins with zero counts were included in the minimization for the fit if they occurred within the pulse. They were previously excluded.

- Hold and release fitting was implemented for the double-pulse fits. The four-parameter double-pulse fit was changed from a one-stage fit to a two-stage fit. In the first stage, the time for the first pulse was fixed at the time found from the single-pulse fit while the other three parameters were allowed to wander. In the second stage, the values from these three parameters were used as initial guesses and all four parameters were allowed to wander.

- The maximum number of target fibers that were fit was increased to 31 from 15.

- The previous restriction that the two pulses in a double-pulse fit had to be within ± 10 ns of each other was lifted due to a number of observed events with undesirable double-pulse fit solutions.

Additional small bug fixes found in the previous fitter code were also made by the author. Throughout this appendix, the nomenclature "fiber channel" will be used when discussing each the high-gain and low-gain CCD channels for each target fiber. For example, a statement beginning with "For each fiber channel" will describe a situation in which each of the high-gain and each of the low-gain CCD channels for each target fiber was examined.

For single-pulse fits, the single pulse was often referred to as the "kaon pulse". For double-pulse fits, the first pulse was often referred to as the "kaon pulse" and the second as the "pion pulse".

C.1   Creation of Standardized Pulses

For each fiber channel, a collection of standardized K^+ pulses was created using $K_{\mu 2}$ monitor trigger data and the following criteria for fibers identified as K^+ fibers:

- The energy of the K^+ fiber $\texttt{E}_\texttt{K}$ was greater than 4 MeV;

- The pulse did not saturate the 8-bit dynamic range of the CCD;

- The time of the K^+ fiber was within ± 3 ns of time zero;

- The event passed the target reconstruction criteria.

These pulse shapes were normalized to unit area, aligned with a timing granularity of 0.5 ns by interpolation, and these average "standardized" shapes stored. The effects due to saturated pulses and outliers in each time bin were removed by determining the average

from the peak of a Gaussian fit. Based on these standardized pulses, the reliability of each of the fiber channels was determined with a typical reliability of 0.99.

C.2 Overview of the Fitter

For each fiber, the fitting procedure was performed on each of the low-gain and the high-gain CCD information independently. Fits were only attempted on fiber channels that passed the following criteria:

- The reliability for that fiber channel had to be greater than 0.8 for that run.

- The energy had to be greater than the threshold energy for 90% efficiency for a CCD hit for that fiber channel. Typical thresholds were 2 MeV for low-gain and 0.5 MeV for high-gain CCD channels.

- The time for that target kaon fiber had to be earlier than track time t_{rs}.

- The edge finder had to find a good leading edge.

Additionally, a maximum of 31 low-gain and 31 high-gain CCD channel fits were stored. The cut ALLKFIT removed events where a fit was performed on neither the high-gain nor the low-gain CCD channels of a given target fiber if the energy in that fiber was above 3 MeV.

A single-pulse fit was attempted for each fiber channel passing the above criteria. The single-pulse fit used two parameters, the kaon-pulse amplitude and the time. Pedestal subtraction had already occurred previous to the target CCD fitter so the pedestal was not included in the fit.

If the probability of the single-pulse fit was less than 25%, a double-pulse fit was performed. The double-pulse fit used a second copy of the standardized kaon pulse and added it to the first pulse. The double-pulse fit used four parameters, the amplitudes and times for each of the kaon and pion pulses.

234

These fits minimized χ^2 by varying the above-mentioned parameters using the MINUIT function minimization library [81]. The uncertainty input for each bin of height N of the pulse used experimentally determined uncertainty parameters:

$$\text{High-gain} = 0.74 + 0.69 \times \sqrt{N}, \tag{C.1}$$

$$\text{Low-gain} = 1.21 + 0.35 \times \sqrt{N}, \tag{C.2}$$

where the first term was a constant related to instrumental noise and the second term scaled with the square-root of the number of photo-electrons in the pulse. This general form for the uncertainties was retained in the modifications made by the author, but two modifications were made as detailed in the following section. For these fits, time bins which have saturated the 8-bit dynamic range of the CCDs were not included in the fit and the fit was performed using only the unsaturated bins.

C.3   Optimization of the Error Input

A sample of $K_{\mu 2}$ monitor trigger data was used for optimizing the uncertainty inputs for the target fitter. For the sample, the following cuts were applied as setup cuts: TGQUALT, DELC, NPITG, TARGET, TGCUT, UTC, RD_TRK, TRKTIM, RDUTM. This left approximately 50,000 events to which CCDBADFIT, CCDPUL and EPIONK were applied. The resulting components of acceptance of these cuts are shown in the row labeled "No fixes" of Table C.1 before the fixes detailed below.

C.3.1   Low-Count Error Fix

Two sub-samples of the $K_{\mu 2}$ monitor trigger data sample described above were created by choosing only pulses that had above a 25% probability for the single-pulse fit. One sub-sample was created for low-gain CCD fits meeting this criteria and another for the

high-gain CCD fits meeting this criteria. One at a time, each time bin was removed from the single-pulse fit and the difference between the pulse-height for that bin as predicted by the fitter and the actual number of counts "*predicted−actual*" was tabulated as a function of the actual number of counts in that bin. The bin numbering in this study was such that bin number 1 was the first bin found to have a non-zero pulse-height. For each time bin, the shape given by the Equation (C.1) or (C.2) was plotted against the above distribution, with a typical comparison plot being shown in Figure C.1. It was found that for time bins having counts (N) below 10, the uncertainty functions (Equations C.1 and C.2) were underestimating the uncertainty. Plots similar to C.1 were visually examined for each time bin and it was found that time bins having counts less than 10 were consistently underestimated, with the turn-up in the distribution occurring typically in the first 5 to 10 time bins. This was fixed by applying the uncertainty corresponding to $N = 10$ counts for all channels having 10 or less counts.

C.3.2   First Bin Error Fix

It was found that the fit was very sensitive to the pulse-height of the first bin. A very low number of counts (such as 1 or 2) in the first bin tended to give a very large contribution to the chi-squared of the fit due to the reference pulse predicting a larger number of counts. This sensitivity to very low pulse-heights in the first bin was found to be present even with the low-count uncertainty fix applied. As shown in Figure C.2, a reasonable looking fit can have a large chi-squared contribution due to the first bin, resulting in a fit probability of zero and thus causing it to fail the fit. The contribution due to this first-bin sensitivity was reduced by doubling the uncertainty associated with the first bin.

The improved components of acceptance due to this fix are shown in the row labeled "First bin and low-count uncertainty fixes" in Table C.1. The results of the single- and double-pulse fits were examined for many (40-50) events where the "low-count error"
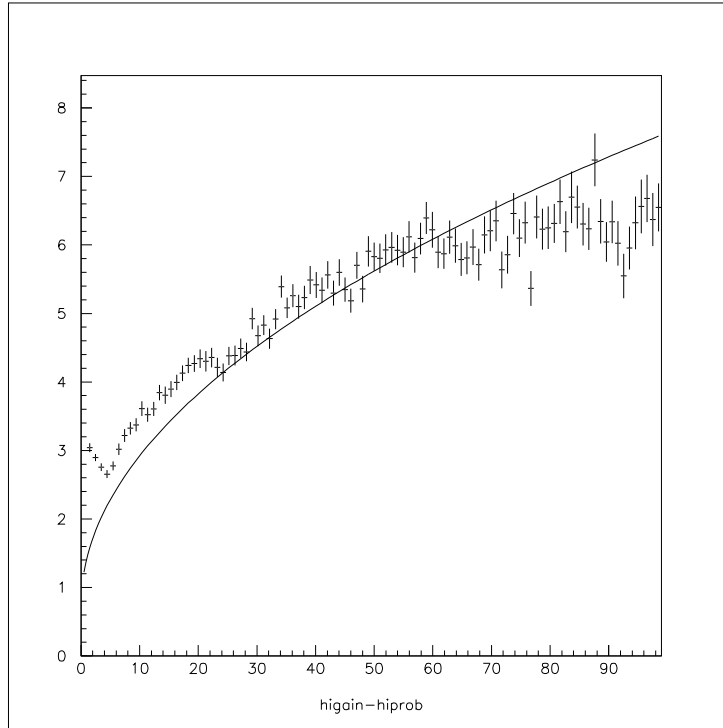
Figure C.1: This plot shows the results of leaving the second bin out of the fitter and comparing the actual counts in that bin to those predicted by the fit. The x-axis shows the number of counts in that second bin. The y-axis shows the difference $predicted - actual$ counts for only positive values of this difference. The line shows the uncertainty for each bin from the equation $0.74 + 0.69 \times \sqrt{\text{counts}}$.

and "first bin uncertainty" fixes resulted in improvements of the fit probability from zero to some non-zero value. Examination of these events showed that these fixes improved the fitter's ability to identify single-pulse events while creating a negligible number of false-positives (none were observed in the events examined).

C.3.3 Intermediate Zero-Count Bins Included in the Fit

The previous fitter did not include intermediate bins having zero counts in the fit. This was changed so that the fitter first identified the first and last bins of the pulse. Then up to the first 30 bins of this pulse were fit with bins having zero counts being included. Bins which were identified as saturated were excluded from the fit.

The resulting components of acceptance due to this fix relative to the two previous fixes detailed in this section are shown in the row labeled "First bin and low-count uncertainty fixes + 0-count bins included" in Table C.1. This fix resulted in a slight drop in the combined acceptance of CCDBADFIT, CCDPUL and EPIONK due to an increase in single-pulse fit probabilities below 25% resulting in more double-pulse fits being performed. A fiber channel can only cause an event to fail CCDBADFIT or CCDPUL if a double-pulse fit was performed.

C.4 Hold and Release Double-Pulse Fit

The fitter was modified so that the double-pulse fit became a two-stage process. For the first stage of the double-pulse fit process, the kaon-pulse time was fixed at the time returned from the single-pulse fit. The three other parameters (kaon-pulse amplitude, pion-pulse time and pion-pulse time) were allowed to wander in the fit. For the second stage of the double-pulse fit, the values returned from the first stage of the double-pulse fit were used as the initial guesses.

The sample used to optimize this modification to the fitter was $K_{\mu 2}$ monitor trigger

Fix	CCDBADFIT	CCDPUL	ALL
No fixes	0.797	0.454	0.362
First bin and low-count uncertainty fixes	0.876	0.518	0.453
First bin and low-count uncertainty fixes + 0-count bins included	0.881	0.504	0.443

Table C.1: Components of acceptance for various target fitter fixes. The "ALL" column shows the combined acceptance of the set of cuts consisting of CCDBADFIT, CCDPUL and EPIONK applied sequentially. The acceptance of the EPIONK cut was 0.999 for all 3 situations so it was not given a column in the table. The row "First bin and low-count uncertainty fixes" includes both the first bin uncertainty fix (doubling the uncertainty for this bin) and the low-count uncertainty fix (assigning an uncertainty equal to that for 10 counts for all bins having less than 10 counts). The row "First bin and low-count uncertainty fixes + 0-count bins included" includes the above fixes in addition to including intermediate zero count bins in the fit.

data with the following cuts applied: TARGET, TGCUT, UTC, RD_TRK, TRKTIM, RDUTM, TGQUALT, DELC and NPITG. After these cuts were applied, 7021 events remained. With the two-stage fit used instead of the previous one-stage fit, the total acceptance of CCDBADFIT and CCDPUL went from 0.402 to 0.451.
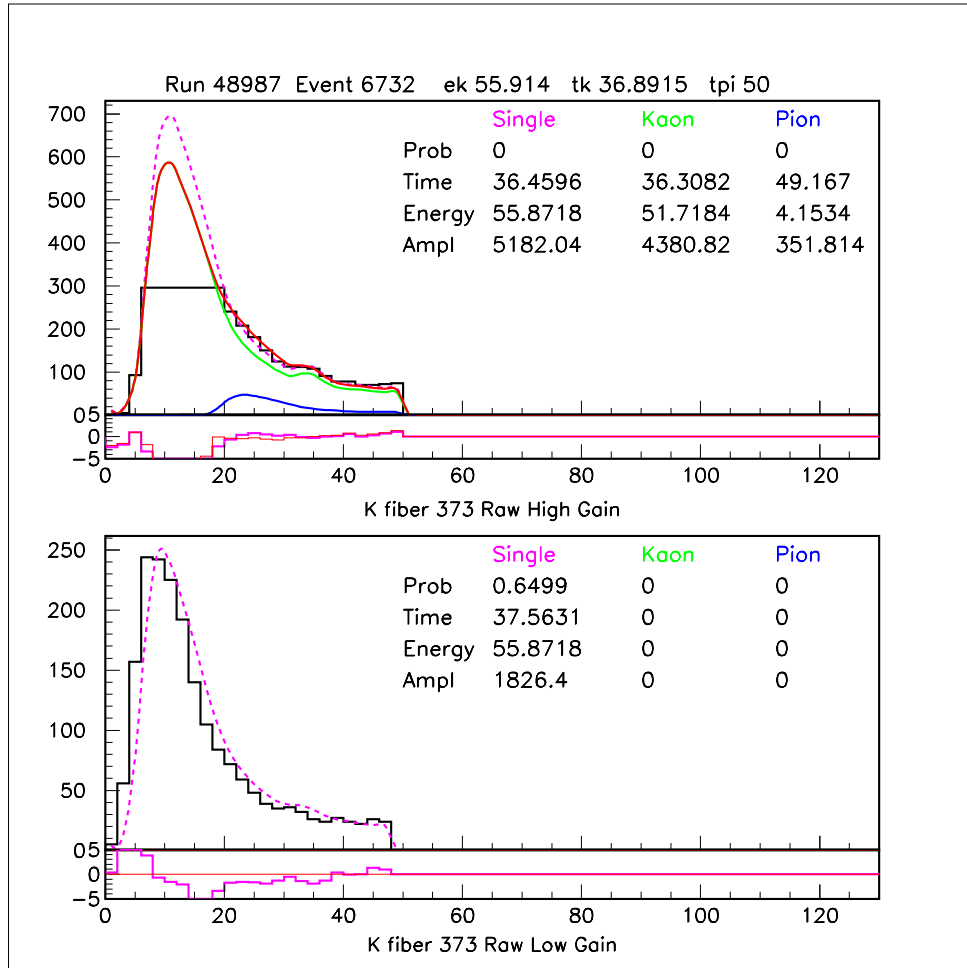
Figure C.2: The high-gain single-pulse probability of 0 when the uncertainty associated with the first bin was treated as usual. This was due to the first bin having only two counts versus where the shape of the reference pulse predicted a larger number of counts. Had the first bin had a pedestal subtraction that left it with zero counts, the next bin would have been used for the fit and the resulting fit would have been a non-zero probability. To reduce the effect of this sensitivity to the first bin, the uncertainties assigned to the first bin were always doubled. When the fit was performed with this increased first bin uncertainty, the single-fit probability for the high-gain was 0.069 instead of the zero probability shown in this figure.

Appendix D

Detailed List of Cuts

D.1 PASS1 Cuts

These cuts were applied to all the background studies and thus were excluded from the lists of setup cuts for the individual bifurcation branches.

D.1.1 Event Reconstruction Quality Cuts

TRBIT - The event passed the $\pi\nu\bar{\nu}(1)$ or $\pi\nu\bar{\nu}(2)$ triggers.

BAD_RUN - Removed runs where problems occurred in the beam, detector or electronics.

RD_TRK - The charged track was reconstructed in the Range-Stack.

TRKTIM - An average track time was found in the Range-Stack.

STLAY - There was agreement in the Range-Stack stopping counter as identified by the offline track finding routine and the online Stopping Counter Finder (SCF).

BAD_STC - Runs were identified during calibration in which a set of TD channels had unreliable signals. For these runs, events were removed if the Range-Stack stopping

241

counter contained these unreliable TD channels.

UTC - The charged track was reconstructed in the UTC.

RDUTM - The extrapolation of the reconstructed UTC track intersected the triggered T•2 sector.

TARGET - The event was reconstructed in the target.

PDC - The momentum of the charged track as measured by the UTC was less than 280 MeV/c. This removed high-momentum beam particles and failures in UTC pattern recognition.

D.1.2 Muon Background Rejection Cuts

FITPI - The double-pulse $\pi^+ \rightarrow \mu^+$ signature was observed in the fitted TD pulses from the Range-Stack stopping counter.

RSHEX - Event was rejected if there were additional hits in (1) the counter after the Range-Stack stopping counter, or (2) the hextants that did not have track hits.

RSHEX2 - Event was rejected if the charged track in the Range-Stack crossed from one sector to another in the stopping layer.

D.2 PASS2 Cuts

The PASS2 cuts consisted of looser versions of the PASS3 cuts. The PASS2 cuts were applied in certain combinations to enhance specific backgrounds, reducing processing time when developing cuts and evaluating background levels.

P2PVCUT - A very loose photon veto was applied in the Barrel Veto (± 2.0 ns, 1.5 MeV), End Cap (± 1.5 ns, 3.5 MeV), and Range-Stack (± 1.5 ns, 3.0 MeV). Events

were rejected if total coincident energy was above the listed threshold for the listed time window about the Range-Stack track time t_{rs}.

P2TGCUT - Events failed this target reconstruction cut if they did not meet all of the following conditions:

- The kaon decay vertex identified by target reconstruction was found inside the target.

- The average time of the kaon fiber hits (t_k) and the B4 Hodoscope hit time (t_{b4}) were within 4.0 ns.

- The average time of the pion fiber hits (t_{pi}) and the Range-Stack track time (t_{rs}) were within 5.0 ns.

- The I-Counter time (t_{IC}) and the Range-Stack track time (t_{rs}) were within 5.0 ns. This condition involved a small time offset: $|t_{IC} - t_{rs} + 0.3\text{ns}| \leq 5.0\text{ns}$.

- The energy deposited in the I-Counter was within 4 MeV of that expected for a minimum ionizing pion track.

P2TDCUT - Event was rejected if accidental activity in the Range-Stack coincident with the second pulse in the Range-Stack stopping counter exceeded a threshold.

P2PSCUT - Beam pion events were removed by requiring that (1) the energy deposited in the B4 Hodoscope was consistent with a kaon (> 1.0 MeV), and (2) there was no beam particle coincident with the T●2-trigger time. These beam-particle times were determined by the times of hits in the B4 Hodoscope and the pion Čerenkov counters.

P2TGPVCUT - Event was rejected if the total coincident activity in the target photon fibers at track time was above 5 MeV. The coincidence condition with respect to Range-Stack track time was $|t_\gamma - t_{rs} + 0.8\,\text{ns}| \leq 1.0\,\text{ns}$.

DELCO2 - Required that the beam kaon decayed at least 2.0 ns after entering the target. The times used for this condition were the average time of the kaon fiber hits (t_k) and the average time of the pion fiber hits (t_{pi}).

D.3   Kinematic Cuts

The kinematic cuts, collectively referred to as *KINCUTS*, were designed to remove events having kinematics inconsistent with signal.

D.3.1   Fiducial Cuts

LAYER14 - Event was rejected if it came to rest in the second Range-Stack Straw Chamber layer. This condition was accomplished by rejecting stopping layer 14 events having a prompt RSSC hit in the same sector or one sector clockwise of the stopping counter.

COS3D - Event was rejected if the cosine of the track polar angle was greater than 0.5. This removed events likely to interact with the dead material of the Range-Stack support structure.

LAYV4 - Event was rejected if the charged track did not come to rest in between Range-Stack stopping layers 6 to 18 inclusive.

ZFRF - The charged track was required to come to rest inside of the Range-Stack fiducial region based on the stopping z-position. This condition was applied for stopping layers 11-12 ($|z \leq 35$ cm$|$), 13 ($|z \leq 40$ cm$|$), 14 ($|z \leq 30$ cm$|$), and 15-18 ($|z \leq 50$ cm$|$).

ZUTOUT - The charged track was required to pass through the UTC outer layer within the active region ($|z \leq 25$ cm$|$).

D.3.2 Track Reconstruction Cuts

UTCQUAL - Good track reconstruction was required in the UTC based on a likelihood condition in the x-y plane. The quantities considered in this likelihood condition were the number of hits used in the UTC track fit, the number of hit UTC layers, and the number of unused hits within 1.5 cm of the fitted track.

PRRF - Event was rejected if the charged-track scattered in the Range-Stack, as determined by matching between Range-Stack track reconstruction and UTC track extrapolation. The following conditions were examined:

- Event was rejected if it failed a χ^2 probability condition for the Range-Stack track reconstruction in the x-y plane. The Range-Stack track fitting used sector crossing positions, RSSC hit positions and the energy deposit in the stopping counter.

- Event was rejected if the track reached the first layer of RSSCs and the matching between the UTC track extrapolation and the RSSC hit positions was poor.

- Event was rejected if the matching in the r-z plane was poor between the UTC track extrapolation and the track hit positions in the Range-Stack counters as determined by end-to-end timing.

D.3.3 dE/dx Cuts in Range-Stack

RSDEDX - The following conditions based on energy deposits in the Range-Stack were examined:

- Event was rejected if the energy deposited in any Range-Stack track counter was inconsistent with that expected for a pion. The deviation between mea-

sured E^i_{meas} and expected E^i_{exp} energies for the ith track counter was given by:

$$\chi_i = \frac{\log E^i_{\mathrm{meas}} - \log E^i_{\mathrm{exp}}}{\sigma^i}, \tag{D.1}$$

where the event was rejected if $|\chi_i| \geq 4$.

- Event was rejected if the confidence level calculated from the probability of χ^2 from Equation (D.1) was less than 0.04.

- Event was rejected based on a likelihood condition constructed from the energy deposits in the track counters.

- Event was rejected based on additional constraints on the fit times and energies determined by the `fitpi4` routine [57].

D.3.4 Range-Momentum Consistency Cut

RNGMOM - Event was rejected if the measured range `rtot` and the expected range based on momentum $\mathtt{r}_{\mathrm{exp}}$ were not consistent under the assumption of a charged track due to a pion. This cut targeted muon backgrounds due to the different regions of the range-momentum phase-space occupied by pions and muons. Event was rejected if the deviation $\chi_{\mathrm{r-p}}$ was greater than 2.2, where

$$\chi_{\mathrm{r-p}} = \frac{\mathtt{rtot} - \mathtt{r}_{\mathrm{exp}}}{\sigma_{\mathtt{rtot}}}. \tag{D.2}$$

D.4 Phase Space Cuts

The kinematic constraints of the PNN2 phase space (PNN2BOX) were split into loose (BOXLOOSE) and tight (BOXTIGHT) versions. For each cut, the outgoing charged track was required to pass the listed kinematic conditions on momentum (`ptot`), energy (`etot`) and range in plastic scintillator (`rtot`).

BOXLOOSE - The acceptance conditions for the loose kinematic box were:

$$140.0 \text{ MeV}/c \leq \quad \texttt{ptot} \quad \leq 199.0 \text{ MeV}/c;$$

$$60.0 \text{ MeV} \leq \quad \texttt{etot} \quad \leq 100.5 \text{ MeV};$$

$$12.0 \text{ cm} \leq \quad \texttt{rtot} \quad \leq 28.0 \text{ cm}.$$

BOXTIGHT - The acceptance conditions for the tight kinematic box, created to heavily suppress the K_{e4} background, were:

$$165.0 \text{ MeV}/c \leq \quad \texttt{ptot} \quad \leq 197.0 \text{ MeV}/c;$$

$$72.0 \text{ MeV} \leq \quad \texttt{etot} \quad \leq 100.0 \text{ MeV};$$

$$17.0 \text{ cm} \leq \quad \texttt{rtot} \quad \leq 28.0 \text{ cm}.$$

There were two additional sets of kinematic constraints that did not define the signal region, but were used for various studies in this analysis: KP2BOX to choose events in the $K_{\pi 2}$ peak, and KM2BOX to choose events in the $K_{\mu 2}$ peak. Figure 3.2 shows where these other kinematic boxes were found with respect to the kinematic signal region PNN2BOX in range versus momentum phase space.

KP2BOX - The acceptance conditions for the $K_{\pi 2}$-peak kinematic region were:

$$199.0 \text{ MeV}/c \leq \quad \texttt{ptot} \quad \leq 215.0 \text{ MeV}/c;$$

$$100.5 \text{ MeV} \leq \quad \texttt{etot} \quad \leq 115.0 \text{ MeV};$$

$$28.0 \text{ cm} \leq \quad \texttt{rtot} \quad \leq 35.0 \text{ cm}.$$

KM2BOX - The acceptance conditions for the $K_{\mu 2}$-peak kinematic region were:

$$226.0 \text{ MeV}/c \leq \quad \texttt{ptot} \quad \leq 246.0 \text{ MeV}/c;$$

$$37.0 \text{ cm} \leq \quad \texttt{rtot}.$$

D.5   Beam Cuts

The beam cuts, collectively referred to as *BEAMCUTS*, were designed to remove events with beam-pions scattering into the fiducial region of the detector and double-beam events.

D.5.1   Particle Identification

B4DEDX - Beam pion events were removed by requiring that the energy deposited in the B4 Hodoscope was consistent with a kaon (> 1.1 MeV).

D.5.2   Double-Beam Cuts

B4CCD - Double-beam events were removed based on fits in the B4 Hodoscope CCDs fitted with a double-pulse assumption. A double-pulse signature was considered present when the ratio of χ^2 for the double-pulse fit versus the single-pulse fit was greater than 2.5 for second-pulse amplitudes above a certain threshold. Event was rejected when the difference between the average time from hit modules having having double-pulse signatures and t_{rs} was greater than 3.5 ns.

B4TRS - Event was rejected if there was activity in the B4 Hodoscope at track time in the Range-Stack t_{rs}. This activity was considered present if (1) the average TDC time from B4 hit modules was within 2.5 ns of t_{rs}, or (2) the average CCD time from B4 hit modules was within 1.5 ns of t_{rs} when the B4 energy sum was above 0.7 MeV.

BWTRS - Event was rejected if there was activity in the Beam-Wire Chamber at track time in the Range-Stack t_{rs}. This activity was considered present if there was a hit cluster in any of the Beam-Wire Chambers within 4.5 ns of t_{rs}.

CKTRS - Event was rejected if the average TDC or CCD time of the Čerenkov kaon counter hits was within 2.0 ns of t_{rs}.

CKTAIL - Event was rejected if the average time of the trailing edge of pulses in the Čerenkov kaon counters minus the average TDC width was within t_{window} of t_{rs}. The time window varied based on the difference between the average time of the kaon fiber hits t_k and the average time of the pion fiber hits t_{pi}:

- $t_{\texttt{window}} = 3$ ns when $t_{\texttt{pi}} - t_{\texttt{k}} < 15.0$ ns;

- $t_{\texttt{window}} = 3.5$ ns when 15.0 ns $\leq t_{\texttt{pi}} - t_{\texttt{k}} < 25.0$ ns;

- $t_{\texttt{window}} = 3$ ns when 15.0 ns $\leq t_{\texttt{pi}} - t_{\texttt{k}}$.

CPITRS - Event was rejected if the average TDC or CCD time of the Čerenkov pion counter hits was within 2.0 ns of $t_{\texttt{rs}}$.

CPITAIL - Event was rejected if the average time of the trailing edge of pulses in the Čerenkov pion counters minus the average TDC width was within $t_{\texttt{window}}$ of $t_{\texttt{rs}}$. The time window varied based on the difference between the average time of the kaon fiber hits $t_{\texttt{k}}$ and the average time of the pion fiber hits $t_{\texttt{pi}}$:

- $t_{\texttt{window}} = 3$ ns when $t_{\texttt{pi}} - t_{\texttt{k}} < 15.0$ ns;

- $t_{\texttt{window}} = 3.5$ ns when 15.0 ns $\leq t_{\texttt{pi}} - t_{\texttt{k}} < 25.0$ ns;

- $t_{\texttt{window}} = 3$ ns when 15.0 ns $\leq t_{\texttt{pi}} - t_{\texttt{k}}$.

UPVTRS - Event was rejected if there was a hit in the Upstream Photon Veto (UPV) coincident with $t_{\texttt{rs}}$. Timing information from both the CCDs ($t_{\texttt{CCD}}$) and TDCs ($t_{\texttt{TDC}}$) was used. Event was rejected if either condition was met:

- -3.5 ns $< t_{\texttt{CCD}} - t_{\texttt{rs}} < 2.4$ ns;

- -3.75 ns $< t_{\texttt{TDC}} - t_{\texttt{rs}} < 2.5$ ns.

RVTRS - Event was rejected if there was a hit in the Ring Veto (RV) within 4 ns of $t_{\texttt{rs}}$. Timing information from both the CCDs and TDCs was used.

D.5.3 Beam Pathology Cuts

Pathology cuts were cuts designed to remove specific types of abnormal events that were not properly suppressed by the regular cuts designed to suppress the various backgrounds.

These undesirable pathologies could have been due to behaviors such as inconsistencies between quantities measured in different detectors or known abnormal behavior in a reconstruction algorithm.

B4ETCON - Event was rejected if the timing or energy information in the B4 Hodoscope was inconsistent between the CCDs and the TDCs. Event was rejected if the times from these two systems were not within 2.0 ns of each other or if the energies from these two systems were not within 1.5 MeV.

TGGEO - Event was rejected by this cut if it had certain topological signatures associated with with double-beam events known to fool target reconstruction. The three types of signatures for rejected events were:

- Both beam-particles entered the target from the target edge or I-Counter;

- The first beam-particle or its charged decay product deposited a large amount of energy in the I-Counter;

- The charged decay product of the first beam-particle was not detected due to decaying downstream or decaying late. The second beam-particle scattered such that it missed some of the beam counters, but by multiple scattering enters the target and intersects with target fibers hit by the first beam-particle.

TGQUALT - The target reconstruction algorithm successfully reconstructed the event with at least one of the target fibers being classified as a pion fiber.

TIMCON - Event was rejected if it failed to meet either of the following timing consistency checks:

- The average time of the kaon fiber hits (t_k) and the B4 Hodoscope hit time (t_{bm}) were within 3.0 ns;

- The average time of the pion fiber hits (t_{pi}) was consistent with track time in the Range-Stack (t_{rs}), -4.75 ns $\leq t_{pi} - t_{rs} \leq 3.75$ ns.

TGTCON - Event was rejected if the time difference between an individual target kaon fiber and the average time of the kaon fiber hits t_k was greater than an energy dependent value varying between 2.05 and 3.68 ns.

D.6 Delayed Coincidence Cuts

The delayed coincidence cuts, collectively referred to as DELCO, rejected the same type of events as the beam cuts. The delayed coincidence cuts were split into loose (DELC3) and tight (DELC6) versions. Each version of the cut ensured that the incoming K^+ had come to rest before decaying by requiring a minimum time difference `delco` between the average time of the kaon fiber hits (t_k) and the average time of the pion fiber hits (t_{pi}):

$$t_{pi} - t_k \geq \texttt{delco}. \tag{D.3}$$

DELC3 - Event was required to meet the minimum delayed coincidence requirement of `delco` = 3 ns. Additional constraints were placed on the delayed coincidence requirement when the timing consistency between detector systems was degraded. The cut threshold was the maximum of the following conditions, with a minimum value of 3 ns:

- `delco` = 5 ns when the difference between the average time of the kaon fiber hits (t_k) and the B4 Hodoscope hit time (`tb4strob`) was greater than 1.0 s.

- `delco` = 6 ns when the difference between the average time of the pion fiber hits (t_{pi}) and track time in the Range-Stack (t_{rs}). was greater than 1.5 s.

- `delco` = 5 ns when t_{pi} was determined using I-Counter hit time (t_{IC}) instead

of the average time of the pion fiber hits (t_{pi}).

- delco = 4 ns when the energy deposit in target kaon fibers is less than or equal to 50 MeV.

- delco = 4 ns if the time of any of the individual target kaon fibers differed from the average time of the kaon fiber hits (t_k) by more than 2.0 ns.

- delco = 4 ns if the time of any of the individual target pion fibers differed from the average time of the pion fiber hits (t_{pi}) by more than 3.5 ns.

DELC6 - Event was required to meet the tight delayed coincidence requirement of delco = 6 ns. Additional constraints like those in DELCO3 were not applied.

D.7 Target Quality Cuts

The target quality cuts, collectively referred to as *TGCUTS*, were designed to select events having good event signatures in the target. Note that the cut KPIGAP was not included in the group *TGCUTS*, nor was it applied as an analysis cut used to define the signal region.

B4EKZ - Event was rejected if the beam particle identified as a kaon by event reconstruction did not behave like a kaon. A likelihood function was created using the z-position of the kaon decay in the target as determined by UTC track extrapolation, the expected z-position of the kaon decay as determined by the total energy deposited in target kaon fibers, and the energy deposited by the kaon in the B4 Hodoscope. This cut suppressed the beam pion scatter single-beam background. A tighter rejection condition was placed on this likelihood function if t_{pi} was determined using I-Counter timing information instead of the average hit times in the target pion fibers.

TGZFOOL - Event was rejected if the z-position of the kaon decay vertex was too close to the upstream end of the target or was not in the fiducial region of the target at all. This z-position was determined by UTC track extrapolation.

EPITG - Event was rejected if an individual target pion fiber had an energy greater than 3.0 MeV. This rejected potential pion target-scatters since the nominal energy deposited in a pion fiber was 1.2 MeV.

TARGF - Event was rejected if the minimum distance between the target kaon and pion fibers was greater than one fiber (0.6 cm). This cut suppressed CEX and double-beam backgrounds.

DTGTTP - Event was rejected if the charged-product tracks in the target and UTC were not well-matched at the target edge.

RTDIF - Event was rejected if the uncertainty in the calculation of the pion path length in the target was greater than 1.5 cm.

DRP - Event was rejected if there was a kink in the target pion track as determined by a large spread between the minimum and maximum radius of the UTC reconstructed track.

TGKTIM - Event was rejected if the time of an individual target kaon fiber hit ($\mathtt{t}_\mathtt{k}^i$) was more than 3.5 ns later than the B4 Hodoscope hit time ($\mathtt{t}_\mathtt{B4}$). Event was also rejected if $2\mathtt{t}_\mathtt{k}^i - \mathtt{t}_\mathtt{B4} - \mathtt{t}_\mathtt{rs} > -1.0$ ns, where $\mathtt{t}_\mathtt{rs}$ is track time in the Range-Stack.

EIC - Consistency was required between the energy measured in the I-Counter ($\mathtt{E}_\mathtt{IC}$) and the expected energy ($\mathtt{E}_\mathtt{exp}$) based on path length in the I-Counter, -5.0 MeV $\leq \mathtt{E}_\mathtt{IC} - \mathtt{E}_\mathtt{exp} < 1.75$ MeV.

TIC - Event was rejected if the I-Counter hit time $\mathtt{t}_\mathtt{IC}$ and track time in the Range-Stack $\mathtt{t}_\mathtt{rs}$ were not within 5.0 ns of each other.

TGEDGE - Event was rejected if there was more than 4.0 MeV in a multiplexed target edge-fiber PMT within 5.0 ns of $\mathtt{t_{rs}}$.

TGDEDX - Events was rejected if the charged track dE/dx in the target was inconsistent with that of a pion. This cut used a likelihood function based on the following quantities of the charged track: momentum ($\mathtt{ptot}$), range in the target , energy deposited in the target and expected range in the target based on the measured energy deposited in the target and the momentum $\mathtt{ptot}$.

TGENR - Event was rejected if the total energy of the hit pion fibers in the target was not in the range of 1 to 28 MeV.

PIGAP - Event was rejected if a gap greater than 1.5 cm was found between target pion fibers. This cut was tightened to reject gaps greater than 1.0 cm when the z-position of the track in the I-Counter was less than -7.0 cm and the cosine of the polar angle was negative (charged-track pointed upstream).

TGB4 - Consistency was required between the positions of the target kaon decay vertex, the kaon and pion clusters, and the beam particle in the B4 Hodoscope. The following conditions were examined:

- Event was rejected if the distance in the xy-plane between the hit position in the B4 Hodoscope and the nearest target kaon cluster tip was greater than 1.8 cm. The kaon cluster tips were the two kaon fibers furthest apart from each other.

- Event was rejected if the distance in the xy-plane between the kaon decay vertex and the nearest kaon cluster tip was greater than 0.7 cm.

- Event was rejected if the distance in the xy-plane between the kaon decay vertex and the nearest pion fiber was greater than 1.5 cm.

PHIVTX - Event was rejected if it had back-to-back charged decay-product tracks in the target.

OPSVETO - Event was rejected if the total energy in target opposite-side pion fibers was more than 1.0 MeV within 4.0 ns of the average pion fiber hit time t_{pi}. This energy threshold was reduced to 0.5 MeV if the likelihood function from B4EKZ was less than 200. Opposite-side pion fibers were pion fiber hits found on the opposite side of the kaon cluster relative to the main pion cluster (see Section 3.3).

TGLIKE - Event was rejected if a target pion fiber showed evidence of hidden energy as determined by two target pion-fiber likelihood functions. The first likelihood function was constructed for each pion fiber from the distance to the extrapolated UTC track, the time and the energy of the pion fiber hit. The rejection condition for the first likelihood function was based on the average likelihood for all pion fibers. A second likelihood function was constructed using only the distance between the pion fiber hit positions and the extrapolated UTC track and had a tighter rejection threshold than the first likelihood function.

TIMKF - Event was rejected if the times of the target kaon fiber hits were not consistent with a kaon approaching the kaon decay vertex. This consistency was checked by tabulating the times of the kaon fiber hits against the distance to the decay vertex in the x-y plane and against the range of the kaon as determined by deposited energy.

NPITG - Event was rejected if no target fibers were identified as pion fibers.

ALLKFIT - Event was rejected if any of the target kaon fibers having more than 3.0 MeV of energy were not successfully fit by the target CCD fitter. A fiber was considered successfully fit if the probability of the fit for the single-pulse or double-pulse assumptions was greater than 0.01. See Appendix C for more detailed discussion of the target CCD fitter.

TPICS - Event was rejected if the standard deviation of hit times for the target pion fibers was greater than 4.0 ns.

EPIONK - Event was rejected if a target fiber classified as both a kaon and a pion fiber had more than 1.25 MeV assigned to the pion pulse. The target reconstruction was able to find pion hits in kaon fibers when the average hit time for pion fibers t_{pi} was at least 15 ns greater than the average hit time for kaon fibers t_k.

CHI567 - Event was rejected if the probability of a sum of three χ^2-like quantities was below a certain threshold. These χ^2-like quantities had contributions from target pion fibers and the target π^+ track fitter [72] as follows:

- χ_5^2 - Contributions for hit pion fibers which were part of the reconstructed pion track were based on observed versus expected energy.

- χ_6^2 - Contributions for fibers with no energy, but lying along the projected pion track were based on the minimum distance between the projected track and the corners of the fiber. This forced the fitted track to go between the fibers.

- χ_7^2 - Contributions for hit pion fibers which were not part of the reconstructed pion track were based on their distance from the track.

CHI5MAX - Event was rejected if the contribution to χ_5^2 (see CHI567) due to any single fiber was greater than 10.

VERRNG - Event was rejected if the fitted track in the target did not intersect the vertex fiber as identified by target reconstruction.

ANGLI - Event was rejected if the range of the charged track in the target was less than 2.0 cm, and the angle between the track from target reconstruction and the UTC extrapolated track was greater than 0.01 radian.

KIC - Event was rejected if a hit in the I-Counter was coincident with target kaon time and kaon fibers were found near this counter.

CCDBADFIT - Event was rejected if the target CCD fitter was unable to make a successful fit for a kaon fiber having more than 1.25 MeV of energy. The fit was considered unsuccessful if the probability of the fit for both the single-pulse and double-pulse assumptions was zero. This cut is discussed in more detail in Appendix E.

CCDBADTIM - Event was rejected if the target CCD fitter found a known incorrect solution for a kaon fiber having more than 1.25 MeV of energy. These known incorrect solutions were as follows:

- The first-pulse time from the double-pulse fit was less than -9.98 ns.

- The second-pulse time from the double-pulse fit was less than -4.99 ns.

- The first-pulse time from the double-pulse fit t_1 was inconsistent with the average target kaon fiber hit time t_k. The rejection conditions were $t_1 - t_k < -6$ ns or $t_1 - t_k > 7$ ns.

- The time from the single-pulse fit was less than -9.98 ns when the probability of the single-pulse fit was greater than 0.25 and thus the double-pulse fit was not performed.

- The time from the single-pulse fit t_0 was inconsistent with t_k when the probability of the single-pulse fit was greater than 0.25. The rejection conditions were $t_0 - t_k < -6$ ns or $t_0 - t_k > 7$ ns.

This cut is discussed in more detail in Appendix E.

CCD31FIB - Event was rejected if the 31st fiber fit by the target CCD fitter had a fit probability for the single-pulse assumption of less than 0.25. When this occurred,

257

the results of the subsequent fit for the double-pulse assumption were not stored correctly.

CCDPUL - Event was rejected if the second-pulse found in a kaon fiber by the target CCD fitter had more than 1.25 MeV of energy and was coincident with target pion time $\mathtt{t_{pi}}$. This coincidence condition was quite loose: -7.5 ns $< \mathtt{t_2} - \mathtt{t_{pi}} < 10.0$ ns. This cut is discussed in more detail in Appendix E.

KPIGAP - This was not one of the analysis cuts used to define the signal region. This cut was used to identify events where the pion track did not emerge directly from the target kaon fibers. This cut, used in the charge exchange background evaluation (see Section 4.8), was designed to provide a cleaner sample of this type of event than that produced by inverting TARGF. The target reconstruction algorithm identified potential pion fibers having large energy deposits as photon fibers. Allowing these photon fibers (within 3.0 ns of Range-Stack track time $\mathtt{t_{rs}}$) to fill the gap created a cleaner sample of events having true gaps between the kaon and pion fibers.

D.8 $\pi^+ \to \mu^+ \to e^+$ Decay-Sequence Cuts

The $\pi^+ \to \mu^+ \to e^+$ decay-sequence cuts, collectively referred to as *TDCUTS*, were designed to reject events with a μ^+ as the primary charged particle from the kaon decay. This set of cuts was split into loose (*TDLOOSE*) and tight (*TDTIGHT*) versions. The loose set *TDLOOSE* consisted of P2TDCUT, IPIFLG, ELVETO, TDFOOL and a loose version of TDNN. The tight set *TDTIGHT* consisted of P2TDCUT, IPIFLG, ELVETO, TDFOOL, EV5 and a tight version of TDNN.

IPIFLG - Event was rejected if the $\pi^+ \to \mu^+$ decay sequence in the Range-Stack stopping counter was emulated by an accidental hit in conjunction with the muon track. The event was rejected if the time of the first pulse, obtained from TD double-pulse

fitting, was not within 2.5 ns of Range-Stack track time $\mathtt{t_{rs}}$.

ELVETO - Event was rejected if there was accidental activity coincident with the time of the second pulse in the Range-Stack stopping counter. The coincident energy was searched for in the Range-Stack, Barrel Veto, Barrel Veto Liner and End Caps, and the event was rejected if the total coincident energy in a given subsystem was above the threshold energy shown in Table D.1.

Category	Time Window (ns)	Energy Threshold (MeV)
Both-ends hit category		
Range-Stack (RS)	±3.00	0.20
RS (TD)	±0.25	5.20
Barrel Veto (BV)	±1.25	0.20
Barrel Veto Liner (BVL)	±2.75	0.20
Single-end hit category		
RS single energy, both times	±7.00	0.20
RS both energy, single time	±4.50	9.40
RS single energy, single time	±8.75	6.60
RS no energy, both times	±5.00	-
RS (TD) single energy, single time	±3.00	3.20
BV single energy, both times	±3.00	1.60
BV both energy, single time	±0.25	0.40
BV single energy, single time	±3.00	1.80
BV no energy, both times	±5.75	-
BVL both energy, single time	±0.75	0.10
BVL single energy, single time	±5.00	1.00
BVL no energy, both times	±5.50	-
Other category		
End Cap (EC)	±0.25	22.00

Table D.1: The energy threshold and time window relative to muon time in the Range-Stack for each category of accidental hits for the ELVETO cut. Table reproduced from [55].

TDFOOL - Event was rejected if accidental activity was causing the second-pulse in the Range-Stack stopping counter. The second-pulse was considered to have come from

accidental activity when there was double-pulse activity present in one of the two layers preceding the stopping counter having second-pulse timing consistent with the second-pulse found in the stopping counter.

TDNN - Based on a neural-net function, events having tail fluctuations in the TD pulse or K^+ decays involving μ^+ particles were rejected. The five variables used to construct the neural-net function were the TD single-pulse fit χ^2, the ratio of χ^2 for single-pulse fit to double-pulse fit, the time and energy of the fitted second pulse, and the difference between both ends for the second pulse time. The cut position was tighter for *TDTIGHT* than for *TDLOOSE* (see Section 6.2.3).

EV5 - Event was rejected if the signature of the $\mu^+ \rightarrow e^+$ decay was not present in and around the Range-Stack stopping counter. The signature of this decay was a cluster of hits on only one side of the stopping counter, consistent with the time of the third pulse in the stopping counter. This cut was included in the named group of cuts *TDTIGHT*, but not in *TDLOOSE*.

D.9   Photon Veto Cut

The event was rejected if there was activity in any of the photon veto subsystems coincident with Range-Stack track time t_{rs}. The photon veto (PVCUT) used to define the signal region was split into loose (PV60) and tight (PV30) versions. The photon veto was loosened even further (PV90) for use in the outside-the-box studies. Table D.2 shows the photon veto parameters for each subsystem with the ability to detect photons, where activity above the energy threshold and falling within the time window (defined relative to t_{rs}) caused the event to fail the photon veto cut. Table D.3 shows the parameters used for the BV, BVL and RS when the both-end requirements for time and energy were not met. In addition to the parameters listed in the tables, the PASS2 photon veto P2PVCUT

was always applied as part of this photon veto cut.

The optimization of the photon veto was based on a process of optimizing the parameters for each of the photon veto subsystems to maximize background rejection while maintaining a reasonable signal acceptance. The PV optimization for E949 had previously been performed for the PNN1 analysis [83], but had to be re-optimized due to the PNN2 analysis including TD hits in the BVL [37]. The acceptance and rejection samples used for this optimization were the $K_{\mu 2}$ monitor trigger data and $K_{\pi 2}$-peak events from signal data respectively. The optimization process started from an initial set of cut parameters for each subsystem (time offsets, time window and energy thresholds). The cut parameters were changed in small steps, one subsystem at a time, and the acceptance and rejection remeasured. It was considered to be an improved set of parameters if both the acceptance and rejection were increased or if one was increased without the other being lowered. The optimization process continued until no further gains in rejection could be attained without losing acceptance. Nine different goal levels of acceptance were chosen and the entire optimization process was repeated for each of these goal levels of acceptance to produce the profile curve of maximum achievable rejections as functions of acceptance as shown in Figure D.1. The details of this optimization can be found in [37].

The Active Degrader was not used in the E949 PNN1 analysis, but was used in this PNN2 analysis since it was essential in suppressing the most problematic type of $K_{\pi 2}$ target-scatter events as described in 4.1. The optimization of the AD, which required great care be taken not to veto on beam activity at beam time, is detailed in [37].

An additional set of parameters ("early BV") was added to the PV to remove a class of events observed in the photon veto optimization acceptance sample. These events had large hits in the BV in the time range of 5 to 35 ns earlier than $\mathtt{t_{rs}}$. It was found that these hits, due to accidentals, blinded the BV TDCs so that they could not register the hits from the decay photons. The ADC gates for the BV were approximately 50 ns wide so the energy from both the decay photon and the accidental was measured and these
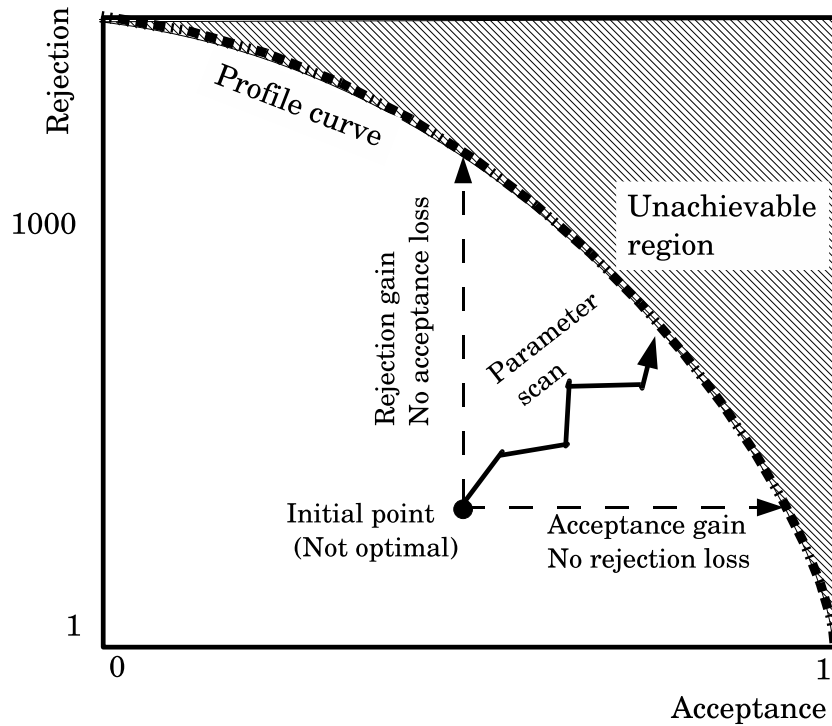
Figure D.1: Illustration of the optimization process used to determine the photon veto parameters. The "Profile curve" defines the maximum achievable rejection as a function of acceptance, along which it is no longer possible to further increase the acceptance or rejection without decreasing the other. Reprinted figure with permission from S. Adler *et al.* (E949 Collaboration), Phys. Rev. D **77** 052003 (2008), http://link.aps.org/abstract/PRD/v77/e052003. Copyright 2008 by the American Physical Society.

Category	PV60 (Loose)			PV30 (Tight)		
	Timing (ns)		Energy	Timing (ns)		Energy
	Offset	Window	(MeV)	Offset	Window	(MeV)
BV	2.25	7.95	0.20	1.35	8.85	0.70
early BV	-20.70	15.0	30.00	-22.5	15.0	30.0
BVL	3.15	7.55	0.30	3.15	7.55	0.30
RS	0.05	4.30	0.30	2.25	5.55	0.60
EC	1.80	6.15	0.40	1.75	7.75	0.20
EC inner-ring	0.99	4.64	0.20	-2.45	11.55	0.20
EC 2nd pulse	-1.60	4.07	10.60	-1.51	4.19	1.70
TG	-0.25	2.40	2.00	-2.15	4.40	1.40
IC	1.25	3.25	5.00	3.20	6.10	5.00
VC	-2.40	4.15	6.80	-0.20	7.25	6.00
CO	2.90	2.95	0.60	2.15	2.95	1.60
μCO	-1.60	3.90	3.00	-0.60	3.90	0.60
AD	3.00	5.00	0.60	3.00	5.00	0.60
DPV	2.50	7.50	0.00	2.50	7.50	0.00
early BVL	-3.50	1.50	10.00	-3.50	1.50	10.00

Table D.2: The parameters for the loose (PV60) and tight (PV30) photon vetoes. The parameters shown for BV, BVL and RS are for when the detector met the requirement that both ends obtained measurements of time and energy. Table reproduced from [56].

blinded BV modules recorded unusually large energies. These events were rejected by adding the "early BV" parameters with a threshold energy of 30 MeV.

Category			PV60 (Loose)			PV30 (Tight)		
	hit-ends		Timing (ns)		Energy	Timing (ns)		Energy
	Energy	Time	Offset	Window	(MeV)	Offset	Window	(MeV)
BV	both	single	3.05	15.95	1.00	0.55	13.05	0.40
BV	single	both	4.80	1.50	1.40	4.00	3.10	0.60
BV	single	single	-8.10	8.50	1.60	-8.30	6.90	1.00
BVL	both	single	-5.65	11.80	8.19	-5.65	11.80	8.19
RS	both	single	-2.85	0.70	5.20	0.01	5.36	0.20
RS	single	both	6.60	1.35	0.00	3.70	6.10	0.00
RS	single	single	-6.80	1.22	3.40	-11.54	4.53	0.60

Table D.3: The parameters for the loose (PV60) and tight (PV30) photon vetoes when the requirement was not met that both ends obtained measurements of time and energy. Table reproduced from [56].

Category	PV90 (Very Loose)		
	Timing (ns)		Energy
	Offset	Window	(MeV)
BV	-0.15	4.00	0.50
early BV	-19.15	15.0	30.00
BVL	0.35	1.75	0.40
RS	-0.85	1.45	0.20
EC	0.15	1.80	2.20
EC inner-ring	-0.35	2.30	1.20
EC 2nd pulse	-2.75	0.32	18.80
TG	0.25	1.50	5.20
IC	-0.50	2.75	13.00
VC	-0.25	1.50	3.80
CO	2.60	1.23	1.80
μCO	-1.50	2.50	3.60
AD	3.00	5.00	0.60
DPV	2.50	7.50	0.00
early BVL	-3.50	1.50	10.00

Table D.4: The parameters for the very loose (PV90) photon veto. The parameters shown for BV, BVL and RS are for when the detector met the requirement that both ends obtained measurements of time and energy. Table reproduced from [56].

Category	hit-ends		PV90 (Very Loose)		
	Energy	Time	Timing (ns) Offset	Window	Energy (MeV)
BV	both	single	0.55	13.05	0.40
BV	single	both	4.00	3.10	0.60
BV	single	single	-8.30	6.90	1.00
BVL	both	single	-5.65	11.80	8.19
RS	both	single	0.01	5.36	0.20
RS	single	both	3.70	6.10	0.00
RS	single	single	-11.54	4.53	0.60

Table D.5: The parameters for the very loose (PV90) photon veto when the requirement was not met that both ends obtained measurements of time and energy. Table reproduced from [56].

Appendix E

Target Pulse Cuts

The original CCDPUL cut, as it was used in the analysis of the PNN2 kinematic region for the E787 experiment, performed the function of both the CCDBADFIT and CCDPUL cuts described in this appendix. It was split into two for this analysis since CCDBADFIT was meant as a safety cut against events where the target CCD fitter was unable to find valid solutions. The CCDPUL cut was inverted for many of the classes used in the $K_{\pi 2}$ target-scatter rejection branch (Section 4.1.3) and a much cleaner sample of target-scatter events was created by applying CCDBADFIT and inverting CCDPUL than by inverting both of them.

The CCDBADTIM cut was a safety cut created as a result of an event observed in the single-cut failure study (Section 5.2) that enforced timing consistency between the times found using the target CCD fitter and those expected from target reconstruction. This cut had a very similar overall structure to CCDBADFIT and CCDPUL.

E.1   Description of CCDPUL

The CCDPUL cut removed events that had kaon fibers with second-pulse energies above 1.25 MeV and coincident with the average hit time of the target pion fibers $t_{\texttt{pi}}$. The

CCDPUL cut had three stages:

- In the first stage, the low-gain and high-gain CCDs of each kaon fiber was examined to determine if a double-pulse fit had been successfully performed.

- In the second stage, an algorithm determined if the information from the high-gain CCD, the low-gain CCD or a combination of the two should be used for each fiber that had successful double-pulse fits.

- In the third stage, each fiber from the second stage was examined for second pulse energies above a 1.25 MeV and rejected the event if the second pulse was coincident with the global pion time t_{pi}.

E.1.1 CCDPUL First Stage

For each kaon fiber, the results of the fits from the low-gain and high-gain CCDs were examined independently. The high-gain CCD data were not passed onto the second stage if any of the following conditions were met:

- The single-pulse fit probability was greater than 0.25 as the double-pulse fit was only performed if the single fit probability was less than or equal to 0.25.

- The number of bins in the second pulse having a non-zero amplitude was less than 3.

- The double-pulse fit probability was equal to zero.

The same conditions as above were applied to the low-gain CCDs with one additional condition, if the fiber was found to be multiplexed with at least one other fiber having activity within ± 5 ns of t_k or t_{pi} then the target low-gain CCD de-multiplexing algorithm would determine the first- and second-pulse energies of the fiber being examined. This de-multiplexing algorithm is detailed in Section E.6.

E.1.2 CCDPUL Second Stage

During the second stage of CCDPUL, an algorithm decided for each kaon fiber which CCD information was to be used in the third CCDPUL stage: the low-gain, the high-gain, or a weighted average of the two. If only the high-gain or or only the low-gain CCD data for a given fiber was passed on from the first CCDPUL stage, that is what was used. If the first stage passed on both the high-gain and the low-gain CCD information for a given fiber, the decision of how to use this information in the third CCDPUL stage was based on the following conditions, which were checked in sequence:

- An average of the high-gain and low-gain CCD information was used if the fiber energy as determined by ADC was between 10 MeV and 30 MeV and the fractional uncertainty in the second-pulse amplitude for both the low-gain and high-gain CCD channels was greater than 0.05. A typical pulse started to saturate at around 25 MeV so the ADC energy condition included high-gain CCD information that showed small amounts of saturation. The second-pulse energy and the relative time between the first and second pulses were the quantities calculated via the weighted average. For the remaining quantities (such as fit probabilities), the information from the high-gain channel was used. The following equations show how the weighted average was determined for a quantity x:

$$w_{hi} = \frac{dA_{hi}^2}{dA_{hi}^2 + dA_{lo}^2};$$

$$w_{lo} = \frac{dA_{lo}^2}{dA_{hi}^2 + dA_{lo}^2};$$

$$x = x_{hi}w_{hi} + x_{lo}w_{lo};$$

where dA_{lo} and dA_{hi} were the uncertainties on the fitted second-pulse amplitudes of the low-gain and high-gain double pulse fits, respectively.

- The high-gain CCD information was used if it had not saturated.

- The low-gain CCD information was used if the high-gain CCD had saturated and the ADC energy in the fiber was greater than 40 MeV. The low-gain target CCDs typically started to saturate at around 40 MeV.

- The most appropriate CCD channel was chosen based on the expected quality of the double-pulse fit given the fiber energy E_k (from ADC) and the time difference between the average time of the pion fiber hits t_{pi} and the average time of the kaon fiber hits t_k, The high-gain CCD information was used if either of these sets of conditions were met:

$$(15 < E_k < 25) \text{ and } (t_{pi} - t_k > 12);$$

$$(25 < E_k < 40) \text{ and } (t_{pi} - t_k > 20).$$

The low-gain CCD information was used if either of these sets of conditions were met:

$$(15 < E_k < 25) \text{ and } (t_{pi} - t_k < 12);$$

$$(25 < E_k < 40) \text{ and } (t_{pi} - t_k < 20).$$

This information was then passed onto the third stage.

E.1.3 CCDPUL Third Stage

The information for all fibers that were passed onto the third stage were checked for second-pulse energy above 1.25 MeV when the timing of the second pulse was consistent with the average pion fiber hit time t_{pi}. The event failed if any fiber in stage three met both of the following conditions:

- The second-pulse energy was above 1.25 MeV.

- The quantity `deltat` fell between -7.5 and 10 ns inclusive. The quantity `deltat` was a measure of consistency between t_{pi} and t_k, and the first (t_1) and second (t_2) pulse times from the double-pulse fit for that kaon fiber,

$$\texttt{deltat} = (t_2 - t_1) - (t_{pi} - t_k) . \tag{E.1}$$

E.2   Description of CCDBADFIT

The CCDBADFIT safety cut removed events where the target CCD fitter was unable to successfully fit a kaon fiber. This occurred when the probabilities for both the single- and double-pulse fits were equal to zero. As with CCDPUL, this cut also had three stages.

E.2.1   CCDBADFIT First Stage

For each kaon fiber, the results of the fits from the low-gain and high-gain CCDs were examined independently. The high-gain CCD data were not passed onto the second stage if any of the following conditions were met:

- The single-pulse fit probability was greater than 0.25 as the double-pulse fit was only performed if the single fit probability was less than or equal to 0.25.

- The number of bins in the second pulse having a non-zero amplitude was less than 3 when the double-pulse fit probability was greater than zero.

- The double-pulse fit probability was equal to zero and the single-fit probability was greater than zero.

The same conditions as above were applied to the low-gain CCD for each kaon fiber.

E.2.2 CCDBADFIT Second Stage

During the second stage of CCDBADFIT, a similar decision making process to that used in CCDPUL was used to determine which CCD information was to be passed onto the third stage for each kaon fiber: the low-gain or the high-gain. The difference in CCDBADFIT was that a weighted average of the low-gain and high-gain was not used, but the rest of the decision making sequence was the same.

E.2.3 CCDBADFIT Third Stage

All kaon fibers passed onto the third stage were checked for probabilities equal to zero for both the single- and double-pulse fits. If this condition was met and the fiber energy as determined by the ADC was greater than 1.25 MeV, the event failed the CCDBADFIT cut.

E.3 Description of CCDBADTIM

The CCDBADTIM cut was a safety cut designed to reject events if the target CCD fitter found a known incorrect solution for a kaon fiber having more than 1.25 MeV of energy. The known incorrect solutions fell into two main categories

1. The fitter fell into a local minimum where it attempted to fit the tail of the reference pulse to the actual pulse. The signature for this was a time of -9.9939 ns for the single-pulse fit (t_0) or for the first pulse of the double-pulse fit (t_1). Times lower than -9.9939 ns were stored in the ntuple as -9.9939 ns due to range limits placed on these variables when stored to the ntuple. A time of -4.9939 represented the same situation for the second pulse of the double-pulse fit.

2. Due to a large second pulse in the fiber, the fitter fit the second pulse as the primary pulse as shown in Figure E.1. The signature of this failure mode was either t_0 or

t_1 was inconsistent with the average time of the kaon fiber hits (t_k).

CCDBADTIM had three similar stages to those found in CCDPUL and CCDBADFIT. An additional fourth stage existed in CCDBADTIM whose purpose was to reject events with known incorrect solutions for the single-pulse fit times.

The first stage of CCDBADTIM was identical to that for CCDPUL (Section E.1.1). The second stage of CCDBADTIM was identical to that for CCDBADFIT (Section E.2.2). The third and fourth stages of CCDBADTIM are described below.

E.3.1   CCDBADTIM Third Stage

In the third stage of CCDBADTIM each kaon fiber passed on from the second stage was checked to see if the fiber energy as determined by the ADC was greater than 1.25 MeV. If the energy was above threshold and any of the following conditions were met, the event failed the cut.

- The time of the first-pulse in the double-pulse fit t_1 was less than -9.98 ns.

- The time of the second-pulse in the double-pulse fit t_2 was less than -4.99 ns.

- The time t_1 was not consistent with the average time of the kaon fiber hits t_k. The flagging conditions were $t_1 - t_k < -6$ns or $t_1 - t_k > 7$ns. This choice of cutting parameters is discussed in Section E.5.

E.3.2   CCDBADTIM Fourth Stage

In the fourth stage of CCDBADTIM, the times found in the single-pulse fit were examined for both the high-gain and the low-gain CCDs for each kaon fiber. This process was completely independent of the first three stages of the cut and an event failed CCDBAD-TIM if it failed due to the conditions laid out in the first three stages or if it failed due to the conditions checked in the fourth stage. The fourth part of the cut was designed
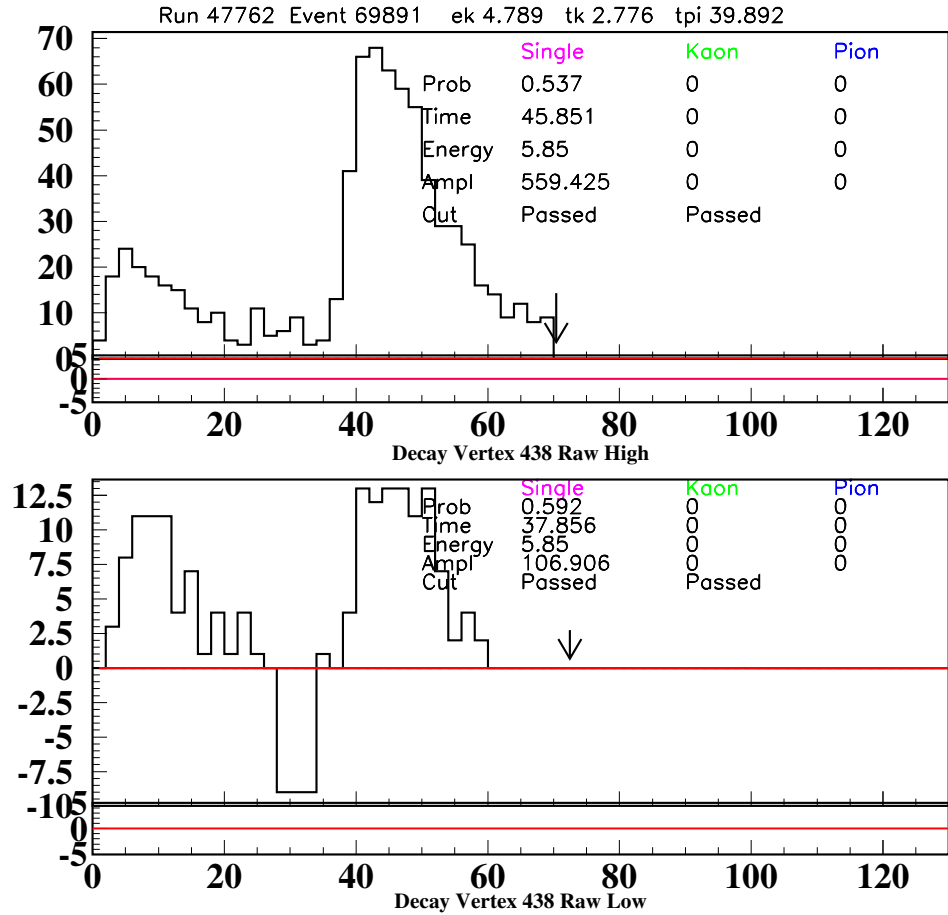
Figure E.1: An event that failed the CCDBADTIM cut due to the fitter trying to fit the energetic second pulse as the kaon pulse. The single-fit probabilities for both the high-gain (top) and low-gain CCDs were above 0.5 as shown in the row "Prob" and column "Single". The times of the single-pulse fits (row "Time") show that the second pulse in each of the high-gain and low-gain CCDs were fit as the single-pulse since the fit times agreed with t_{pi} ("tpi 39.892") and not t_k ("tk 2.776").

to reject events where a known incorrect solution was found for the single-pulse fit when (1) a double-pulse fit was not performed or (2) a good solution to the double-pulse fit was not found.

For each fiber, each of the two CCD channels were checked to see if they had a single-pulse fit probability above 0.25 and that the energy from ADC was above 1.25 MeV. If so and either of the following conditions were met, the examined CCD channel for that kaon fiber was flagged for possible rejection by CCDBADTIM.

- The single-pulse fit time t_0 was less than -9.98 ns.

- The single-pulse time (t_0) was not consistent with t_k. The failing conditions were $t_1 - t_k < -6$ns or $t_1 - t_k > 7$ns. This choice of cutting parameters is discussed in Section E.5.

A fiber having a CCD channel that has been flagged for possible rejection by CCDBADTIM caused the event to fail CCDBADTIM if

- Both CCD channels were flagged for possible rejection by CCDBADTIM;

- One CCD channel was flagged for possible rejection by CCDBADTIM and the other CCD channel had a double-pulse fit probability of zero;

- One CCD channel was flagged for possible rejection by CCDBADTIM and information from the other CCD channel was missing.

E.4   CCDPUL Optimization

Based on the previous PNN2 analysis of data from the E787 experiment [20], the second-pulse energy threshold above which would cause an event to be rejected by CCDPUL was initially set to 1.5 MeV. The coincidence window for the `deltat` coincidence condition (Equation E.1) between the second-pulse time of the double-pulse fit t_2 and the average

time of the pion fibers hits $\mathtt{t_{pi}}$ was initially set to ±10ns. Due to correlations between the cuts CCDBADFIT, CCDPUL and EPIONK, the optimization of these cuts was performed together.

The acceptance sample used for the optimization of CCDBADFIT, CCDPUL and EPIONK was the $K_{\mu2}$ monitor trigger data with very similar setup cuts as were used for measuring the components of acceptance of A_{beam} (Section 6.1.3). Figure E.2 shows the setup cuts applied to measure the acceptance of CCDBADFIT, CCDPUL and EPI-ONK with 136263 events remaining upon which to measure the acceptance. These cuts selected signal-like events for the target reconstruction by selecting K^+ decays with a single charged track, no photons, no beam contamination and no other activity in the detector. To minimize the μ^+ scatters in the target, the events were further constrained to be in the $K_{\mu2}$-peak by restricting the momentum $\mathtt{ptot}$ to be between 229 and 245 MeV/c (PTOT_229_245) and restricting the energy deposited in the Range-Stack ($\mathtt{E_{rs}}$) to be between 120 and 150 MeV (ERS_120_150). The BV and BVL subsystems were excluded from the photon veto to gain a larger acceptance for $K_{\mu2}$ events.

The rejection sample used for the optimization of CCDBADFIT, CCDPUL and EPI-ONK was very similar to the $K_{\pi2}$ target-scatter normalization branch (Section 4.1.2). This sample used $\pi\nu\bar{\nu}(1)$ and $\pi\nu\bar{\nu}(2)$ triggers from the 1/3 data set with an inverted photon veto, where the target was excluded from the photon veto. The setup cuts are shown in Figure E.3.

The optimization was performed by varying the second-pulse energy threshold ($\mathtt{E_2}$), and the lower and upper bounds ($\mathtt{t_{lo}}$ and $\mathtt{t_{hi}}$) of the timing coincidence quantity $\mathtt{deltat}$ (Equation E.1). Recall that an event failed CCDPUL if any of the kaon fibers had a second-pulse energy above $\mathtt{E_2}$ and had second-pulse timing coincident with the outgoing charged decay product as indicated by $\mathtt{deltat}$ falling within the bounds of $\mathtt{t_{lo}}$ and $\mathtt{t_{hi}}$. These three parameters ($\mathtt{E_2}$, $\mathtt{t_{lo}}$ and $\mathtt{t_{hi}}$) were varied and the optimal values were chosen based on maximizing the product of acceptance and rejection from their respective

275
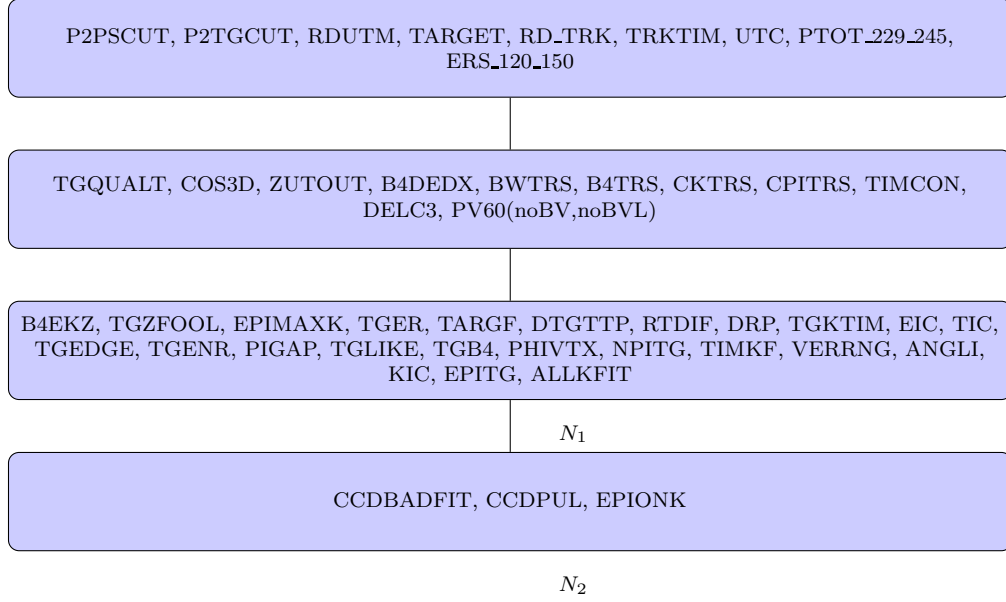
Figure E.2: Setup cuts for the CCDBADFIT, CCDPUL, EPIONK acceptance sample using $K_{\mu 2}$ monitor trigger data. The acceptance was the ratio of the number of events N_2/N_1, where N_1 was 136263 events.
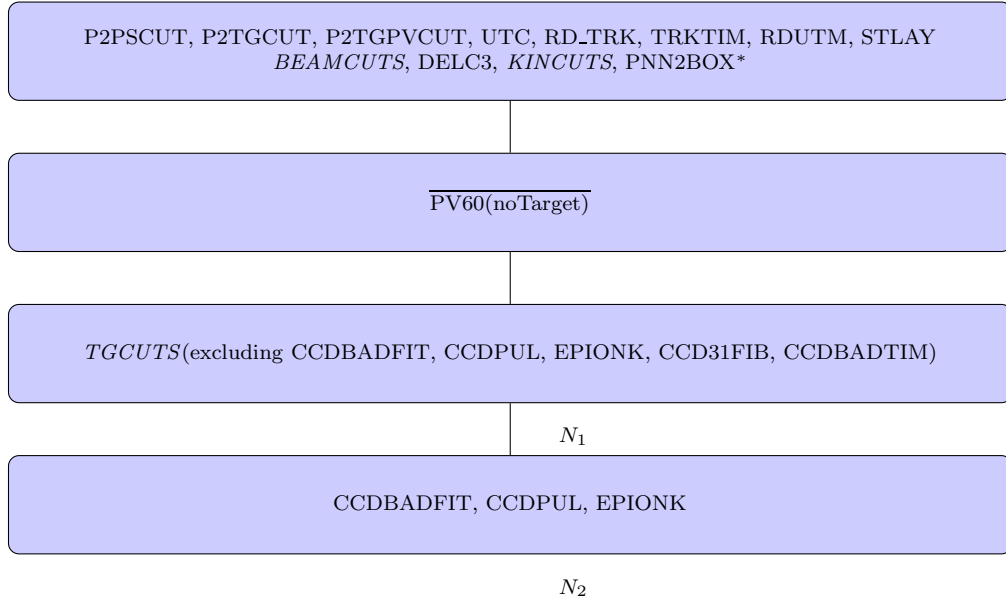
Figure E.3: Setup cuts for the CCDBADFIT, CCDPUL, EPIONK rejection sample using $\pi\nu\bar{\nu}(1)$ and $\pi\nu\bar{\nu}(2)$ triggers from the 1/3 data set. The rejection was the ratio of the number of events N_1/N_2, where N_1 was 3692 events.

samples. For similar values of Acceptance $\times$ Rejection, it was preferred to choose the parameters that corresponded to the largest acceptance. Note that the energy parameter E_2 was also used in the cuts CCDBADFIT and EPIONK.

Table E.1 shows the components of acceptance and rejection when a single parameter was varied and the other two were held fixed. Although the optimization allowed all the parameters to vary at the same time, the table presents only this subset of the parameter space for the sake of readability. Based on this optimization, the final values for the parameters were as follows:

- $E_2 = 1.25\text{MeV}$;

- $t_{lo} = -7.5\text{ns}$;

- $t_{hi} = 10.0\text{ns}$.

E.5   CCDBADTIM Parameters

The section discusses the choice of time parameters for the CCDBADTIM cut:

$$t_1 - t_k < -6, \; t_1 - t_k > 7 \tag{E.2}$$

and

$$t_0 - t_k < -6, \; t_0 - t_k > 7. \tag{E.3}$$

as originally described in Section E.3.

A sample was created using $K_{\mu2}$ monitor trigger data with all the cuts shown in Figure E.2 applied, including CCDBADFIT, CCDBADTIM and EPIONK. The time difference $t_1 - t_k$ was plotted for each kaon fiber passed onto the third stage of CCDBADTIM (Section E.3.1) that also passed the conditions $t_1 > -9.98\,\text{ns}$ and $t_2 > -4.99\,\text{ns}$ in the third stage. Figure E.4 shows the distribution of these events. The target CCD

277

$t_{lo} = -10$ns, $t_{hi} = 10$ns			
E_2 (MeV)	Acceptance	Rejection	Acceptance × Rejection
0.75	0.299	9.764	2.917
0.875	0.324	9.079	2.944
1.0	0.353	8.625	3.041
1.125	0.384	7.916	3.037
1.25	0.415	7.289	3.025
1.375	0.447	6.561	2.935
1.5	0.479	6.097	2.923
1.75	0.538	5.287	2.847
2.0	0.591	4.585	2.708

$E_2 = -10$ns, $t_{hi} = 10$ns			
t_{lo} (ns)	Acceptance	Rejection	Acceptance × Rejection
-6	0.475	6.142	2.918
-7	0.453	6.592	2.988
-7.5	0.445	6.787	3.017
-8	0.437	6.877	3.005
-9	0.425	7.126	3.025
-10	0.415	7.289	3.025
-12	0.401	7.486	3.001
-15	0.388	7.638	2.966
-18	0.382	7.709	2.946

$E_2 = -10$ns, $t_{lo} = -10$ns			
t_{hi} (ns)	Acceptance	Rejection	Acceptance × Rejection
6	0.434	6.809	2.952
7	0.428	6.946	2.971
7.5	0.425	7.005	2.979
8	0.423	7.077	2.993
9	0.419	7.163	2.998
10	0.415	7.289	3.025
12	0.409	7.514	3.070
15	0.402	7.782	3.128
18	0.397	7.977	3.169

Table E.1: Acceptance and rejection results for the combined group of cuts CCDPUL, CCD-BADFIT and EPIONK. The three parameters E_2, t_{lo} and t_{lo} were varied to maximize the product of acceptance and rejection. Each of the three sections of the table show one of the three parameters being varied while the other two were held constant.
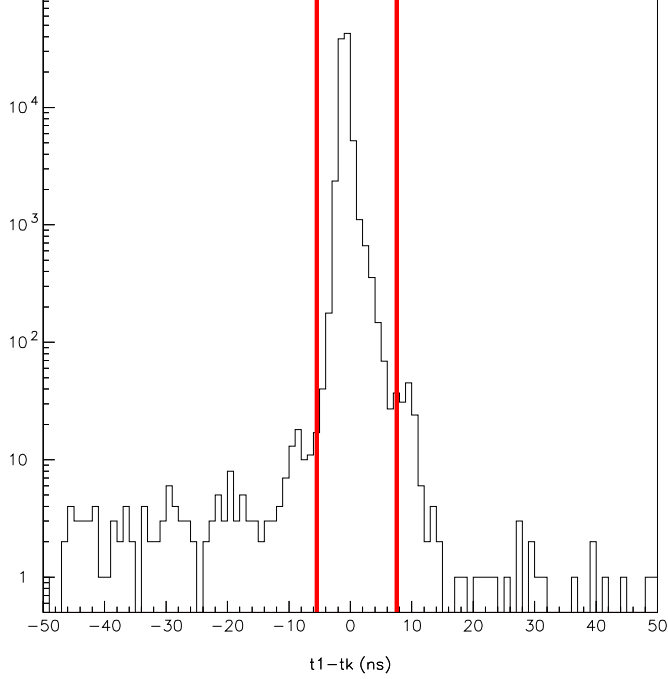
Figure E.4: Setting the allowed time window for consistency between t_1 and t_k in the CCD-BADTIM cut. The plot shows $t_1 - t_k$ for the sample of events described in the text of Section E.5. The bounds for the cut were set to $t_1 - t_k < -6\,\text{ns}$ and $t_1 - t_k > 7\,\text{ns}$ as indicated by the red lines on the plot.

information for many events falling outside these bounds were visually examined and were found to be consistent with the second target CCD fitter failure mode described in this section.

A similar study was performed for the time difference $t_0 - t_k$ and the same bounds as chosen for $t_1 - t_k$ were found to be appropriate.

The final acceptance of the safety cut CCDBADTIM was measured to be 0.99 as detailed in Section 6.1.3.

E.6 Updating the De-multiplexing Algorithm

An event in the single-cut failure study for the 1/3 sample data sample (Section 5.2.1) revealed a mistake in the way low-gain target fiber CCD information was being de-multiplexed for use in the CCDPUL cut. The low-gain target fiber CCDs were multi-plexed in groups of five fibers that were spatially found far apart from each other within the target. When more than one fiber in a multiplexed group had a hit at the same time, the amplitude information for that group had to be de-multiplexed using ADC informa-tion from each of the fibers to determine if second-pulse activity in a studied fiber was due to activity in that fiber of in another fiber within the same group.

E.6.1 Previous De-multiplexing Algorithm

In the previous de-multiplexing algorithm the second-pulse energy E_2 found by the double-pulse fitter was corrected for the ADC energies from the other fibers in the group for energy within ± 5 ns of t_{pi}. This energy came from fibers assigned as pion, opposite-side pion or gamma fibers (see Section 3.3.4 for a discussion of target fiber assignment). The sum of the coincident energy from the other fibers was called the multiplexed pion energy and this energy was subtracted from the E_2 value found by the fitter to give a corrected second-pulse energy E_2(corr.).

The total ADC energy for a fiber was split between the two pulses in a double-pulse fit to give an energy E_1 to the first pulse and an energy E_2 to the second pulse. This energy was split up based on the relative amplitudes of the two pulses as found by the double-pulse fitter. The flaw in the just described de-multiplexing algorithm was that if any multiplexed pion energy was found, the sum of E_1 and E_2(corr.) was not equal to the original ADC energy of the fiber. Since the target fiber ADCs were not multiplexed, the corrected energies of the two pulses should always have added up to the total ADC energy for that fiber.

E.6.2   New De-multiplexing Algorithm

The algorithm was modified so that the ADC energies near t_k and near t_{pi} from the other fibers in a group were taken into account when dividing the ADC energy in the studied fiber between the first and second pulse. The steps in the new de-multiplexing algorithm were as follows:

1. The multiplexed pion energy was determined using the same method described in Section E.6.1.

2. ADC energies within ± 5 ns of t_k from the other kaon fibers within the group were summed to create the multiplexed kaon energy.

3. The pion and kaon multiplexed energies were added to the ADC energy of the studied fiber to get a total energy as seen by the low-gain CCD channel of that fiber.

4. This total CCD energy was split between the first and second pulses according the ratio of the fitted amplitudes to give E_1 and E_2, respectively.

5. The kaon multiplexed energy was subtracted from E_1 to give the corrected energy $E_1(\text{corr.})$ and the pion multiplexed energy was subtracted from E_2 to give the corrected energy $E_2(\text{corr.})$.

6. If either of the resulting corrected energies was below 0.001 MeV, it was assigned an energy of 0.001 MeV and the other pulse was assigned the remaining ADC energy ensuring the total energy from the two pulses was equal to the ADC energy of the fiber.

This new de-multiplexing algorithm resulted in slightly less than 1% additional events failing the CCDPUL cut in both the acceptance and rejection samples used for the optimization of CCDPUL (Section E.4). Figure E.5 shows an event that passed CCDPUL

when the previous de-multiplexing algorithm was used, but failed the cut after the new algorithm was implemented. These events typically had a corrected E_2 that was slightly below the 1.25 MeV threshold when the old algorithm was used and slightly above the 1.25 MeV threshold when the new algorithm was used.

Run 49120 Event 151548   ek 12.316   tk −0.254   tpi 5.806

	Single	Kaon	Pion
Prob	0.287	0	0
Time	−1.019	0	0
Energy	12.282	0	0
Ampl	1298.45	0	0
Cut	Passed	Passed	

Kaon fiber   278 Raw High

	Single	Kaon	Pion
Prob	0.167	0.966	0.966
Time	−0.465	−1.293	5.535
Energy	12.282	9.529	2.752
Ampl	320.358	261.593	75.559
Cut	Passed	Passed	

Kaon fiber   278 Raw Low
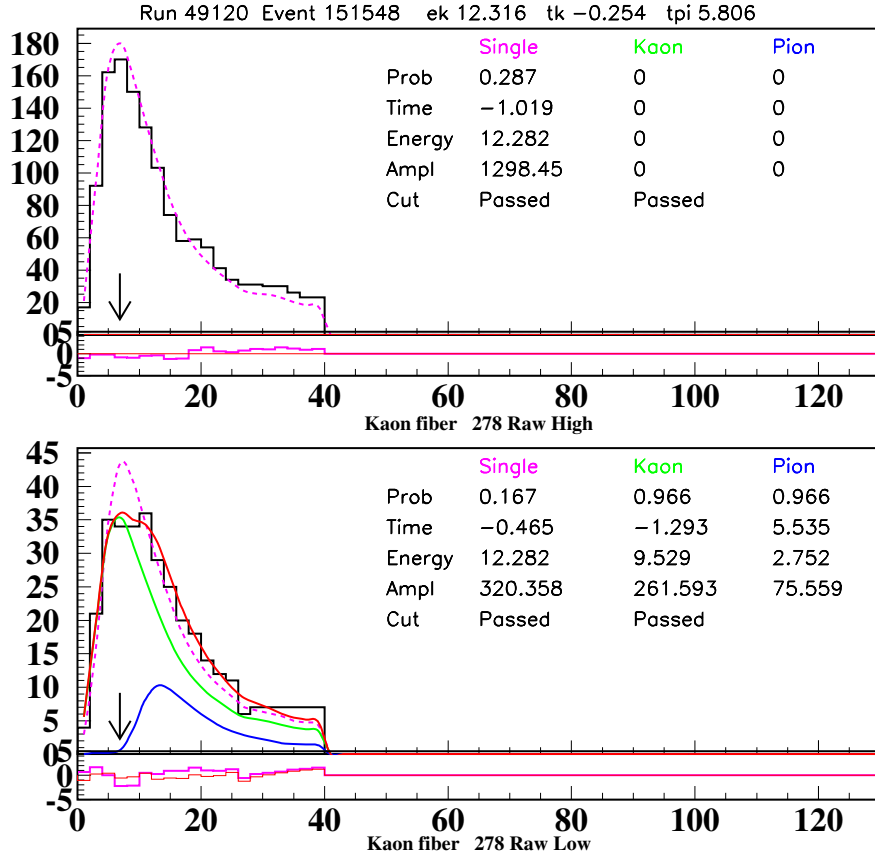
|	Old Algorithm	New Algorithm
Multiplexed kaon and pion energies (MeV)		
E_k(mux)	N/A	0.
E_π(mux)	1.58	1.58
Fitted pulse energies from ADC energy (MeV)		
Total Energy	12.28	$12.28 + 0.00 + 1.58 = 13.86$
E_1	9.53	10.76
E_2	2.75	3.10
Corrected energies (MeV)		
E_1(corr.)	9.53	10.76
E_2(corr.)	$2.75 − 1.58 = 1.17$	$3.10 − 1.58 = 1.52$

Figure E.5: Newly Rejected CCDPUL event due to new de-multiplexing algorithm. Using the old algorithm, the event passed CCDPUL with 1.17 MeV in the second pulse (E_2(corr.)). Using the new algorithm, the event passed CCDPUL with E_2(corr.) = 1.17 MeV. The multiplexed pion energy E_π(mux) came from a pion fiber in the same group that had a time of 5.98 ns and energy of 1.58 MeV.

Appendix F

Acceptance Factors for the $K^+ \rightarrow \pi^+\pi^0$ Branching Ratio

This appendix details the acceptance measurements used to find the total acceptance ($A_{\pi 2}$) used in the measurement of the $K_{\pi 2}$ branching ratio.

F.1 Acceptance Factors Using Monte Carlo

The trigger ($A_{\text{trig}}^{\text{MC}}$) and kinematic ($A_{\text{trig}}^{\text{kin}}$) components of acceptance were measured using $K_{\pi 2}$ events from the Monte Carlo simulation. The acceptance losses due to pion decay-in-flight and pion nuclear interactions were also measured due to the inclusion of these processes in Monte Carlo. The cut KP2STOP required that the stopping layer be between layers 8 and 15 inclusive. The cut UFATE required that the pion stopped without decay or interaction. The cut USTMED required that the pion stopped in the Range-Stack scintillator. The cut USTOP_HEX required that the offline reconstructed stopping counter agreed with the true stopping counter. These four cuts used information taken directly from the Monte Carlo event and not the subsequent reconstruction. The cut SETUP was a requirement that the reconstructed momentum `ptot` was less than 300 MeV. The

Cut	Events	Acceptance
SETUP	99993	
T•2	44891	0.4489
$6_{ct} + 7_{ct}$	37605	0.8377
$\overline{19_{ct}}$	36986	0.9835
UFATE	31222	0.8442
USTMED	30518	0.9775
USTOP_HEX	27426	0.8987
$A_{\text{trig}}^{\text{MC}}$	0.2743 ± 0.0014	
RDUTM	27426	1.0000
UTCQUAL	26910	0.9812
TARGET+TGQUALT	25659	0.9535
KP2STOP	24639	0.9603
COS3D	23671	0.9607
KP2BOX	20213	0.8539
$A_{\text{kin}}^{\text{MC}}$	0.7878 ± 0.0026	

Table F.1: Monte-Carlo-based components of acceptance for the $K_{\pi 2}$ branching ratio calculation. The cuts "RDUTM", "UTCQUAL" and "TARGET+TGQUALT" were used as setup cuts for the acceptance $A_{\text{kin}}^{\text{MC}}$. Table reproduced from [55].

results for these measurements are found in Table F.1.

F.2 Acceptance Factors from $K_{\pi 2}$ Monitor Trigger Events

The setup cuts applied to measure each of A_{rd}, A_{recon} and $A_{\text{bm-tg}}$ are shown in Table F.2. For each of the measurements, three additional setup cuts were applied as part of the TRIGGER cut: (1) RNGMOM to remove $K_{\mu 2}$ events, (2) the offline stopping layer had to be found in the Range Stack, and (3) the momentum was required to be in the range of $0\text{MeV}/c < \texttt{ptot} < 300\text{MeV}/c$. The second and third cuts were used to ensure good reconstruction. The results of these acceptance measurements are found in Tables

$K_{\mu 2}$ Setup Categories	Measured Quantities	Setup Cuts
$Setup_{\rm rd}$	$A_{\rm rd}$	TRIGGER, ICBIT, $t_{\rm IC} - t_{\rm CK} > 5$ns, B4DEDX, UTC, TARGET
$Setup_{\rm recon}$	$A_{\rm recon}$	TRIGGER, ICBIT, $t_{\rm IC} - t_{\rm CK} > 5$ns, B4DEDX, CPITRS, CPITAIL, CKTRS, CKTAIL, BWTRS, RVUPV, $A_{\rm rd}$ cuts
$Setup_{\rm bm-tg}$	$A_{\rm bm-tg}$	TRIGGER, ICBIT, $A_{\rm rd}$ cuts, $A_{\rm recon}$ cuts, KP2BOX, KP2STOP, IPIFLG, COS3D

Table F.2: The setup cuts applied for the components of acceptance measured for the $K_{\pi 2}$ branching ratio calculation. The notation "$A_{\rm rd}$ cuts" means that all the cuts whose acceptance were measured to determine the quantity $A_{\rm rd}$ were applied as setup cuts. Table reproduced from [55].

Cut	Events	Acceptance
$Setup_{\rm rd}$	490579	
RD_TRK	490579	1.0000
TRKTIM	490579	1.0000
$A_{\rm rd}$		1.0000 ± 0.0000

Table F.3: The acceptance $A_{\rm rd}$ for the $K_{\pi 2}$ branching ratio calculation. Table reproduced from [55].

F.3, F.4 and F.5.

F.3 Calculation of Total Acceptance

The total acceptance, $A_{\pi 2}$, used in the measurement of the $K_{\pi 2}$ branching ratio was the product of the components of acceptance determined in this appendix thus far in addition to four more acceptance factors previously determined in the PNN1 analysis [33]:

$$A_{K_{\pi 2}} = A_{\rm trig}^{\rm MC} \times A_{\rm kin}^{\rm MC} \times A_{\rm rd} \times A_{\rm recon} \times A_{\rm bm-tg} \times A_{\mu}^{\rm acc} \times A_{\rm ipiflg} \times f_s \times \epsilon_{\rm T\bullet 2}^{K\pi 2} \qquad (\text{F.1})$$

Cut	Events	Acceptance
$Setup_{\text{recon}}$	449621	
RDUTM	449621	1.0000
UTCQUAL	407402	0.9061
TARGET+TGQUALT	386491	0.9487
A_{recon}	0.8596 ± 0.0005	

Table F.4: The acceptance A_{recon} for the $K_{\pi 2}$ branching ratio calculation. Table reproduced from [55].

Cut	Events	Acceptance
$Setup_{\text{bm-tg}}$	336407	
TIC	336173	0.9993
TIMCON	334866	0.9961
TGTCON	331041	0.9886
DCBIT	293685	0.8872
DELC	257163	0.8756
CKTRS	250305	0.9733
CKTAIL	243233	0.9718
B4DEDX	239389	0.9842
CPITRS	237015	0.9901
CPITAIL	236833	0.9992
TARGF	226972	0.9584
DTGTTP	226965	1.0000
RTDIF	224789	0.9904
TGQUALT	224789	1.0000
PIGAP	222488	0.9898
TGB4	207545	0.9328
KIC	204785	0.9867
TGGEO	169847	0.8294
B4EKZ	157338	0.9264
B4ETCON	156673	0.9958
TGZFOOL	154703	0.9874
BWTRS	148013	0.9568
RVUPV	145339	0.9819
$A_{\text{bm-tg}}$	0.4320 ± 0.0009	

Table F.5: The acceptance $A_{\text{bm-tg}}$ for the $K_{\pi 2}$ branching ratio calculation. Table reproduced from [55].

	Value	Source
$A_{\mathrm{trig}}^{\mathrm{MC}}$	0.2743 ± 0.0014	Table F.1
$A_{\mathrm{kin}}^{\mathrm{MC}}$	0.7878 ± 0.0026	Table F.1
A_{rd}	1.0000 ± 0.0000	Table F.3
A_{recon}	0.8596 ± 0.0005	Table F.4
$A_{\mathrm{bm-tg}}$	0.4320 ± 0.0009	Table F.5
A_{μ}^{acc}	0.9931 ± 0.0002	[33]
A_{ipiflg}	0.8350 ± 0.8350	[33]
f_s	0.7740 ± 0.0011	[33]
$\epsilon_{\mathrm{T}\bullet 2}^{K\pi 2}$	0.9383 ± 0.0027	[33]
$A_{K_{\pi 2}}$	0.04833 ± 0.00047	

Table F.6: Summary of the components of acceptance used to find $A_{K_{\pi 2}}$ for the $K_{\pi 2}$ branching ratio calculation.

The conditions for these additional acceptance factors were the same for PNN2 as they were for PNN1. These acceptance factors were:

- $\boldsymbol{A_{\mu}^{\mathrm{acc}}}$ - the acceptance loss due to the $\overline{19_{ct}}$ requirement in the $K_{\pi 2}$ monitor trigger (Section 2.7.2);

- $\boldsymbol{A_{\mathrm{ipiflg}}}$ - Acceptance of the IPIFLG cut as measured using π_{scatter} monitor trigger data;

- $\boldsymbol{f_s}$ - K^+ stopping fraction (discussed previously in Section 6.7);

- $\boldsymbol{\epsilon_{\mathrm{T}\bullet 2}^{K\pi 2}}$ - Correction due to T$\bullet$2 trigger inefficiencies for $K_{\pi 2}$ events. This correction for $K^+ \to \nu\bar{\nu}$ events in the PNN2 phase space was discussed in Section 6.6.

The resulting acceptance $A_{K_{\pi 2}}$ was 0.04833 ± 0.00047, where the values used in this acceptance calculation can be found in Table F.6.